Structure-Activity Relationships Governing the Interaction of Nanoparticles With Mammalian Cells- Predictive Models for Toxicology and Medical Appliances

Marcus A. Maher
Technological University Dublin, Marcus.Maher@mydit.ie

Structure-Activity Relationships Governing the Interaction of Nanoparticles with Mammalian Cells – Predictive Models for Toxicology and Medical Applications.

By

Marcus A. Maher
B.Sc. Biochemistry and Molecular Biology

Ph.D. Thesis

Supervisor
Prof. Hugh J. Byrne

FOCAS Research Institute
School of Physics
Dublin Institute of Technology
Kevin Street, Dublin 8

March 2016

Abstract

Nanoscience is seen as one of the key enabling technologies of the 20th century and as its range of applications increases it is important to look at how nanomaterials interact with biological environments. Some of these interactions have given rise to toxic effects and thus, the creation of the field of nanotoxicology, it has also been noted that current methods of evaluating toxicity may not be sufficient to keep up with the rapidly emerging range of nanomaterials becoming available. It is clear that alternatives are necessary.

In this thesis, a phenomenological rate equation model is constructed to simulate nanoparticle uptake and subsequent cellular response. Poly (amido amine) (PAMAM) dendrimers, generations 4 – 6 were employed to model the response due to their well defined physico-chemical properties. Upon particle uptake, the model simulates the temporal evolution of: increased reactive oxygen species (ROS) generation, decrease in cellular anti-oxidants, caspase activation, mitochondrial membrane potential decay (MMPD), Tumour Necrosis Factor – alpha (TNF-α) and Interleukin 8 (IL-8) activation, based on previously obtained experimental data.

The simulated results match well the experimental observations over a range of different doses and time points, and over a range of different cell lines: including HaCaT (human keratinocytes), SW480 (human colon andenocarcinoma cells) and J774A.1 (mouse macrophages). Furthermore, differences in the cytotoxic responses of each cell line is understood via variation of intracellular antioxidant levels and differences in the responses to several assays is understood in terms of their sensitivity to different cellular events.

The model is able to simultaneously visualise the dose and time dependence of the toxic response of these cells to nanoparticle uptake and describes this interaction using a system

of rates, which decouple the cell and particle based parameters. This rate based approach may form the basis of a valid alternative to effective concentrations for the classification of nanotoxicity and can lay the foundation for Quantitative Structure Activity Relationships (QSARs) and a better understanding of nanoparticle Adverse Outcome Pathways (AOPs).

To further the range of applicability, the model was extended to simulate the toxicity of Polystyrene Nanoparticles with amine modified surface groups (PSNP-NH_2). PSNP-NH_2 did not share the same well-defined physico-chemical properties as PAMAM dendrimers, therefore, information on the size and extent of surface functionalisation was obtained via Scanning Electron Microscopy (SEM) and Nuclear Magnetic Resonance (NMR), respectively. The toxicity was evaluated using Alamar Blue (AB) and 3-(4,5-Dimethylthiazol-2-yl)-2,5-diphenyltetrazolium bromide (MTT) at various time points from 6 − 72 hours. Again, the model results were seen to faithfully simulate the experimental results, with identical model parameters, with the exception of the endocytosis rate (a particle size dependant property, which was modified to account for the huge disparity in size between PAMAM dendrimers and PSNP-NH_2) and rate of generation of ROS (determined by the number of surface functional groups). The consistancy of the model over a range of differnt nanopaticle types adds validity to such an approach to evaluate nanoparticle toxic potential.

Nanoparticle uptake is a critical process in the induction of toxicity. Therefore, to bypass this process could eliminate the subsequent toxic response. PAMAM dendrimers (G4 and 6) and HaCaT cells were again employed. Cells were treated with DL-Buthionine-(S,R)-sulfoximine (BSO) to enduce membrane permeability and endosomal activity was tracked

using confocal laser scanning microscopy (CLSM), ROS generation tracked with the dye Carboxy-H$_2$DCFDA and viability measued with AB and MTT.

A dramatic change compared to untreated cells occured: reduced uptake of both generations of PAMAM dendrimer, reduced ROS generation and huge increases in mitochondrial activity were observed. These results indicated that dendrimer uptake appeared to be occuring via passive diffusion into the cell, thereby avoiding the endocytosis associated ROS production. Toxicity was still noted for the higher dose regime. BSO is also known to reduce cellular Glutathione and the study highlights the importance of GSH in maintaining the redox balance of the mitochondria, but also points to the potential of controling nanoparticle toxicity via control of the uptake mechanism employed by the cell.

Finally, an acellular assay was designed to quantify the potential for a nanoparticle to generate ROS. The enzyme Monoamine Oxidase – A (MAO-A) was used to generate ROS (Hydrogen Peroxide – H$_2$O$_2$) and the effect of PAMAM and PPI dendrimer poylmers on this production were examined. The acellular reaction rate (ARR) was found to be dependant on the particle physico-chemical properties, and within a series of nanoparticles can also be related to the toxicity. The difference in relating the acellular data to experimental results between different series of particles points to the importance of cellular parameters such as uptake rate in determining toxicity. The acellular results were then modelled based on a similar series of equations as used in the cellular studies.

The cellular and acellular modelling approaches developed within this thesis, indicate that such a method may form an efficient and cost effective alternative for the evaluation of nanoparticle toxicity and furthermore, this toxicity is primarily associated with two

parameters: the cellular dependant uptake rate and the particle dependant number of surface groups.

Declaration

I certify that this thesis which I now submit for examination for the award Doctor of Philosophy (Ph.D), is entirely my own work and has not been taken from the work of others, save and to the extent that such work has been cited and acknowledged within the text of my work.

This thesis was prepared according to the regulations for postgraduate study by research of the Dublin Institute of Technology and has not been submitted in whole or in part for another award in any other third level institution. The work reported on in this thesis conforms to the principles and requirements of the DIT's guidelines for ethics in research.

DIT has permission to keep, lend or copy this thesis in whole or in part, on condition that any such use of the material of the thesis be duly acknowledged.

Signature _____ Date _____

Candidate

Acknowledgements

I would like to take a moment to acknowledge all the people who, not only helped make this thesis a success, but also made FOCAS feel more like a home away from home.

Firstly, I would like to thank Professor Hugh J Byrne, without him, none of this would have happened. Hugh was an unending fountain of information and always there to offer some help and advice during this entire process. He always had time for a meeting and I can remember feeling more motivated and driven after each one. Overall, Hugh, you were the best supervisor a student could hope for and I'm happy that I was able to get to know you during my time in FOCAS.

I would like to thank Dr. Alan Casey, his experience, knowledge and patience were invaluable while working in the lab, even when things were going wrong Alan always kept a humours and positive attitude towards it all. I would also like to thank Humza Khalid, who definitely made working on the acellular experiments a much more enjoyable time.

I would also like to thank Esen Efeoglu, always a source of optimistic happiness and amazing support; you were there when things were going well and helped me through some of the rougher times too. I can't fully put into words how much you mean to me, so I will just say: Thank you so much! Furthermore, I would like to thank everyone in NanoLab, but in particular: Zeineb Farhane, Mina Khalid and Giuliana Vozza, not only for their help with the research, but also for making the lab a much more enjoyable and friendly place to work and, of course, for the countless lunches, cups of tea and chats, which helped keep me sane

through all this! I would also like to thank Thomas, Evan, Conor, Ciara and Stephen, great friends who were always around to help me relax and blow off some steam during the more stressful times.

Finally, I would like to thank my parents, Katherine and William for their constant love, caring, support and for always listening to me go on about my research, even though sometimes they may not have known what I was talking about! Without them I certainly wouldn't be where I am today, and for that I will be forever grateful.

Abbreviations

Section 1: General Abbreviations

A549	Human Lung Adenocarcinoma Cell Line
AB	Alamar Blue
AOP	Adverse Outcome Pathway
AFM	Atomic Force Microscopy
APAF-1	Apoptotic Protease Activating Factor 1
APF	Aminophenyl Fluorescein
ARR	Acellular Reaction Rate
ATP	Adenosine Tri-Phosphate
Bcl-2	B-cell lymphoma 2
BH3	Bcl-2 Homology Domain 3
BID	BH3 interacting-domain death agonist
BSO	DL-Buthionine-(S,R)-sulfoximine
Caco-2	Human epithelial colorectal adenocarcinoma cells
Carboxy-H_2DCFDA	6-carboxy-2',7'-dichlorodihydrofluorescein diacetate
CD-95	Cluster of Differentiation 95
CLSM	Confocal Laser Scanning Microscopy
CMV	CytoMegaloVirus
CXC	Cysteine - other Amino Acid – Cysteine Homology
CXCR	Cysteine - other Amino Acid – Cysteine Homology Receptor
DCF	DiChlorodihydro Fluorescein

DEM	Diethylmaleate
DIT	Dublin Institute of Technology
DMEM	Dublecco's Modified Eagle's Medium
DNA	Deoxyribonucleic Acid
EC_{50}	Effective Concentration for 50% loss of viability
ELISA	Enzyme-Linked ImmunoSorbent Assay
EU	European Union
EuTc	Europium TetraCycline
Fas	Type-II transmembrane protein, belonging to the TNF family.
FBS	Fetal Bovine Serum
FAD	Flavin Adenine Dinucleotide
FADD	Fas Associated Death Domain
FE-SEM	Field Emission Scanning Electron Microscopy
FLICE	FADD-like interleukin-1 beta-converting enzyme
FLIP	FLICE-like inhibitory protein
G(#)	Generation (number)
gH625	Peptide derived from Herpes simplex virus – 1
GS	Ground State
GSSG	Glutathione Disulphide
GSA	Global Sensitivity Analysis
GSH	Glutathione
H_2O_2	Hydrogen Peroxide
HaCaT	Human keratinocyte cell line

HEK293	Human Embryonic Kidney cells
HIV	Human Immunodeficiency Virus
HPF	Hydroxyphenyl Fluorescein
HRP	HorseRadish Peroxidase
IATA	Integrated Approaches to Testing and Assessment
IL-6	Interleukin 6
IL-8	Interleukin 8
INSPIRE	Integrated Nano Science Platform IREland
ISC	Inter System Crossing
ISO	International Organization for Standardization
J774A.1	Murine Macrophage cell line
JACoP	Just Another Colocalization Plugin
JRC	Joint Research Centre
λ_{abs}	Absorption wavelength
λ_{ex}	Excitation wavelength
λ_{em}	Emission wavelength
LPS	LipoPolySaccharide
MAPK	Mitogen Activated Protein Kinase
MAO-A	MonoAmine Oxidase A
MIE	Molecular Initiating Event
MMP	Mitochondrial Membrane Potential
MMPD	Mitochondrial Membrane Potential Decay
MRI	Magnetic Resonsnce Imaging

MTS	3-(4,5-dimethylthiazol-2-yl)-5-(3-carboxymethoxyphenyl)-2-(4-sulfophenyl)-2H-tetrazolium dye
MTT	3-(4,5-Dimethylthiazol-2-yl)-2,5-diphenyltetrazolium bromide
NAC	N-acetyl cysteine
NACA	N-acetyl cysteine amide
NADPH	Nicotinamide Adenine Dinucleotide Phosphate
NF-κB	Nuclear Factor kappa-light-chain-enhancer of activated B cells
NMR	Nuclear Magnetic Resonance
NP	Nano Particle
NR	Neutral Red
ODE	Ordinary Differential Equation
OECD	Organisation for Economic Co-operation and Development
PAMAM	Poly (amido amine)
PBS	Phosphate Buffered Saline
PEN	Project on Emerging Nanotechnologies
PPI	Poly (propylene imine)
PSNP	Polystyrene Nanoparticle
PSNP-NH$_2$	Amine Surface Modified Polystyrene Nanoparticles
QNAR	Quantative Nanostructure-Activity Relationship
QSAR	Quantative Structure-Activity Relationship
Rab-5A	Protein involved with endosomal formation and maturation
RAW276.4	Abelson murine leukaemia virus-induced tumour cells
RFP	Red Fluorescent Protein

ROS	Reactive Oxygen Species
S(#)	Singlet State
SBML-SAT	Systems Biology Markup Language - Sensitivity Analysis Tool
SEM	Scanning Electron Microscope
SCENIHR	Scientific Committee on Emerging and Newly Identified Health Risks
SSoE	Systematic Sequence of Events
SW480	Human colon adenocarcinoma cell line
T(#)	Triplet State (#)
TNF-α	Tumour Necrosis Factor - alpha
TTV	Thiol Tracker Violet
TUNEL	Terminal deoxynucleotidyl transferase dUTP Nick-End Labeling
US	United States
UV	Ultra Violet
WI38	Human Fibroblast Cell Line

Section 2: Equation/Model Abbreviations

Rates

k_{12} Dose and Generation dependant rate constant for acellular model

k_{21} Reverse reaction rate constant of MAO-A enzyme involving N_{ald} and N_{ami}

k_{31} Rate constant of generation of fluorescence of DCF dye

k_{apop} Rate Constant of Apoptosis

k_{endo} Rate Constant of Endocytosis

k_{enz} Forward reaction rate of MAO-A involving N_{sero} and N_{H2O}

k_{exo} Rate Constant of Exocytosis

k_{GSH} Rate Constant of Glutathione Increase

$k_{IL\text{-}8}$ Rate Constant of Increase in Interleukin-8

k_{inflam} Rate Constant of Inflammation

k_{λ} Rate Constant of Cell Replication

k_{mito} Rate Constant of Mitochondrial Damage

k_{MMP} Rate Constant of loss of Mitochondrial Membrane Potential

k_{q} Rate Constant of Reactive Oxygen Species Quenching

k_{rec} Recovery Rate Constant of a Cell

k_{ROS} Rate Constant of Reactive Oxygen Production

k_{TNF} Rate Constant of Tumour Necrosis Factor Release

k_{V} Rate Constant of loss of Viable Cells

Amounts

N_{ald} Amount of Aldehyde Formed

N_{amg} Number of Surface Amino Groups

N_{ami} Amount of Amine Formed

N_{apop} Amount of cells undergoing Apoptosis

N_D Dendrimer Dose (Acellular Model)

N_{DCF} Amount of DCF Activated

N_{endo} Amount of Endocytosed Nanoparticles

N_F Amount of DCF Fluorescence

N_{ground} Amount of Cells in Ground State

N_{GSH} Amount of Glutathione in the Cell

N_{H2O} Amount of Water

N_{H2O2} Amount of Hydrogen Peroxide

N_{IL-8} Amount of Interleukin 8 released

N_{inflam} Amount of Cells in the Inflammatory Cascade

N_{mito} Amount of Cells with Mitochondrial Damage

N_{MMP} Amount of Cells with loss of Mitochondrial Membrane Potential

N_{ROS} Amount of Reactive Oxygen Species Produced

N_{sero} Amount of Serotonin

N_{source} Amount of Source material for production of Reactive Oxygen Species

N_{TNF} Amount of Tumour Necrosis Factor – alpha released

N_V Amount of Non-Viable Cells

Table of Contents

xviii

Tables

Chapter 1:

Table 1.1: Table of the physico-chemical properties and toxicity data for PAMAM dendrimers Generations 4 – 6.

Chapter 3:

Table S3.1: Parameters employed for the final simulated datasets.

Chapter 4:

Table 4.1: EC_{50} data for 50nm PSNP-NH$_2$ at each time point in HaCaT cells, according to the AB and MTT assay (expressed as µM ± standard error as calculated by SigmaPlot v10.0).

Table 4.2: EC_{50} data for 100nm PSNP-NH$_2$ at each time point in HaCaT cells, according to the AB and MTT assay (expressed as µM ± standard error as calculated by SigmaPlot v10.0).

Table 4.3: EC_{50} data for 50nm and 100nm PSNP-NH$_2$ at each time point in HaCaT cells, according to the AB and MTT assay (expressed as particle number (± standard error), based on the EC_{50} data obtained by SigmaPlot v10.0^{TM} and calculated in accordance with manufacturers guidelines).

Table S4.1: P-values calculated from the fitting of EC_{50} data for 50nm and 100nm PSNP-NH_2 at each time point in HaCaT cells, according to the AB and MTT assay as calculated by SigmaPlot v10.0.

Table S4.2: R^2 values calculated from the fitting of EC_{50} data for 50nm and 100nm PSNP-NH_2 at each time point in HaCaT cells, according to the AB and MTT assay as calculated by SigmaPlot v10.0.

Table S4.3: Parameters employed for the final simulated datasets for both the PSNP-NH_2 and PAMAM dendrimer.

Chapter 6:

Table S6.1: Table showing all the factors and rates used for modelling the PAMAM and PPI nanoparticles (**bold** used to highlight changes in rates between the two models).

Table S6.2: Comparison of PAMAM and PPI dendrimer blank values at comparable concentrations.

Figures

Chapter 1

Figure 1.1: Image of G1, G2, G3 and G4 PAMAM nanoparticles, here the increasing size and number of terminal groups, as a function of increasing Generation, is visible. (*Image adapted from: Kim et al., 2013, Patent Number: EP2604289 A2*)

Figure 1.2: Image showing the stages of endosome formation and intake into the cytosol. (*Image adapted from: Vácha et al, 2011, Nano Lett. 11, 5391–5395*)

Figure 1.3: Reaction of Glutathione with Hydrogen Peroxide, oxidation of glutathione and subsequent reduction of glutathione disulphide via glutathione reductase.

Figure 1.4: Image showing the interaction of the components involved in aminated dendritic polymer nanoparticle induced toxicity and subsequent apoptosis. (*Image adapted from the supplementary material of: Mukherjee and Byrne, 2013, Nanomed: Nanotech. Bio. Med., 9(2), 202-211*).

Figure 1.5: Schematic of systematic sequence of events upon nanoparticle uptake.

Chapter 2

Figure 2.1: A Jablonski diagram showing electron energy levels after excitation by an incidence beam of radiation. (*Image adapted from: Einstein, A. Verhandlungen der Deutschen Physikalischen Gesellschaft, **18**, 318–323 (1916)*)

$\lambda_{ex} \approx 517nm - 527nm$). (Image adapted from product supplier: Invitrogen (part of Thermo Fisher Scientific, available online at:

https://www.thermofisher.com/order/catalog/product/C369)

Chapter 3

Figure 3.2: Experimental (*Naha et al., 2010*) and simulated cellular responses of J744A.1 murine macrophages to exposure to G4 PAMAM dendrimers at a fixed dose of 1μM. Results are normalised to a maximum value of 1 for visualisation purposes, with the exception of the MTT data (viability), which experimentally have been normalized to the unexposed control.

Figure 3.3: Experimentally observed (symbols) (expressed as the % increase in Carboxy-H_2DCFDA fluorescence compared to control, at a fixed timepoint of 4hrs (*Naha et al., 2010*)) and simulated (lines) dose and generation dependent intracellular ROS generation after 4hr exposure of J744A.1 mouse macrophages to PAMAM dendrimers.

Figure 3.4: A 3D graph showing both the simulated time and dose dependence of the ROS evolution, in J744A.1 mouse macrophages, upon G4 PAMAM nanoparticle uptake.

Figure 3.5: Experimental (symbols) and simulated (lines) dose dependent viability, as measured using the MTT assay, for J744A.1 murine macrophages at 6hr, 12hr and 24hr (experimental data from *Naha et al., 2010*).

Figure 3.6: Experimental (symbols) and simulated (lines) dose dependent J744A.1 mouse macrophage viability at 12 hrs, as measured using the MTT assay, for PAMAM generations G4, G5 and G6 (experimental data from *Naha et al., 2010*).

Figure 3.7: 3D simulated time and dose dependence of MTT response for exposure of J744A.1 murine macrophage cells to PAMAM G4.

Figure 3.8: Experimental (symbols) and simulated (lines) viability of different cell lines, as measured using the MTT assay, after exposure to PAMAM G4 for 24hrs. Experimental data for J774A.1 derived from *Naha et al.* (*2010*). Experimental data for SW480 and HaCaT derived from *Mukherjee et al.* (*2010-A*).

Figure 3.9: Comparison of Experimental (symbols) and simulated (lines) viabilities as measured by MTT, Alamar Blue and Neutral Red, for exposure of SW480 cells to PAMAM G4 after 24 hrs. Experimental data from *Mukherjee et al. (2010-A)*. For each assay, the data has been normalized to unexposed control.

Figure S3.1: Dose dependent ROS generation for all generations simulated according to Equation 3.10.

Figure S3.2: Simulated time dependent uptake of PAMAM dendrimers of generation G4, G5, G6, according to Equation 3.2, at a fixed dose of 1μM.

Figure S3.3(A-C): Variation in simulated (lines) increase in ROS levels on the parameter k_{endo} in Equation 3.2, compared to experimental data (symbols) for G4, G5, G6. A: $k_{endo} = 0.25hr^{-1}$, B: $k_{endo} = 0.75\ hr^{-1}$, C: $k_{endo} = 1.25hr^{-1}$.

Figure S3.4(A-C): Variation in simulated (lines) increase in ROS levels on the parameter $(N_{amg})^c$ in Equation 3.2, compared to experimental data (symbols) for G4, G5, G6. A: $c = 0$, B: $c = 0.25$ and C: $c = 1$.

Figure S3.5(A-C): Variation in simulated (lines) increase in ROS levels on the parameter k_A compared to experimental data (symbols) for G4, G5, G6. A: $k_A = 0.0004\ hr^{-1}$, B: $k_A = 0.0011 hr^{-1}$ and C: $k_A = 0.0018\ hr^{-1}$.

Figure S3.6(A-C): Variation in simulated (lines) increase in ROS levels on the exponential value in the equation $G* = 1/(N_{amg}^{0.25})$, compared to experimental data (symbols) for G4, G5, G6. A: *Exponent value = 0.083*, B: *Exponent Value = 0.25*, C: *Exponent Value = 0.42*.

Figure S3.7(A-C): Variation in simulated (lines) increase in ROS levels on the exponential value in the equation $A = (N_{amg}/64)^{0.75}$, compared to experimental data (symbols) for G4, G5, G6. A: *Exponent value = 0.25*, B: *Exponent Value = 0.75*, C: *Exponent Value = 1.25*.

Figure S3.8(A-C): Variation in simulated (lines) increase in ROS levels on the parameter B in Equation 3.11/3.12, compared to experimental data (symbols) for G4, G5, G6. A: $B = 1$, B: $B = 3$ and C: $B = 5$.

Figure S3.9(A-C): Effect of variation of the parameter k_{MMP} on simulated (lines) viability compared to experimental data (symbols) for G4 at timepoints: 6hrs, 12hrs and 24hrs. A: $k_{MMP} = 0.0007$, B: $k_{MMP} = 0.0010$ and C: $k_{MMP} = 0.0013$.

Figure 4.3(a-e): AB and MTT dose dependant toxicity results for 50nm PSNP-NH$_2$ in HaCaT cells after 6, 12, 24, 48 and 72hrs. Viability is calculated as the percentage of living cells as compared to an unexposed control. Results are shown as mean ± standard deviation. The solid line represents the EC$_{50}$ curve fit to the AB data and the dotted line represents the EC$_{50}$ curve fit to the MTT data.

Figure 4.4: Toxicity of the 100nm PSNP-NH$_2$ according to the Alamar Blue (a) and MTT (b) assays. The lines shown were generated by SigmaPlot v10.0 for calculation of the EC$_{50}$ values. Data points are shown as the mean ± standard deviation.

Figure 4.5(a-e): AB and MTT dose dependant toxicity results for 100nm PSNP-NH$_2$ in HaCaT cells after 6, 12, 24, 48 and 72hrs. Viability is calculated as the percentage of living cells as compared to an unexposed control. Results are shown as mean ± standard deviation. The solid line represents the EC$_{50}$ curve fit to the AB data and the dotted line represents the EC$_{50}$ curve fit to the MTT data.

Figure 4.6: Comparison of 50nm and 100nm (a) Alamar Blue (AB) and (b) MTT EC$_{50}$ values as calculated by SigmaPlot V10.0; error bars show ± standard error on the EC$_{50}$ value.

Figure 4.7: Comparison of 50nm and 100nm (a) Alamar Blue (AB) and (b) MTT EC$_{50}$ values expressed as particle number; error bars were calculated based on the standard error of the EC$_{50}$ value.

Figure 4.8: Experimental (symbols) and simulated (lines) dose dependent HaCaT cell viability at 24 hrs, for 50nm (●) and 100nm (○) PSNP-NH$_2$ as measured using the MTT assay. Error bars are the standard deviation of the experimental data.

Figure 4.9: Experimental (symbols) and simulated (lines) dose dependent HaCaT cell viability at 6 (●), 12(○) and 24(▼) hours, for 50nm PSNP-NH$_2$ as measured using the MTT assay. Error bars are the standard deviation of the experimental data.

Figure S4.1: Additional SEM images of spin coated 50nm(a and b) and 100nm(c and d) polystyrene nanoparticles PSNP-NH$_2$. Images were taken on a Hitachi SU 6600 FESEM and low eV (0.8 – 2.5) was used due to the non-conductive nature of the sample.

Figure S4.2: 1H-NMR spectra of 50nm PSNP-NH$_2$(a), 100nm PSNP-NH$_2$(b) and 100nm PSNP-neu(c) taken on a Bruker Advance II 400 MHz instrument, with D$_2$O used as the solvent for a 128 scan cycle.

Chapter 5

Figure 5.1: CLSM images of HaCaT (live) cells, upon exposure to 3.21μM PAMAM G4 dendrimer at 3 hours (no BSO is present in this sample). Image a) shows the bright field image of the cells, Image b) shows the fluorescence generated by the early endosomal red fluorescent protein, Image c) shows the fluorescence generated by the ROS (interacting

with the carboxy-H$_2$DCFDA dye) and Image d) shows the overlay of images a-c, where yellow coloured areas indicate simultaneous endosomal and ROS activity.

Figure 5.2: Confocal images of HaCaT (live) cells, upon exposure to 3.21μM PAMAM G4 dendrimer at 3 hours, with pre-treatment of BSO: 200μM for 18 hours. Image a) shows the bright field image of the cells, Image b) shows the fluorescence generated by the early endosomal red fluorescent protein, Image c) shows the fluorescence generated by the ROS (interacting with the carboxy-H$_2$DCFDA dye) and Image d) shows the overlay of images a-c, where yellow coloured areas indicate simultaneous endosomal and ROS activity.

Figure 5.3: Dose dependant generation of ROS in HaCaT cells (shown for 24 hours for the PAMAM G4). ROS is compared to BSO control which was set to equal 0%. The X-axis is plotted logarithmically to allow for better visualisation of lower concentrations. Data points are the mean of 18 samples, with error bars showing (±) the standard deviation.

Figure 5.4: Alamar Blue (a) and MTT (b) dose dependant viability results for PAMAM G4 dendrimers in HaCaT cells after 6, 12, 24, 48 and 72 hours. Viability is calculated as the percentage of living cells as compared to BSO control. Data points are the mean of 18 samples, with error bars showing (±) the standard deviation.

Figure 5.5: Confocal images of HaCaT (live) cells, upon exposure to 1μM PAMAM G6 dendrimer at 1 hour (no BSO is present in this sample). Image a) shows the bright field image of the cells, Image b) shows the fluorescence generated by the early endosomal red

fluorescent protein, Image c) shows the fluorescence generated by the ROS (interacting with the carboxy-H₂DCFDA dye) and Image d) shows the overlay of images a-c, where yellow coloured areas indicate simultaneous endosomal and ROS activity.

Figure 5.6: Confocal images of HaCaT (live) cells, upon exposure to 1μM PAMAM G6 dendrimer at 1 hour, with pre-treatment of BSO: 200μM. Image a) shows the bright field image of the cells, Image b) shows the fluorescence generated by the early endosomal red fluorescent protein, Image c) shows the fluorescence generated by the ROS (interacting with the carboxy-H₂DCFDA dye) and Image d) shows the overlay of images a-c, where yellow coloured areas indicate simultaneous endosomal and ROS activity.

Figure 5.7: Dose dependant generation of ROS in HaCaT cells (shown at 24 hours for the PAMAM G6). ROS is compared to BSO control which was set to equal 0%. The X-axis is plotted logarithmically to allow for better visualisation of lower concentrations. Data points are the mean of 18 samples, with error bars showing (±) the standard deviation.

Figure 5.8: Alamar Blue (a) and MTT (b) dose dependant toxicity results for PAMAM G6 dendrimers in HaCaT cells after 6, 12, 24, 48 and 72 hours. Viability is calculated as the percentage of living cells as compared to a BSO control. The X-axis is plotted logarithmically to allow for better visualisation of lower doses. Data points are the mean of 18 samples, with error bars showing (±) the standard deviation.

Figure 5.9: Alamar Blue (AB) dose dependant toxicity results comparing the PAMAM G4 and G6 dendrimers in HaCaT cells after 48 hours (a) and 72 hours (b). Viability is calculated as the percentage of living cells as compared to BSO control. Data points are the mean of 18 samples, with error bars showing (±) the standard deviation. The x-axis is plotted logarithmically to allow for better visualisation of lower doses. 6, 12 and 24 hour graphs can be seen in the supplementary information section (Figure S5.6).

Figure 5.10: MTT dose dependant toxicity results comparing the PAMAM G4 and G6 dendrimers in HaCaT cells after 48 hours (a) and 72 hours (b). Viability is calculated as the percentage of living cells as compared to BSO control. Data points are the mean of 18 samples, with error bars showing (±) the standard deviation. The X-axis is plotted logarithmically to allow for better visualisation of lower doses. 6, 12 and 24 hour graphs can be seen in the supplementary information section (Figure S5.7).

Figure 5.11: Dose dependant generation of ROS in HaCaT cells (shown at 24 hours for PAMAM G4 and G6). Data is compared to BSO control which was set to equal 0%. The X-axis is plotted logarithmically to allow for better visualisation of lower concentrations. Data points are the mean of 18 samples, with error bars showing (±) the standard deviation.

Figure S5.1: Graph comparing unexposed control cells (dashed line) to cells with 200μM BSO at 6, 12, 24, 48 and 72 hours as registered by the AB and MTT assays (white and grey bars, respectively). Data points are the mean of 18 samples, with error bars showing (±) the standard deviation.

Figure S5.2: Confocal images of HaCaT (live) cells, upon exposure to 1μM PSNP 100nm with green fluorescent dye bound. Image a) shows the greyscale picture of the cells, Image b) shows the fluorescence generated by the early endosomal red fluorescent protein, Image c) shows the fluorescence generated by 100nm PSNP and Image d) shows the overlay of images a-c, where yellow coloured areas indicate the simultaneous presence of endosomes and PSNP (100nm).

Figure S5.3: The % Cellular Viability (compared to unexposed control) according to the AB and MTT assays, for 200μM BSO in the Human Keratinocyte (HaCaT) cell line.

Figure S5.4: The full dose dependant ROS production for PAMAM G4 for times: 0, 1, 2, 3, 4, 6, 12 and 24 hours. a) Shows the results with the associated error bars (± standard deviation) and b) Shows the data without the error bars, to allow for easier visualisation of the overall trend. As with graphs in the main text, the x-axis is plotted logarithmically to allow for better visualisation of lower doses. Data points are the mean of 18 samples, with error bars showing (±) the standard deviation.

Figure S5.5: The full dose dependant ROS production for PAMAM G6 for times: 0, 1, 2, 3, 4, 6, 12 and 24 hours. a) Shows the results with the associated error bars (± standard deviation) and b) Shows the data without the error bars, to allow for easier visualisation of the overall trend. As with graphs in the main text, the x-axis is plotted logarithmically to

allow for better visualisation of lower doses. Data points are the mean of 18 samples, with error bars showing (±) the standard deviation.

Figure S5.6: Alamar Blue (AB) dose dependant toxicity results comparing the PAMAM G4 and G6 dendrimers in HaCaT cells after 6(a), 12(b) and 24 hours(c). Viability is calculated as the percentage of living cells as compared to a 200μM BSO control. Results are shown as mean ± standard deviation. The X-axis is plotted logarithmically to allow for better visualisation of lower doses. Data points are the mean of 18 samples, with error bars showing (±) the standard deviation.

Figure S5.7: MTT dose dependant toxicity results comparing the PAMAM G4 and G6 dendrimers in HaCaT cells after 6(a), 12(b) and 24 hours(c). Viability is calculated as the percentage of living cells as compared to a 200μM BSO control. Results are shown as mean ± standard deviation. The X-axis is plotted logarithmically to allow for better visualisation of lower doses. Data points are the mean of 18 samples, with error bars showing (±) the standard deviation.

Chapter 6

Figure 6.1: Generalised reaction mechanism of Monoamine Oxidase-A In the case of this study, serotonin was used as a substrate (therefore R' is H) and the products are 5-hydroxyindole acetaldehyde, hydrogen peroxide (H_2O_2) and ammonia (NH_3) (*Sigma-Aldrich, 2015*).

Figure 6.2 (a): Plot of the concentration dependent fluorescence intensity for PAMAM dendrimers G4(●), G5(○), G6(▼), G7(Δ) (b): Plot of the concentration dependent fluorescence intensity for PPI dendrimers G0(■), G1(Δ), G2(●), G3(○) , G4 (▼). The lines are a linear regression fit to the data.

Figure 6.3: (a) Plot of the slope as a function of Number of Surface Amino Groups (N_{amg}) for all PAMAM and PPI dendrimers. The solid line shows a fit to a linear dependence for the combined dendrimer series. (b) Plot of the slope as a function of Number of Surface Amino Groups for PPI dendrimers. The solid line shows a fit to a linear dependence.

Figure 6.4 (a): Plot of the Acellular reaction rate (ARR) for all PAMAM and PPI dendrimers versus the inverse cytotoxicity as previously measured using the MTT assay (*Mukherjee et al., 2010-A and B* and *Naha et al., 2010*) (b): Plot of the Acellular reaction rate (ARR) for PPI dendrimers versus the inverse cytotoxicity as previously measured using the MTT assay. The lines show a fit of linear dependences.

Figure 6.5: Simulated generation of fluorescence based on the rate equation model of Equations 6.2-6.4, for dendrimer generations 3-7 (lines). Also shown are the experimental data for PAMAM dendrimers G4(●), G5(○), G6(▼), G7(Δ), and PPI dendrimers G2(■), G3(▽), G4(●).

Figure 6.6: Simulated generation of fluorescence based on the rate equation model of Equations 6.2-6.4, for PPI dendrimer generations 0-4 (lines). Also shown are the experimental data for PPI dendrimers G4(●), G3(▽), G2(■), G1(◇), G0(▲).

Figure S6.1: Schematic representation of the experimental set-up of the 96 well plates.

Chapter 7

Figure 7.1: Classic AOP format, adapted from the Systematic sequence of events upon amine modified PAMAM exposure to HaCaT cells. This shows particle uptake by endocytosis, leading to increased ROS production, causing mitochondrial membrane potential decay (MMPD) and the subsequent induction of the inflammatory cascade and apoptosis. However, it should be noted that this is a simplified representation of an AOP.

Figure 7.2: Chemically agnostic AOP design. Again a simplified representation of amine modified PAMAM toxicity is depicted here, based on the SSoE of Chapter 3: Numerical simulations of *in vitro* nanoparticle toxicity − the case of Poly (amido amine) dendrimers (*Maher et al., 2014*). Here the central AOP presented is chemically agnostic; meaning that all the steps occurring within it are based on cellular events, these events were initiated by a Molecular Initiating Event (MIE), which in this case is identified as increased ROS production. In this set up several different MIEs could be incorporated into the AOP at the appropriate step in the pathway.

Figure 7.3: Here the proposed AOP of Figure 7.2, based on PAMAM exposure to HaCaT cells is expanded upon to take nanoparticle entry route into account. The MIE for passive diffusion is not fully defined, but is currently associated with localisation to and subsequent disruption of the mitochondria, such an AOP system can be updated when a molecular event is found and, critically, the central AOP is maintained in a chemically agnostic state. Again, this representation is a simplified version of an AOP.

Chapter 1

Introduction

1.1 Nano-Science

Nanomaterial science is a relatively new and still rapidly advancing area, with potential uses in a vast and diverse range of applications, such as: medicine, medical devices, light weight construction materials, surface coatings, clothing and many more (*Wagner et al, 2006, Rana et al., 2009, Davis, 1997* and *Montazer et al., 2011-A*). In fact, the "Project on Emerging Nanotechnologies (PEN)" website, nanotechproject.org, lists over 1600 products which contain or in some way use nanotechnology (*PEN, 2016*). The use of nanomaterials in medicine and medical devices is of particular importance.

Nanomaterials have the ability to easily enter living cells (by known uptake mechanisms, such as endocytosis) (*Vácha et al., 2011*) and this property gives them huge potential for the targeted delivery of drugs and other biologically relevant molecules, which, traditionally have poor bio-availability (*De Jong and Borm, 2008*). This delivery method can be used for the treatment of many conditions, including; cancer (*Haley and Frenkel, 2008*), heart disease (*Liu et al., 2014*), lung disease (*Kuzmov and Minko, 2015*), inflammation (*Clares et al., 2012*), abnormal blood pressure (*Bonner et al., 2009*) and immune response (*Zolnik et al., 2010*). However, the uptake of nanomaterials into cells has also, in some cases, been shown to elicit a toxic response (*Nel et al., 2006* and *Jain et al., 2010*) and the study of this response has led to the creation of the field of: nanotoxicology (*Donaldson et al., 2004*).

In this work, the *in vitro* toxic response of nanoparticles is studied with the aim of exploring predictive models which will simulate experimentally determined toxic responses based on the physical parameters of the nanoparticle and the biological properties of the cell. Using this modelling approach, and decoupling the particle and cell dependant

properties, will allow for the elucidation of which key particle parameters and cellular events govern the toxicity. Such a model would aid toxicology by reducing the time needed to run *in vitro* tests and, ultimately, could be extended to cover *in vivo* experiments (*Clark et al., 2011*). Additionally, the acellular reactivity of known toxic nanoparticles is examined and the key physico-chemical properties which effect reactivity are identified and related to the cellular response, thus allowing better understanding, and therefore, control of the key particle parameters governing toxicity. Such an acellular model could be used, initially, to screen nanoparticles for activity which indicates potential toxicity using high throughput techniques.

Critically, to model such a set of events, it is essential to study particles with well defined physico-chemical properties. Poly (amido amine) (PAMAM) dendritic polymer nanoparticles have well defined physico-chemical properties and are known to enter into cells and induce a toxic response. Furthermore, systematic variation of the physico-chemical properties of the nanoparticle elicits systematic changes to the observed toxic response (*Mukherjee et al., 2010 – A and B, Naha et al., 2009, 2010 and 2013* and *Mukherjee and Byrne, 2013*). Therefore, PAMAM dendrimers were chosen as the primary particle for modelling.

1.2 Definition of a nanoparticle

Although there is still debate over the exact definition of a nanoparticle, for the purposes of this project, the European Union (EU) definition will be used, which in 2011 defined a nanoparticle as a particle with an external dimension of the range 1nm – 100nm (*EU, 2011*):

Official Journal of the European Union,

Commission Recommendation of 18 October 2011 on the definition of

nanomaterials: (2011/696/EU). Adopted recommendation number 2 (page:

L275/40):

" 'Nanomaterial' means a natural, incidental or manufactured material containing

particles, in an unbound state or as an aggregate or as an agglomerate and where,

for 50 % or more of the particles in the number size distribution, one or more

external dimensions is in the size range 1 nm-100 nm."

This definition is set to be reviewed in December 2015, although, the report of the

European Commission: Joint Research Centre (JRC) from June 2015 strongly recommends

that this current definition be upheld (*Rauscher et al., 2015*).

Most current debate appears to chiefly concern what is to be considered a "dimension" of a

nanoparticle. However, in this thesis the Poly (amido amine) (PAMAM), poly (propylene

imine) (PPI) and polystyrene nanoparticles (PSNP), were used and all fit within the EU

definition. PAMAM dendrimers were chosen due to their well defined structure and

because by systematically varying that structure similar systematic variations in toxic

response have been observed (*Mukherjee et al., 2010 – A and B, Naha et al., 2009 and

2010, Naha and Byrne, 2013* and *Mukherjee and Byrne, 2013*), making them an invaluable

tool for modelling. PAMAM dendrimers are used in Chapter 3, in which the cellular

response to PAMAM endocytosis is modelled and compared to a set of published results

(*Maher et al., 2014*), in Chapter 5, in which the effect of endocytosis of PAMAM

dendrimers is evaluated in relation to the production of ROS and Chapter 6, in which the acellular reactivity of dendritic polymer nanoparticles is explored (*Maher et al., 2016*). PPI dendrimers have similar properties to PAMAM dendrimers (*Khalid et al., 2016*) and were used in Chapter 6, again analysing the acellular reactivity of dendritic polymer nanoparticles (*Maher et al., 2016*).

Polystyrene nanoparticles (PSNP) are commercially available in a range of different sizes and surface functionalisations and have been used in many studies as, for example: cytotoxicity standards (*Anguissola et al., 2014*), cellular localisation probes (*Dorney et al., 2012* and *Efeoglu et al., 2015*) and targeted drug delivery vehicles (*Yacobi et al., 2008*, *Kloet et al., 2011*, *Lunov et al., 2011* and *Anguissola et al., 2014*), but are not as structurally defined as PAMAM and PPI dendrimers. Nevertheless, they are thus useful in testing the accuracy of the model when there is a degree of variability in nanoparticle properties, and these are used in Chapter 4, in which their cytotoxic response is evaluated and modelled with the same set of equation as used in Chapter 3.

1.3 PAMAM Dendritic Polymer Nanoparticles

In this study, to elucidate the mechanisms underlying nanoparticle toxicity: Poly (amido amine) (PAMAM) dendrimer nanoparticles were used. PAMAM dendrimers are branched nanoparticles consisting of three main parts, (i) the initiator core, (ii) the interior branches and (iii) the exposed branch termini (*Tomalia and Fréchet, 2002*). These particles are created via addition of branches onto the initiator core; each branch then has two more sites, where additional branches can be added (see figure 1.1), forming larger and larger structures. Each successive set of these branches is called a generation (G). The generation

determines the number of surface groups (in this thesis: primary amine groups), according to the formula:

$$N_{amg} = N_{BP(G0)} \cdot 2^{G}$$

Equation 1.1

In Equation 1.1: N_{amg} is the number of surface amino groups, $N_{BP(G0)}$ is the number of initial branching points at generation zero (G0) and G denotes the generation number. Thus, the diameter and number of surface amino-groups increases systematically with increasing generation (as can be seen in Table 1.1).
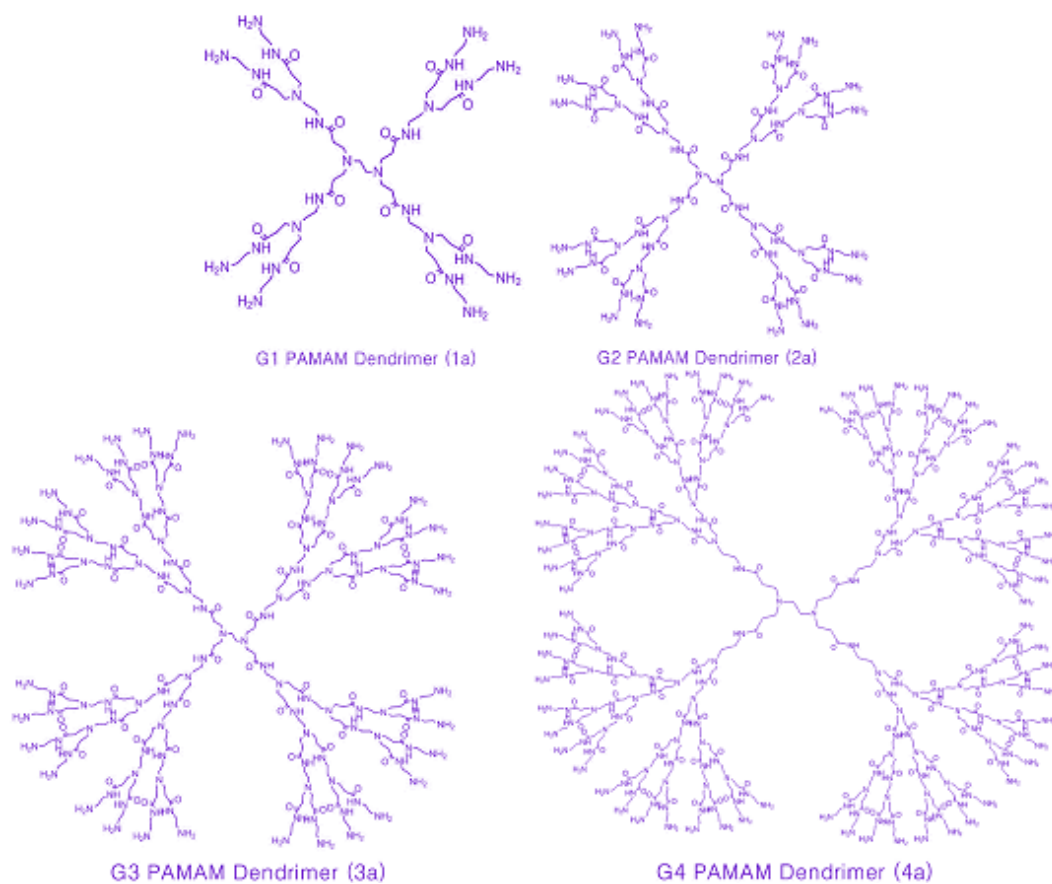
Figure 1.1: Image of G1, G2, G3 and G4 PAMAM nanoparticles, here the increasing size and number of terminal groups, as a function of increasing Generation is visible.

(*Image adapted from: Kim et al., 2013, Patent Number: EP2604289 A2*)

Table 1.1: Table of the physico-chemical properties and toxicity data for PAMAM dendrimers Generations 4 – 6. Toxicity data is expressed as EC_{50} obtained from HaCaT cells using the MTT assay (*Mukherjee et al., 2010 – A*).

	Molecular Weight (g/mol)	Number of Surface Amino Groups (N_{amg})	Particle size (Nominal) (nm)	Particle size (as measured by AFM) (nm)	EC_{50} (µM)
PAMAM G4	14,215	64	4.5	2.1-2.8	3.21 [2.89– 3.52]
PAMAM G5	28,826	128	5.4	4.1-4.6	1.07 [0.64– 1.50]
PAMAM G6	58,408	256	6.7	4.2-5.8	1.02 [0.92– 1.33]

PAMAM dendrimers are of particular interest as they are a homologous series of nanoparticles with well defined physico-chemical properties, which are systematically variable and elicit systematically variable cellular responses (*Mukherjee et al., 2010 – A and B, Naha et al., 2009 and 2010, Naha and Byrne, 2013* and *Mukherjee and Byrne, 2013*). Therefore, systematic variation of their structure allows examination of how different characteristics impact the cell-nanoparticle interaction. The variable properties in question include: generation number (G1, G2, G3, *etc*.), effective surface charge (cationic, anionic, neutral), zeta potential, terminal modification and size (which is dependent on generation and branch length). Notably, previous studies of exposure of aquatic species (*Naha et al., 2009* and *Naha and Byrne, 2013*) and *in vitro* mammalian cell cultures (*Mukherjee et al., 2010 – A and B, Naha et al., 2010* and *Mukherjee and Byrne, 2013*) have demonstrated that the aminated dendrimer series elicit toxic responses which are well correlated with the variations in physico-chemical properties (see Table 1.1). Such traits are

advantageous in predictive modelling and in the development of a Quantitative Structure Activity Relationship (QSAR) governing their toxic response.

1.4 Polystyrene Nanoparticles

Polystyrene is a synthetic aromatic polymer made from the monomer styrene. It has been shown that polystyrene can readily enter into cells via endocytosis, similar to PAMAM dendrimers (*Lunov et al., 2011*). PSNPs have been proposed for several different potential uses as they possess advantages such as easy uptake (*Lunov et al., 2011* and *Anguissola et al., 2014*) and translocation between cells (*Kloet et al., 2011*), entry into the blood stream and localising in distal organs(*Yacobi et al., 2008*), making them ideal for drug delivery applications. They have also been used to probe cell nanoparticle interactions with methods such as Confocal Laser Scanning Microscopy (CLSM) and Raman spectroscopy (*Dorney et al., 2012* and *Efeoglu et al., 2015*). Additionally, unlike the PAMAM and PPI dendrimers, where size varies only slightly with generation, the PSNPs have a much more diverse range of sizes enabling studies of the effect of nanoparticle size.

PSNPs have been studied *in vitro* and the key physico-chemical parameters of size and surface modification have been identified as those governing toxicity. The cationic, amine modified PSNP (PSNP-NH$_2$) have been shown to elicit a toxic response in several cell lines (*Dorney, 2013*, *Anguissola et al., 2014* and *Bannunah et al.*, *2014*), while similar doses of anionic (carboxylated) and neutral (unmodified) PSNPs shown no appreciable toxicity (*Xia et al., 2006*, *Dorney, 2013* and *Efeoglu et al., 2015*). Furthermore, as PSNP increase in size (up to 100nm) the toxicity is also seen to increase (*Bannunah et al.*, *2014*), even though the

rate of uptake is faster for the smaller sizes of PSNP, this may be due to the larger sizes having a much larger surface area and therefore more amine surface groups present.

1.5 General paradigm of toxicity

The PAMAM and PSNP-NH$_2$ particles studied in this thesis follow a similar general paradigm of toxicity and it should be noted that other amine modified nanoparticles are also believed to follow such a paradigm (*Xia et al., 2006*). Initially, the particle comes into contact with the cell membrane and is taken into the cell via endocytosis. An increase in the production of ROS occurs in and around the endosome, which is counteracted by anti-oxidants such as glutathione (GSH) (*Mukherjee et al., 2010 – B*, *Naha et al., 2009* and *Naha and Byrne, 2013*). However, if the increase in ROS exceeds the antioxidant capacity of the cell, oxidative stress occurs. Following this, the higher generation PAMAM dendrimers have been seen to undergo endosomolysis, the breaching of the endosome and release of the contents into the cytosol (*Sonawane et al., 2003* and *Watson et al., 2005*). A similar process occurs for PSNP-NH$_2$, but at a later stage when the particle is in a lysosome, a process therefore called: lysosomolysis (*Wang et al., 2013*). After this, particle localisation to and subsequent disruption of the mitochondria occurs. This causes the activation of several different signalling molecules, which initiate a cascade leading to the induction of inflammatory factors and a second phase increase in ROS generation. Ultimately, this causes the production of pro-apoptotic factors and the activation of effector caspases, leading to cell death via apoptosis (*Xia et al., 2006*, *Lee et al., 2009*, *Mukherjee et al., 2010 – A and B, Naha et al., 2009 and 2010, Naha and Byrne, 2013*, *Mukherjee and Byrne, 2013*, *Wang et al., 2013* and *Anguissola et al., 2014*). Sections 1.5.2 through to 1.5.7

contain a brief description of each step in this cascade. However, due to the complexity and vast number of signalling molecules produced, only a select few of the most relevant have been described.

1.5.1 Endocytosis

Endocytosis is a process carried out by nearly all living cells as a way to bring extracellular material into the cell in a controlled and non-damaging manner (*Alberts et al., 2002*) and has been demonstrated to be the dominant uptake mechanism of nanoparticles by cells (*Anguissola et al., 2014*). In this process, the nanoparticle comes into contact with the cell and is engulfed by the cell membrane which propagates into the cytosol. The section of membrane around the nanoparticle then detaches from the cell surface, forming an endosome (*Vácha et al., 2011*), as can be seen in figure 1.2.
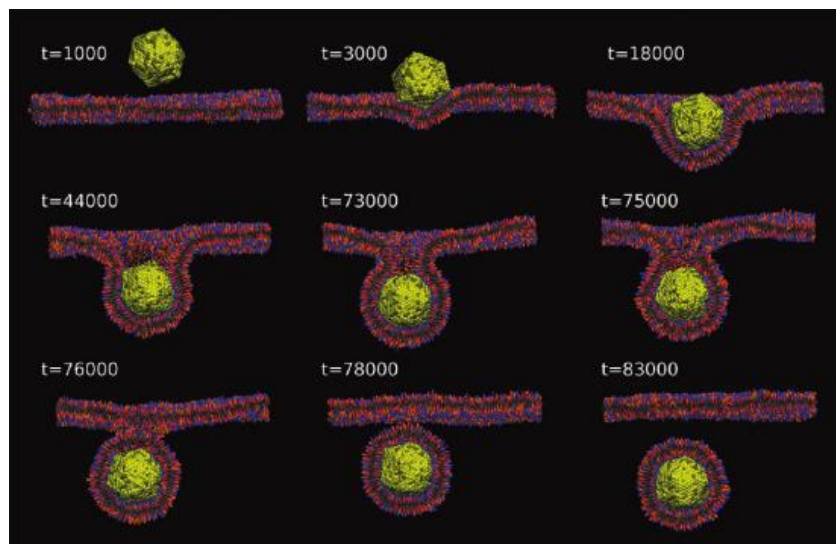
Figure 1.2: Image showing the stages of endosome formation and intake into the cytosol.
(*Image adapted from: Vácha et al, 2011, Nano Lett. 11, 5391–5395*)

The endosome is used as a way to contain extracellular material and protect the cell form any damage. Therefore, the cell will attempt to break down material within the endosome and this is accomplished via the acidification of the compartment. This process is continued as the endosome progresses and fuses with a lysosome, where any remaining material is to be broken down (*Alberts et al., 2002*). However, for synthetic particles such as PAMAM dendrimers and PSNP-NH$_2$ the conditions within the endosome/lysosome are not sufficient to cause degradation of the particles, and via processes involving the swelling and retention of charged ions, the endosome/lysosome can breach, spilling the contents (including the now free nanoparticle) into the cytosol. This process of breaching is called endosomolysis/lysosomolysis and is discussed in section 1.5.5: Endosomolysis/ Lysosomolysis (*Sonawane et al., 2003*, *Watson et al., 2005* and *Wang et al., 2013*).

1.5.2 ROS Production

After endocytosis, as part of the digestion process, increases in Reactive Oxygen Species (ROS) are observed (*Mukherjee et al., 2010 – B, Naha et al., 2009* and *Naha and Byrne, 2013*). ROS are known to damage cells via interaction with DNA, proteins and membranes (*Aceworth and Bailey, 1995*). They have also been implicated as causative factors in many different disease states, such as: HIV (*Banerjee et al., 2010*), Alzheimer's and Parkinson's disease (*Penugonda et al., 2005* and *Lee et al., 2007*), cataract formation (*Carey et al., 2011*), retinal degeneration (*Schimel et al., 2011*) and several more which have been reviewed by *Sunitha et al.* (*2013*). Hydrogen Peroxide (H$_2$O$_2$) is the ROS of primary interest in the context of endocytosis of a nanoparticle. Endosomes are known to contain the enzyme NADPH oxide (EC Number 1.6.3.1) in the somal membrane (*Chamulitrat et*

al., 2004), which generates superoxide anions (O_2^-), accomplished by an electron transfer from NADPH, via FAD, to diatomic oxygen (O_2) (*Shuvaev et al., 2011*).

$$O_2 + e^- \rightarrow O_2^-$$
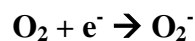
It is worth noting that this is not the only source of superoxide production within the cell. In standard metabolism, the electron transport chain of the mitochondria utilises diatomic oxygen (O_2) to drive the production of adenosine tri-phosphate (ATP) and at this site electron transfer to diatomic oxygen can occur, generating superoxide (*Aceworth and Bailey, 1995*).

However, the activity of the vATPase proton pump has also been noted in endosomes and this supplies an excess of H^+ ions to the interior of the endosome, as it is reported that the unsaturated surface amino groups, (such as those of cationic PAMAM dendrimers and PSNP-NH$_2$) sequester protons supplied by this mechanism, which keeps the pump functioning (*Nel et al., 2009*). This presence of excess protons will promote the rapid dismutation of superoxide to hydrogen peroxide via the floowing two step process, whereby superoxide encounters a proton leading the creation of the hydroperoxyl radical, which dimerises generating hydrogen peroxide and diatomic oxygen (*Aceworth and Bailey, 1995*).

Step 1: $O_2^{-\cdot} + H^+ \rightarrow HO_2^\cdot$ *(hydroperoxyl radical)*

Step 2: $2HO_2^\cdot \rightarrow H_2O_2 + O_2$
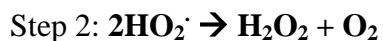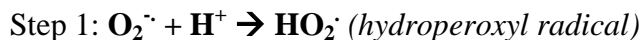
The generation of H_2O_2 in this way is most likely a form of cellular defence designed to break down the contents of the endosome; however, this does not occur in the case of synthetic nanoparticles, such as PAMAM and PSNP-NH$_2$.

For the PAMAM dendrimers, ROS build up in and around the endosome (*Mukherjee et al., 2010 – B*, *Naha et al., 2009* and *Naha and Byrne, 2013*), coupled with the proton pump effect supplying protons to the endosome (*Nel et al., 2009*), can cause lysis of the somal body, a process called endosomolysis (see section: 1.5.5: Endosomolysis/Lysosomolysis) (*Sonawane et al., 2003* and *Watson et al., 2005*). A similar process occurs for PSNP-NH$_2$, although it happens at a later time, at which stage the particle is within a lysosome (lysosomolysis) and may not be as strongly linked with the production of ROS in the way described above (see section: 1.5.5: Endosomolysis/Lysosomolysis) (*Wang et al., 2013*).

It should also be noted that, while ROS are implicated in many different diseases and toxic responses, they are also essential to normal cell function and are produced via ligand-induced specialised plasma membrane oxidases as important components of several cell signalling pathways, such as: Antimicrobial defence, growth inhibition, proliferation, NF-κB, IL-6, MAPK kinase, tyrosine and p38 activation, the induction of apoptosis and many more, the full list of which is too long to include in this thesis, but has been reviewed by: *Thannickal and Fanburg* (*2000*).

1.5.3 ROS Defence: Anti-Oxidants

Cellular defence against ROS damage occurs via anti-oxidant enzymes and compounds. Anti-oxidants work to stop ROS build up before it gets to a level that could be damaging to the cell (oxidative stress). There are many different molecular and enzymatic anti-oxidants

present in the cell including: thioredoxin reductase, superoxide dismutase, catalase, ascorbic acid (vitamin C), γ-tocopherol (vitamin E) and many molecules with a thiol reactive group, including glutathione (*Rahman, 2007*). Glutathione (GSH) is a cysteine containing tri-peptide which has previously been studied and is known to have an important role in relation to PAMAM toxicity (*Mukherjee and Byrne, 2013*). GSH functions as an antioxidant molecule, but its amount and activity are governed by enzymatic processes (*Deponte, 2013*): in GSH, the hydrogen on the sulphur hydroxide terminal of cysteine is the active molecular component and readily reduces most oxidants (*Pastore et al., 2003*), the resulting oxidised glutathione then dimerising with another oxidised glutathione to form glutathione disulphide (GSSG). The enzymatic action of glutathione reductase (EC Number 1.8.1.7) then reduces it back to two molecules of glutathione (*Deponte, 2013*), completing the cycle depicted in Figure 1.3.
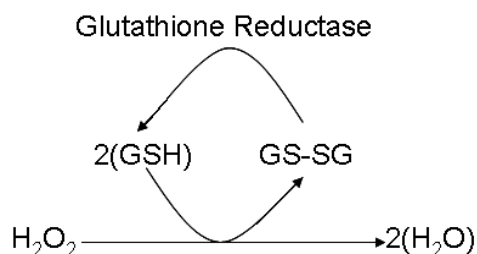
Figure 1.3: Reaction of Glutathione with Hydrogen Peroxide, oxidation of glutathione and subsequent reduction of glutathione disulphide via glutathione reductase.

GSH is the front line of defence against ROS production in the mitochondria, which occurs as part of normal metabolism and changes to the amount of GSH in the cell can leave it highly susceptible to ROS damage (*Lash, 2006*). However, GSH is not only vital to maintaining the redox balance of the mitochondria, it is also involved with the regulation of

Ca^{2+} distribution (*Beatrice et al., 1984*, *Lotscher et al., 1979* and *Olafsdottir et al., 1988*) and many other signalling cascades which control growth, differentiation and apoptosis (*Circu and Aw, 2008*, *Davis et al., 2001*, *Petit et al., 1996* and *Skulachev, 1996*). Reductions in the levels of cellular (and mitochondrial) GSH have been linked to many diseases and disorders including: hypoxia, ischemia/reperfusion injury, aging, liver diseases, and neurologic disorders (reviewed by: *Lash, 2006*). Reductions have also been shown to open the mitochondrial membrane permeability transition pore, which can lead to the release of ROS and several other key molecules causing further damage to the cell (*Armstrong and Jones, 2002*, *Chernyak and Bernardi, 1996* and *Reed and Savage, 1995*). The effect of reduced GSH levels is explored in the context of nanotoxicity in Chapter 5: Modification of the *in vitro* uptake mechanism and antioxidant levels in HaCaT cells and resultant changes to toxicity and oxidative stress of G4 and G6 Poly (amido amine) dendrimer nanoparticles.

1.5.4 Oxidative Stress

Oxidative stress is the condition that is created when the ROS production in the cell overwhelms its antioxidant defence, leading to several adverse effects. This appears to be the case when a nanoparticle enters the cell (*Xia et al., 2006*, *Mukherjee et al., 2010 – B, Naha et al., 2010 and Mukherjee and Byrne, 2013*). Since GSH is such a key component of the antioxidant defence, it is not surprising that the ratio of GSH:GSSG (glutathione:glutathione disulfide, the oxidised form of glutathione) is often used to indicate the induction of oxidative stress (*Circu and Aw, 2008*).

1.5.5 Endosomolysis/Lysosomolysis

While ROS appear to be the initial toxic effectors, another factor which can affect the toxicity is the process of endosomolysis/lysosomolysis: rupturing of the endosome/lysosome and release of its contents (including the nanoparticle) into the cytosol (*Sonawane et al., 2003* and *Watson et al., 2005*, *Wang et al., 2013*). Endosomolysis has mainly been observed for the PAMAM dendrimers (*Sonawane et al., 2003*) and lysosomolysis for the PSNP-NH$_2$ (*Wang et al., 2013*).

In the case of endosomolysis, the contents of the endosome, mainly ROS, can then have an additional toxic effect on the cell. This process is thought to be caused by a build up of protons and chloride anions in the endosome caused by the vATPase proton pump mechanism (*Nel et al., 2009*), although membrane permeabilisation by lipid peroxidation via ROS production can not be completely ruled out. It is most likely to be a combined effect of both processes which leads to the swell and eventual rupture of the endosome.

A similar process occurs for PSNP-NH$_2$, but happens at the later stage when the lysosome has formed (lysosomolysis), and its rupture has been linked to swelling caused by the proton sponge effect and the build up and retention of neutral and phospholipids within the somal body (*Wang et al., 2013*).

It is notable that, traditionally, the induction of endosomolysis has been a strategy in drug delivery (*Watson et al., 2005*) and so understanding and controlling this process could be key to emerging nanoparticle based drug delivery strategies. However, caution must be taken as the induction of endosomolysis may not be a wise strategy for nanoparticle based therapies, especially for the amine modified particles, as it has been seen to cause significant damage to the cytoskeleton (*Mukherjee, 2012*).

1.5.6 Inflammatory Response

The inflammatory response involves a huge number of cytokines and chemokines and a full description is not within the scope of this work. However, outlined here is a selection of elements which have been experimentally measured by *Mukherjee and Byrne* (*2013*).

1.5.6.1 Caspases

The name caspase comes from **c**ysteine-dependant **asp**artate directed prote**ase** and they are essential to mammalian life (*Earnshaw et al., 1999*). This group of proteins is generally involved with inflammation, apoptosis and necrosis and can be split into two types: initiator caspases (caspases which function to activate other pro-apoptotic factors and effector caspases) and effector caspases (caspases directly involved with cellular degradation). In the studies of *Mukherjee and Byrne* (*2013*), Caspase 8 and Caspase 3 were measured.

Caspase 8:

Caspase 8 falls into the category of initiator caspase. This protein is inactive in its monomeric form, but is activated due to proximity induced dimerisation via the following sequence (*MacKenzie and Clark, 2012*). Firstly, CD-95, a cellular death receptor (also known as the Fas receptor), recruits the protein FADD (Fas Associated Death Domain) to its cytosolic terminal. FADD then binds two molecules of caspase 8. The two caspase 8 proteins then dimerise and activate via cross-phosphorilation. The now active form of caspase 8 proceeds to activate caspase 7 and caspase 3 (both effector caspases) and other factors such as BH3 interacting-domain death agonist (BID), which induces Mitochondrial Membrane Potential Decay (MMPD) (*Kaufmann et al., 2012, Weinlich et al., 2011*).

Interestingly, caspase 8 also has a vital role to play in cell survival. It has recently been found that caspase 8, when hetero-dimerised with FLIP (a protein very similar to caspase 8, but without the catalytic active site), has an anti-necrotic effect in chicken embryos, and, if not present, leads to death (*Weinlich et al., 2011*). While this dual function in both cell death and cell survival might seem counter intuitive, it is a commonly seen occurrence in the apoptotic/survival signalling pathways.

Caspase 3:

Caspase 3 is an effector caspase and is the main effector of cell death in the apoptotic pathway (*Porter and Jänicke, 1999*). Caspase 3 is expressed in virtually all cells and exists in it non-active form (pro-caspase 3). There are several ways in which caspase 3 can be activated. Caspase 8 can directly activate caspase 3, via cleavage of the inhibitor domain converting pro-caspase 3 to caspase 3 (*Kumar, 2007*). If mitochondrial damage has occurred, then caspase 3 can be activated in the following way: the mitochondria releases cytochrome-c and APAF-1, these 2 proteins combine with ATP forming the apoptosome, which is capable of activating large amounts of caspase 9, which then activate caspase 3 (*Weinlich et al., 2011*). Caspase 3 targets and degrades both DNA and proteins in the cell, meaning it has thousands of potential targets.

1.5.6.2 Tumour Necrosis Factor – alpha (TNF-α)

TNF-α is part of the TNF super-family of proteins and binds to receptors on virtually every cell type in the body (with the exception of erythrocytes)(*Hehlgans and Pfeffer, 2005*). It can act both locally, within the cell where it was produced, or distally via transport to

distant cells. In this study, it is discussed in terms of its action within the cell in which it was produced (its autocrine action) (*Idriss and Naismith, 2000*).

As seen with caspase 8, TNF-α has both anti-apoptotic and pro-apoptotic effects, depending on the cellular environment and upstream activators which have been involved (*Hehlgans and Pfeffer, 2005*). Its pro-apoptotic effect involves activation of the Mitogen Activated Protein Kinase (MAPK) pathway (*McLeish et al., 1998*). In an anti-apoptotic role, it is associated with the activation of **N**uclear **F**actor **kappa**-light-chain-enhancer of activated **B** cells (NF-κB), which is involved with induction of inflammation and is generally pro-survival (*Lipniackil et al., 2007*). A comprehensive description of TNF-alpha and its role within the cell is available from *Hehlgans and Pfeffer* (*2005*).

1.5.6.3 Interleukin 8 (IL-8)

Part of the CXC super-family and also known as CXCL8, IL-8 is a 77 amino acid protein (72 amino acids in immune cells), found in virtually all cells (*Harada et al., 1994*). IL-8 has two main receptors to which it will bind: CXCR-1 and CXCR-2. Generally associated with the acute inflammatory response, IL-8 acts as a strong chemo-attractant and brings neutrophils and macrophages toward the site of inflammation (*Waugh and Wilson, 2008*).

It has been found that IL-8 is very sensitive to oxidative stress in the cell. Oxidative stress increases the generation of IL-8 at a genetic level, while anti-oxidants down regulate it. Also, IL-8 is a very stable protein and will remain in the cell from days to weeks before degradation (*Ito et al., 2004*).

The factors mentioned constitute a tiny fraction of all the signalling components involved in inflammation and cell death. A graphical representation of how these factors interact can be seen in Figure 1.4.
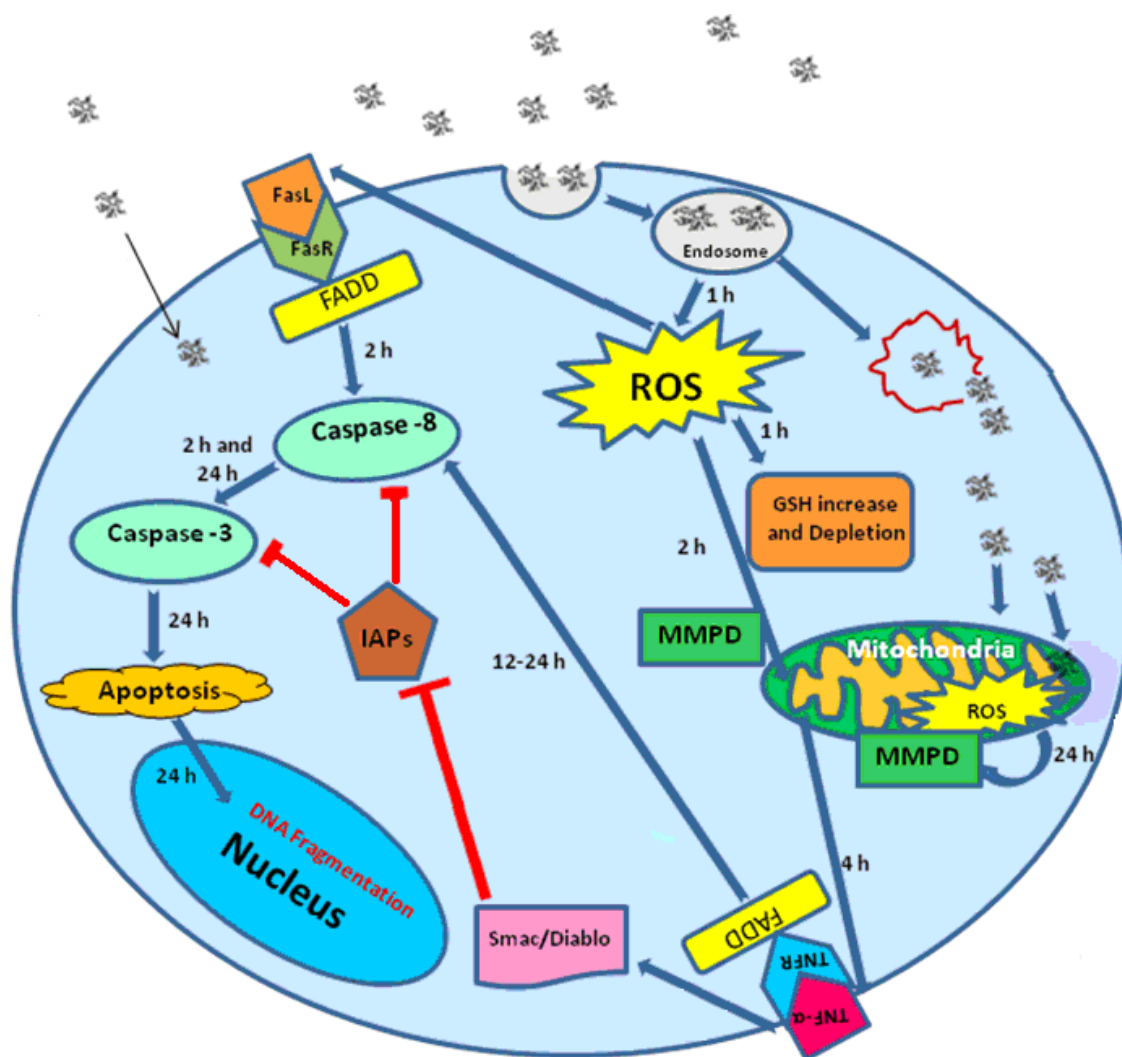
Figure 1.4: Image showing the interaction of the components involved in aminated dendritic polymer nanoparticle induced toxicity and subsequent apoptosis. (*Image adapted from the supplementary material of: Mukherjee and Byrne, 2013, Nanomed: Nanotech. Bio. Med., 9(2), 202-211*).

It is interesting to note the dual functionality of some of these proteins, in that they can be involved in both pro-apoptotic and anti-apoptotic pathways, which makes sense in terms of regulation. Apoptosis is one of the most heavily regulated pathways in the cell and is essential to normal mammalian growth and development. This heavy regulation is because, if a cell is perfectly viable then unnecessary/accidental activation of apoptosis would be useless and wasteful, and, of equal importance, when apoptosis is necessary, perhaps due to irreparable damage to the cell, it needs to be able to occur. To highlight the importance of apoptosis, it should be noted that failure of proper apoptotic action allows cancer cells to proliferate (*Evan and Vousden, 2001*).

1.6 Adverse Outcome Pathways (AOPs) and Quantitative Structure Activity Relationships (QSARs)

Such a sequential set of events naturally lends itself to the formulation of an Adverse Outcome Pathway (AOP) (*OECD, 2013*). In terms of nanoparticle toxicity, AOPs have been promoted as a way to potentially classify nanoparticles based on their toxic mode of action and the way in which they initiate this toxicity, via a Molecular Initiating Event (MIE) (*Oomen et al., 2014*). The set of events described above can be visualised by a systematic sequence of events, such as in Figure: 1.5, whereby, upon exposure to a nanoparticle, the sequence of events starts with endocytosis (1), progresses to ROS formation (2), ROS quenching by anti-oxidants (3), mitochondrial damage, if ROS quenching is insufficient (3) and the induction of the inflammatory cascade of caspases, TNF-α and interleukins (4). If the cell recovery mechanisms are insufficient, this finally culminates in apoptosis.
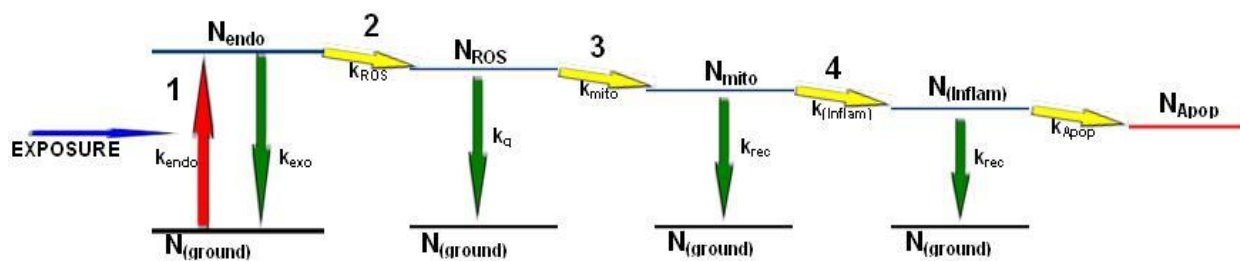
Figure 1.5: Schematic of systematic sequence of events upon nanoparticle uptake.

However, to fit with the formalism of AOPs with defined MIEs, it may be necessary to adapt such a sequence to the inclusion of an MIE, which may potentially be identified as the induction of ROS via NADPH oxidase, thus making the rest of the AOP dependant on the cellular response only. Potential modifications of this AOP format, in relation to the results of this thesis, are discussed in more detail in Chapter 7 (Section 7.2: Modelling and current nanoparticle testing strategies).

The AOP formalism will also aid in the development of QSARs based on the cellular response to nanoparticle uptake. The OECD has recognised the potential of QSARs and has provided guidelines for the development of QSAR models in general, (*OECD, 2007*) which, for regulatory purposes, promote the principles of:

(a) A definable endpoint

(b) An unambiguous algorithm

(c) A defined domain of applicability

(d) Appropriate measures of goodness-of-fit, robustness and predictivity

(e) A mechanistic interpretation.

The systematic sequence of events identified for nanoparticle uptake and subsequent response by cells satisfies (a), (b) and (c), while (d) can be achieved with further testing and development. However, the system is lacking in a full mechanistic interpretation, part

(e). It is the aim that extension of such AOPs to include the MIE will give a partial mechanistic interpretation, laying the groundwork for a more complete QSAR of nanoparticle toxicity in general (*Puzyn et al., 2009*).

Overall, a better quantitative understanding of the mechanisms of response will allow for a better insight into the progression of nanoparticle toxicity and help in understanding how the toxic endpoints vary systematically with nanoparticle properties, but also with cell dependant factors, ultimately laying the foundation for the development of quantitative predictive models for cellular response (*Clark et al., 2011*).

1.7 Aims and Objectives

The main aim of this study was to explore methodologies to augment existing protocols for *in vitro* toxicological assessment of nanoparticles.

Firstly, this entailed the generation of a mathematical model capable of simulating the toxicity induced upon nanoparticle uptake into a mammalian cell, using a rate equation approach. Initially, previously obtained experimental data for PAMAM dendritic polymer nanoparticles was used as a guide. PAMAMs were chosen due to their well defined physico-chemical parameters and it had been shown that systematic variation of these parameters caused a similar systematic variation in the cellular response. Furthermore, in an effort to both validate such a system to evaluate nanoparticle toxicity and increase its domain of applicability, the model was extended to a different type of nanoparticle, specifically: aminated polystyrene. The polystyrene nanoparticles are not as well defined as the PAMAM dendrimers, in terms of degree of surface functionalization, and the effect of this variation on the model simulation was explored. Subsequently, both the rate of particle

endocytosis and the intra-cellular anti-oxidant levels have been indentified as important in the initial stages of toxicity and so these were varied experimentally to evaluate their effect on the cellular response. Finally, using an enzyme based assay system, the reactivity of PAMAM and PPI dendrimers was evaluated, based on their ability to generate ROS. This data was used to guide the development of an acellular predictive model, capable of simulating toxicity based solely on the physico-chemical properties of the nanoparticle. PAMAM and PPI dendrimers were chosen due to their well defined physico-chemical parameters.

Overall, the decoupling of the nanoparticle and cellular properties allows for a better understanding of nanotoxicity. The simulation model will aid the current EU approach to the classification of nanoparticle toxic potential based on chemically agnostic adverse outcome pathways, with well defined molecular initiating events. Such an approach will also have applications in the field of nanomedicine, as a way to reduce the time intensive and costly initial steps involved in nano-toxicity evaluation.

1.8 Thesis Summary

1.8.1 Chapter 2: Methodology

Chapter 2 outlines the methodology employed in chapter's three to six of this thesis. In section 2.2, the generation of the simulation model from initial concept to functional program is explored. Section 2.3 follows with information regarding the cellular assays and dyes used to measure viability, ROS, anti-oxidants and endosomal formation. Finally, section 2.4 describes the imaging technologies of Confocal Laser Scanning Microscopy (CLSM) and Scanning Electron Microscopy (SEM) which were used, respectively, to

visualise events associated with toxicity in a live cell environment and to gain information for the characterisation of the nanoparticles. This methodology chapter gives general information about the methods employed, although the specifics of each experimental set-up are detailed in the materials and method section of the appropriate chapter.

1.8.2 Chapter 3: Numerical simulations of *in vitro* nanoparticle toxicity – the case of Poly (amido amine) dendrimers (*Maher et al., 2014*).

Chapter 3 details a phenomenological rate equation model which successfully simulates nanoparticle toxicity. In this model, PAMAM dendritic polymer nanoparticles are used due to their unambiguous physico-chemical properties. HaCaT (human keratinocytes), J774A.1 (murine macrophages) and SW480 (human colon adenocarcinoma) cell lines were employed due to their previously observed well defined responses to PAMAM induced toxicity. The model successfully simulates the temporal evolution of nanoparticle uptake, ROS induction and inflammatory cascade leading to cell death and the dose dependant responses are also seen to well represent the experimental observations for three generations of PAMAM dendrimer (G4, G5 and G6). Furthermore, the model allows the differences in cell line responses to be understood in terms of different anti-oxidant levels and differences of responses to several assays (within a given cell line) to be understood in terms of sensitivities to different cellular events. Critically, the model describes toxicity based on independent nanoparticle properties and cellular parameters, which are based on reaction rates.

The model in the form presented in this thesis has been published in Toxicology *in Vitro*:

Maher, M.A., Naha, P.C., Mukerjee, S.P. and Byrne, H.J. 2014. Numerical simulations of *in vitro* nanoparticle toxicity – the case of Poly (amido amine) dendrimers. *Toxicol. In Vitro*, **28**(8), 1449-1460.

1.8.3 Chapter 4: Numerical simulations of *in vitro* nanoparticle toxicity – the case of aminated Polystyrene (*Maher and Byrne, 2016 – A*).

Building on the model in chapter 3, chapter 4 aims to extend its range to cover aminated polystyrene nanoparticles (PSNP-NH$_2$). Again, the HaCaT cell line was employed for this study. Initially, the cytotoxicity of PSNP-NH$_2$ particles was explored using the Alamar Blue (AB) and 3-(4,5-Dimethylthiazol-2-yl)-2,5-diphenyltetrazolium Bromide (MTT) viability assays at time points of: 6, 12, 24, 48 and 72 hours. PSNP-NH$_2$ nanoparticles are not as well defined as PAMAM dendrimers, therefore, Scanning Electron Microscopy (SEM) and Nuclear Magnetic Resonance (NMR) were used to gain insight on the size distribution and extent of surface functionalisation, respectively. Even with the associated uncertainty in nanoparticle physico-chemical properties, the model was able to faithfully simulate the PSNP-NH$_2$ toxicity with the same set of equations as used in chapter 3, with changes made only to the size dependant uptake rate and number of surface amine groups (which determines the rate of ROS generation). The consistency of the model to replicate toxicity for a different range of nanoparticles and cells adds to the validity of such an approach to support toxicity screening strategies and supports the development of QSARs and AOPs with defined MIEs.

The polystyrene model of chapter 4, in the form presented in this thesis, is currently under review for publication in Toxicology *in Vitro*: Maher, M.A. and Byrne, H.J. 2016 – A.

Numerical simulations of *in vitro* nanoparticle toxicity – the case of aminated Polystyrene. Submit to: *Toxicol. In Vitro*, January 2016.

<u>1.8.4 Chapter 5: Modification of the *in vitro* uptake mechanism and antioxidant levels in</u>

<u>HaCaT cells and resultant changes to toxicity and oxidative stress of G4 and G6 Poly</u>

<u>(amido amine) dendrimer nanoparticles (*Maher and Byrne, 2016 – B*).</u>

Initially, the aim of this chapter was to reduce cellular anti-oxidants, thereby causing a large increase in production of ROS upon PAMAM dendrimer endocytosis. However, due to apparent increased cell permeabilisation (possibly due to DL-Buthionine-(S,R)-sulfoximine (BSO)), instead, it was possible to observe differences in the progression of toxicity when it was possible to bypass endocytosis. Again PAMAM dendrimers of generations 4 and 6 were employed, as were HaCaT cells. ROS was tracked with caboxy-H_2DCFDA dye and cytotoxicity was evaluated with Alamar Blue (AB) and 3-(4,5-Dimethylthiazol-2-yl)-2,5-diphenyltetrazolium Bromide (MTT). Endocytosis was also observed using a transfected red fluorescent protein (RFP) and viewed with Confocal Laser Scanning Microscopy (CLSM). The resultant cellular response to the proposed passive diffusion of particles into the cell showed a marked increase in mitochondrial activity, most likely associated with the initial effect of BSO treatment, the reduction of cellular GSH and resultant changes in the redox state of the mitochondria. The second major change was the reduction of endocytosis in favour of passive diffusion and resultant reduction of the initial phase of ROS production. This chapter points to the potential for controlling cellular uptake mechanisms as a way to overcome the ROS production and toxicity associated with

nanoparticle endocytosis, which could have important implications for nanomedical applications such as drug delivery.

The uptake dependence study of chapter 5, in the form presented in this thesis has been published in Analytical and Bioanalytical Chemistry: Maher, M.A. and Byrne, H.J. 2016 – B. Modification of the *in vitro* uptake mechanism and antioxidant levels in HaCaT cells and resultant changes to toxicity and oxidative stress of G4 and G6 Poly (amido amine) dendrimer nanoparticles. *Anal. Bioanal. Chem.,* DOI: 10.1007/s00216-016-9623-8.

1.8.5 Chapter 6: Acellular reactivity of polymeric dendrimer nanoparticles as an indicator of oxidative stress *in vitro* (*Maher et al., 2016*).

Nanoparticle toxicity is currently measured via time and resource intensive viability assays and procedures. It is apparent that there is a need for more rapid and cost effective screening methods. It has also been noted that the primary source of toxicity is derived from the initial phase production of ROS, which is dependant mainly on the extent of surface amine modification of the particle. Therefore, an enzyme based assay (using monoamine oxidase A (MAO-A), which produces hydrogen peroxide (H_2O_2)) was derived to allow for the examination of the effect of nanoparticles on this ROS production. PAMAM and PPI dendrimers were tested and the Acellular Reaction Rate (ARR) of each was calculated and found to be well behaved as a function of both number of surface amino groups and dose. The ARR also correlates well with previously reported cytotoxicity data, although, the correlation is different for each nanoparticle series, which may highlight the importance of size dependant uptake rates in cellular studies. Critically, it does appear that faster methods of nanoparticle screening are possible and in conjunction with the

cytotoxicity models of chapters 3 and 4, such an approach could yield fast and more efficient ways to detect potentially toxic nanoparticles.

The acellular model in the form presented in this thesis has been published in Analytical and Bioanalytical Chemistry: Maher, M.A., Khalid, H. and Byrne, H.J. 2016. Acellular reactivity of polymeric dendrimer nanoparticles as an indicator of oxidative stress *in vitro*. *Anal. Bioanal. Chem.,* **408**(3), 695–703.

1.8.6 Chapter 7: Summary and Conclusions.

Chapter 7 summarises the main findings of the thesis and puts them in context of the current European strategy for the Integrated Approaches to Testing and Assessment (IATA) and shows how the modelling techniques can form an important part of such a strategy. Additionally, the current trend in the reporting of nanotoxicity data is critiqued and the idea of how a more standardised reporting metric could be beneficial is explained. Finally, it promotes the idea of chemically agnostic AOPs for cellular toxicity with defined MIEs and multiple entry routes, as a more rational way to classify nanoparticles and their toxicity.

1.9 References

- Aceworth, I. N. and Bailey, B. 1995. The Handbook of Oxidative Metabolism. *Chelmsford: ESA Inc.*

- Alberts, B., Johnson, A., Lewis, J., Raff, M., Roberts, K. and Walter, P. 2002. Molecular Biology of the Cell. **4th edition.** *New York: Garland Science*.

- Anguissola, S., Garry, D., Salvati, A., O'Brien, P.J. and Dawson, K.A. 2014. High content analysis provides mechanistic insights on the pathways of toxicity induced by amine-modified polystyrene nanoparticles. *PLoS One.* **9**(9), e108025 (doi: 10.1371/journal.pone.0108025).

- Armstrong, J.S. and Jones, D.P. 2002. Glutathione depletion enforces the mitochondrial permeability transition and causes cell death in Bcl-2 overexpressing HL60 cells. *FASEB J.,* **16**(10), 1263-1265.

- Banerjee, A., Zhang, X., Manda, K.R., Banks, W.A. and Ercal, N. 2010. HIV proteins (gp120 and Tat) and methamphetamine in oxidative stress-induced damage in the brain: potential role of the thiol antioxidant N-acetylcysteine amide. *Free Radic. Biol. Med.* **48**(10): 1388-1398.

- Bannunah, A.M., Vllasaliu, D., Lord, J. and Stolnik, S. 2014. Mechanisms of nanoparticle internalization and transport across an intestinal epithelial cell model: effect of size and surface charge. *Mol. Pharm.* **11**(12), 4363-4373.

- Beatrice, M.C., Stiers, D.L. and Pfeiffer, D.R. 1984. The role of glutathione in the retention of Ca^{2+} by liver mitochondria. *J. Biol. Chem.,* **259**(2), 1279–1287.

- Bonner, J.C., Card, J.W. and Zeldin, D.C. 2009. Nanoparticle-Mediated Drug Delivery and Pulmonary Hypertension. *Hypertension,* **53**(5), 751–753.

- Carey, J.W., Pinarci, E.Y., Penugonda, S., Karacal, H. and Ercal, N. 2011. *In vivo* inhibition of l-buthionine-(S,R)-sulfoximine-induced cataracts by a novel antioxidant, N-acetylcysteine amide. *Free Radic. Biol. Med*. **50**(6): 722–729.

- Chamulitrat, W., Stremmel, W., Kawahara, T., Rokutan, K., Fujii, H., Wingler, K., Schmidt, H.H. and Schmidt, R. 2004. A constitutive NADPH oxidase-like system containing gp91phox homologs in human keratinocytes. *J. Invest. Dermatol.,* **122**(4), 1000-1009.

- Chernyak, B.V. and Bernardi, P. 1996. The mitochondrial permeability transition pore is modulated by oxidative agents through both pyridine nucleotides and glutathione at two separate sites. *Eur. J. Biochem.,* **238**(3), 623–630.

- Circu, M.L. and Aw, T.Y. 2008. Glutathione and apoptosis. *Free Radic. Res.,* **42**(8), 689–706.

- Clares, B., Ruiz, M.A., Gallardo, V. and Arias, J.L. 2012. Drug delivery to inflammation based on nanoparticles surface decorated with biomolecules. *Curr. Med. Chem.,* **19**(19), 3203-3211.

- Clark, K.A., White, R.H. and Silbergeld, E. K. 2011. Predictive models for nanotoxicology: Current challenges and future opportunities. *Regul. Toxicol. Pharm.*, **59**(3), 361-512.

- Davis, S.S. 1997. Biomedical applications of nanotechnology - implications for drug targeting and gene therapy. *Trends in Biotechnology*, **15**(6), 217-224.

- Davis, W. Jr., Ronai, Z. and Tew, K.D. 2001. Cellular thiols and reactive oxygen species in drug-induced apoptosis. *J. Pharmacol. Exp. Ther.,* **296**(1), 1–6.

- De Jong, W. H. and Borm, P.J.A. 2008. Drug delivery and nanoparticles: Applications and hazards. *Int. J. Nanomed.,* **3**(2), 133–149.

- Deponte, M. 2013. Glutathione catalysis and the reaction mechanisms of glutathione-dependent enzymes. *Biochim. Biophys. Acta.,* **1830**(5), 3217-3266.

- Donaldson, K., Stone, V., Tran, C.L., Kreyling, W. and Borm, P.J.A. 2004. Nanotoxicology. *Occup. Environ. Med.* **61**(9), 727-728.

- Dorney, J. (2013) Polystyrene: A Potential Standard for Developing *In Vitro* Cellular Tracking Methods for Nanotoxicology. *Thesis (PhD)*, Dublin Institute of Technology: 2013. Dublin: DIT.

- Dorney, J., Bonnier, F., Garcia, A., Casey, A., Chambers, G. and Byrne, H.J. 2012. Identifying and Localizing Intracellular Nanoparticles Using Raman Spectroscopy. *Analyst,* **137**(5), 1111-1119.

- Earnshaw, W.C., Martins, L.M. and Kaufmann, S.H. 1999. Mammalian Caspases: Structure, Activation, Substrates, and Functions during Apoptosis. *Annu. Rev. Biochem.,* **68**(1999), 383-424.

- Efeoglu, E., Keating, M., McIntyre, J., Casey, A. and Byrne, H.J. 2015. Determination of nanoparticle localisation within subcellular organelles *in vitro* using Raman spectroscopy. *Anal. Methods,* **7**(23), 1759-9660.

- European Union. 2011. Commission Recommendation of 18 October 2011 on the definition of nanomaterials. *Official Journal of the European Union*, **2011/696/EU**, L275/40.

- Evan, G.I. and Vousden, K.H. 2001. Proliferation, cell cycle and apoptosis in cancer. *Nature,* **411**(6835), 342-348.

- Haley, B. and Frenkel, E. 2008. Nanoparticles for drug delivery in cancer treatment. *Urol. Oncol.,* **26**(1), 57-64.

- Harada, A., Sekido, N., Akahoshi, T., Wada, T., Mukaida, N. and Matsushima, K. 1994. Essential involvement of interleukin-8 (IL-8) in acute inflammation. *J. Leukoc. Biol.,* **56**(5), 559-564.

- Hehlgans, T. and Pfeffer, K. 2005. The intriguing biology of the tumour necrosis factor/tumour necrosis factor receptor superfamily: players, rules and the games. *Immunology,* **115**(1), 1-20.

- Idriss, H.T. and Naismith, J.H. 2000. TNFα and the TNF receptor superfamily: Structure-function relationship(s). *Microsc. Res. Tech,* **5**(3), 184-195.

- Ito, K., Hanazawa, T., Tomita, K., Barnes P.J. and Adcock, I.M. 2004. Oxidative stress reduces histone deacetylase 2 activity and enhances IL-8 gene expression: role of tyrosine nitration. *Biochemical and Biophysical Research Communications,* **315**(1), 240-245.

- Jain, K.K., P. Gupta, U. and Jain, N.K. 2010. Dendrimer toxicity: Let's meet the challenge. *Int. J. Pharm.,* **394**(1-2), 122–142.

- Kaufmann, T., Strasser, A. and Jost, P.J. 2012. Fas death receptor signalling: roles of Bid and XIAP. *Cell Death and Differentiation*, **19**(1), 42-50.

- Khalid, H., Mukherjee, S.P., O'Neill, L. and Byrne, H.J. 2016. Structural dependence of the *In vitro* cytotoxicity, oxidative stress and uptake mechanisms of Poly (propylene imine) dendritic nanoparticles. *J. Appl. Toxicol.*, **36**(3), 464–473.

- Kim, Y., Kim, D-E., Jung, H-Y., Choe, Y.H. 2013. Radial shape of polymer compound containing iodine, preparation method thereof, and ct contrast medium composition containing same. *Patent Number: EP2604289 A2*, Publication date: 19-06-2013.

- Kloet, S.K., Walczak, A.P., Louisse, J., van den Berg, H.H., Bouwmeester, H., Tromp, P., Fokkink, R.G., Rietjens, I.M. 2015. Translocation of positively and negatively charged polystyrene nanoparticles in an *in vitro* placental model. *Toxicol. In Vitro.* **29**(7), 1701-1710.

- Kumar, S. 2007. Caspase function in programmed cell death. *Cell Death Differ.,* **14**(1), 32-43.

- Kuzmov, A. and Minko, T. 2015. Nanotechnology approaches for inhalation treatment of lung diseases. *J. Control Release,* **219**(part 1), 500-518.

- Lash, L.H. 2006. Mitochondrial Glutathione Transport: Physiological, Pathological and Toxicological Implications. *Chem. Biol. Interact.,* **163**(1-2), 54–67.

- Lee, J.H., Cha, K.E., Kim, M.S., Hong, H.W., Chung, D.J., Ryu, G. and Myung, H. 2009. Nanosized polyamidoamine (PAMAM) dendrimer-induced apoptosis mediated by mitochondrial dysfunction. *Toxicol. Lett.,* **190**(2), 202–207.

- Lee, K.S., Kim, S.R., Park, H.S., Park, S.J., Min, K.H., Lee, K.Y., Choe, Y.H., Hong, S.H., Han, H.J., Lee, Y.R., Kim, J.S., Atlas, D. and Lee, Y.C. 2007. A novel thiol compound, N-acetylcysteine amide, attenuates allergic airway disease by regulating activation of NF-kappaB and hypoxia-inducible factor-1alpha. *Exp. Mol. Med.* **39**(6), 756-768.

- Lipniacki1, T., Puszynski, K., Paszek, P., Brasier, A.R. and Kimmel, M. 2007. Single TNFα trimers mediating NF-κB activation: stochastic robustness of NF-κB signaling. *BMC Bioinformatics,* **8**(376), (doi: 10.1186/1471-2105-8-376).

- Liu, M., Li, M., Wang, G., Liu, X., Liu, D., Peng, H. and Wang, Q. 2014. Heart-targeted nanoscale drug delivery systems. *J. Biomed. Nanotechnol.,* **10**(9), 2038-2062.

- Lotscher, H.R., Winterhalter, K.H., Carafoli, E. and Richter, C. 1979. Hydroperoxides can modulate the redox state of pyridine nucleotides and the calcium balance in rat liver mitochondria. *Proc. Natl. Acad. Sci. USA.,* **76**(9), 4340–4344.

- Lunov, O., Syrovets, T., Loos, C., Beil, J., Delacher, M., Tron, K., Nienhaus, G.U., Musyanovych, A., Mailänder, V., Landfester, K. and Simmet, T. 2011. Differential uptake of functionalized polystyrene nanoparticles by human macrophages and a monocytic cell line. *ACS Nano,* **5**(3), 1657-1669.

- MacKenzie, S.H. and Clark, A.C. 2012. Death by Caspase Dimerization. *Adv. Exp. Med. Biol.,* **747**(2012), 55-73.

- Maher, M.A. and Byrne, H.J. 2016 – A. Numerical simulations of *in vitro* nanoparticle toxicity – the case of aminated Polystyrene. Submit to: *Toxicol. In Vitro*, January 2016.

- Maher, M.A. and Byrne, H.J. 2016 – B. Modification of the *in vitro* uptake mechanism and antioxidant levels in HaCaT cells and resultant changes to toxicity and oxidative stress of G4 and G6 Poly (amido amine) dendrimer nanoparticles. *Anal. Bioanal. Chem.,* DOI: 10.1007/s00216-016-9623-8.

- Maher, M.A., Khalid, H. and Byrne, H.J. 2016. Acellular reactivity of polymeric dendrimer nanoparticlesas an indicator of oxidative stress *in vitro*. *Anal. Bioanal. Chem.,* **408**(3), 695−703.

- Maher, M.A., Naha, P.C., Mukerjee, S.P. and Byrne, H.J. 2014. Numerical simulations of *in vitro* nanoparticle toxicity − the case of Poly(amido amine) dendrimers. *Toxicol. In Vitro*, **28**(8), 1449-1460.

- McLeish, K.R., Knall, C., Ward, R.A., Gerwins, P., Coxon, P.Y., Klein, J.B. and Johnson, G. L. 1998. Activation of mitogen-activated protein kinase cascades during priming of human neutrophils by TNF-a and GM-CSF. *Journal of Leukocyte Biology,* **64**(4), 537-545.

- Montazer, M., Pakdel, E. and Behzadnia, A. 2011-A. Novel feature of nano-titanium dioxide on textiles: Antifelting and antibacterial wool. *Journal of Applied Polymer Science,* **121**(6), 3407−3413.

- Mukherjee, S.P. 2012. Towards Structure Activity Relationships for *in vitro* Toxicity of Polyamidoamine Dendritic Nanoparticles. *Thesis (PhD)*, Dublin Institute of Technology: 2012. Dublin: DIT.

- Mukherjee, S.P. and Byrne H.J. 2013. Poly amidoamine dendrimer nanoparticle cytotoxicity oxidative stress, caspase activation and inflammatory response:

experimental observation and numerical simulation. *Nanomed: Nanotech. Bio. Med.,* **9**(2), 202-211.

- Mukherjee, S.P., Davoren, M. and Byrne H.J. 2010-A. *In vitro* mammalian cytotoxicological study of PAMAM dendrimers - towards quantitative structure activity relationships. *Toxicol. in Vitro,* **24**(1), 169-177.

- Mukherjee, S.P., Lyng, F.M., Garcia, A., Davoren, M. and Byrne H.J. 2010-B. Mechanistic studies of *in vitro* cytotoxicity of poly(amidoamine) dendrimers in mammalian cells. *Toxicol. Appl. Pharm.,* **248**(3), 259–268.

- Naha, P.C. and Byrne, H.J. 2013. Generation of Intracellular Reactive Oxygen Species and Genotoxicity effect to Exposure of Nanosized Polyamidoamine (PAMAM) dendrimers in PLHC-1 cells *in vitro*. *Aquatic Toxicology,* **132-133**(2103), 61-72.

- Naha, P.C., Davoren, M., Casey, A. and Byrne H.J. 2009. An Ecotoxicological Study of Poly(amidoamine) Dendrimers-Toward Quantitative Structure Activity Relationships. *Env. Sci. Technol.,* **43**(17), 6864–6869.

- Naha, P.C., Davoren, M., Lyng, F.M. and Byrne, H.J. 2010. Reactive oxygen species (ROS) induced cytokine production and cytotoxicity of PAMAM dendrimers in J774A.1 cells. *Toxicol. Appl. Pharm.,* **246**(1-2), 91–99.

- Nel, A., Xia, T., Mädler, L. and Li N. 2006. Toxic potential of materials at the nanolevel. *Science,* **311**(5761), 622-627.

- Nel, A.E., Mädler, L., Velegol, D., Xia, T., Hoek, E.M.V., Somasundaran, P., Klaessig, F., Castranova, V. and Thompson, M. 2009. Understanding biophysicochemical interactions at the nano–bio interface. *Nature Materials,* **8**(7), 543 – 557.

- Olafsdottir, K., Pascoe, G.A. and Reed, D.J. 1988. Mitochondrial glutathione status during Ca^{2+} ionophore-induced injury to isolated hepatocytes. *Arch. Biochem. Biophys.,* **263**(1), 226–235.

- Oomen, A.G., Bos, P.M.J., Fernandes, T.F., Hund-Rinke, K., Boraschi, D., Byrne, H.J., Aschberger, K., Gottardo, S., von der Kammer, F., Kühnel, D., Hristozov, D., Marcomini, A. and Migliore, L. 2014. Concern-driven integrated toxicity testing strategies for nanomaterials - Report of the NanoSafety Cluster Working Group 10. *NanoToxicology,* **8**(3), 334-348.

- Organisation for Economic Co-Operation and Development (OECD), 2007. Guidance Document on the Validation of (Quantative) Structure Activity Relationships [(Q)SAR] Models, *OECD*, **ENV/JM/MONO(2007)2**, 2007.

- Organisation for Economic Co-Operation and Development (OECD), 2013. Guidance Document On Developing and Assessing Adverse Outcome Pathways, *OECD,* **ENV/JM/MONO(2013)6**. 2013.

- Pastore, A., Federici, G., Bertini, E. and Piemonte, F. 2003. Analysis of glutathione: implication in redox and detoxification. *Clin. Chim. Acta.,* **333**(1), 19-39.

- Penugonda, S., Mare, S., Goldstein, G., Banks, W.A. and Ercal, N. 2005. Effects of N-acetylcysteine amide (NACA), a novel thiol antioxidant against glutamate-induced cytotoxicity in neuronal cell line PC12. *Brain Research.* **1056**(2): 132–138.

- Petit, P.X., Susin, S.A., Zamzami, N., Mignotte, B. and Kroemer, G. 1996. Mitochondria and programmed cell death: Back to the future. *FEBS Lett.,* **396**(1), 7–13.

- Porter, A.G. and Jänicke, R.U. 1999. Emerging roles of caspase-3 in apoptosis. *Cell Death Differ.,* **6**(2), 99-104.

- Project on Emerging Nanotechnologies (PEN). 2016. Accessed on 26-02-2016 – Available at: *http://www.nanotechproject.org/*

- Puzyn, T., Leszczynska, D. and Leszczynski, J. Toward the Development of "Nano-QSARs": Advances and Challenges, *Small,* **5**(22), 2494-2509.

- Rahman, K. 2007. Studies on free radicals, antioxidants, and co-factors. *Clin. Interv. Aging., ***2**(2), 219–236.

- Rana, A.K., Rana, S.B., Kumari, A. and Kiran, V. 2009. Significance of Nanotechnology in Construction Engineering. *International Journal of Recent Trends in Engineering*, **1**(4), 46-48.

- Rauscher, H., Roebben, G., Boix Sanfeliu, A., Emons, H., Gibson, N., Koeber, R., Linsinger, T., Rasmussen, K., Riego Sintes, J., Sokull-Klüttgen, B. and Stamm, H. 2015. Towards a review of the EC Recommendation for a definition of the term "nanomaterial" Part 3: Scientific-technical evaluation of options to clarify the definition and to facilitate its implementation. *Publications Office of the European Union,* **EUR 27240 EN**, 2015.

- Reed, D.J. and Savage, M.K. 1995. Influence of metabolic inhibitors on mitochondrial permeability transition and glutathione status. *Biochim. Biophys. Acta., ***1271**(1), 43–50.

- Schimel, A.M., Abraham, L., Cox, D., Sene, A., Kraus, C., Dace, D.S., Ercal, N. and Apte, R.S. 2011. N-acetylcysteine amide (NACA) prevents retinal degeneration by up-regulating reduced glutathione production and reversing lipid peroxidation. *Am. J. Pathol.* **178**(5): 2032-2043.

- Shuvaev, V.V., Han, J., Yu, K.J., Huang, S., Hawkins, B.J., Madesh, M., Nakada, M. and Muzykantov, V.R. 2011. PECAM-targeted delivery of SOD inhibits endothelial inflammatory response. *FASEB,* **25**(1), 348-357.

- Skulachev, V.P. 1996. Why are mitochondria involved in apoptosis? Permeability transition pores and apoptosis as selective mechanisms to eliminate superoxide-producing mitochondria and cells. *FEBS Lett.,* **397**(1), 7–10.

- Sonawane, N.D., Szoka, F.C.Jr. and Verkman A.S. 2003. Chloride accumulation and swelling in endosomes enhances DNA transfer by polyamine-DNA polyplexes. *J. Biol. Chem.,* **278**(45), 44826-44831.

- Sunitha, K., Hemshekhar, M., Thushara, R.M., Santhosh, M.S., Yariswamy, M., Kemparaju, K. and Girish, K.S. 2013. N-Acetylcysteine amide: a derivative to fulfill the promises of N-Acetylcysteine. *Free Radic. Res.* **47**(5): 357-367.

- Thannickal, V.J. and Fanburg, B.L. 2000. Reactive oxygen species in cell signalling. *Am. J. Physiol. Lung. Cell. Mol. Physiol.* **279**(6): L1005-L1028.

- Tomalia, D.A. and Fréchet, J.M.J. 2002. Discovery of Dendrimers and Dendritic Polymers: A Brief Historical Perspective. *J. Polym. Sci. Pol. Chem.,* **40**(16), 2719–2728.

- Vácha, R., Martinez-Veracoechea, F.J. and Frenkel, D. 2011. Receptor-Mediated Endocytosis of Nanoparticles of Various Shapes. *Nano Letters,* **11**(12), 5391-5395.

- Wagner, V., Dullaart, A., Bock, A-K. and Zweck, A. 2006. The emerging nanomedicine landscape. *Nature Biotechnology*, **24**(10), 1211-1217.

- Wang, F., Bexiga, M.G., Anguissola, S., Boya, P., Simpson, J.C., Salvati, A. and Dawson K.A. 2013. Time resolved study of cell death mechanisms induced by amine-modified polystyrene nanoparticles. *Nanoscale,* **5**(22), 10868-10876.

- Watson, P., Jones, A.T. and Stephens, D.J. 2005. Intracellular trafficking pathways and drug delivery: fluorescence imaging of living and fixed cells. *Adv. Drug Deliver. Rev.,* **57**(1), 43-61.

- Waugh, D.J.J. and Wilson, C. 2008. The Interleukin-8 Pathway in Cancer. *Clin. Cancer Res.,* **14**(21), 6735-6741.

- Weinlich, R., Dillon, C.P. and Green, D.R. 2011. Ripped to Death. *Trends in Cell Biology,* **21**(11), 630-637.

- Xia, T., Kovochich, M., Brant, J., Hotze, M., Sempf, J., Oberley, T., Sioutas, C., Yeh, J.I., Wiesner, M.R. and Nel, A.E. 2006. Comparison of the Abilities of

Ambient and Manufactured Nanoparticles to Induce Cellular Toxicity According to an Oxidative Stress Paradigm. *Nano Lett.,* **6**(8), 1794-1807.

- Yacobi, N.R., Demaio, L., Xie, J., Hamm-Alvarez, S.F., Borok, Z., Kim, K.J. and Crandall, E.D. 2008. Polystyrene nanoparticle trafficking across alveolar epithelium. *Nanomedicine,* **4**(2), 139-145.

- Zolnik, B.S., González-Fernández, Á., Sadrieh, N. and Dobrovolskaia, M.A. 2010. Nanoparticles and the Immune System. *Endocrinology,* **151**(2), 458–465.

Chapter 2

Methodology

2.1 Introduction and Overview

A vast array of different methodologies were employed to obtain and analyse the simulation and experimental data of chapters three to six, and this chapter gives an explanation of the theory and function of these methods. In Section 2.2 a description of the method used to develop the predictive model from initial concept to generation of equations and finally functioning program is described. Section 2.3 details test methods employed for cellular work including the Viability assays: Alamar Blue (AB) and 3-(4,5-Dimethylthiazol-2-yl)-2,5-diphenyltetrazolium Bromide (MTT), the ROS and GSH detection dyes: Carboxy-H_2DCFDA and Thiol Tracker Violet (TTV), and the early endosome transfection vector kit: Celllight® Early Endosomes-RFP, BacMam 2.0. Finally Section 2.4 details the imaging methods of Confocal Laser Scanning Microscopy (CLSM) and Scanning Electron Microscopy (SEM). The general methodology is explained in this chapter; however, the specifics of how each experiment was performed will be described in the materials and methods section of the relevant chapter.

2.2 Modelling Methods

This section will give an overview of the methods which were used to generate a predictive model. Initially a Jablonski diagram described by Einstein's rate equations (for stimulated emission) was adapted to form a systematic sequence of events which occur upon nanoparticle endocytosis and eventually lead to apoptosis. Each step in the sequence is then described by a rate equation (in the form of an Ordinary Differential Equation (ODE)). Iterative Euler integration was then performed on the equations so that a numerical solution could be obtained for each, these solved equations where then written into a program script

for use with the SigmaPlot^{TM} v10.0 software and a simulation of the time and dose dependant toxicity was possible.

2.2.1 Systematic Sequence of Events (SSoE)

The model is based on a system of populations and differential (rate) equations which govern the changes in these populations. This phenomenological rate equation model is quite similar to those seen in molecular photodynamics (*Einstein, 1916*) illustrated in the Jablonski diagram of figure 2.1.
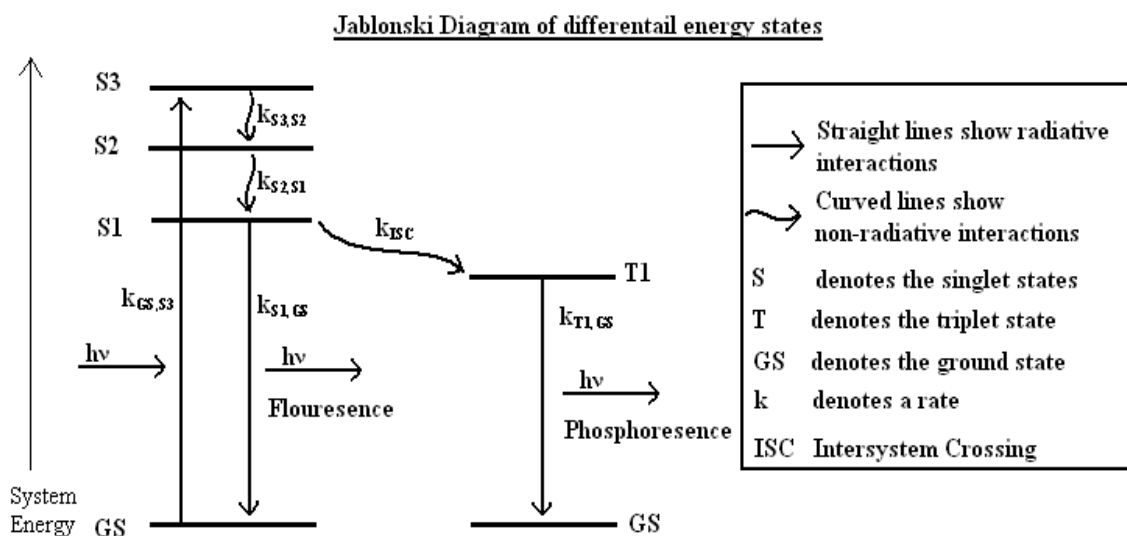
Figure 2.1: A Jablonski diagram showing electron energy levels after excitation by an incidence beam of radiation. *(Image adapted from: Einstein, A. Verhandlungen der Deutschen Physikalischen Gesellschaft, **18, 318–323 (1916))***

A Jablonski diagram shows a system of dynamic energy levels. In this system, the ensemble of molecules represents a population and all members of that population are in the ground state at the starting point (GS). When the molecules are exposed to energy (in

the form of photons) some of them are promoted to a higher energy level (S2 and S3), then as they lose energy, through non-radiative relaxation, they reach the level S1, where they can either return to the ground state (involving fluorescent emission) or are transferred, via inter-system crossing, into another system of energy levels (the triplet state, T1) and eventually return to the ground state (phosphorescence), as shown in figure 2.1. The population of any given level at a time, **t,** depends on the intensity of exposure, and the rate of relaxation from each state.

The system modelled in the current study does not involve energy levels as in the Jablonski diagram, but when the cell population is first exposed to a nanoparticle, a system of events does take place in a similar pattern, as represented in figure 2.2.
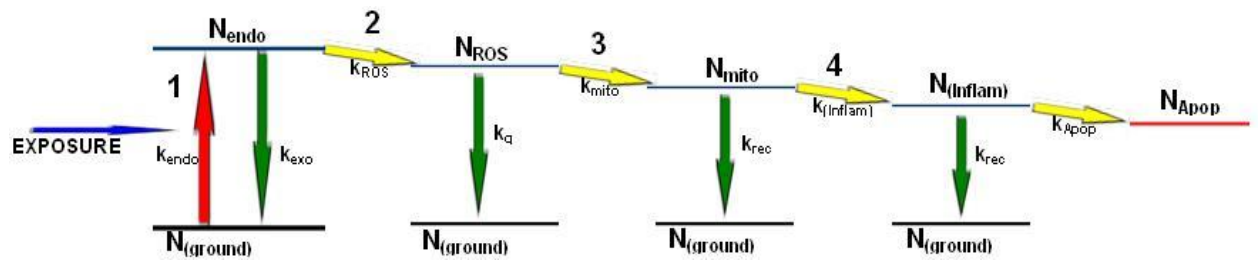
Figure 2.2: Schematic of systematic sequence of events upon nanoparticle uptake in a cell population.

Step 1: Some cells take up nanoparticles (endocytosis) on exposure, creating two populations: N_{ground} (cells without nanoparticle uptake) and N_{endo} (cells with an endocytosed nanoparticle). The amount of particles in N_{ground} and N_{endo} will depend on the initial exposure dose, and the rate of endocytosis k_{endo}. k_{exo} describes a possible exocytosis (moving out of the cell) of nanoparticles. However, this has been shown not to occur for polymeric nanoparticles (*Salvati et al., 2011*) and therefore, has not been included in the equations describing the model.

Step 2: At this point, there is a cross over where some of the cells containing nanoparticles start showing increased generation of ROS, described by the rate constant k_{ROS}, there is then quenching of ROS by the cellular defences, the intracellular anti-oxidants, at a rate constant k_q. Overall, this generates two more populations; N_{ground} (where the ROS have been removed and the cell has returned to its pre–exposure "ground state") and N_{ROS} (cells where the ROS production has overwhelmed the cellular antioxidant levels).

Step 3: Cells with increased levels of ROS, N_{ROS}, undergo mitochondrial damage, leading to two populations N_{ground} (where cells have recovered from the damage and returned to the ground state) and N_{mito} (where the mitochondria are damaged at a rate constant k_{mito}). The rate constant k_{rec} here describes the recovery rate of the cell.

Step 4: If the mitochondria do not recover, the cell will enter an inflammatory cascade (N_{inflam}), described here by the rate constant k_{inflam}. At this point, the release of caspases and cytokines occurs (as discussed in Chapter 1: Section: 1.4.4). If the cellular recovery rates are unable to repair the damage, the cell can enter into apoptosis (N_{apop}), governed by the rate constant (k_{apop}). Once the cells enter into apoptosis the cycle is irreversible.

The model described is analogous to that initially derived for the excited state dynamics of molecules, whereby the molecular ensemble is replaced by a cell population, the excitation energy by exposure dose of nanoparticles, and the relaxation rates by the rates which govern the sequence of cellular responses, as described.

The systematic sequence of events above is better described by a system of Ordinary Differential Equations (ODEs) as will be seen in Chapter 3: Numerical simulations of *in vitro* nanoparticle toxicity – the case of Poly (amido amine) dendrimers (*Maher et al., 2014*).

2.2.2 Iterative Euler Integration

ODEs were generated to model the nanoparticle populations; however, these needed to be solved for a numerical solution for input into the computer program. To obtain such a solution, integration was performed using an iterative Euler approach. The iterative Euler approach is a first order, explicit method for numerically solving an ODE with known initial conditions, such as the equations used in this model. The Euler method was chosen due to its applicability to these equations and because the system of equations generated is readily adaptable to the inclusion and exclusion of cellular processes (and the equations which model them), as necessary. However, the error associated with such an approach must be considered. The Euler method is first order, therefore, the error associated with each step in the process (the local truncation error) is proportional to the square of the step size taken. Furthermore, the cumulative effect of this error over the entire range iterated (the global truncation error) is approximately proportional to the step size. Therefore, to keep the error at a minimum it is important to, initially, take a small step size relative to the range over which the method will be applied. In this study, the step size used was 0.1 hours, over a total range of 72 hours. Equation 2.1 – Equation 2.7 show (for a general case) how this method was applied to the equations used in the model. This equation system shows a population (P2) which increases over time at a rate constant k_{12}, while another

process depletes the population (P2) at a rate constant k_{21}, which increases another population (P1). This can be depicted schematically as in figure 2.3.

N_{P2} (Population 2)

k_{12} k_{21}
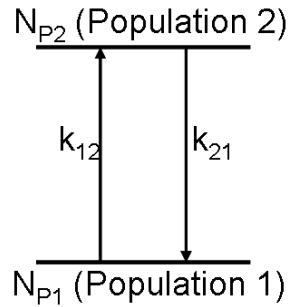
N_{P1} (Population 1)

Figure 2.3: Schematic representation of two populations, where the amount in population two (P2) is being increased by a rate constant k_{12} and decreased by a rate constant k_{21}. Conversely k_{12} is decreasing population one (P1) and k_{21} is increasing it.

$$\frac{\Delta N_{P2}}{\Delta t} = N_{P2}(t).k_{12} - N_{P1}(t).k_{21}$$

Equation 2.1

let: $\Delta N_{P2} = N_{P2}(t+1) - N_{P2}(t)$

Equation 2.2

$$\frac{N_{P2}(t+1) - N_{P2}(t)}{\Delta t} = N_{P2}(t).k_{12} - N_{P1}(t).k_{21}$$

Equation 2.3

$$\rightarrow \frac{dN}{dt} = \frac{\Delta N}{\Delta t}, \ dt \xrightarrow{\lim} 0, \ \therefore \ let \ \Delta t = dt$$

Equation 2.4

$$\frac{N_{P2}(t+1) - N_{P2}(t)}{dt} = N_{P2}(t).k_{12} - N_{P1}(t).k_{21}$$

Equation 2.5

$$\therefore N_{P2}(t+1) - N_{P2}(t) = (N_{P2}(t).k_{12}.dt) - (N_{P1}(t).k_{21}.dt)$$

Equation 2.6

$$\therefore N_{P2}(t+1) = N_{P2}(t) + (N_{P2}(t).k_{12}.dt) - (N_{P1}(t).k_{21}.dt)$$

Equation 2.7

Using this method, even if the ODEs are not analytically solvable, the value of $N_{P2}(t)$ can be numerically calculated by iterating over the desired range. The process above was applied in the same way to Equations: 3.1 - 3.13. Thus, the time, dose and generation dependence of each cellular process upon nanoparticle uptake (ROS generation, GSH depletion, Inflammatory Cascade progression and Apoptosis), observed in the experimental measurements (*Mukherjee et al., 2010 – A and B, Naha et al., 2009 and 2010, Naha and Byrne, 2013* and *Mukherjee and Byrne, 2013*) can successfully be simulated by the system of equations.

In using this system of rate equations, it is possible to de-couple processes which are dependant on the physico-chemical properties of the nanoparticle from events which are dependant on the cell type. Therefore, it may be possible to predict how a new nanoparticle will affect the same type of cell, simply by changing the nanoparticle dependant properties (such as: number of charged terminal groups). Following on from this, it would also be possible to predict the effect of the same nanoparticle on a different cell line by changing one of the cell dependant properties (such as: anti-oxidant quenching rate or rates of events

within the inflammatory cascade). These can also be correlated with the responses of different assays at different time-points, corresponding to different cellular events.

Overall, these rates will aid in the development of a predictive model (as a pre-cursor to a full QSAR) and may ultimately form an alternative to the EC_{50} values as the primary method of classifying toxicity.

2.2.3 Program Structure and Sigma Plot

The following figure (figure 2.4) shows the progress of the computer program as it solved each equation for a numerical solution.

In the flow chart (figure 2.4) "For loops" are used to iterate the program, making it repeat the same set of calculations until a certain set of conditions are met, such as: Results have been obtained for all twenty one dose values or calculations have been preformed for all three generations.

"If statements" are used to extract data about certain time points or dose values for plotting. For example, if data about ROS production when the dose is equal to 1μM was needed, then an "If statement" would be used to extract only data for that dose. These are particularly useful due to the large amounts of data calculated by the program.

Program Flow Chart

Declaration of Time, Dose, initial values and constants (as per table Ap.1 in the Appendix)

Equation for N_{amg} (Equation 1) defined, Equation for k_A and G^* defined

Open For Loop A — For loop to allow calculation of all equations for 3 generations

Open For Loop B — For loop to allow calculation of all equations for 21 doses

Open For Loop C — For loop for calculation of endocytosis

Calculation Of Endocytosis, N_{endo} (Equation 2)

Close For Loop C — *If statements output endocytosis values for all timepoints, at every dose, for all 3 generations.*

Open For Loop D — For loop for calculation of Source, ROS and GSH

Calculation Of ROS Source, N_{Source} (Equation 11)

Calculation Of ROS Production, N_{ROS} (Equation 12)

Calculation Of GSH Production, N_{GSH} (Equation 4)

Close For Loop D — *If statements output Nsource, NROS and NGSH values for all timepoints, at every dose, for all 3 generations.*

Open For Loop E — For loop for calculation of inflammatory cascade and viability

Calculation of N_{MMP} (Equation 6)   Calculation of $N_{Caspase}$ (Equation 5)

Calculation of N_{TNF} (Equation 7)

Calculation of N_{IL-8} (Equation 8)

Calculation Of Cellular Viability (Equation 9)

Close For Loop E — *If statements output values from inflammatory cascade and viability for all timepoints, at every dose, for all 3 generations.*

Close For Loop B

Close For Loop A

Figure 2.4: A flowchart showing how the program, sequentially, solves each equation.

For each run detailed above the simulation generates over 400,000 values.

2.3 Cellular Assays

2.3.1 Viability assays

Viability assays are performed with the aim of calculating an EC_{50} value. The EC_{50} is the concentration of the toxic substance needed to cause a loss of 50% of the cell population and can be a useful initial step in the evaluation of a toxic substance. While there are many different methods available for this analysis, a dye based assay system was employed in this work to evaluate the percentage cell viability upon exposure to PAMAM dendrimer nanoparticles of generations 4, 5 and 6; and aminated polystyrene nanoparticles (of 50nm and 100nm diameter), in particular Alamar Blue and MTT were used. Each dye has a different localisation site within the cell and therefore gives slightly different results, while this can lead to two assays giving different percentage viability for the same situation, it can also be advantageous in that insight can be gained into which areas of the cell the nanoparticle is affecting at different time points during the toxic response.

2.3.1.1 Alamar Blue (AB)

Alamar Blue is a reasurin based dye which measures viability based on the cytosolic activity of the cell (*O' Brien et al., 2000*). It does not localise to any specific organelle within the cell and therefore usually registers toxicity at a later time point in the cascade; at least this is the case for PAMAM dendrimer nanoparticles, as they are seen to localise in the mitochondria (*Lee et al., 2009*). However, not all particles initiate toxicity via the mitochondria and for these the Alamar Blue may in fact be a more sensitive dye for probing the earlier time points.

In living cells, the active component of Alamar Blue, reasurin, undergoes a colour changing reaction, from blue to red (figure 2.5). The red form generated is highly fluorescent and can therefore be used to gauge the number of living cells in a sample (by comparing it to cells which have not been exposed to any toxic substance, and are therefore 100% viable)(*Khazalpour and Nematollahi, 2014*).
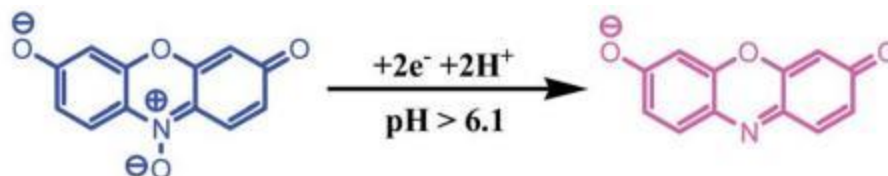
Figure 2.5: Reduction mechanism of Reasurin dye (in pH values over 6.1), the reduction leads to Resorufin, the fluorescent component of the Alamar Blue Assay.

*(Image adapted from: Khazalpour and Nematollahi, 2014, RSC Adv., **4**(17), 8431-8438)*

2.3.1.2 3-(4,5-Dimethylthiazol-2-yl)-2,5-diphenyltetrazolium Bromide (MTT)

MTT (figure 2.6) is a more specific dye than AB, as it is seen to localise in the mitochondria of living cells (*Mosmann, 1983*). PAMAM dendrimers also localise to the mitochondria after endocytosis (and subsequent endosomolysis) and therefore MTT has been shown to be more sensitive to earlier time points when analysing the PAMAM toxicity. In the mitochondria the MTT undergoes a dehydrogenase mediated reaction from a soluble yellow dye to an insoluble purple dye. This will only occur if the mitochondria are still functional (*id est* in living cells) and thus the conversion of the dye by the cell population will give an indication of the amount of cells which are viable (*Mosmann, 1983*).
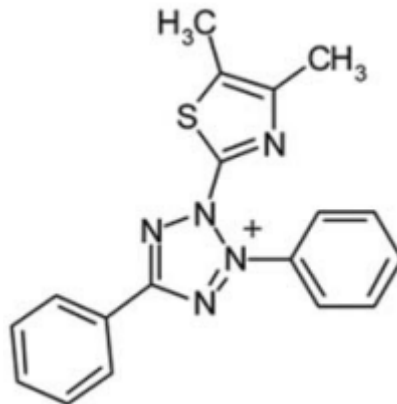
Figure 2.6: MTT (3-(4,5-dimethylthiazol-2-yl)-2,5-diphenyltetrazolium bromide, active component of MTT Assay. (*Image adapted from: Berridge et al., 2005, Biotechnol. Annu. Rev., **11**(2005), 127-152*)

However, it is important to note that for MTT to function normally it requires the mitochondria of the viable cells to also function normally, therefore if there is disruption to the mitochondria it may affect the results obtained from the assay.

Both AB and MTT assays measure viability, but have different localisation sites within the cell. Resulting in the dyes measuring slightly different biomarkers (or lack thereof) for apoptosis and therefore measuring different points within the toxic response cascade. Comparisons between these could yield interesting results when studying how apoptosis occurs due to nanoparticle exposure and the first areas to be affected within the cell.

2.3.2 ROS and Anti-Oxidants

PAMAM dendrimers are known to cause toxicity via the generation of ROS upon endocytosis (*Mukherjee et al., 2010 – B, Naha et al., 2009* and *Naha and Byrne, 2013*); therefore, it was necessary to evaluate the amount of ROS produced. The process of ROS

generation is thought to be mediated by the enzyme NADPH oxidase (*Chamulitrat et al., 2004*), which produces O_2^- (*Shuvaev et al., 2011*), however, the v-ATPase proton pump also supplies an excess of H^+ ions (*Nel et al., 2009*), the O_2^- and H^+ rapidly dismutate to hydrogen peroxide H_2O_2 in the cell (*Aceworth and Bailey, 1995*). Therefore H_2O_2 was monitored by the dye Carboxy-H_2DCFDA. Also important is the cellular anti-oxidant response. Previous reports have shown that glutathione (GSH) is an important mediator of the anti-oxidant defence (*Mukherjee and Byrne, 2013*) and as the model indicates may be the sole differing factor when it comes to different levels of toxicity observed in different cell lines (Chapter 3: Numerical simulations of *in vitro* nanoparticle toxicity – the case of Poly (amido amine) dendrimers (*Maher et al., 2014*)). GSH was monitored by Thiol Tracker Violet[®] (TTV).

2.3.2.1 5-(and-6)-carboxy-2',7'- dichlorodihydrofluorescein diacetate (Carboxy-H₂DCFDA)

Caboxy-H_2DCFDA is a carboxylated derivative of the fluorescein dye which has been modified to have two additional acetyl groups (Figure: 2.7: a). Upon uptake into the cell the acetate groups are cleaved forming a negative charge, reducing the possibility of dye leakage (Figure: 2.7: b). Both forms of the dye are non fluorescent, until interaction with ROS, where the dye is oxidised to produce the fluorescent product: DiChlorodihydroFluorescein (DCF) (Figure 2.7: c). The intensity of the fluorescence can then be measured and compared to a control to assay for the increase or decrease in the amount of ROS in a cell population (Figure 2.7: d) (*Invitrogen, 2016 – A*).
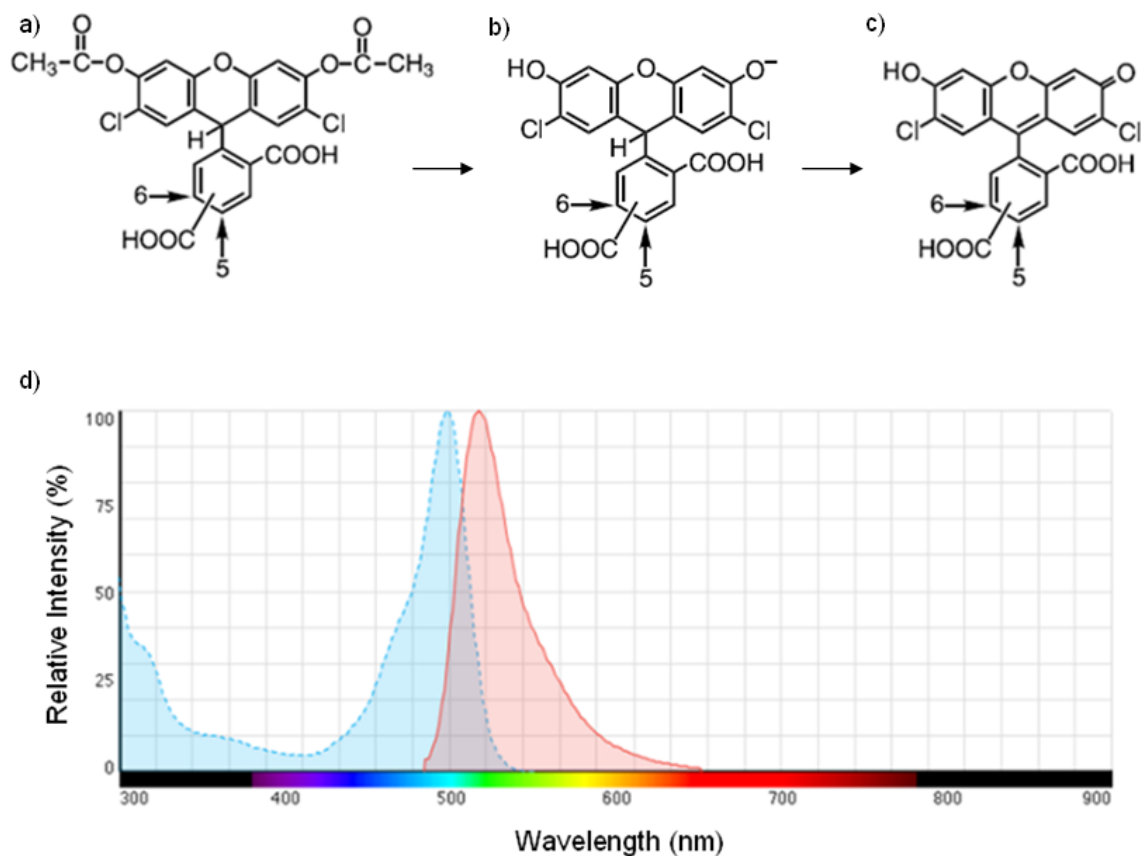
Figure 2.7: a) shows the 5-(and-6)-carboxy-2′,7′- dichlorodihydrofluorescein diacetate dye, b) shows the de-acetylated from of the dye, both a and b are non-fluorescent. c) Shows the de-acetylated, oxidised and fluorescent form of the dye: DiChlorodihydroFluorescein (DCF). d) Shows the absorption and emission spectrum of the DCF ($\lambda_{ex} \approx 492nm - 495nm$, $\lambda_{ex} \approx 517nm - 527nm$). (Image adapted from product supplier: Invitrogen (part of Thermo Fisher Scientific, available online at: *https://www.thermofisher.com/order/catalog/product/C369*)

2.3.2.2 Thiol Tracker Violet[®] (TTV)

TTV binds directly to reduced thiols in the cell, GSH accounts for the vast majority of these, therefore, TTV can be used to assay for the amount of intracellular GSH (*Mandavilli*

and Janes, 2010). Upon conjugation with GSH, TTV becomes fluorescent (Figure 2.8) and can be detected spectrophotometrically. Unfortunately, a more detailed discussion of the mode of action of TTV is not possible as the structure is proprietary and therefore, not freely available.
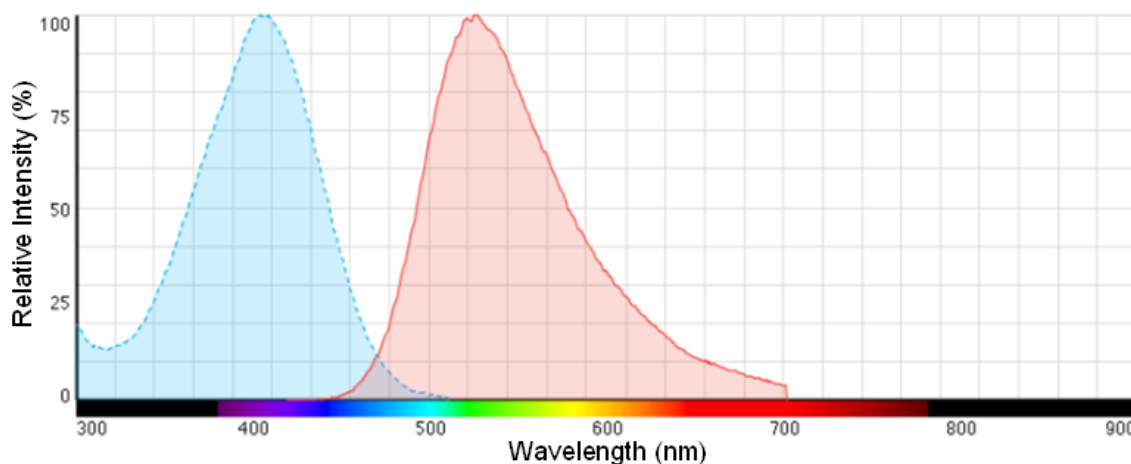
Figure 2.8: The absorption and emission spectrum of the TTV dye when conjugated with intracellular GSH. ($\lambda_{ex} \approx 405nm, \lambda_{ex} \approx 525nm$). (Image adapted from product supplier: Invitrogen (part of Thermo Fisher Scientific), available online at: *https://www.thermofisher.com/order/catalog/product/T10095*)

2.3.3 Endosomal Labelling

Endosomes were labelled for Confocal Laser Scanning Microscopy (CLSM) imaging. To do this the Celllight® Early Endosomes-RFP, BacMam 2.0 kit was employed, this allows the labelling of the early endosomes with a fusion construct of Rab5a and TagRFP (Red Fluorescent Protein) (Figure 2.9). This is delivered to the cell via the insect cell virus: baculovirus, which transfects the fusion construct under the control of a mammalian promoter. The viral promoter and genes are not recognised and therefore not replicated in

the mammalian cell (which decreases risks associated with employing viral transfection agents). The transfection efficiency is aided by several factors, such as: a pseudotyped capsid protein for more efficient cell entry and enhanced CMV promoter and Woodchuck Post-Transcriptional Regulatory Element, which both aid expression levels. The protein expression is effective for up to five days after exposure.
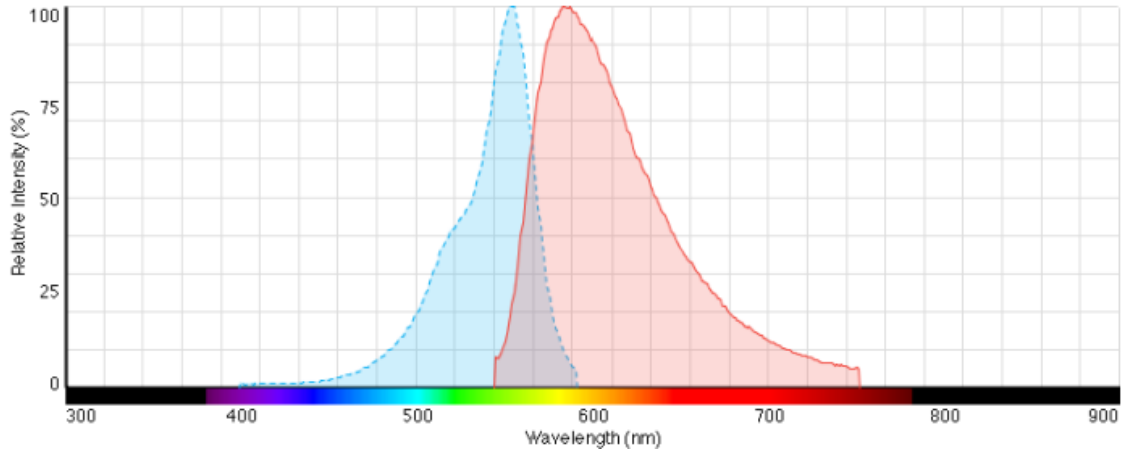
Figure 2.9: The absorption and emission spectrum of the TagRFP (Red Fluorescent Protein)($\lambda_{ex} \approx 555nm$, $\lambda_{ex} \approx 584nm$). (Image adapted from product supplier: CellLight (part of Thermo Fisher Scientific, available online at: *https://www.thermofisher.com/order/catalog/product/C10587*)

2.4 Imaging

2.4.1 Confocal Laser Scanning Microscopy (CLSM)

CLSM is a technique which allows the real time visualisation of fluorescently active components of a sample, in the case of this work, a living HaCaT cell. The advantage of CLSM over other forms of fluorescent microscopy is that the focal plane can be varied, so that the internal cell components can be scanned directly.
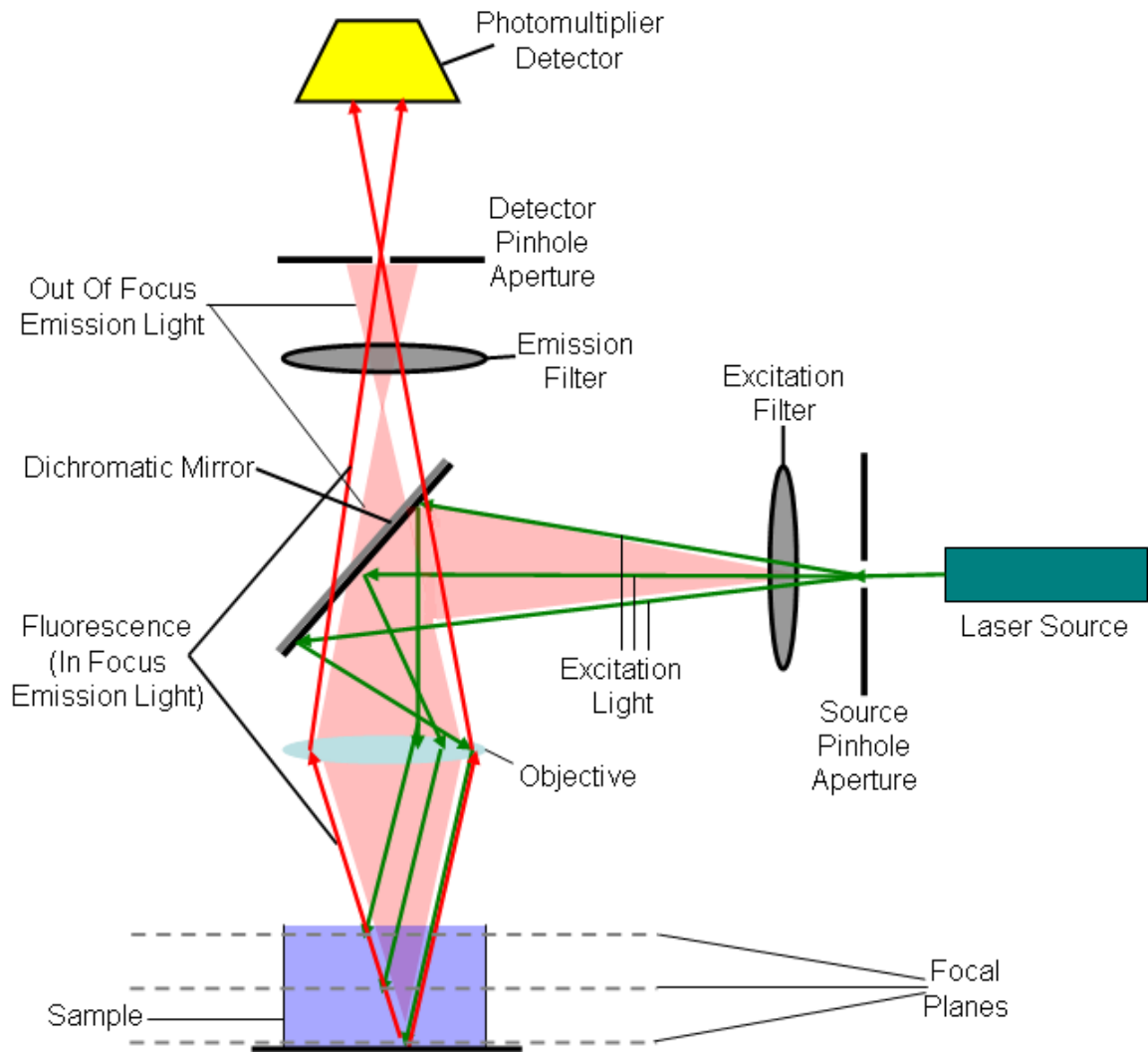
Figure 2.10: Schematic representation of a CLSM. (Image adapted from: Zeiss, Available online at: *http://zeiss-campus.magnet.fsu.edu/articles/livecellimaging/techniques.html*)

In Figure 2.10, coherent light is passed through a pinhole aperture situated in a conjugate plane with a point on the specimen and a second pinhole aperture before the detector. The excitation light is directed by a dichromatic mirror through an objective, finally focussing on a point on the sample, the light is then scanned across the sample (at the selected focal plane) and fluorescent emission occurs. The emitted light passes back through the objective, some then passes through the dichromatic mirror and emission filter (which

63

filters out background from the excitation source). At this point, only light which is confocal to the pinhole aperture will pass through and be detected by the photomultiplier tube. The focal plane can be changed by refocusing the objective, which will shift both the excitation and emission points on the sample; this new plane will then become confocal with the pinhole aperture of the source and detector (*Zeiss, 2012*). In this way, by successively scanning each plane, it could be possible to generate a 3 dimensional image of a sample, with the correct imaging software. The detection of multiple, non-interfering fluorescent signals is possible using a multi-channel CLSM.

2.4.2 Scanning Electron Microscope (SEM)

Field Emission Scanning Electron Microscopy (FE-SEM) was performed in this work to examine the size of the 50 and 100nm polystyrene nanoparticles (PSNPs). SEM works by generating a beam of electrons from a source, these electrons are then accelerated through an anode, passed through a magnetic condenser to focus the electron beam. The beam is then passed through an aperture which eliminates any off-axis or off-speed electrons. The beam is finally passes through a scanning coil, which consist of two solenoids, which create opposing magnetic fields which are used to direct the beam toward the sample area (*Zhou and Wang, 2007*). In the SEM used for this study a raster scan pattern is used. The electrons interact with the sample and produce secondary electrons which are detected and then visualised.

2.5 References

- Aceworth, I. N. and Bailey, B. 1995. The Handbook of Oxidative Metabolism. *Chelmsford: ESA Inc*.

- Berridge, M.V., Herst, P.M. and Tan, A.S. 2005. Tetrazolium dyes as tools in cell biology: new insights into their cellular reduction. *Biotechnol. Annu. Rev.,* **11**(2005), 127-152.

- CellLight. 2016. Early Endosomes-RFP, BacMam 2.0. Accessed on 26-02-2016. Available at: *https://www.thermofisher.com/order/catalog/product/C10587*.

- Chamulitrat, W., Stremmel, W., Kawahara, T., Rokutan, K., Fujii, H., Wingler, K., Schmidt, H.H. and Schmidt, R. 2004. A constitutive NADPH oxidase-like system containing gp91phox homologs in human keratinocytes. *J. Invest. Dermatol.,* **122**(4), 1000-1009.

- Einstein, A. 1916. Strahlungs-emission und -absorption nach der Quantentheorie. *Verhandlungen der Deutschen Physikalischen Gesellschaft,* **18**(1916), 318–323.

- Invitrogen. 2016 – A. 5-(and-6)-carboxy-2′,7′- dichlorodihydrofluorescein diacetate dye. Accessed on 26-02-2016. Available at: *https://www.thermofisher.com/order/catalog/product/C369*.

- Invitrogen. 2016 – B. ThiolTracker Violet (TTV). Accessed on 26-02-2016. Available at: *https://www.thermofisher.com/order/catalog/product/T10095*.

- Khazalpour, S. and Nematollahi, D. 2014. Electrochemical study of Alamar Blue (resazurin) in aqueous solutions and room-temperature ionic liquid 1-butyl-3-methylimidazolium tetrafluoroborate at a glassy carbon electrode. *RSC Adv.,* **4**(17), 8431-8438.

- Lee, J.H., Cha, K.E., Kim, M.S., Hong, H.W., Chung, D.J., Ryu, G. and Myung, H. 2009. Nanosized polyamidoamine (PAMAM) dendrimer-induced apoptosis mediated by mitochondrial dysfunction. *Toxicol. Lett.,* **190**(2), 202–207.

- Maher, M.A., Naha, P.C., Mukerjee, S.P. and Byrne, H.J. 2014. Numerical simulations of *in vitro* nanoparticle toxicity – the case of Poly(amido amine) dendrimers. *Toxicol. In Vitro*, **28**(8), 1449-1460.

- Mandavilli, B.S. and Janes, M.S. 2010. Detection of intracellular glutathione using ThiolTracker violet stain and fluorescence microscopy. *Curr. Protoc. Cytom.,* **53**(9.35), 1-9.

- Mosmann, T. 1983. Rapid Colorimetric Assay for Cellular Growth and Survival: Application to Proliferation and Cytotoxicity Assays. *Journal of lmmunological Methods,* **65**(1-2), 55-63.

- Mukherjee, S.P. and Byrne H.J. 2013. Poly amidoamine dendrimer nanoparticle cytotoxicity oxidative stress, caspase activation and inflammatory response: experimental observation and numerical simulation. *Nanomed: Nanotech. Bio. Med.,* **9**(2), 202-211.

- Mukherjee, S.P., Davoren, M. and Byrne H.J. 2010-A. *In vitro* mammalian cytotoxicological study of PAMAM dendrimers - towards quantitative structure activity relationships. *Toxicol. in Vitro,* **24**(1), 169-177.

- Mukherjee, S.P., Lyng, F.M., Garcia, A., Davoren, M. and Byrne H.J. 2010-B. Mechanistic studies of *in vitro* cytotoxicity of poly (amido amine) dendrimers in mammalian cells. *Toxicol. Appl. Pharm.,* **248**(3), 259–268.

- Naha, P.C. and Byrne, H.J. 2013. Generation of Intracellular Reactive Oxygen Species and Genotoxicity effect to Exposure of Nanosized Polyamidoamine (PAMAM) dendrimers in PLHC-1 cells *in vitro*. *Aquatic Toxicology,* **132-133**(2103), 61-72.

- Naha, P.C., Davoren, M., Casey, A. and Byrne H.J. 2009. An Ecotoxicological Study of Poly(amidoamine) Dendrimers-Toward Quantitative Structure Activity Relationships. *Env. Sci. Technol.,* **43**(17), 6864–6869.

- Naha, P.C., Davoren, M., Lyng, F.M. and Byrne, H.J. 2010. Reactive oxygen species (ROS) induced cytokine production and cytotoxicity of PAMAM dendrimers in J774A.1 cells. *Toxicol. Appl. Pharm.,* **246**(1-2), 91–99.

- Nel, A.E., Mädler, L., Velegol, D., Xia, T., Hoek, E.M.V., Somasundaran, P., Klaessig, F., Castranova, V. and Thompson, M. 2009. Understanding biophysicochemical interactions at the nano–bio interface. *Nature Materials,* **8**(7), 543 – 557.

- O'Brien, J., Wilson, I., Orton, T. and Pognan, F. 2000. Investigation of the Alamar Blue (resazurin) fluorescent dye for the assessment of mammalian cell cytotoxicity. *Eur. J. Biochem.* **267**(17): 5421-5426.

- Salvati, A., Aberg, C., dos Santos, T., Varela, J., Pinto, P., Lynch, I. and Dawson K.A. 2011. Experimental and theoretical comparison of intracellular import of polymeric nanoparticles and small molecules: toward models of uptake kinetics. *Nanomed: Nanotech. Bio. Med.,* **7**(6), 818-826.

- Shuvaev, V.V., Han, J., Yu, K.J., Huang, S., Hawkins, B.J., Madesh, M., Nakada, M. and Muzykantov, V.R. 2011. PECAM-targeted delivery of SOD inhibits endothelial inflammatory response. *FASEB,* **25**(1), 348-357.

- Zeiss. 2012. Education in Microscopy and Digital Imaging. Accessed on 26-02-2016. Available at:

  http://zeiss-campus.magnet.fsu.edu/articles/livecellimaging/techniques.html.

- Zhou, W and Wang, Z.L. 2007. Scanning Microscopy for Nanotechnology: Techniques and Applications. *New York: Springer Science and Business Media*.

Chapter 3:

Numerical simulations of in vitro nanoparticle toxicity – the case of Poly (amido amine) dendrimers.

3.1 Abstract

A phenomenological rate equation model is constructed to numerically simulate nanoparticle uptake and subsequent cellular response. Poly (amido amine) dendrimers (generations 4-6) are modelled and the temporal evolution of the intracellular cascade of; increased levels of reactive oxygen species, intracellular antioxidant species, caspase activation, mitochondrial membrane potential decay, tumour necrosis factor and interleukin generation is simulated, based on experimental observations.

The dose and generation dependence of several of these response factors are seen to well represent experimental observations at a range of time points. The model indicates that variations between responses of different cell-lines, including murine macrophages, human keratinocytes and colon cells, can be simulated and understood in terms of different intracellular antioxidant levels, and, within a given cell-line, varying responses of different cytotoxicity assays can be understood in terms of their sensitivities to different intracellular cascade events.

The model serves as a tool to interpolate and visualise the range of dose and temporal dependences and elucidate the mechanisms underlying the *in vitro* cytotoxic response to nanoparticle exposure and describes the interaction in terms of independent nanoparticle properties and cellular parameters, based on reaction rates. Such an approach could be a valid alternative to that of effective concentrations for classification of nanotoxicity and may lay the foundation for future quantitative structure activity relationships and predictive nanotoxicity models.

3.2 Introduction

Research involving nanoparticles has seen a huge increase in recent years. This is undoubtedly due to the novel properties these particles possess and their potential uses in a variety of fields including: medicine, electronics, engineering, cosmetics, food, textiles, packaging and many more (*PEN, 2015*).

Medical applications is a sector where nanomaterials have shown great potential and have already been used in several areas including: *in vivo* and *in vitro* diagnostic tools, biocompatible materials for implants, nutraceuticals, cancer therapy and, in particular, drug delivery (*Jain, 2007, Balasundaram et al., 2006, Nishimura et al., 2007, Nair et al., 2010, Bharali et al., 2009, Koo et al., 2005* and *Hans and Lowman, 2002*).

In terms of drug delivery, this interest is due to properties such as the ability to cross biological barriers easier than some more traditional delivery vehicles and the potential to escape from intracellular compartments such as lysosomes and endosomes (*Watson et al., 2005*). A full list of properties and potential uses for nanoparticles in drug delivery is somewhat outside the scope of this paper and has been reviewed elsewhere (*De Jong and Borm, 2008*). While the avenue of new medical applications does look promising, it has been found that some nanoparticles, when exposed to mammalian cells, elicit a toxic response (*Jain et al., 2010*).

In vitro studies indicate this toxicity to be the result of oxidative stress, manifest as increased Reactive Oxygen Species (ROS) production shortly after endocytosis (*Xia et al., 2006*), with subsequent trafficking of the nanoparticle seen to occur through endosomes and lysosomes (*Nel et al., 2006* and *Salvati et al., 2011*). The oxidative stress leads to a release of inflammatory factors (*Kennedy et al., 2009*, *Mukherjee et al., 2010-A*, *Naha et*

al., 2010, *Rothen-Rutishauser et al., 2007*, *Schins et al., 2000*, *Shedova et al., 2003* and reviewed by: *Medina et al., 2007*) and potential activation of apoptotic pathways (*Lee et al., 2009*, *Mukherjee et al., 2010-B*, *Naha and Byrne, 2013* and *Jeng et al., 2006*). It is also important to consider processes such as endosomal rupture (endosomolysis) (*De Jong and Borm, 2008* and *Salvati et al., 2011*), which can enhance the toxic response as released nanoparticles have been shown to localise in and subsequently damage organelles such as the mitochondria (*Kennedy et al., 2009, Lee et al., 2009* and *Mukherjee et al., 2010-A*). If medical applications are to remain a viable option for nanomaterials, then it will be essential to explore and better define the mechanisms involved in the toxic response.

However, in the majority of current studies, *in vitro* toxicity is quantified using the effective concentration for 50% loss of viability (EC_{50}) endpoint as an indicator of overall toxic effect. The EC_{50}, is the result of a complex cascade of events which occur between the initial exposure and cell death; it gives no indication of the mechanisms, kinetics or efficacy of the interim processes. Additionally, the measured EC_{50} is dependent on the assay employed and the responses of different cell lines to the same exposure conditions have been shown to vary significantly (*Mukherjee et al., 2010-A*). Coupled with the broad range of nanoparticle compositions, structures, sizes and possible surface functionalisations, the result is a vast array of studies from which it is difficult to derive clear systematic trends.

A more rationalised approach to nanotoxicity classification is becoming increasingly important because, as more and more nanoparticles are made available, testing via a case-by-case approach will not be sufficient (*Oomen et al., 2014* and *Clark et al., 2011*). If nano-toxicology, and by extension nanomedicine, is to advance, the focus should be on:

(i) Identification of the particle based properties which induce the cellular response,

(ii) The cellular parameters which result in variations in that response, and

(iii) The variability introduced by the use of different assays.

By doing this, it may be easier to elucidate processes and events which are common to a large set of nanoparticles. Initial screening methods should be conducted *in vitro*, as there is a drive for a reduction in the use of animal models for evaluating toxicity, due to regulatory developments in both the EU and US (*EU - Directive 2010/63/EU, 2010* and *US - Public Law 106-545, 2000*) generally based on the 3 R's of Russell and Burch to replace, reduce and refine the use of animals for scientific purposes (*Russell and Burch, 1959*). Therefore, there is currently much promotion of the development of *in vitro* models which can accurately infer *in vivo* results. One strategy to help meet these requirements, recently endorsed by the OECD (*OECD, 2013*), is the analysis of Adverse Outcome Pathways (AOPs), by which a sequential chain of causally linked events at different levels of biological organization that lead to an adverse health or ecotoxicological effect is identified. The aim of advancing AOPs is to i) guide the development of (*in vitro*) Test Guidelines, ii) provide a basis for the design of Integrated Approaches to Testing and Assessment (IATA), and iii) guide the development of molecular profilers for the QSAR toolbox. A QSAR (Quantitative Structure Activity Relationship) can be used to identify and model traits which are common to entire sets of nanoparticles and hopefully elucidate how these properties/traits impact the overall toxicity (*OECD, 2007*). By advancing the knowledge of these models, it is hoped that, eventually, it will be viable to predict the full toxic profile of a cell which has taken up a nanoparticle (*Puzyn et al., 2009*).

In the field of nano-toxicology (*in vitro*), the endpoint is usually the median EC_{50} of a colorometric assay, but the choice of both assay and cell-line is large and little consideration has been given to the different modes of action of the assay within the cell. Many studies have explored the mechanisms underlying the toxic response, but little attention has been devoted to quantifiable comparison between different particles or cell lines, and the relationship between endpoint and nanoparticle properties. The domain of nanoparticles is vast, but the paucity of systematic studies renders it difficult to establish domains of applicability of any structure-activity paradigm, and therefore, to define unambiguous algorithms or to validate based on statistical goodness-of-fit, robustness and predictability.

In the drive to develop a better understanding of the structural dependence of toxicity and mechanisms, studies using a homologous series of nanoparticles with systematically varied physico-chemical properties can play a vital role. Systematic variations of cellular uptake and mechanisms of response, such as oxidative stress and inflammatory responses can be compared to the systematic changes in the physico-chemical properties of the nanoparticle. A better quantitative understanding of the mechanisms of response allows a better insight into the function of the cytotoxicity assays, and how the endpoints vary systematically with nanoparticle properties, but also with cell line, ultimately laying the foundation for the development of quantitatively predictive models for cellular response (*Clark et al., 2011*).

Poly (amido amine) (PAMAM) dendrimer nanoparticles are a homologous series of nanoparticles of well defined physico-chemical properties which are systematically variable and elicit systematically variable cellular responses. PAMAM dendrimers are branched in conformation and consist of three main parts, (i) the initiator core, (ii) the

interior branches and (iii) the exposed branch termini (*Tomalia and Fréchet, 2002*). Each set of these branches is called a Generation (G) and the generation determines the number of surface amino groups according to the formula:

$$N_{amg} = N_{BP(G0)} . 2^G$$

Equation 3.1

Where N_{amg} is the number of surface amino groups, $N_{BP(G0)}$ is the number of initial branching points at generation zero (*G0*) and *G* denotes the generation number. Thus, the diameter and number of surface amino-groups increases systematically with increasing generation.

This well defined branched system allows for the variation of parameters such as: Terminal modification via addition of cationic, anionic or neutral molecules, zeta potential and in particular generation, which will govern: number of amino groups and therefore effective surface charge, diameter and overall particle size. Ultimately this system lets us examine how these characteristics impact the cell-nanoparticle interaction and therefore may shed light on the processes involved in toxicity. Previous studies of exposure of aquatic species (*Naha et al., 2009*) and *in vitro* mammalian cell cultures (*Mukherjee et al., 2010-A* and *B*) have demonstrated that the polymeric dendrimer series with systematically varied structures elicit toxic responses which are well correlated with the variations in physico-chemical properties.

Uptake of these PAMAM dendrimers occurs via endocytosis, where the nanoparticle is enveloped in cellular membrane and transported into the cell (*Mukherjee et al., 2010-B, Kitchens et al., 2007* and *Hong et al., 2004*). The toxic response has been shown to derive from an increased production of intracellular Reactive Oxygen Species (ROS) after endocytosis (*Mukherjee et al., 2010 – B* and *Naha et al., 2009* and *Naha and Byrne, 2013*).

The ROS production is counteracted by cellular anti-oxidants, one example of these being Glutathione (GSH), a thiol based tri-peptide (*Mukherjee and Byrne, 2013*). After this, a cascade of different events and the release of several characteristic cytokines and chemokines occurs. Studies have shown that, for PAMAM dendrimers in HaCaT cells, an immortalized human keratinocyte line, activation of caspases 8 and 3 occurs at around 1-2 hrs, followed by mitochondrial membrane potential decay (MMPD) (3-4hrs), after which there is a release of TNF-α (4-5hrs) and eventually IL-8 which then maximises at 24 hours (*Mukherjee and Byrne, 2013*). It has also been proposed that larger generation dendrimer nanoparticles and/or doses can cause the endosome to rupture (endosomolysis), via the so-called proton pump mechanism. (*Guillot-Nieckowski et al., 2000*, *Kukowska-Latallo et al., 1996* and *Zhou et al., 2006*). Supported by the fact that after ~16hrs the PAMAM dendrimers have been seen to be located in the mitochondria (*Lee et al., 2009* and *Mukherjee and Byrne, 2013*) whereupon the oxidative stress is further increased, resulting in further MMPD, which can culminate in apoptosis. A similar inflammatory cascade has been reported in murine macrophages, although the evolution of the responses was observed to be somewhat slower (*Naha et al., 2010*).

In both cases, the temporal profile was seen to be systematically dependent on dendrimer generation and dose, pointing towards the basis of potential structure property relationships. However, more than a single measurement at a single time point by a cytotoxic assay, the measurement of the time evolution of the cascade provides a clearer picture of the set of events and the visualisation of different timescales allows for a better evaluation of differences due to nanoparticle properties and cell lines.

It is proposed that, by measuring and numerically modelling the kinetics of the cellular responses and their dependence on nanoparticle properties, a more intuitive formulism of the nanotoxic response which more clearly tracks the cellular response related to nanoparticle properties can be established. The approach lends itself naturally to an AOP formalism, but the systems biology like approach adds quantification of the rates of response, which are related to the physico-chemical properties of the nanoparticles, such that the approach may ultimately lead to QSARs and predictive models of cytotoxic response. These predictive models would be able to provide some preliminary data on toxicity which could be used to inform initial testing strategies.

The model presented in this study looks at PAMAM toxicity based on previously published experimental data (*Mukherjee et al., 2010-A* and *B*, *Mukherjee and Byrne, 2013, Naha et al., 2009* and *2010).* A preliminary form of the model faithfully reproduced the time course of the toxic responses of the HaCaT cell-line to PAMAM dendrimer exposure, including the experimentally observed generation dependence (*Mukherjee and Byrne, 2013*). This study critically extends the model to the dose dependent responses of cell lines to nanoparticle exposure, and elucidates the origin of the dependence of EC_{50} on cell-type and cytotoxic assay dependent results. The approach argues for a classification of toxic responses based on activity of the particles, expressed as particle and cell dependent reaction rates, rather than Effective Concentration end points.

3.3 Materials and Methods

Experimental results are derived and adapted from previous work by the authors (*Mukherjee et al., 2010-A* and *B*, *Mukherjee and Byrne, 2013, Naha et al., 2009* and *2010)* and details of the materials and methods used can be viewed in these publications. However, below is a brief summary of the experimental methods employed.

Naha et al. detail the dose and generation dependence of the toxic responses of murine macrophages, the J774A.1 cell line, to exposure to PAMAM generations G4, G5 and G6. The J774A.1 cells were cultured in Dublecco's Modified Eagle's Medium (DMEM), supplemented with 10% FBS, 2 mM L-Glutamine and 45 IU/mL streptomycin and penicillin at 37˚C in 5% CO_2. The following exposure dose ranges were used: 0.08μM to 6μM for G4, 0.03μM to 2μM for G5 and 0.013μM to 1μM for G6. For all generations, the dose dependence of ROS production was monitored by the fluorimetric assay, Carboxy-H_2DCFDA and was performed in black 96 well plates with a cell concentration of $4x10^5$cells/mL. DMEM was used as a negative control and H_2O_2 was used as positive control. Readings were taken at 1hr, 2hrs, 4hrs and 6hrs, with λ_{ex} (excitation wavelength) = 485nm and λ_{em} (emission wavelength) = 520nm.

The temporal evolution of the inflammatory cascade of TNF-α and Interleukin 6 (IL-6) was monitored at a fixed dose of 1μM using the ELISA assay, where LPS was used as a positive control to verify the procedure and the absorbance was read at 405nm. Cytotoxicity was measured using the MTT assay, with 0.5mg/mL dye concentration and readings were taken for time points: 6hrs, 12hrs, 24hrs, 48hrs and 72hrs, at an absorbance of 595nm (*Naha et al., 2010* and *Mukherjee and Byrne, 2013*).

Mukherjee et al. detail the dose and generation dependences of the toxic responses of the immortalised human keratinocyte (HaCaT) and primary adenocarcinoma colon (SW480) cell lines. The cell lines were cultured in the same conditions as described above using DMEM F12 HAM and with an additional 1µg/mL hydrocortisone added for the HaCaT cells. The following exposure dose ranges were used: 0.01µM to 21.1µM for G4, 0.03µM to 5.2µM for G5 and 0.01µM to 5.168µM for G6. Dose and generation dependent cytotoxicity for both cell lies was measured using the MTT, Alamar Blue and Neutral Red assays at 24hrs.

The MTT assay was performed with 5mg/mL dye concentration and read at an absorbance of 595nm. Alamar Blue and Neutral Red were performed in the same 96 well plates which were seeded at a concentration of 1×10^5 cells/mL.

Alamar Blue was performed with a concentration of 5% [v/v] and results were measured using a fluorimeter with the $\lambda_{ex} = 485$nm and $\lambda_{em} = 520$nm.

Neutral Red was performed with a dye concentration of 1.25% [v/v] and results were measured using a fluorimeter with the $\lambda_{ex} = 531$nm and $\lambda_{em} = 642$nm. The temporal evolutions of ROS, apoptosis and DNA damage were monitored for the HaCaT cell line. ROS was again measured with the Carboxy-H_2DCFDA and was performed with a cell concentration of 1×10^5 cells/mL. Readings were taken between 1-4hrs and at 24hrs for HaCaT cells, and between 30mins-6hrs and at 24hrs for SW480 cells with $\lambda_{ex} = 490$nm and $\lambda_{em} = 545$nm. Apoptosis was measured with flow cytometry, using the YO-PRO-1/Propidium dyes at a concentration 1µL per 1×10^6 cells/mL. The TUNEL assay was used to detect DNA damage at a time point of 24hrs (*Mukherjee et al., 2010-A* and *B*).

Numerical results for all equations were obtained by integration using the iterative Euler approach (*Atkinson, 1989*) and SigmaPlot™ (v.10.0) was used to generate the values and graphs.

3.4 Results

3.4.1 Generation of the Equations

In order to better visualise the full range of dose and temporal dependencies and elucidate the mechanisms of response, the system was modelled using a relatively simple phenomenological rate-equation model. This model is similar, in concept, to ones commonly employed for modelling molecular-photodynamics (*Einstein, 1916*).
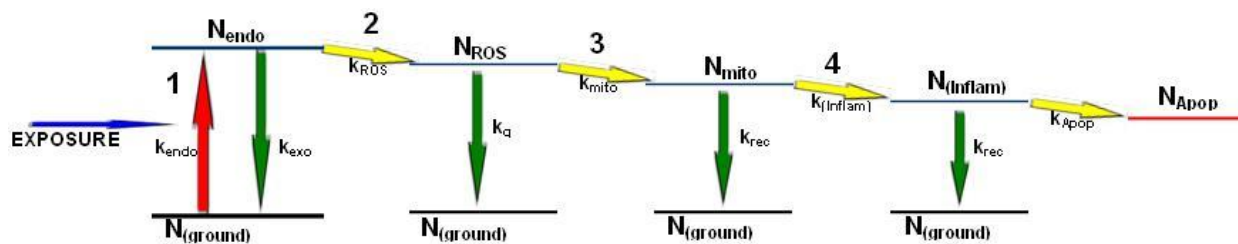
Figure 3.1: Schematic of systematic sequence of events upon nanoparticle uptake. A schematic representation of the sequence of events upon nanoparticle uptake, where the cell (system) takes up a particle, progresses to ROS damage (quenched by anti-oxidants), then onto mitochondrial damage, inflammatory cascade and finally apoptosis (if the cellular recovery rates are insufficient).

Figure 3.1 illustrates the systematic sequence of events which can occur when a nanoparticle is taken into a mammalian cell. 1: Upon exposure, the cells take up nanoparticles at a rate constant k_{endo}, leading to two populations: cells without nanoparticles (i.e. in a ground/non-toxic state), N_{ground}, and cells with an endocytosed nanoparticle N_{endo}.

Also indicated is a possible "exocytosis" process, characterised by a rate constant k_{exo}. However, *Salvati et al.* have indicated that this does not occur for polymeric nanoparticles and therefore it is not included in the equations (*Salvati et al., 2011*). 2: The next step in the sequence is ROS generation at a rate constant k_{ROS}, again generating a new population N_{ROS}. The ROS can then be quenched by the action of antioxidants, at a rate constant denoted here by k_q. 3: Alternatively, the system progresses to mitochondrial damage at a rate constant k_{mito}. 4: This process continues through a cascade and can culminate in apoptosis if the cellular recovery rates (k_{rec}) are not sufficient.

The complex system illustrated schematically in Scheme 1 can be better described using a series of rate equations. The process of nanoparticle endocytosis by cells *in vitro*, taking into account the cell replication rate constant (k_λ), has previously been described by *Salvati et al.* (*2011*) and is here described by Equation 3.2. As the dose (*D*) is expressed as the molar dose, for ease of comparison with the experimental data, N_{endo} is an expression of the molar quantity (number per unit volume) of endocytosed dendrimer nanoparticles. In subsequent equations, the term "N" is used to denote the equivalent quantity denoted by the subscript text that follows.

$$\frac{dN_{endo}}{dt} = k_{endo}.(N_{amg})^c.D - k_\lambda.N_{endo}(t)$$

Equation 3.2

where k_{endo} is the rate constant of endocytosis (in units of inverse time), N_{amg} is the number of amino groups per particle, *c* is an empirically determined fit factor, k_λ accounts for cellular replication and *D* is the molar dose. Assuming a cell duplication half life of 24hrs, k_λ has a value of $(0.69/24)\text{hr}^{-1}$.

After endocytosis, nanoparticles generate ROS and this build-up of ROS is counteracted by the intrinsic intracellular anti-oxidants, in this study exemplified by GSH, and the interaction quenches both the levels of ROS and GSH. These processes have previously been described by Equations 3.3 and 3.4 (*Mukherjee and Byrne, 2013*).

$$\frac{dN_{ROS}}{dt} = k_{ROS}.G.N_{endo}(t) - k_q.N_{ROS}(t).N_{GSH}(t)$$

Equation 3.3

$$\frac{dN_{GSH}}{dt} = k_{GSH} - N_{ROS}(t).N_{GSH}(t).k_q$$

Equation 3.4

The first term in Equation 3.3 is a generation (*G*) and dose (*D*) dependent term describing continuous ROS generation at a rate constant k_{ROS} ($N_{ROS}(0) = 0$). The second term describes the quenching of the ROS at a rate constant k_q, and depends on both; ROS levels, N_{ROS}, and antioxidant levels, N_{GSH} ($N_{GSH}(0) = 0$). In the study by *Muhkerjee et al.*, the antioxidant levels were represented by the experimentally measured values of Glutathione (GSH) (*Mukherjee and Byrne, 2013*).

In Equation 3.4, the experimentally observed linear increase of the control levels of GSH, at a rate constant of k_{GSH}, is described by the first-term, and the second-term, which is the same as in Equation 3.3, describes the quenching of the GSH levels. Values of k_{GSH} and k_q are derived from the experimental data and simulations of *Mukherjee and Byrne* (*2013*).

The subsequent, experimentally observed, cascade of cellular responses can be similarly simulated. The cascade elements examined were: caspase activation, mitochondrial membrane potential decay (MMPD), tumour necrosis factor alpha (TNF-α) and interleukin-8 (IL-8) for HaCaT cells, or interleukin-6 (IL-6) for mouse macrophages. In the model of *Mukherjee and Byrne* (*2013*) the early stage caspase activation and MMPD are both a result of increased levels of ROS, although through independent pathways. Thus:

$$\frac{dN_{Casp}}{dt} = k_{Casp} . N_{ROS}(t) - k_{Casp2} . N_{Casp}(t)$$

Equation 3.5

$$\frac{dN_{MMP}}{dt} = k_{MMP} . N_{ROS}(t) - k_{TNF} . N_{MMP}(t)$$

Equation 3.6

$$\frac{dN_{TNF}}{dt} = k_{TNF} . N_{MMP}(t) - k_{IL\text{-}8} . N_{TNF}(t)$$

Equation 3.7

$$\frac{dN_{IL\text{-}8}}{dt} = k_{IL\text{-}8} . N_{TNF}(t)$$

Equation 3.8

Again, in Equations 3.5 to 3.8; *N* describes the respective populations at time (t) and *k* the respective rates and the initial conditions for all cases are such that *N(0) = 0*. Overall, these equations show a possible cascade of events involving; ROS production, followed by the parallel rather than sequential processes of caspase activation and loss of MMP, the latter leading to activation of TNF-α and IL-8, as described for HaCaT cells exposed to PAMAM dendrimers by *Mukherjee and Byrne* (*2013*).

Cell viability was monitored using the MTT assay (*Mukherjee et al., 2010-A* and *Naha et al., 2010*). MTT measures the mitochondrial activity and is thus experimentally most associated with changes in the mitochondrial membrane potential, loss of which can, at certain levels, lead to apoptosis. The following equation was used to calculate the change in the population of viable cells, N_V:

$$\frac{dN_V}{dt} = k_{Rec} . N_{MMP}(t)^b . N_V(t) - k_V . N_{MMP}(t) . N_V(t)$$

Equation 3.9

The second term of Equation 3.9 describes the process of cell death, dependent on the change in the mitochondrial membrane potential, and the number of viable cells. As not all cells would undergo apoptosis as a result of loss of MMP, the first term of Equation 3.9

allows for a process of cell recovery, at a rate constant k_{Rec}, and an empirically determined sub-linear dependence (b) on N_{MMP} makes this process more prominent at lower doses. N_V is initially set equal to a value of 1 to represent 100% cellular viability.

The phenomenological rate equation model thus enables simulation of the time evolution of the cellular responses as well as the measured cytotoxic response.

Notably, the only particle dependent parameters are the nanoparticle dose (D) and generation (G). It is demonstrated that the model can reproduce the experimentally observed variations of cytotoxic response as a function of dose and generation, as well as measurement time-point and the dependence on cell-line parameters such as intrinsic intracellular antioxidant levels.

3.4.2 Temporal Evolution

For a fixed dose and generation, the temporal evolution of the cellular responses has previously been faithfully simulated using the rate equation model with the HaCaT cell-line (*Mukherjee and Byrne, 2013*). The model can be extended to the J774A.1 cell-line, for G4 exposure at a fixed dose of 1μM, as shown in Figure 3.2 (experimental data reproduced from *Naha et al.* (*2010*)). Experimental data (as symbols) is shown only for ROS and TNF-α as well as the temporal dependence of the MTT viability assay (as symbols and dotted line as a guide to the eye). The solid red line indicates the simulated ROS production and the other dotted lines show the temporal evolution of: Caspases (Green), MMPD (Orange) and TNF-α (Purple) as simulated according to Equations 3.3 to 3.8. For both experimental and simulated data, results are normalised to a maximum value of 1 for visualisation purposes, with the exception of the MTT data (viability – blue dotted line), which

experimentally have been normalized to the unexposed control (*Naha et al., 2010*). Parameters employed for the simulated data of Figure 3.2, and for all subsequent figures, are listed in Section 3.8: Supplementary Information, Table S3.1. The sensitivities of the temporal, dose and generation dependences of the simulated data to variations of these parameters are analysed in Section 3.5: Discussion and, where appropriate, in the Section 3.8: Supplementary Information.
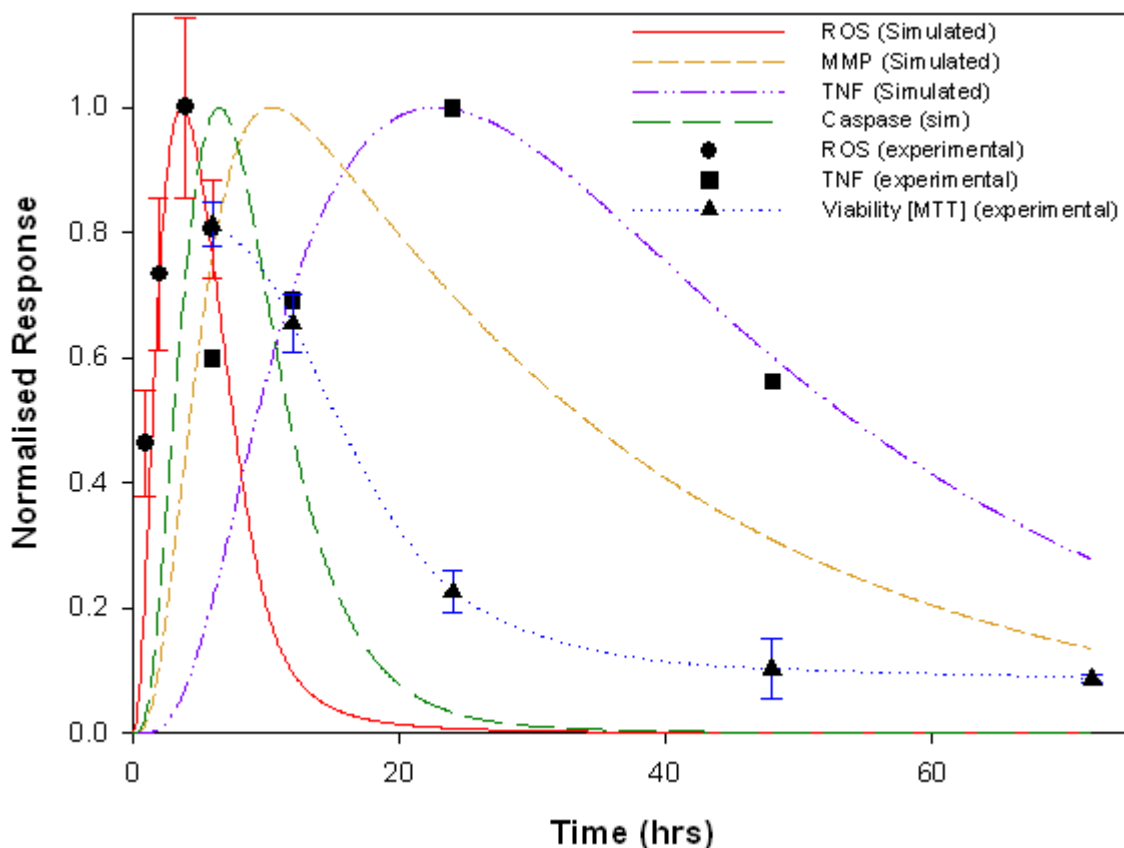

Figure 3.2: Experimental (*Naha et al., 2010*) and simulated cellular responses of J744A.1 murine macrophages to exposure to G4 PAMAM dendrimers at a fixed dose of 1μM. Results are normalised to a maximum value of 1 for visualisation purposes, with the exception of the MTT data (viability), which experimentally have been normalized to the unexposed control.

3.4.3 ROS Dose Dependence

The rate equation model can therefore be applied to simulate the temporal evolution of the cellular responses of exposure to PAMAM dendrimers at a fixed dose. Furthermore, in the previous study by *Mukherjee et al.*, the generation dependences of Equations 3.2 and 3.3 were seen to faithfully reproduce the experimentally observed more rapid onset of ROS production with increasing dendrimer generation (*Mukherjee and Byrne, 2013*). Notably, however, using a constant ROS generation rate constant, k_{ROS}, the ROS levels were found to increase monotonically as a function of time, and it was found necessary to constrain the rate of generation to decrease, dependent on the amount of ROS generated, indicative of a depletion of the source of ROS. In the preliminary model of *Mukherjee and Byrne* (*2013*) this was achieved through the relationship of Equation 3.10.

$$\frac{dk_{ROS}}{dt} = -k_{ROS}.N_{ROS}(t)$$

Equation 3.10

While this approach allowed the faithful reproduction of the temporal evolution of the ROS levels, it does not accurately model the complex dose/generation dependence of the ROS levels at a fixed time point, as shown in Supplementary Figure S3.1. Figure 3.3 shows the dose and generation dependent levels of ROS in the J774A.1 cell-line, expressed as the percentage increase in Carboxy-H_2DCFDA fluorescence compared to control, at a fixed timepoint of 4hrs (data derived from *Naha et al.* (*2010*)).

The dose dependence of Figure 3.3 can however be reproduced by considering that the increased levels of ROS are the result of an interaction of the endocytosed nanoparticles with an intracellular source of ROS, N_{source}, which is depleted by the ROS generation process. Thus,

$$\frac{dN_{Source}}{dt} = -k_A.G*.(N_{endo}(t)^A).(N_{Source}(t)^B)$$

<div align="right">Equation 3.11</div>

Where k_A is the interaction rate constant for the nanoparticles and source, $G*$ is a generation dependant factor and the values for A and B are empirical constants. The generation of ROS, previously described by Equation 3.3, is then described by:

$$\frac{dN_{ROS}}{dt} = k_A.G*.(N_{endo}(t)^A).(N_{Source}(t)^B) - k_q.N_{ROS}(t).N_{GSH}(t)$$

<div align="right">Equation 3.12</div>

The continuous lines of Figure 3.3 show the simulation of the dose and generation dependent increase in ROS in the J774A.1 cell-line, as calculated at 4hrs, in comparison to the experimentally observed values. The simulated data are expressed in arbitrary units, and have been scaled to give a best match to the experimental data. Experimentally, a background level of ~ 10% was observed at even the lowest doses and thus the simulated data, which begins at a value of zero, are offset for comparison.
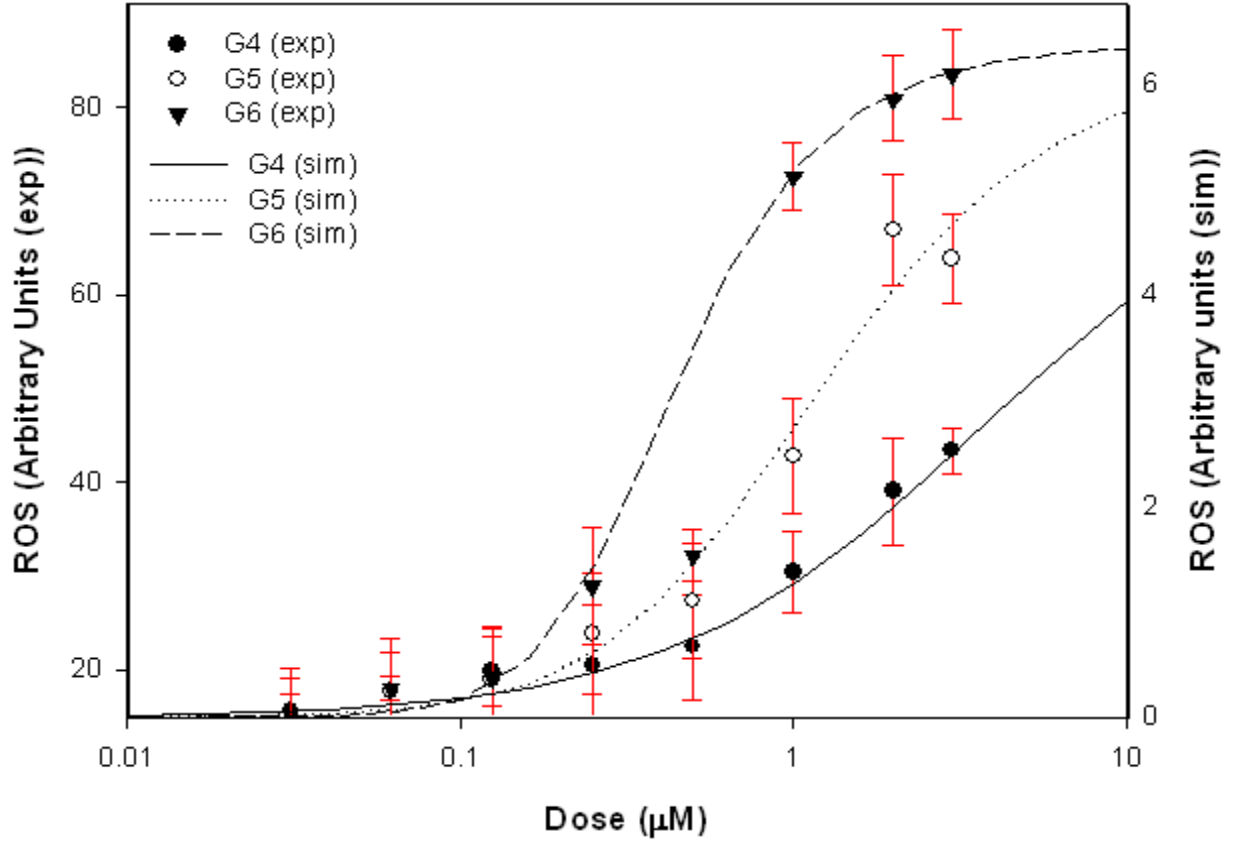
Figure 3.3: Experimentally observed (symbols) (expressed as the % increase in Carboxy-H$_2$DCFDA fluorescence compared to control, at a fixed timepoint of 4hrs (*Naha et al., 2010*)) and simulated (lines) dose and generation dependent intracellular ROS generation after 4hr exposure of J744A.1 mouse macrophages to PAMAM dendrimers.

The simulated data of Figure 3.3 are generated from Equations 3.1-3.14, simultaneously for all three dendrimer generations, with only *G* and *D* as variables. The closest simulated reproduction of the experimental data was achieved using a generation dependent expression of *G** and *A*, with a constant value of *B = 3*, such that:

$$G* = \left(\frac{1}{N_{amg}^{0.25}} \right)$$

$$A = \left(\frac{N_{amg}}{64} \right)^{0.75}$$

Note, in the simulated data of Figure 3.3, a value of 0.25 was used for *"c"* of Equation 3.2. The initial value of $N_{source}(t=0)$ was chosen to be 10μM, the maximum dose level used in the simulation.

The simulation faithfully reproduces the dose and generation (number of surface amino groups) dependence of the production of ROS. Notably, for each generation, the maximum levels of ROS production saturate at the same value, consistent with experimental observations supporting the proposition that the surface amino groups are the primary source of the response to the nanoparticle intake (*Naha and Byrne, 2013*). The evolution of the equations (from Equation 3.10 to Equations 3.11 and 3.12) to account for the dose dependence of the ROS response has little effect on the temporal profiles of the cellular responses at a fixed dose, and the responses represented in figure 3.2 are calculated using the latter formalism rather than that of Equations 3.3 and 3.4.

Experimentally, the evaluation of the dose (seven dose measurements) and generation (three generations) dependent increases in ROS levels as well as their temporal evolution (1-24hrs) is an extensive series of measurements, in independent triplicates. Having established a model which can faithfully simulate the responses of the cell line, a 3-D representation of the combined and continuous dose dependence and temporal evolution can be constructed, as shown in figure 3.4 for the case of G4. Similar 3-D representations can be constructed for G5 and G6, and the model can be readily extrapolated to higher and lower generations. Although the 2-D representation of the 3-D system does not do it

justice, the view illustrates the importance of considering the 3-D plane in the system response.
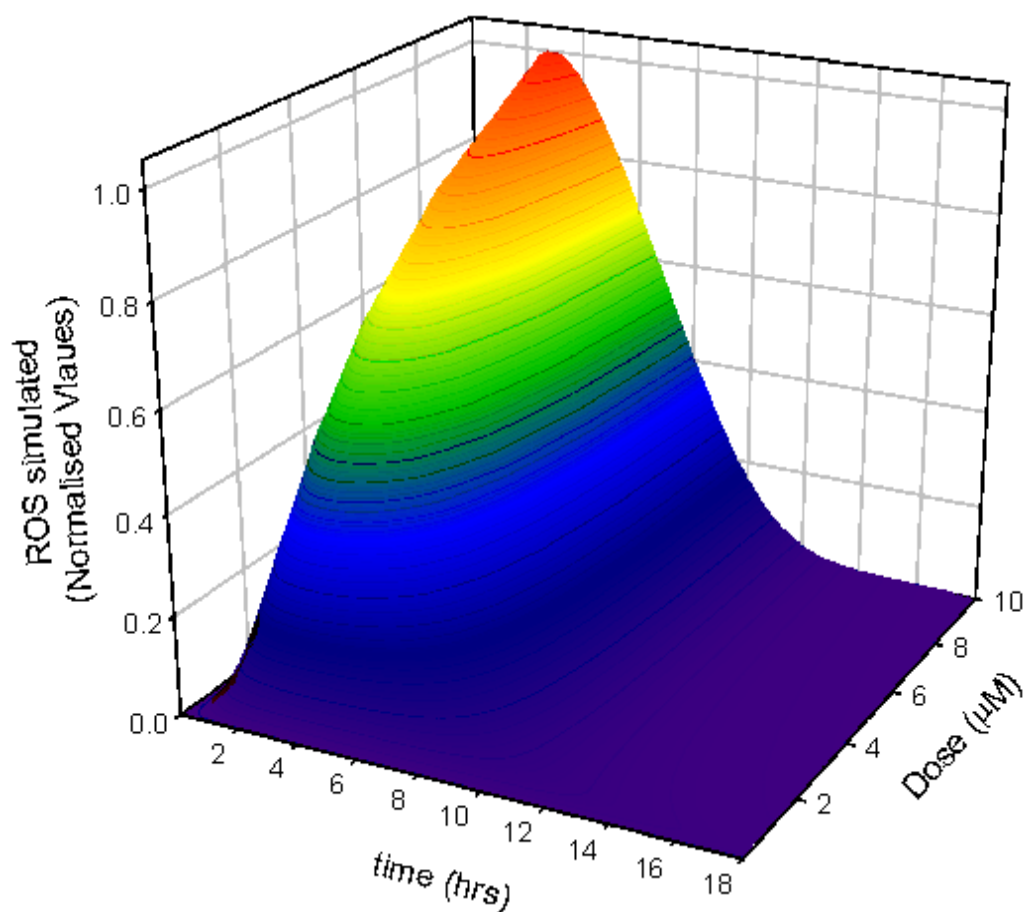
Figure 3.4: A 3D graph showing both the simulated time and dose dependence of the ROS evolution, in J744A.1 mouse macrophages, upon G4 PAMAM nanoparticle uptake.

3.4.5 Cellular Viability

It is clear that the approach of the phenomenological rate equation model can accurately reproduce the experimentally observed cellular responses, as a function of dose and generation, as well as their temporal evolution. For the given cell-line, the responses are determined by the surface reactivity of the nanoparticles, which, in the case of PAMAM dendrimers presented here, depends on the number of surface amino groups per particle for

each generation. Ultimately, the response to nanoparticle exposure is reduced viability in the *in vitro* culture, as measured by cytotoxicological assays such as MTT, and normally represented by the EC_{50}. It has previously been shown that the cytotoxicity of PAMAM dendrimers is systematically dependent on generation, but, given the complex dose and temporal responses, the exact link to nanoparticle structure and reaction mechanisms has not been elucidated.

Figure 3.2 also plots the experimentally observed MTT EC_{50} value at different time points (*Naha et al., 2010*). For a given generation, the dose dependence of the reduction in cellular viability at different timepoints can be simulated according to Equation 3.9. Figure 3.5 illustrates the simulated dose dependence of the cellular viability, for a single generation (G4), at 6hrs, 12hrs and 24hrs, compared to the corresponding experimentally observed MTT response at these timepoints (*Naha et al., 2010*). All parameters used to simulate the dose dependence of the ROS (Figure 3.3) as well as the temporal evolution of the cellular responses (Figure 3.2) are kept constant and only the dose is varied. A value of 0.25 was employed for the parameter b in Equation 3.9. The model, with reasonable accuracy, reproduces the *in vitro* cellular responses observed experimentally. The simulated results are best matched to the experimental responses at the earlier (6hr) and later (24hr) timepoints. The deviation from the observed responses at the intermediate timepoint (12hrs) may be the result, for example, of more complex quenching mechanisms not included in the model at this stage.
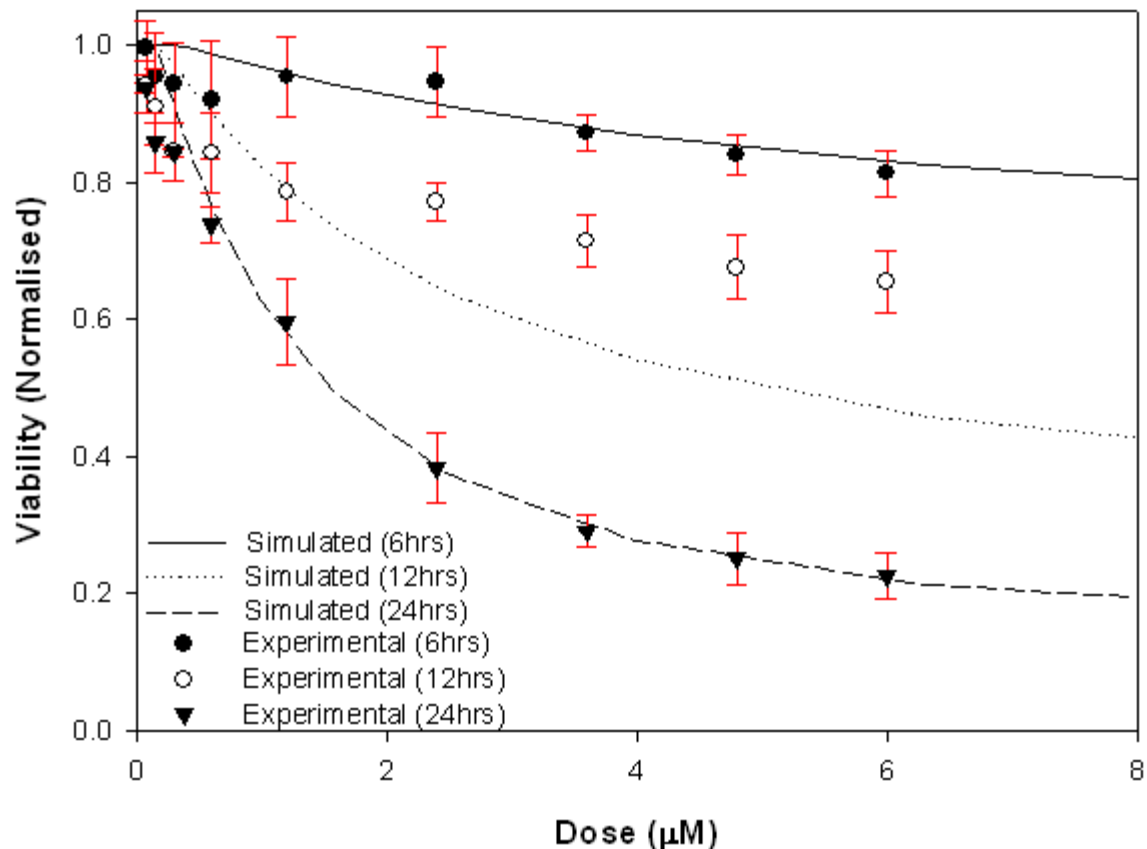
Figure 3.5: Experimental (symbols) and simulated (lines) dose dependent viability, as
measured using the MTT assay, for J744A.1 murine macrophages at 6hr, 12hr and 24hr
(experimental data from *Naha et al., 2010*).

By varying the generation (*G*), for a fixed time point, the dose dependence of the cellular

viability for each generation can be similarly qualitatively reproduced, as shown in Figure

3.6, for the case of 12hr exposure of mouse macrophages (experimental data derived from
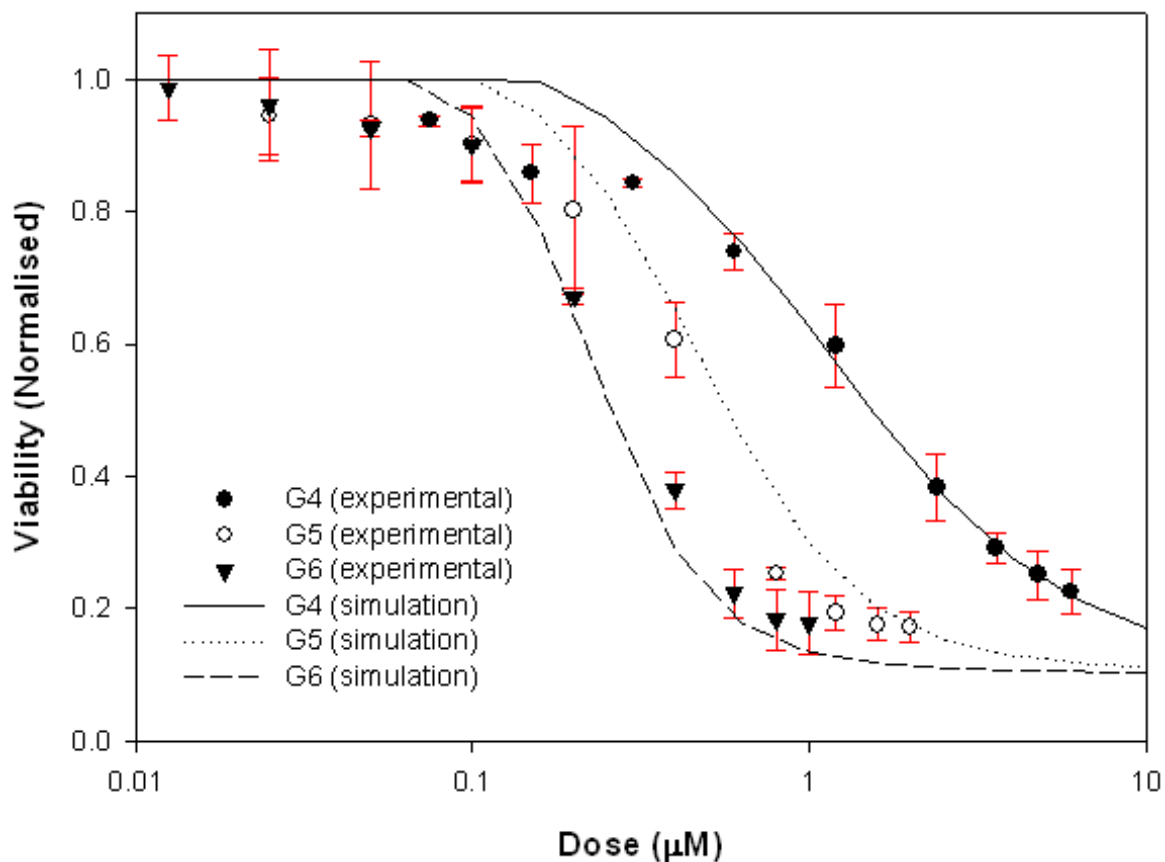
Naha et al., 2010).

Figure 3.6: Experimental (symbols) and simulated (lines) dose dependent J744A.1 mouse

macrophage viability at 12 hrs, as measured using the MTT assay, for PAMAM

generations G4, G5 and G6 (experimental data from *Naha et al., 2010*).

Similar to the case of the ROS, a 3-D representation of the simulated cytotoxic response of

HaCaT cells to PAMAM dendrimer exposure, as a function of dose and time, can be

constructed, as shown in Figure 3.7 for the case of G4. A similar representation can be

made for G5 and G6, and the model is readily extendable to higher or lower PAMAM

generations.
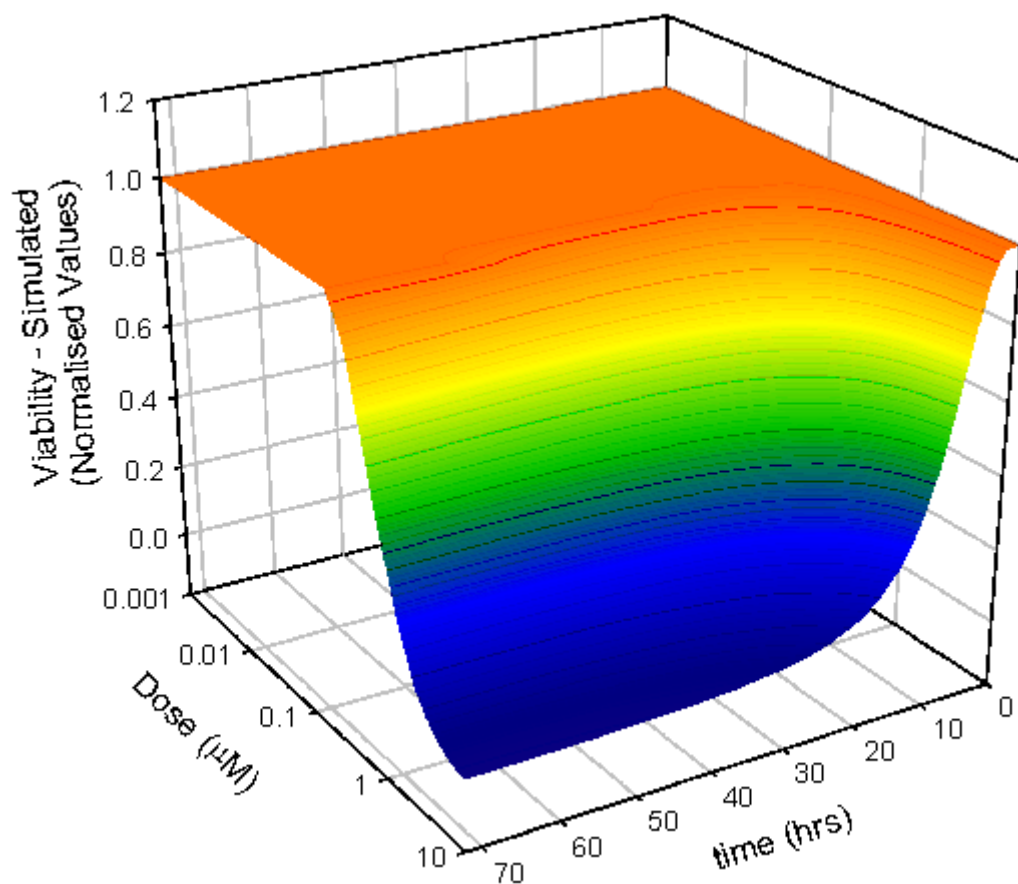
Figure 3.7: 3D simulated time and dose dependence of MTT response for exposure of

J744A.1 murine macrophage cells to PAMAM G4.

The experimental data of Figure 3.6 is a typical representation of a cytotoxicological

screening of nanoparticles. In comparing the responses of the cell line to the different

generations in the dendrimer series, a systematic structural dependence of the response is

clear. The application of the model presented here demonstrates that that dependence is

derived from the number of surface amino groups per dendrimer generation, and the rate of

generation of ROS. The true value of any such model, however, depends on its

applicability to a range of different experimental scenarios (*OECD, 2007*). One notable

source of diversity in the literature on *in vitro* nanotoxicology is the range of different cell

lines used, often justified as models for target organs *in vivo*. Indeed, in the work of *Naha et al.,* and *Mukherjee et al*., a range of different cell lines were employed. (*Mukherjee et al., 2010-A* and *B*, *Naha et al., 2010*, *Naha and Byrne, 2013*, *Mukherjee and Byrne, 2013*). In addition to the murine macrophages already described in this manuscript (*Naha et al., 2010*), the human colon adenocarcinoma cell line (SW480) and the immortalised human keratinocyte line (HaCaT) were employed as models of ingestion and transdermal transport of nanoparticles respectively (*Mukherjee et al., 2010-A* and *B*, *Mukherjee and Byrne, 2013*). Notably, the different cell lines gave significantly different results for the cytotoxicity of PAMAM dendrimers, as shown in figure 3.8 for the examples of the dose dependent viability as measured using the MTT assay upon exposure of the different cell lines to PAMAM G4 for 24hrs. Although an extrapolated EC_{50} from the J774A.1 (*Naha et al., 2010*) and SW480 (*Mukherjee et al., 2010-A*) cell lines would yield similar results, the value for HaCaT (*Mukherjee et al., 2010-A*) is considerably higher, indicating a greater resistance of the skin cell line to external insult, as may be expected.

3.4.6 Variability: Cell lines and Assays

Following the cascade of cellular responses after nanoparticle endocytosis, described in Figure 3.2 and represented by Equations 3.2-3.14, a potential source of the differences in cell type responses to nanoparticle exposure is the constituent levels of cellular antioxidants, redox enzymes *etc*., which help the cell to protect itself from the oxidative stress caused by an external agent. For example, the average activities of three important intracellular redox agents, glutathione (GSH), glutathione-S-transferase, and glutathione reductase are approximately three times higher in WI38 human fibroblast cells than in

HaCaT cells and therefore, upon 24 h exposure to arsenic, HaCaT cells have been reported to be 50% more susceptible to cell death than WI38 cells (*Snow et al., 2005*). Of relevance to the study presented in figure 3.7, the natural intracellular glutathione (GSH) level of HaCaT cells are reported to be 7300 nmol/mg protein (*Snow et al., 2005*), whereas those of SW480 and J774A.1 cells have been reported to be ~40 nmol/mg protein (*Nakagawa et al., 2002*) and 26.7 nmol/mg protein (*Shen and Sevanian, 2001*), respectively.

The higher level of antioxidants in HaCaT cells is therefore consistent with a greater resistance to external insult. In the rate equation approach presented here, this internal resistance to oxidative stress is represented by k_{GSH} in Equation 3.6. The solid/dashed lines of figure 3.8 represent the simulated viability for the different cell lines, calculated according to Equation 3.12, having increased only the rate of generation of GSH for the HaCaT cell line (by a factor of 1.5), in Equation 3.4, keeping all other rates constant. It can be seen that the simple change in the cell dependent response parameter faithfully reproduces the experimentally observed differences in response for the different cell lines. The increased levels of GSH result in a more rapid quenching of the intracellular ROS levels, and this is manifest experimentally as an initial maximum in HaCaT cells after 1-2 hrs (*Mukherjee and Byrne, 2013*), whereas in J774A.1 cells, the maximum is observed at 3-4 hrs (Figure 3.2) (*Naha et al., 2010*).
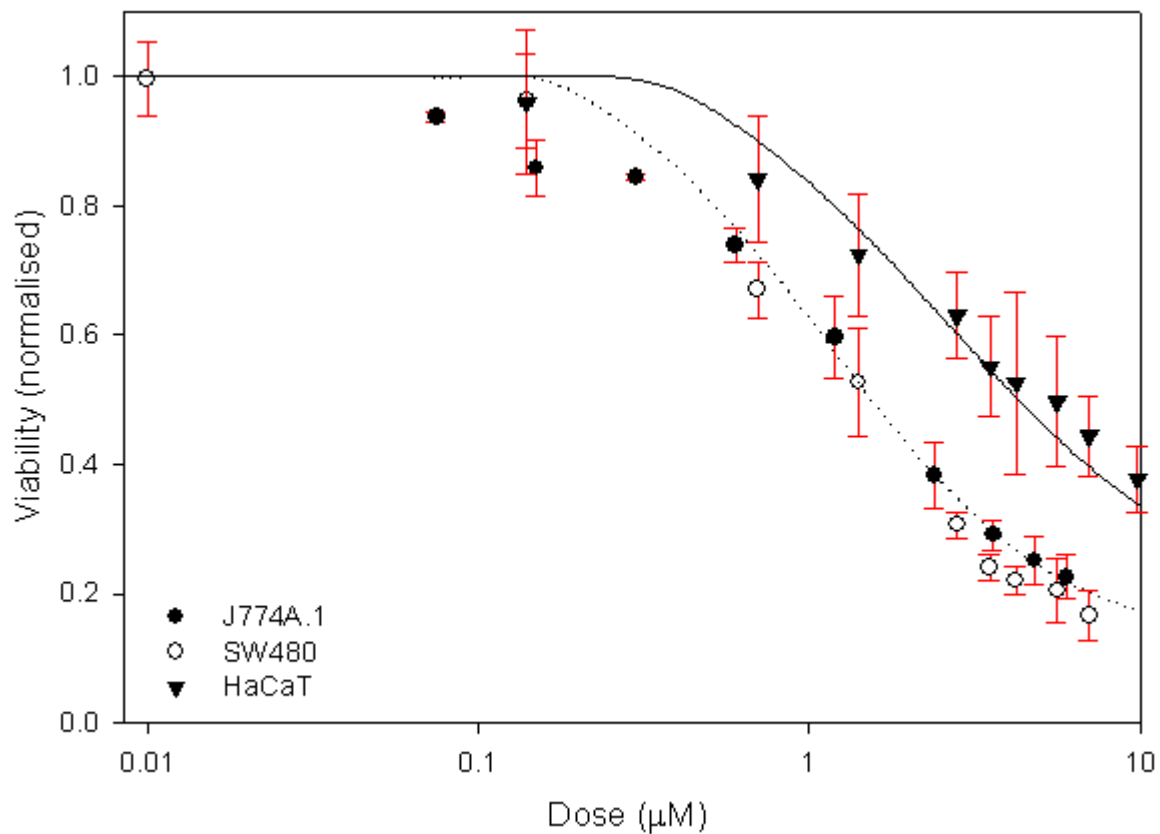
Figure 3.8: Experimental (symbols) and simulated (lines) viability of different cell lines, as
measured using the MTT assay, after exposure to PAMAM G4 for 24hrs. Experimental
data for J774A.1 derived from *Naha et al. (2010).* Experimental data for SW480 and
HaCaT derived from *Mukherjee et al. (2010-A).*
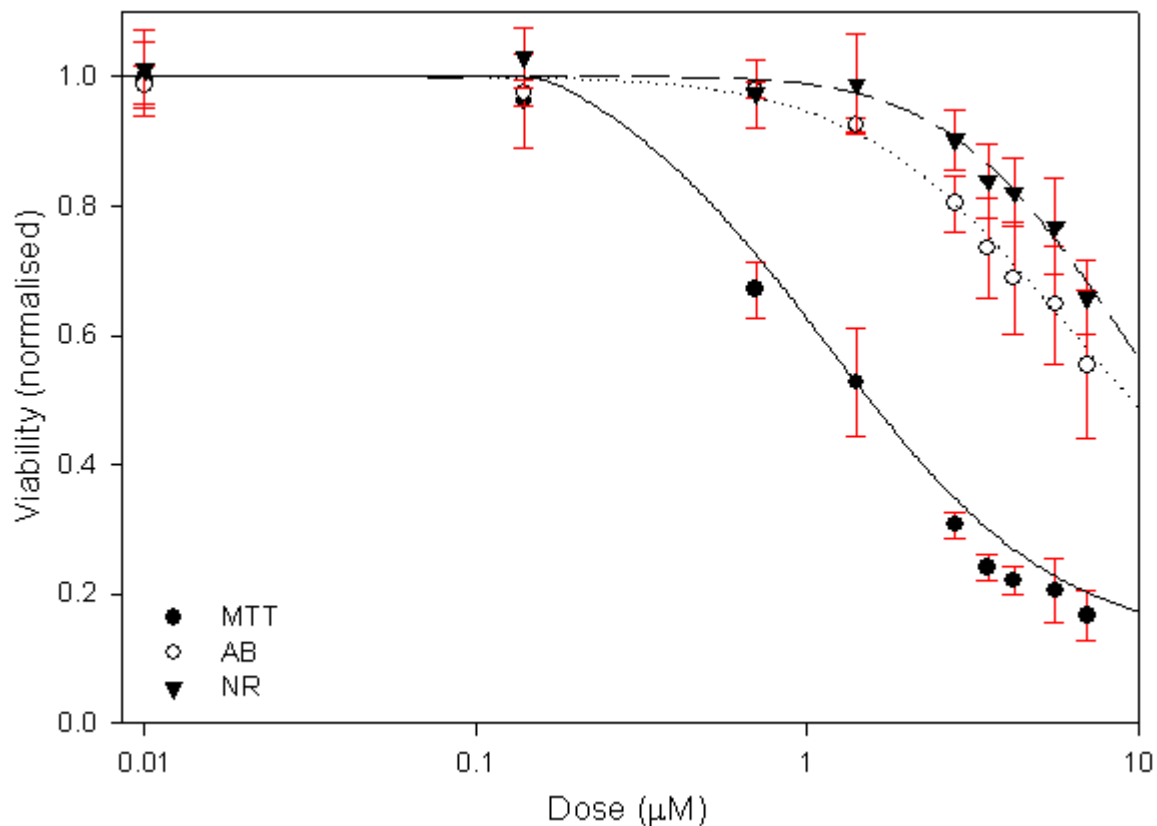
Figure 3.9: Comparison of Experimental (symbols) and simulated (lines) viabilities as measured by MTT, Alamar Blue and Neutral Red, for exposure of SW480 cells to PAMAM G4 after 24 hrs. Experimental data from *Mukherjee et al. (2010-A)*. For each assay, the data has been normalized to unexposed control.

Literature furthermore describes the use of a diverse range of endpoints to evaluate the cytotoxic responses of cell lines *in vitro*. Each assay measures a different underlying cellular response or function. As discussed above, MTT measures the mitochondrial function. Alamar Blue is a fluorescence based assay which is used to assess cell viability and proliferation; this is done by measuring the innate metabolic activity via the conversion of resazurin (non-fluorescent) to resorufin (fluorescent) (*Nociari et al., 1998*). Neutral Red is another fluorometric dye, which measures the lysosomal activity using 3-Trimethyl-2,8-

phenazinediamine, monohydrochloride, which binds to the lysosomes of viable cells (*Repetto et al., 2008*). *Mukherjee and Byrne* (*2013*) have highlighted how the different sensitivities of the assays as a result of the exposure to PAMAM dendrimers are a manifestation of the mechanism of interaction of the nanoparticles with the cells. Figure 3.9 reproduces the experimental values of the dose dependent viability of SW480 cells after 24hr exposure to PAMAM G4 as measured by the MTT, Alamar Blue and Neutral Red assays (from *Mukherjee et al., 2010-A*). For each assay, the data has been normalized to unexposed control.

In the rate equation model presented here, the responses of the assays are represented by different steps in the cascade of cellular responses following exposure. The MTT response is associated with changes in mitochondrial membrane potential, and is simulated by Equation 3.9. The lower sensitivities of the Alamar Blue and Neutral Red assays indicate that they are associated with later responses in the cascade. The Alamar Blue response can be associated with the subsequent phase of generation of TNF-α and modelled according to Equation 3.13.

$$\frac{dN_V'}{dt} = k_{rec}'.N_{TNF-\alpha}(t)^b.N_V'(t) - k_V'.N_{TNF-\alpha}(t)^m.N_V'(t)$$

Equation 3.13

Note that N_V' in Equation 3.13 represents the number of viable cells as registered by Alamar Blue. $N_V'(0) = 1$ represents the initial 100% viability. In modelling the experimental data of Figure 3.9, for Alamar Blue, it is noted that an empirical factor of $m=2$ provides a good fit and a value of $b = 0.25$ was again used.

In a similar fashion, the response of Neutral Red can be associated with a later stage of the cascade of cellular responses and simulated according to Equation 3.14:

$$\frac{dN_V{''}}{dt} = k_{rec}{''}.N_{IL-8}(t)^b.N_V{''}(t) - k_V{''}.N_{IL-8}(t)^p.N_V{''}(t)$$

Equation 3.14

$N_V{''}(0) = 1$ represents the initial 100% viability. A good reproduction of the experimental results is found with an empirical factor of $p=3$ and $b = 0.25$. In Equations 3.13 and 3.14, $k_{rec}{'}$ and $k_{rec}{''}$, and $k_V{'}$ and $k_V{''}$ describe the rates of recovery of the system without apoptosis, and the rates of change of the viability, as measured by the respective assay.

3.5 Discussion

The phenomenological rate equation model presented here is a demonstration of how an integrated approach to analysis of the responses of cells to nanoparticle exposure can be employed to provide a better visualisation of the dependences of those responses on experimental parameters such as dose and exposure time, nanoparticle characteristics (such as number of active surface groups) and even variations in cell line and cytotoxicity assay. The model is constructed on previous experimental observations of the cellular responses to PAMAM dendrimers, which have systematically variable physico-chemical properties, and have been seen to elicit systematically varied cellular responses. The mechanisms of response and their causal nature and inter-relationships have been explored and discussed extensively elsewhere (*Mukherjee et al., 2010-A* and *B*, *Naha et al., 2010*, *Mukherjee and Byrne, 2013*).

While it is impractical at this stage to cover all such potential cellular responses, the model is used to simulate several known cytotoxic markers, simultaneously for all three dendrimer generations, and thus is at least a partial system of events. Such a system of events can be considered as a sub-section of an Adverse Outcome Pathway (*Ankley et al., 2010* and

OECD, 2013) and is consistent with the approach of predictive paradigms for assessing nanotoxicological responses (*Meng et al., 2009* and *Puzyn et al., 2009*).

The initial stage of endocytosis has previously been described using a rate equation approach for the uptake of 40-50 nm fluorescently labelled polystyrene nanoparticles in the A549 human lung adenocarcinoma cell line, as measured by flow cytometry (*Salvati et al., 2011*). Endocytosis rates were measured and simulated according to build up of cellular fluorescence, and the values of k_{endo} in the current model were chosen to yield similar simulated results for the build up of dendrimer nanoparticles in the cells, as shown in Supplementary Figure S3.2. In contrast to the fluorescently labelled PSNP, the dendrimers are not easily visualized within the cells and so the cellular response of increased levels of ROS was used to guide the simulation of the time, dose and generation dependence of the cellular responses. Figure S3.3 shows the sensitivity of the simulated dose dependent ROS generation to variations in the parameter k_{endo}. In the current model, the best simulations were achieved by including a generation (N_{amg}) dependent factor in the uptake, as described in Equation 3.2, with a *c* value of 0.25. For comparison, Supplementary Figure S3.4 compares the dose dependent generation of ROS after 4hrs exposure for all 3 generations, with varying values of the parameter *c*. The best replication of the response for all generations simultaneously is achieved using a value of *c=0.25*. In understanding the potential significance of this factor, it is worth observing that the relationship between the diameter and the number of surface amino groups for PAMAM dendrimers in the region of N_{amg} = 20-1000 is a power law of order 0.25 (data from http://www.dendritech.com/pamam.html). The nominal diameters of PAMAM dendrimers available on the dendritech website are in good agreement with those measured by size

exclusion chromatography (*Crooks et al., 2001*). The values of hydro-dynamic diameter measured by Dynamic Light Scattering in PBS are somewhat larger, as may be expected, but the values still scale systematically with generation and although a slight increase in cell culture medium due to interaction with the medium may be inferred, no significant aggregation/agglomeration of the particles is evident over the dose ranges measured (*Mukherjee et al., 2010-A*). Thus, a dependence of the rate of endocytosis on $N_{amg}^{0.25}$ may represent a dependence on the dendrimer diameter, which varies only slightly with generation number (G4 diameter: 4.5nm, G5 diameter: 5.4nm and G6 diameter: 6.7nm (*Mukherjee et al., 2010-A*)).

The model considers the case of PAMAM dendrimers which have been demonstrated to be taken up in mammalian cell lines by a process of endocytosis (*Salvati et al., 2011*). However, endocytosis can be subcategorised into four different types: Clathrin-mediated endocytosis, Macropinocytosis, Caveolae-mediated endocytosis and Phagocytosis, all of which could be readily modelled via modification of the rate equation approach used in this study. It is also important to note that, for smaller generation dendrimers, a potential for passive uptake is also possible. It would be of great interest to continue to reduce the dendrimer size and explore the transition between the dominance of active and passive uptake mechanisms, which could be incorporated as a parallel uptake process using such a rate equation approach.

While a more primitive version of the model presented here was capable of reproducing the temporal evolution of the cellular responses, and to some extent the dependence on dendrimer generation (*Mukherjee and Byrne, 2013*) an accurate model of the complex dose

dependence of the increase in intracellular ROS is key to extending the model to simulate the dose dependent cytotoxic responses.

The intracellular levels of ROS increase upon nanoparticle endocytosis but are seen to reach a maximum on a time scale of 1-4 hours, depending on the dendrimer generation, dose and cell line (*Naha et al., 2010* and *Mukherjee and Byrne, 2013*). In the rate equation formulation presented here, this transient behaviour cannot be reproduced simply by introduction of an anti-oxidant quenching mechanism. Rather, a limit to the capacity of the cell to generate increased levels of ROS is inferred. This process is represented by the reaction of the endocytosed nanoparticles with a source species, which generates ROS, while consuming the source. The approach enables faithful simulation of both the temporal evolution and the dose and generation dependence of the ROS.

The approach is analogous to that of the Operational Model of Agonist Activation (*Black and Leff, 1983*), which invoked the concept of an agonist receptor, to which the agonist binds, to produce the response. Using the law of Mass Action at equilibrium, a faithful reproduction of a sigmoidal response curve to a linear agonist dose was achieved, based on the agonist concentration, the receptor concentration and the agonist/receptor dissociation rate.

In considering the biological significance of an ROS source, N_{source}, understanding the mechanisms of ROS generation is important and has been discussed in Section 3.8: Supplementary Information (ROS source discussion).

Although the exact process of ROS production has not been experimentally visualised, the model can still faithfully reproduce the dose and generation dependence of the increase in ROS levels, using Equations 3.11 and 3.12, as shown in Figure 3.3. All curves of Figure

3.3 can be modelled with a constant value of k_A. Supplementary Figure S3.5 illustrates how the simulated dose dependent increase in the ROS levels for all three generations at a fixed timepoint of 4hrs depends on variation of the parameter k_A. This value is normalised by the factor $G^* = N_{amg}^{-0.25}$. The sensitivity of the simulations to the exponent of this parameter is shown in Figure S3.6. Notably, this is the inverse of the factor employed for Equation 3.2, and, in the light of the discussion above, can be related to the generation dependence of the dendrimer diameter.

For a given dendrimer generation, the rate of generation of ROS is dependent on $N_{endo}(t)^A.N_{Source}(t)^B$. As the dose ($D$) is expressed as the molar dose, for ease of comparison with the experimental data, N_{endo} is an expression of the molar quantity of endocytosed dendrimer nanoparticles. Supplementary Figures S3.7 and S3.8 demonstrate the sensitivity of the simulated dose dependent ROS generation on the parameters A and B respectively. The dependence of the power law factor, A, on the number of amino groups, N_{amg}, is a reflection of the increasing reactivity per dendrimer nanoparticle with generation. The value of $B=3$ indicates that, in the reaction process, 3 source species are involved.

In understanding the influence of the different parameters of Equation 3.12 on the form of the dose dependent ROS generation of Figure 3.3, and by analogy to the Operational Model of *Black and Leff* (*1983*), $k_A G^*$ is largely responsible for the EC_{50} of the curves, while the factors A and B govern the Hill slope, A accounting for the observed dendrimer generation dependence.

It is however important to note that for these well defined structures, the nanoparticle diameter, number of surface amino groups, and surface area all scale with generation number and are therefore intimately related. It has also been previously demonstrated that

the (positive) zeta potential scales with increasing generation and therefore surface area and number of surface amino groups N_{amg} (*Mukherjee et al., 2010-A*). In cell culture medium, the zeta potential for all generations becomes negative due to interaction with the medium and scales with the generation, surface area and therefore N_{amg}, and notably, the magnitude of the change in the zeta potential scales with the dendrimer surface area. For both the SW480 and HaCaT cell line, the EC_{50} for a range of assays (Neutral Red, Alamar Blue, MTT (all 24hrs) and the clonogenic assay (8 day)) has been seen to scale with the surface area, the zeta potential in cell culture medium, and the change in zeta potential from distilled water to cell culture medium. Zeta potential depends on the dispersion environment, however, and is not an intrinsic nanoparticle parameter, compared to the number of surface amino groups, which is compositionally defined. A similar systematic correlation between the toxic response and the number of surface amino groups has been demonstrated for J774A.1 mouse macrophages (*Naha et al., 2010*).

Using only *G* as a nanoparticle dependent variable, resulting in a reaction rate which is dependent on the systematically varied physico-chemical structure of the dendrimer nanoparticles, the experimentally observed dose and time dependent ROS generation can be simultaneously simulated for all three dendrimer generations. Using this as the initiation stage of an intracellular response cascade, the subsequent changes in viability of the cell population at different timepoints, as measured using the MTT assay, can be modelled simultaneously using the relatively simple rate Equation 3.9. As MTT primarily monitors changes in mitochondrial activity, changes in cell viability are related to the time dependent MMPD, as simulated by Equation 3.6. The sensitivity of the simulations to the parameter k_{MMP} of Equation 3.6 is shown in Supplementary Figure S3.9. It is noted that, using this

relatively simple formalism, an accurate simultaneous reproduction of the experimental results at all timepoints is not achieved. This is not surprising as the cascade process of cytokine activation/production and resultant changes to mitochondrial activity is more complex than that considered here. The first term of Equation 3.9 allows for changes in MMP without reduction of cell viability as measured by the MTT assay, but this did not significantly improve the simultaneous simulation of the dose dependent viability at different time points.

Similarly, Equation 3.9 can be employed to simultaneously simulate the cytotoxicity for all three generations, at a fixed timepoint. In figure 3.6, the simulation provides an accurate reproduction of the experimental data, although the low dose behaviour is less well reproduced. Again, this is most likely a result of the relative simplicity of the model system, which doubtless does not include many processes which are occurring in parallel with those experimentally measured and considered in the model. Supplementary Figure S3.10 explores the sensitivity of the simulated viability to the parameter k_{MMP}. No significant improvement in the discrepancy at low doses is achieved, although the simulated curves of Figure 3.6 fall largely within the experimental error margins.

A potential pitfall of such modelling approaches can be 'over parameterisation' with insufficient experimental data that ultimately leads to 'over fitting'. In modelling the system, the minimum number of sequential processes have been included to describe the system, as observed experimentally. Additional steps in the cascade can be added, as they are elucidated experimentally or by, for example, pathway enrichment approaches.

It should be noted that the ROS response to PAMAM nanoparticle exposure has been observed to be a two stage response (*Mukherjee and Byrne, 2013*), and only the initial

stages are modelled here. The initial response (0-6 hrs) has been associated with encapsulation of the dendrimers in endosomes, while the later, secondary response has been associated with release of the nanoparticles into the cytoplasm by endosomolysis and subsequent incorporation into the mitochondria. A similar behaviour was observed by *Xia et al. (2006)* for ROS generation by aminated polystyrene nanoparticles. While the second phase of ROS generation is not modelled here, a similar rate-equation approach could be employed to simulate the responses, their time evolution and dependences on dose and dendrimer generation. A more complete understanding of generation and dose dependence of the process of endosomal-rupture, particle migration to and uptake by the mitochondria, and recovery of intracellular antioxidant levels would be required. Between the two phases, such phenomena as the quenching of ROS levels to below those of controls, the recovery of antioxidant levels, and migration of antioxidants to localised subcellular sites should be considered. Nevertheless, the phenomenological model is readily adaptable to include more complex phenomena, simply by adding additional terms to the rate-equations. However, it should be noted that while the ROS generation of Figure 3.3 relates exclusively to the early stages of intracellular nanoparticle interactions, the later responses, in particular the later time point viability measurements, may be influenced by the secondary phases of ROS generation.

Nevertheless, the model provides a valuable visualisation of the range of cellular responses to the exposure to nanoparticles and a faithful qualitative reproduction of the nanoparticle structural and dose dependences of the cytotoxic responses based on independent nanoparticle and cell dependent reaction rates. Notably, experimentally observed differences between the responses of different cell lines can be simulated simply by

adjustment of cellular based parameters, in this case the rate of production of GSH, based on established differences in cell-line metabolism. In this context, the robustness of the model can be further validated by monitoring variations of ROS production and cytotoxic responses as a result of externally controlled antioxidant levels (*Nel et al., 2006*, *Issels et al., 1985*, *Tsan et al., 1985* and *1989*, *Vlahopoulos et al., 1999* and reviewed by: *Deneke and Fanburg, 1989*).

Furthermore, the model also elucidates the origin in the differences of the responses of commonly used cytotoxicity assays and clarifies that lower observed values of EC_{50} for different assays as a measure of the same nanoparticle/cell-line system are an indication that the assays are registering cellular responses at later stage in the response cascade. Although the time responses have not explicitly been measured, the simulations of Figure 3.9 indicate that the variations of responses can be well modelled by Equations 3.13 and 3.14, which have the same form as the viability simulations of Equation 3.9, keeping all parameters of the earlier stage responses constant. Figure S3.11 shows the variability of the fits to changes in the parameters *m* and *p*.

The use of such rate equation models for the simulation or fitting of complex systems is by no means novel and has become more prevalent in pharmacokinetics/pharmacodynamics (*Miyazaki et al., 2003* and *Ryan et al., 2011*). In terms of nanobio interactions, *Salvati et al.* employed a rate equation approach to model the uptake of polystyrene nanoparticles in cells as measured by the fluorescent response of the cell populations, although no modelling of the cellular responses was undertaken (*Salvati et al., 2011*). *Dell'Orco et al.* (*2012*) used a similar approach, described in terms of Systems Biology, to model the delivery success rate of engineered nanoparticles and its dependence on the presence and

structure of the protein corona. To our knowledge, however, this is the first use of such models to simulate the time evolution, dose and structural dependence of cellular responses to nanoparticle exposure and to derive toxicological endpoints from the simulated data. Undoubtedly, the approach is crude at this stage, and improvements based on fitting of the data by for example nonlinear regression (*Ryan et al., 2011*) or parameter global sensitivity analysis (GSA) (*Dell'Orco et al., 2012*) could significantly enhance its robustness. Parameter GSA simultaneously varies all the parameters within the parameter space to evaluate their effect on the system (*Dell'Orco et al., 2012*). Program packages are available to aid this analysis, such as: SBML-SAT (Systems biology markup language - sensitivity analysis tool). This program allows for evaluation using a range of different methods, including Sobol's Method, Weighted average of local sensitivity analysis, multi-parametric sensitivity analysis and partial rank correlation co-efficient. The program can also handle discontinuous events, which could be beneficial for the system in question (*Zi et al., 2008*). While this sort of modeling shows potential for the future it is worthy to note that uncertainty still remains an issue. For example a study by *Bennett et al*, shows that when calculating one parameter using a range of different models, the results can be orders of magnitude in difference (*Bennett et al., 2009*). Differences will always be present in these models as different models utilize different methods for prediction. However, the scale of the differences should be reduced, particularly by larger validation sets and more detailed applicability domains.

Nevertheless, the model helps to visualise the complex range of responses which can occur upon exposure of *in vitro* cell cultures to nanoparticles. The experimentally observed cascade of events resulting from oxidative stress and subsequent inflammatory responses

can readily be modelled. The dose dependence is complex, but can be modelled and related to the nanoparticle physico-chemical properties. Critically, the model demonstrates the temporal responses are dynamic and the dose dependences are complex, and therefore that it is not sufficient to measure cellular responses at a fixed dose or time point. Ideally, the complete 3-D profile of time, dose and response should be measured for all particles, structural variations, assays and cell-lines. Such an exercise would be exhaustive, in terms of time and cost, however, and numerical simulation models such as the one presented here can be of great benefit in reducing the effort.

Notably, the model allows to differentiate the impact on the viability endpoint of nanoparticle based parameters from cellular based parameters, and for a single cell line, the entire range of responses to the exposure to three different dendritic nanoparticles has been reduced to the two parameters of rate of endocytosis and rate of ROS generation. Within a single cell line, the differing responses of the different cytotoxicity assays are consistent with sensitivity to different stages of the cellular response cascade. Extending to different cell-lines, the variation of response can be accounted for by differences in intracellular antioxidant levels, although cell-line dependent differences in rate of endocytosis and rate of ROS generation, for the same nanoparticles cannot be ruled out and need to be experimentally verified.

The representation of the cellular responses in terms of a causally related sequence of events leading to cell death lends itself naturally to an AOP formalism, and such a formalism can be advantageous to regulatory bodies as it will identify the critical step in the sequence leading to a toxic response, in this case ROS production. Although AOPs developed to-date are primarily qualitative in nature, the work described in this manuscript

could be described as modelling a 'partial' AOP or Toxicity Pathway that comprises events at the molecular and cellular level. Additionally, the systems biology like approach adds quantification of the rates of response, which are related in the initial stages to the physico-chemical properties of the nanoparticles. By coupling these two approaches it may be possible to calculate an amount or rate of ROS production, from which the cell cannot recover, which would form the cut off point (acceptable limit) of whether the nanoparticle would be considered dangerous or not. Of course cellular quenching of ROS via antioxidant activity would also have to be considered. Such an approach may ultimately lead to predictive models of cytotoxic response and the basis of QSARs. In terms of the development of QSARs, the study and modelling of homologous series of nanoparticles contributes greatly to interpreting the mechanism of response, but also quantifiably relating the endpoint (EC_{50}) to the nanoparticle physico-chemical properties. The model further indicates, at least within the homologous series presented here, that the determining factor of the toxic response is the rate of generation of ROS, and that this may be considered a defined endpoint for the construction of QSARs. Obviously, the domain of applicability of such a model would need to be expanded by studies of a broader range of polymeric and other nanoparticles whose surface chemistry is well defined and ideally systematically variable. Only then can a reliable statistical validation of reliability and robustness of the model be considered. In constructing the model, simulations have been performed simultaneously for either: three dendrimer generations (Figures 3.3 and 3.6), timepoints (Figure 3.5), cell lines (Figure 3.8) or assays (Figure 3.9), keeping all other parameters constant. This suggests that, once the model has been established, it should be readily extendable to, for example, further generations of PAMAM dendrimer, similar homologous

cationic dendrimer series such as Poly (propylene imine), or other aminated polymer nanoparticles such as polystyrene and that the responses should be quantitatively predictable based on the number of surface amino groups. Work is ongoing to demonstrate that the model can be quantitatively translated to such systems, and thereby demonstrate a broader domain of applicability. Ultimately, it may be possible to characterise the surface reactivity, and thus the rate of generation of ROS acellularly (*Venkatachari et al., 2005*) such that the model could readily be extended to other more complex particle types that act via ROS mediated cellular stress pathways such as metal oxides, and the parameter may be used as input into such a model to predict the *in vitro* cytotoxicity.

3.6 Conclusion

The plethora of *in vitro* studies of nanoparticle toxicity demands a more structured approach to classification and understanding. In this context, homologous series of particles of systematically variable physico-chemical properties play an important role, and the systematically varied cellular responses facilitate the development of mathematical models based on the mechanisms of response.

This study demonstrates how such an approach can be used to faithfully reproduce and visualise the time and dose dependant response, for three polymer dendrimer nanoparticles simultaneously, and to construct a 3D toxicity profile to model the structurally dependent nanoparticle uptake and resultant oxidative stress and inflammatory cascade, leading to apoptosis and cell death. The phenomenological rate equation approach lends itself naturally to tracking the kinetics of the response, but the dose dependent toxicological end point at a fixed time point can similarly be modelled.

The model is also readily extendable to different cell lines, simply by changing a cell based parameter such as k_{GSH} and while the full range of components of the inflammatory/apoptotic cascade have not yet been experimentally visualised, the model can replicate the results of the cytotoxicity assays by solving for viability at different steps in the sequence. Furthermore, the system of equations used is versatile and can be readily modified to include additional cascade steps and new parameters as the experimental data become available.

Work is ongoing to apply the model to a range of different particles and cell lines. This current work serves to show that these mathematical models hold potential in predicting nanoparticle toxicity and will, with further development, provide a viable alternative to testing of each particle via a case-by-case approach. The models also have potential uses in a regulatory capacity and by combining these quantative methods with qualitative methods (such as AOPs) it will be easier to evaluate and apply limits of acceptability to the toxic response.

3.7 References

- Ankley, G.T., Bennett, R.S., Erickson, R.J., Hoff, D.J., Hornung, M.W., Johnson, R.D., Mount, D.R., Nichols, J.W., Russom, C.L., Schmieder, P.K., Serrrano, J.A., Tietge, J.E. and Villeneuve, D.L. 2010. Adverse Outcome Pathways: A conceptual framework to support ecotoxicology research and risk assessment. *Environ. Toxicol. Chem.,* **29**(3), 730–741.

- Atkinson, K.A. 1989. An Introduction to Numerical Analysis. **2nd ed.** *New York: John Wiley & Sons.* 1-712.

- Balasundaram, G., Sato, M., Webster T.J. 2006. Using hydroxyapatite nanoparticles and decreased crystallinity to promote osteoblast adhesion similar to functionalizing with RGD. *Biomaterials,* **27**(14), 2798–2805.

- Bennett, E.R., Clausen, J., Linkov, E. and Linkov, I. 2009. Predicting physical properties of emerging compounds with limited physical and chemical data: QSAR model uncertainty and applicability to military munitions. *Chemosphere,* **77**(10), 1412-1418.

- Bharali, D.J., Khalil, M., Gurbuz, M., Simone, T.M., Mousa, S.A. 2009. Nanoparticles and cancer therapy: A concise review with emphasis on dendrimers. *Int. J. Nanomed.,* **4**, 1–7.

- Black, J.W. and Leff, P. 1983. Operational models of pharmacological agonism. *Proceeding of the Royal Society B: Biological Sciences,* **220**(1219), 141-162.

- Clark, K.A., White, R.H. and Silbergeld, E. K. 2011. Predictive models for nanotoxicology: Current challenges and future opportunities. *Regul. Toxicol. Pharm.,* **59**(3), 361-512.

- Crooks, R.M., Lemon III, B.I., Yeung, L.K. and Zhao, M. 2001. Dendrimers III: Design, Dimension, Function: Dendrimer-encapsulated Metals and Semiconductors: Synthesis, Characterisation and Applications. *Topics in Current Chemistry,* **212**, 81-135.

- De Jong, W. H. and Borm, P.J.A. 2008. Drug delivery and nanoparticles: Applications and hazards. *Int. J. Nanomed.,* **3**(2), 133–149.

- Dell'Orco, D., Lundqvist, M., Cedervall, T. and Linse, S. 2012. Delivery success rate of engineered nanoparticles in the presence of the protein corona: a systems-level screening. *Nanomed: Nanotech. Bio. Med.,* **8**(8), 1271-1281.

- Deneke, S.M. and Fanburg, B.L. 1989. Regulation of cellular glutathione. *Am. J. Physiol.,* **257**(4 pt.1), L163-L173.

- Einstein, A. 1916. Strahlungs-emission und -absorption nach der Quantentheorie. *Verhandlungen der Deutschen Physikalischen Gesellschaft,* **18**, 318–323.

- European Union - Directive 2010/63/EU of the European Parliament and of the Council of 22 September 2010 on the protection of animals used for scientific purposes.

- Guillot-Nieckowski, M., Eisler, S. and Diederich, F. 2000. Dendritic vectors for gene transfection. *New J. Chem.,* **31**(7), 1111-1127.

- Hans, M.L. and Lowman, A.M. 2002.Biodegradable nanoparticles for drug delivery and targeting. *Curr. Opin. Solid St. M.,* **6**(4), 319–327.

- Hong, S., Bielinska, A.U., Mecke, A., Keszler, B., Beals, J.L., Shi, X., Balogh, L., Orr, B.G., Baker, J.R.Jr and Banaszak Holl, M.M. 2004. Interaction of poly(amidoamine) dendrimers with supported lipid bilayers and cells: hole formation and the relation to transport. *Bioconjugate Chem.,* **15**(4), 774–782.

- Issels, R.D., Nagele, A., Eckert, K-G. and Wilmanns W. 1985. Promotion of cystine uptake and its utilization for glutathione biosynthesis induced by cysteamine and N-acetylcysteine. *Biochem. Pharmacol.,* **37**(5), 1029-1033.

- Jain, K.K. 2007. Applications of Nanobiotechnology in Clinical Diagnostics. *Clinical Chemistry,* **53**(11), 2002–2009.

- Jain, K., Kesharwani, P., Gupta, U. and Jain, N.K. 2010. Dendrimer toxicity: Let's meet the challenge. *Int. J. Pharm.,* **394**(1-2), 122–142.

- Jeng, H.A. and Swanson, J. 2006. Toxicity of Metal Oxide Nanoparticles in Mammalian Cells. *J. Environ. Sci. Heal. A,* **41**(12), 2699-2711.

- Kennedy, I.M., Wilson, D. and Barakat, A.I. 2009. Uptake and Inflammatory Effects of Nanoparticles in a Human Vascular Endothelial Cell Line. *HEI Research Report* **136**, 3-32.

- Kitchens, K.M., Foraker, A.B., Kolhatkar, R.B., Swaan, P.W., Ghandehari, H. 2007. Endocytosis and interaction of poly (Amidoamine) dendrimers with Caco-2 cells. *Pharmaceut. Res.,* **24**(11), 2138–2145.

- Koo, O.M., Rubinstein, I. and Onyuksel, H. 2005. Role of nanotechnology in targeted drug delivery and imaging: a concise review. *Nanomed: Nanotech. Bio. Med.,* **1**(3), 193– 212.

- Kukowska-Latallo, J.F., Bielinska, A.U., Johnson, J., Spindler, R., Tomalia, D.A. and Baker, J.R.Jr. 1996. Efficient transfer of genetic material into mammalian cells

using Starburst polyamidoamine dendrimers. *P. Natl. Acad. Sci. USA,* **93**(10), 4897-4902.

- Lee, J.H., Cha, K.E., Kim, M.S., Hong, H.W., Chung, D.J., Ryu, G. and Myung, H. 2009. Nanosized polyamidoamine (PAMAM) dendrimer-induced apoptosis mediated by mitochondrial dysfunction. *Toxicol. Lett.,* **190**(2), 202–207.

- Medina, C., Santos-Martinez, M.J., Radomski, A., Corrigan, O.I. and Radomski, M.W. 2007. Nanoparticles: pharmacological and toxicological significance. *Brit. J. Pharmacol.,* **150**(5), 552–558.

- Meng, T., Xia, T., George, S., and Nel, A.E. 2009. A Predictive Toxicological Paradigm for the Safety Assessment of Nanomaterials. *ACS Nano,* **3**(7), 1620 − 1627.

- Miyazaki, M., Nakade, S., Iwanaga, K., Morimoto, K., and Kakemi, M. 2003. Estimation of bioavailability of salmon calcitonin from the hypocalcemic effect in rats (I): pharmacokinetic–pharmacodynamic modeling based on the endogenous Ca regulatory system. *Drug Metabol. Pharmacokinetics,* **18**(6), 350-357.

- Mukherjee, S.P. and Byrne H.J. 2013. Polyamidoamine dendrimer nanoparticle cytotoxicity oxidative stress, caspase activation and inflammatory response:

experimental observation and numerical simulation. *Nanomed: Nanotech. Bio. Med.,* **9**(2), 202-211.

- Mukherjee, S.P., Davoren, M. and Byrne H.J. 2010-A. *In vitro* mammalian cytotoxicological study of PAMAM dendrimers - towards quantitative structure activity relationships. *Toxicol. in Vitro,* **24**(1), 169-177.

- Mukherjee, S.P., Lyng, F.M., Garcia, A., Davoren, M. and Byrne H.J. 2010-B. Mechanistic studies of *in vitro* cytotoxicity of poly(amidoamine) dendrimers in mammalian cells. *Toxicol. Appl. Pharm.,* **248**(3), 259–268.

- Naha, P.C. and Byrne, H.J. 2013. Generation of Intracellular Reactive Oxygen Species and Genotoxicity effect to Exposure of Nanosized Polyamidoamine (PAMAM) dendrimers in PLHC-1 cells *in vitro*. *Aquatic Toxicology,* **132-133**, 61-72.

- Naha, P.C., Davoren, M., Casey, A. and Byrne, H.J. 2009. An Ecotoxicological Study of Poly(amidoamine) Dendrimers-Toward Quantitative Structure Activity Relationships. *Env. Sci. Technol.,* **43**(17), 6864–6869.

- Naha, P.C., Davoren, M., Lyng, F.M. and Byrne, H.J. 2010. Reactive oxygen species (ROS) induced cytokine production and cytotoxicity of PAMAM dendrimers in J774A.1 cells. *Toxicol. Appl. Pharm.,* **246**(1-2), 91–99.

- Nair, H.B., Sung, B., Yadav, V.R., Kannappan, R., Chaturvedi, M.M. and Aggarwal, B,B. 2010. Delivery of anti-inflammatory nutraceuticals by nanoparticles for the prevention and treatment of cancer. *Biochemical Pharmacology,* **80**(12), 1833–1843.

- Nakagawa, Y., Akao, Y., Morikawa, H., Hirata, I., Katsu, K., Naoe, T., Ohishi, N. and Yagi, K. 2002. Arsenic trioxide-induced apoptosis through oxidative stress in cells of colon cancer cell lines. *Life Sciences,* **70**(19), 2253–2269.

- Nel, A., Xia, T., Mädler, L. and Li N. 2006. Toxic potential of materials at the nanolevel. *Science,* **311**(5761), 622-627.

- Nishimura, I., Huang, Y., Butz, F., Ogawa, T., Lin, A. and Wang, C.J. 2007. Discrete deposition of hydroxyapatite nanoparticles on a titanium implant with predisposing substrate microtopography accelerated osseointegration. *Nanotechnology,* **18**(24), 1-9.

- Nociari, M.M., Shalev, A., Benias, P. and Russo, C. 1998. A novel one-step, highly sensitive fluorometric assay to evaluate cell-mediated cytotoxicity. *J. Immunol. Methods,* **213**(2), 157–167.

- Oomen, A., Bos, P., Fernandes, T., Hund-Rinke, K., Boraschi, D., Byrne, H. J., Aschberger, K., Gottardo, S., von der Kammer, F., Kühnel, D., Hristozov, D., Marcomini, A ., Migliore, L., Scott-Fordsmand, J., Wick, P. and Landsiedel, R. 2014. Concern-driven integrated toxicity testing strategies for nanomaterials - Report of the NanoSafety Cluster Working Group 10. *Nanotox.,* **14**, 195-216.

- Organisation for Economic Co-Operation and Development (OECD): Guidance Document On Developing and Assessing Adverse Outcome Pathways, *OECD,* ENV/JM/MONO(2013)**6**. 2013.

- Organisation for Economic Co-Operation and Development (OECD): Guidance Document on the Validation of (Quantative) Structure Activity Relationships [(Q)SAR] Models, *OECD,* ENV/JM/MONO(2007)**2**. 2007.

- Rothen-Rutishauser, B., Mühlfeld, C., Blank, F., Musso, C. and Gehr, P. 2007. Translocation of particles and inflammatory responses after exposure to fine particles and nanoparticles in an epithelial airway model. *Part. Fibre. Toxicol.,* **4**(9). doi: 10.1186/1743-8977-4-9.

- Project on Emerging Nanotechnologies (PEN), 2015. Accessed on 15-10-2015 – *Available at: http://www.nanotechproject.org/*

- Puzyn, T., Leszczynska, D. and Leszczynski, J. 2009. Toward the Development of "Nano-QSARs": Advances and Challenges. *Small,* **5**(22), 2494-2509.

- Repetto, G., del Peso, A. and Zurita, J.L. 2008. Neutral red uptake assay for the estimation of cell viability/cytotoxicity. *Nature Protocols,* **3**(7), 1125-1131.

- Russell, W.M.S. and Burch, R.L. 1959. The Principles of Humane Experimental Technique. *London: Methuen.* 1-238.

- Ryan, S.M., Frías, J.M., Wang, X., Sayers. C.T., Haddleton, D.M. and Brayden, D.J. 2011. PK/PD modelling of comb-shaped PEGylated salmon calcitonin conjugates of differing molecular weights. *J. Controlled Release,* **149**(2), 126–132.

- Salvati, A., Aberg, C., dos Santos, T., Varela, J., Pinto, P., Lynch, I. and Dawson K.A. 2011. Experimental and theoretical comparison of intracellular import of polymeric nanoparticles and small molecules: toward models of uptake kinetics. *Nanomed: Nanotech. Bio. Med.,* **7**(6), 818-826.

- Schins, R.P., McAlinden, A., MacNee, W., Jimenez, L.A., Ross, J.A., Guy, K., Faux, S.P. and Donaldson, K. 2000. Persistent Depletion of I Kappa B Alpha and Interleukin-8 Expression in Human Pulmonary Epithelial Cells Exposed to Quartz Particles. *Toxicol. Appl. Pharm.,* **167**(2), 107–117.

- Shen, L. and Sevanian, A. 2001. OxLDL induces macrophage γ-GCS-HS protein expression: a role for oxLDL-associated lipid hydroperoxide in GSH synthesis. *J. Lipid Res.,* **42**(5), 813-823.

- Shvedova, A.A., Castranova, V., Kisin, E.R., Schwegler-Berry, D., Murray, A.R., Gandelsman, V.Z., Maynard, A. and Baron, P. 2003. Exposure to carbon nanotube material: assessment of nanotube cytotoxicity using human keratinocyte cells. *J. Tox. Env. Heal. A,* **66**(20), 1909-1926.

- Snow E.T., Sykora P., Durham T.R., Klein C.B. 2005. Arsenic, mode of action at biologically plausible low doses: What are the implications for low dose cancer risk? *Toxicol. Appl. Pharm.,* **207**(2 Suppl.), S557 – S564.

- Tomalia, D.A. and Fréchet, J.M.J. 2002. Discovery of Dendrimers and Dendritic Polymers: A Brief Historical Perspective. *J. Polym. Sci. Pol. Chem.,* **40**(16), 2719–2728.

- Tsan, M.F., Danis, E.H., Del Vecchio, P.J. and Rosano, C.L. 1985. Enhancement of intracellular glutathione protects endothelial cells against oxidant damage. *Biochem. Bioph. Res. Co.,* **127**(1), 270-276.

- Tsan, M.F., White, J.E. and Rosano, C.L. 1989. Modulation of endothelial GSH concentrations: effect of exogenous GSH and GSH monoethyl ester. *J. Appl. Physiol.,* **66**(3), 1029-1034.

- United States 106th Congress - Public Law 106-545, Dec. 19, 2000.

- Venkatachari, P., Hopke, P.K., Grover, B.D. and Eatough, D.J. 2005. Measurement of Particle-Bound Reactive Oxygen Species in Rubidoux Aerosols. *J. Atmos. Chem.* **50**, 49-58.

- Vlahopoulos, S., Boldogh, I., Casola, A. and Brasier, A.R. 1999. Nuclear Factor-kB-Dependent Induction of Interleukin-8 Gene Expression by Tumor Necrosis Factor-α: Evidence for an Antioxidant Sensitive Activating Pathway Distinct From Nuclear Translocation. *Blood,* **94**(6), 1878-1889.

- Watson, P., Jones, A.T. and Stephens, D.J. 2005. Intracellular trafficking pathways and drug delivery: fluorescence imaging of living and fixed cells. *Adv. Drug Deliver. Rev.,* **57**(1), 43-61.

- Xia, T., Kovochich, M., Brant, J., Hotze, M., Sempf, J., Oberley, T., Sioutas, C., Yeh, J.I., Wiesner, M.R. and Nel, A.E. 2006. Comparison of the Abilities of Ambient and Manufactured Nanoparticles to Induce Cellular Toxicity According to an Oxidative Stress Paradigm. *Nano Lett.,* **6**(8), 1794-1807.

- Zhou, J., Wu, J., Hafdi, N., Behr, J.P., Erbacher, P. and Peng, L. 2006. PAMAM dendrimers for efficient siRNA delivery and potent gene silencing. *Chem. Commun.,* **22**, 2362–2364.

- Zi, Z., Zheng, Y., Rundell, A.E. and Klipp, E. 2008. SBML-SAT: a systems biology markup language (SBML) based sensitivity analysis tool. *BMC Bioinformatics,* **9**(342).

3.8 Supplementary Information for Chapter 3:

3.8.1 Parameters used for data simulation.

Table S3.1: Parameters employed for the final simulated datasets.

dt	0.1 hr
k_A	0.0011 hr^{-1}
RT_0	10μM
k_{endo}	0.75 hr^{-1}
c	0.25
k_{GSH}	1.00 hr^{-1}
k_q	0.40 hr^{-1}
k_λ	(ln2/24) hr^{-1}
B	3
$N_{source}(t=0)$	10μM
k_{casp}	0.02 hr^{-1}
k_{casp2}	0.30 hr^{-1}
k_{mmp}	0.001 hr^{-1}
k_{tnf}	0.035 hr^{-1}
k_{il8}	0.10 hr^{-1}
k_V	8.00 hr^{-1}
k_{rec}	0.065 hr^{-1}
k_{ROS}	1.20 hr^{-1}

3.8.2 Simulation of ROS Dose Dependence

In previous work (*Mukherjee and Byrne, 2013*), the time dependent rise and subsequent decay of the generation of ROS was modelled according to equation 3.10. However, such a model does not accurately account for the observed dose dependence, as shown in figure S3.1. Although an initial saturation-like behaviour is observable at intermediate doses, at higher doses the levels of ROS continue to increase monotonically.
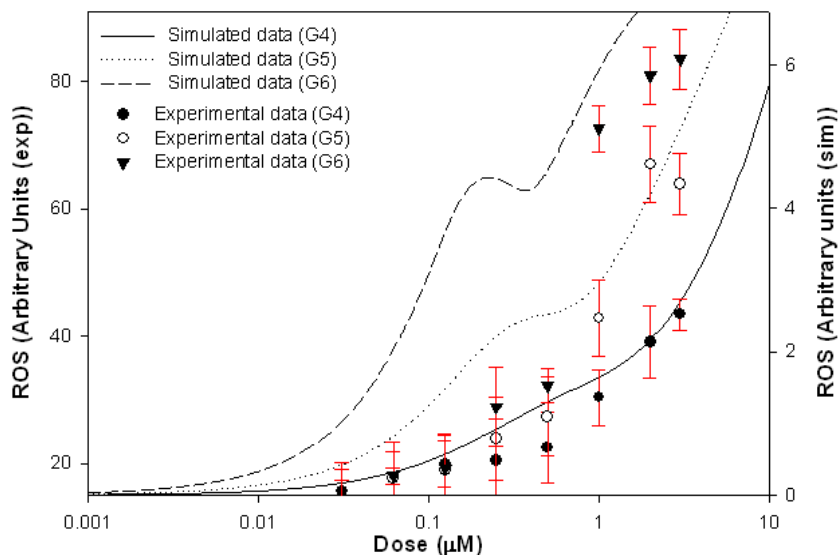

Figure S3.1: Dose dependent ROS generation for all generations simulated according to Equation 3.10.

The experimentally observed dose and time dependence of the increased levels of ROS is faithfully reproduced, however, by invoking the concept of a source of ROS which is depleted according to Equation 3.11, resulting in a dose and time dependent generation of ROS according to Equation 3.12 as shown in Figure 3.3.

Figure S3.2 shows the simulated uptake of nanoparticles, N_{endo}, calculated according to Equation 3.2, for PAMAM generations G4, G5, G6, with values of $c = 0.25$, $k_{\lambda} = (ln2/24)hr^{-1}$. Similar to the behaviour observed by *Salvati et al.* (*2011*) for aminated polystyrene nanoparticles, the response increases approximately linear at early times, but deviates from linearity as the cells divide and the nanoparticles are distributed over a larger cell population. Although no values of k_{endo} are quoted by *Salvati et al.*, the experimental data in their study are best fitted by a regime in which $k_{endo} > k_{\lambda}$. In Figure S3.1, $k_{endo} = 0.75$ $hr^{-1} > k_{\lambda} = 0.03\ hr^{-1}$.
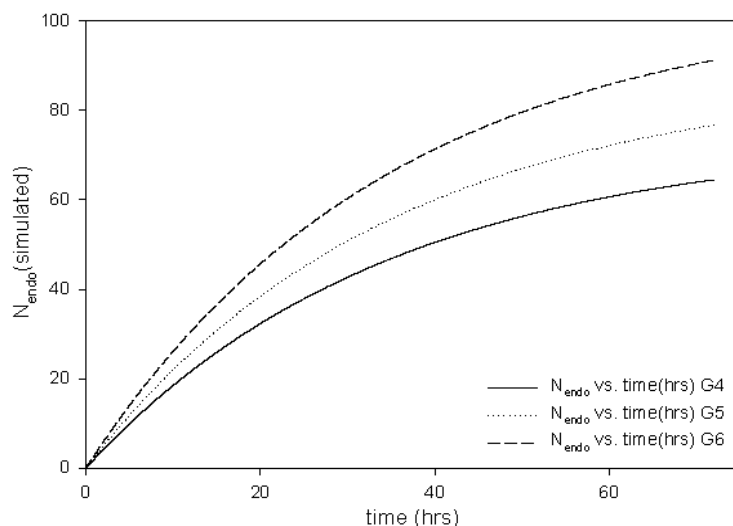
Figure S3.2: Simulated time dependent uptake of PAMAM dendrimers of generation G4, G5, G6, according to Equation 3.2, at a fixed dose of 1μM.

The effect of variation in k_{endo} is also manifest in the dose dependent evolution of the ROS levels for all generations, as shown in Figure S3.3, for the example of 4hrs exposure. Variation of k_{endo} has the effect of systematically shifting the median dose point of ROS

increase. The best reproduction of the experimentally observed behaviour for the combined dataset of three dendrimer generations was found with k_{endo}=0.75 hr^{-1}.

3.8.4 ROS Source Discussion

Confocal microscopic studies of mammalian cell exposure to PAMAM dendrimers by *Mukherjee et al.* have clearly demonstrated co-localisation of the early stage ROS with endosomes (*Mukherjee et al., 2010-A and B*). In the case of cationic nanoparticles in the acidifying environment of endosomes, it is reported that the unsaturated surface amino groups sequester protons that are supplied by the v-ATPase (proton pump) (*Nel et al., 2009*). This process keeps the pump functioning and leads to the retention of one Cl$^-$ ion and one water molecule per proton. It has been proposed that the initial wave of ROS may be produced via NADPH oxidase (*Xia et al., 2006*). NADPH oxidase is an enzyme which produces superoxide anions (O$_2^-$) in phagosomes and endosomes (*Shuvaev et al., 2011*). Evidence also points to the release of the superoxide to the cytoplasm via chloride anion channels (*Shuvaev et al., 2011*). Superoxide production is accomplished by an electron transfer from NADPH, via FAD, to diatomic oxygen (O$_2$). The O$_2^-$ then rapidly dismutases to hydrogen peroxide (H$_2$O$_2$) (*Babior et al., 2002*). It is also believed that the protons from the proton pump mechanism are used in the dismutation of superoxide. NADPH oxidase is present in nearly all cell types (including HaCaT cells (*Chamulitrat et al., 2004*)) and is important in both host defences and redox signalling(Reviewed by: *Bedard and Krause, 2007*and *Masuko, 2006*). NADPH oxidase has been implicated in the production of ROS in nanoparticle induced toxicity for other nanoparticles, including silica, *etc*. (*Dostert et al., 2008* and *Nabeshiet al., 2008*). The idea that NADPH oxidase is responsible for PAMAM

induced toxicity deserves further attention and may aid in a deeper understanding of the underlying processes involved in nano-cytotoxicity.

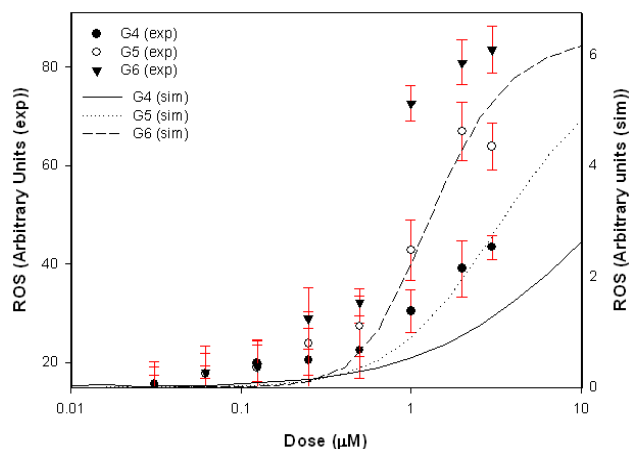### 3.8.5 Graphs Showing the Effect of Parameter Variance.

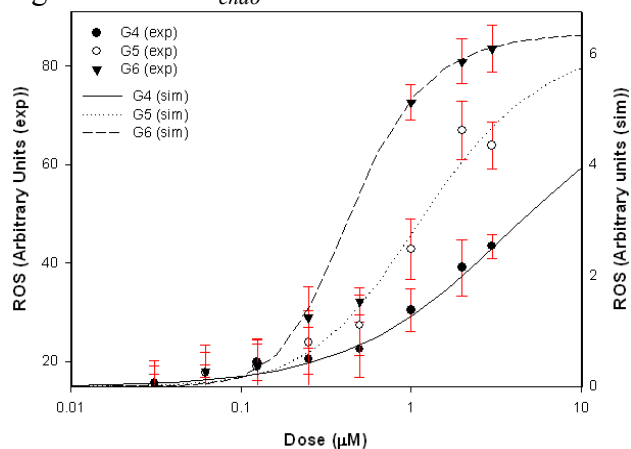Figure S3.3-A: $k_{endo} = 0.25hr^{-1}$

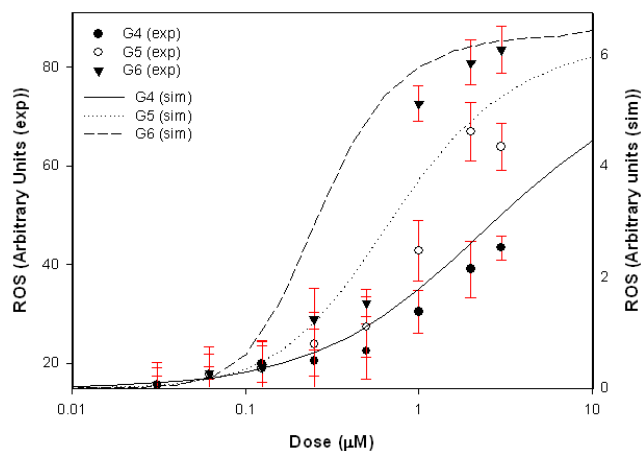
Figure S3.3-B: $k_{endo} = 0.75hr^{-1}$

Figure S3.3-C: $k_{endo} = 1.25hr^{-1}$

Figure S3.3(A-C): Variation in simulated (lines) increase in ROS levels on the parameter k_{endo} in Equation 3.2, compared to experimental data (symbols) for G4, G5, G6. A: $k_{endo} = 0.25hr^{-1}$, B: $k_{endo} = 0.75\ hr^{-1}$, C: $k_{endo} = 1.25hr^{-1}$.

The generation dependence of the uptake (also demonstrated in *Mukherjee and Byrne, 2013*) derives from the term $(N_{amg})^c$ in Equation 3.2, and although the uptake of the dendrimers cannot be directly visualised, the effect of this term on the generation dependent increase in ROS levels is demonstrated in Figure S3.4. The generation dependent factor similarly has the effect of shifting the dose dependent curves along the dose axis, but also systematically varies the separation of the responses for the different dendrimer generations. The best reproduction of the ROS curves was obtained using a value of **c**=0.25, as shown in Figure S3.4:B.
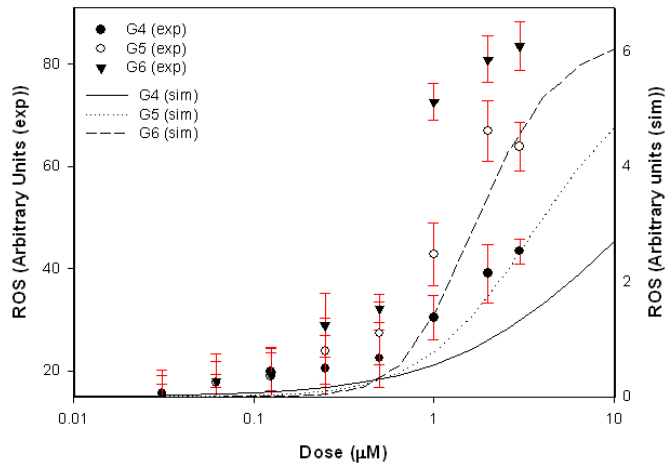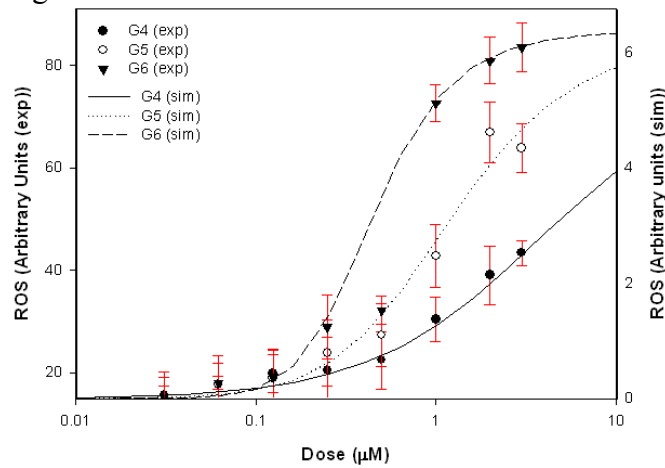
Figure S3.4-A: *c = 0*
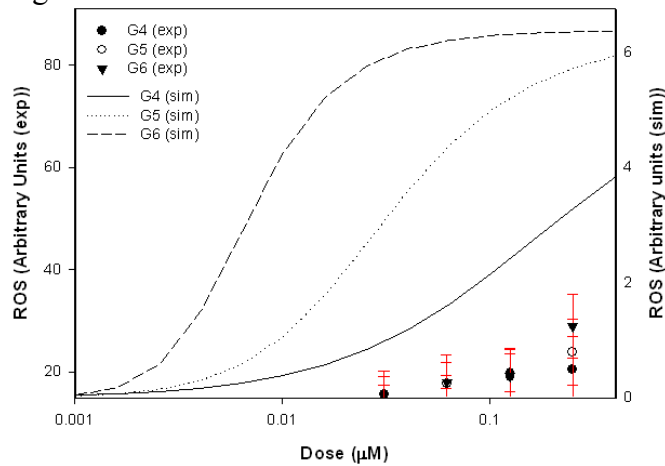

Figure S3.4-B: *c = 0.25*

Figure S3.4-C: *c = 1*

Figure S3.4(A-C): Variation in simulated (lines) increase in ROS levels on the parameter

$(N_{amg})^c$ in Equation 3.2, compared to experimental data (symbols) for G4, G5, G6. A: *c = 0*,

B: *c = 0.25* and C: *c = 1*.

Figure S3.5 illustrates the sensitivity of the simulations to variations in the parameter k_A in Equations 3.11 and 3.12. The parameter largely impacts on the separation of the dose dependences of the different generations. The best reproduction of the experimental behaviour was observed with a value of $k_A = 0.0011 \ hr^{-1}$.
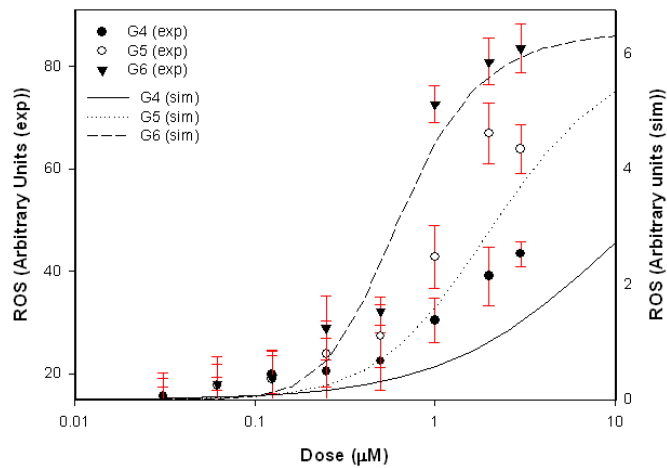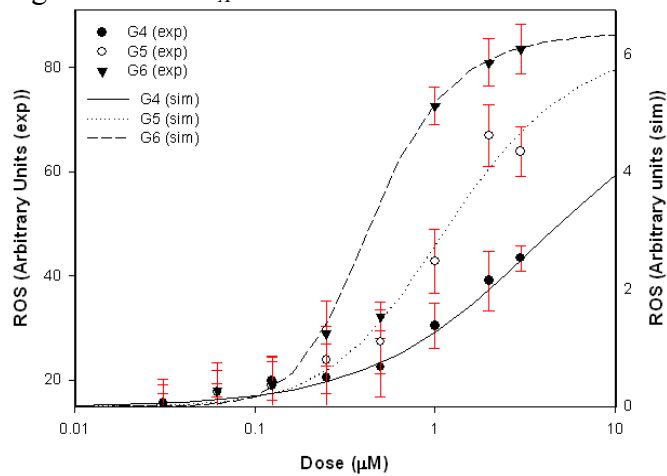

Figure S3.5-A: $k_A = 0.0004 \ hr^{-1}$
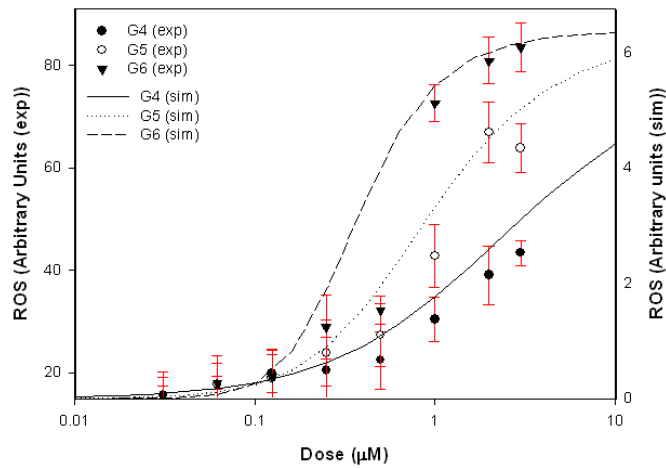

Figure S3.5-B: $k_A = 0.0011 \ hr^{-1}$

Figure S3.5-C: *k_A = 0.0018 hr^{-1}*

Figure S3.5(A-C): Variation in simulated (lines) increase in ROS levels on the parameter k_A

compared to experimental data (symbols) for G4, G5, G6. A: *k_A = 0.0004 hr^{-1}*, B: *k_A*

=0.0011hr^{-1} and C: *k_A = 0.0018 hr^{-1}*.

Figure S3.6 shows how the dose dependant ROS values vary with the *G** parameter. Since

$G* = 1/(N_{amg}^{0.25})$ the variance was observed by changing the exponent value (0.25).
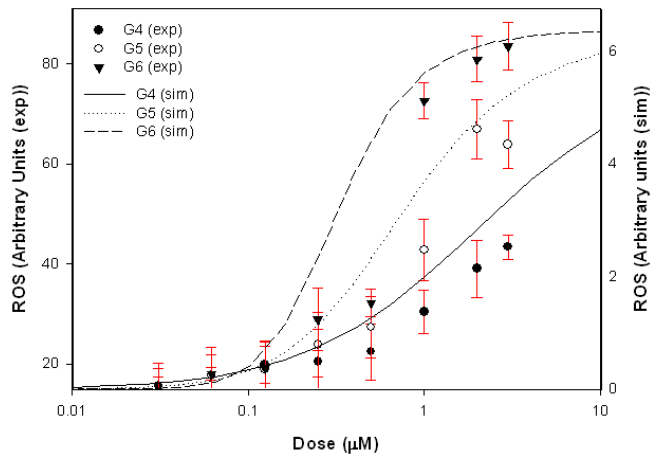

Figure S3.6-A: *Exponent value = 0.083*

Figure S3.6-B: *Exponent value = 0.25*

Figure S3.6-C: *Exponent value = 0.42*

Figure S3.6(A-C): Variation in simulated (lines) increase in ROS levels on the exponential value in the equation $G^*=1/(N_{amg}^{0.25})$, compared to experimental data (symbols) for G4, G5, G6. A: *Exponent value = 0.083*, B: *Exponent Value = 0.25*, C: *Exponent Value = 0.42*.

Figure S3.7 shows how the dose dependant ROS values vary with the parameter A. Since *A = $(N_{amg}/64)^{0.75}$* the variance was observed by changing the exponent value (0.75).
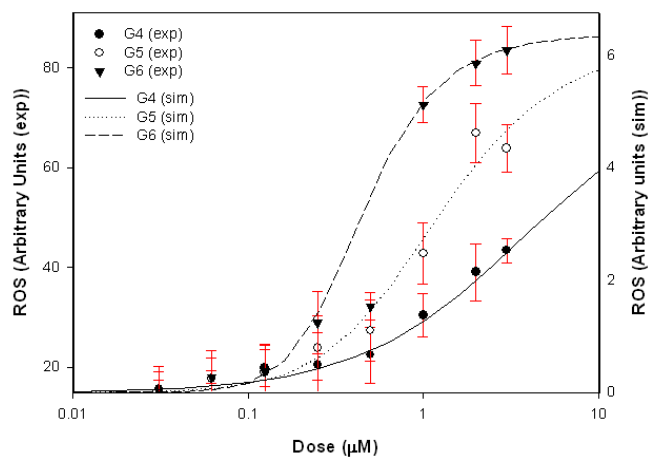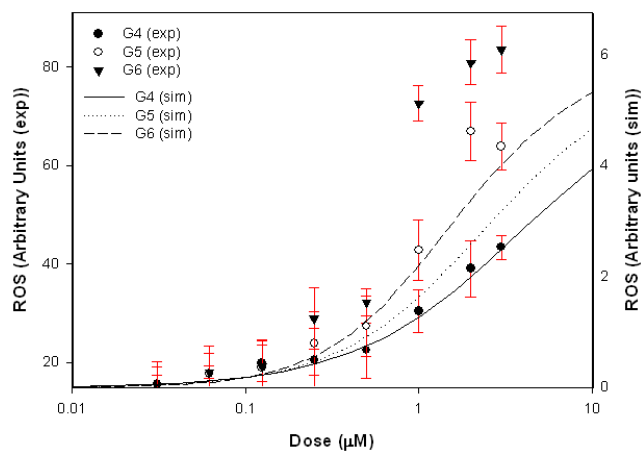
Figure S3.7-A: *Exponent value = 0.25*

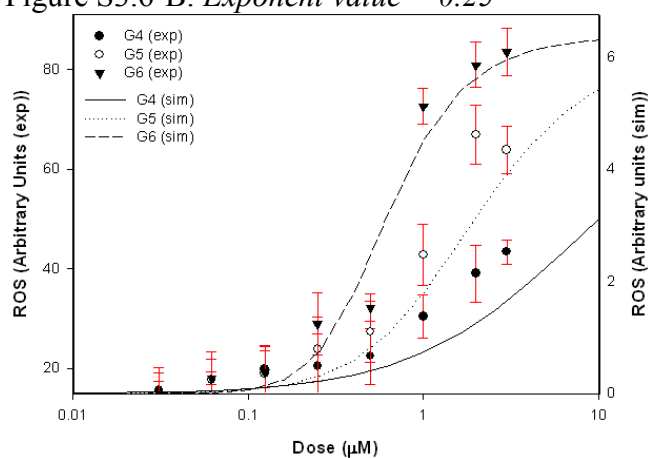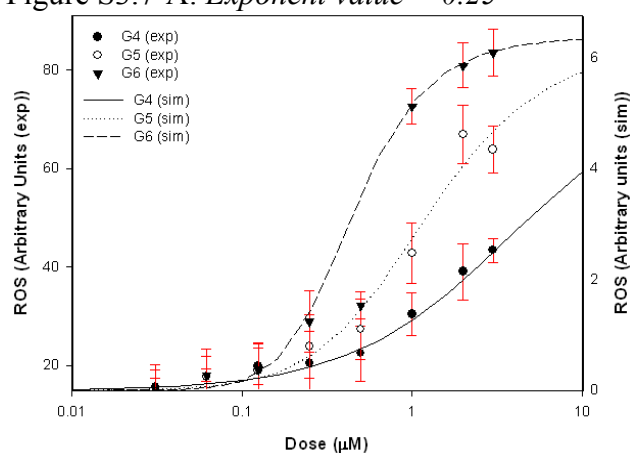Figure S3.7-B: *Exponent value = 0.75*
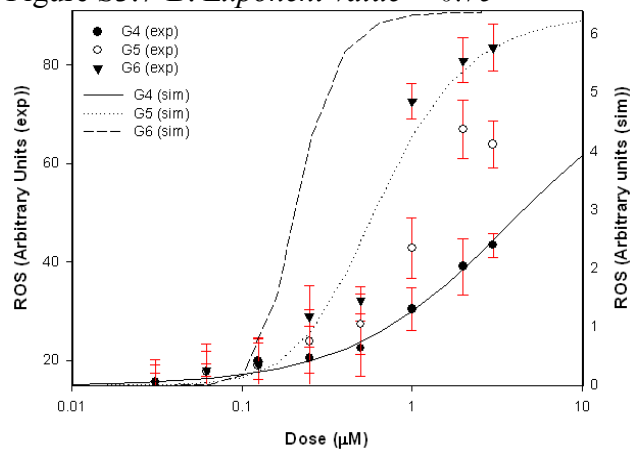
Figure S3.7-C: *Exponent value = 1.25*

Figure S3.7(A-C): Variation in simulated (lines) increase in ROS levels on the exponential value in the equation $A=(N_{amg}/64)^{0.75}$, compared to experimental data (symbols) for G4, G5, G6. A: *Exponent value = 0.25*, B: *Exponent Value = 0.75*, C: *Exponent Value = 1.25*.

Figure S3.8(A-C) shows how the dose dependant ROS production varies with the parameter B of Equations 3.11 and 3.12. It can be seen that this parameter has a dramatic effect on the overall shape, dose and generation dependence of the curves. A best reproduction of the experimental behaviour was obtained with *B=3*.
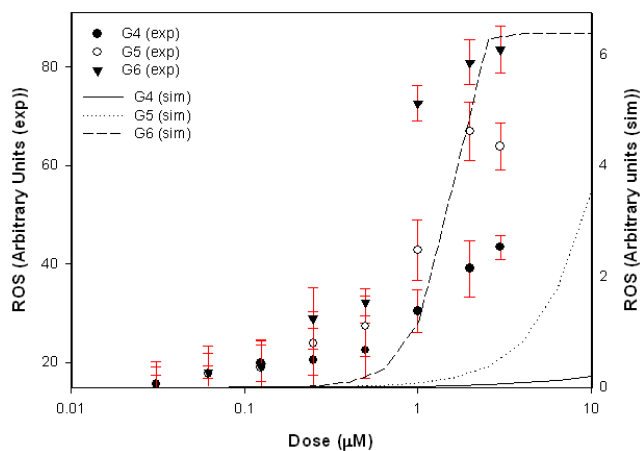
Figure S3.8-A: *B = 1*
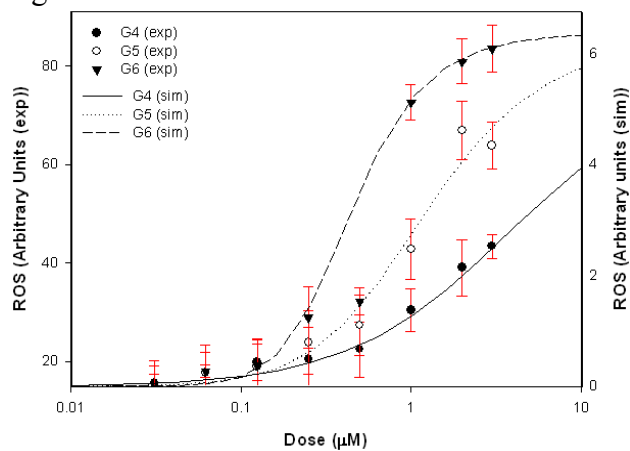
Figure S3.8-B: *B = 3*
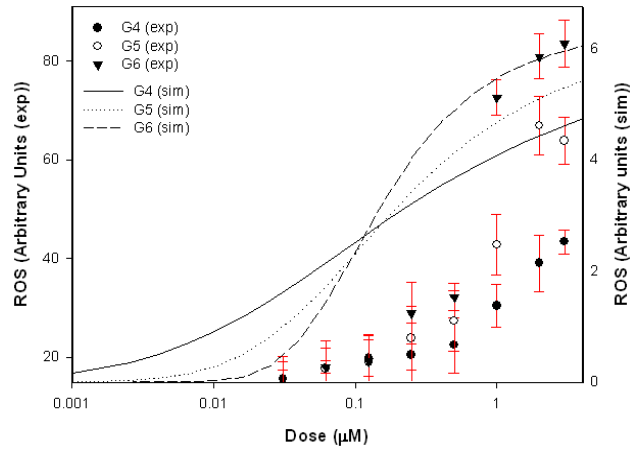
Figure S3.8-C: *B = 5*

Figure S3.8(A-C): Variation in simulated (lines) increase in ROS levels on the parameter *B*

in Equation 3.11/3.12, compared to experimental data (symbols) for G4, G5, G6. A: *B = 1*,

B: *B = 3* and C: *B = 5.*

Figure S3.9 shows how the viability of the cells (for G4 at three timepoints), as calculated

using Equation 3.9 is affected by the parameter k_{MMP}.
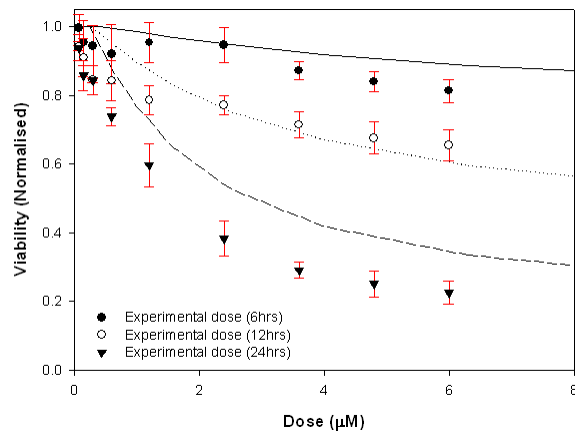
Figure S3.9-A: k_{MMP} = *0.0007*
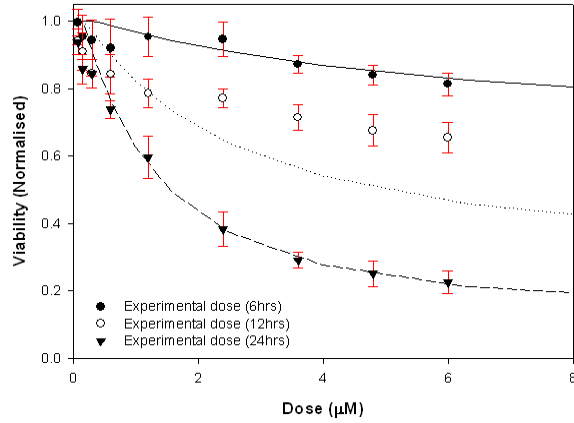
Figure S3.9-B: $k_{MMP} = 0.0010$
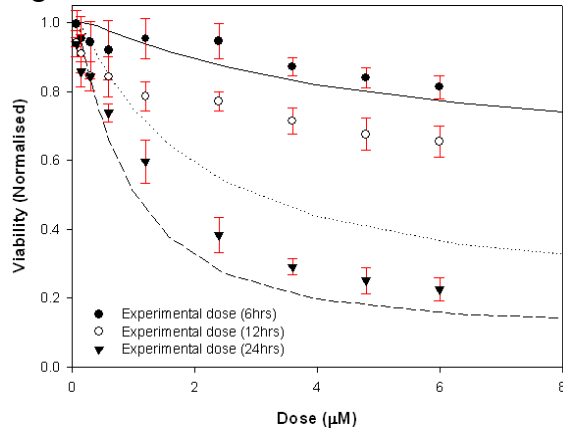
Figure S3.9-C: $k_{MMP} = 0.0013$

Figure S3.9(A-C): Effect of variation of the parameter k_{MMP} on simulated (lines) viability compared to experimental data (symbols) for G4 at timepoints: 6hrs, 12hrs and 24hrs. A: $k_{MMP} = 0.0007$, B: $k_{MMP} = 0.0010$ and C: $k_{MMP} = 0.0013$.

Figure S3.10 shows how the viability of the cells (for 3 generations of nanoparticle), as calculated using Equation 3.9 is affected by the parameter k_{MMP}.
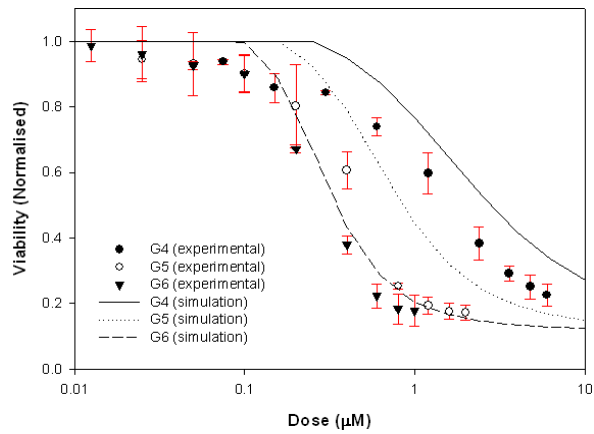
Figure S3.10-A: $k_{MMP} = 0.0007$
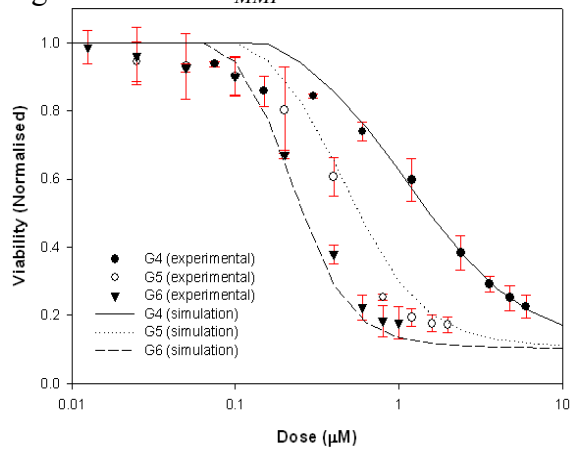
Figure S3.10-B: $k_{MMP} = 0.0010$
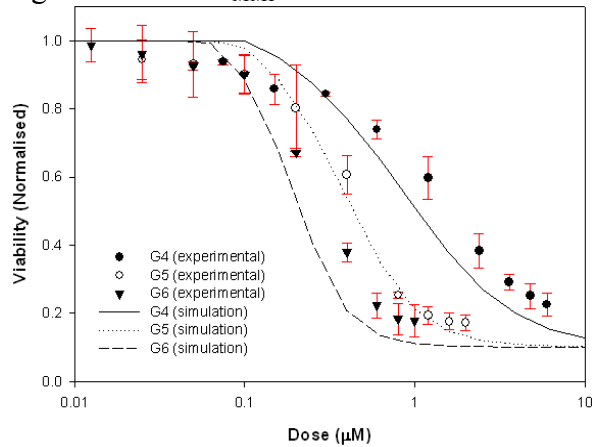
Figure S3.10-C: $k_{MMP} = 0.0013$

Figure S3.10(A-C): Effect of variation of the parameter k_{MMP} on simulated (lines) viability compared to experimental data (symbols) for G4, G5, G6. A: $k_{MMP} = 0.0007$, B: $k_{MMP} = 0.0010$ and C: $k_{MMP} = 0.0013$.

Figure S3.11 shows how the viability of the cells, as calculated using Equation 3.9 is affected by the exponent value "*m*" in equation 3.13.
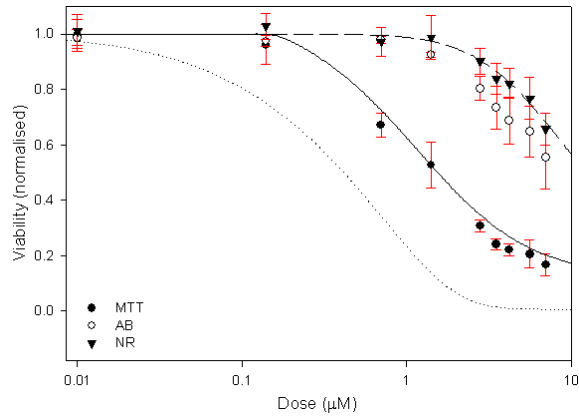
Figure 3.11-A: *m=1*
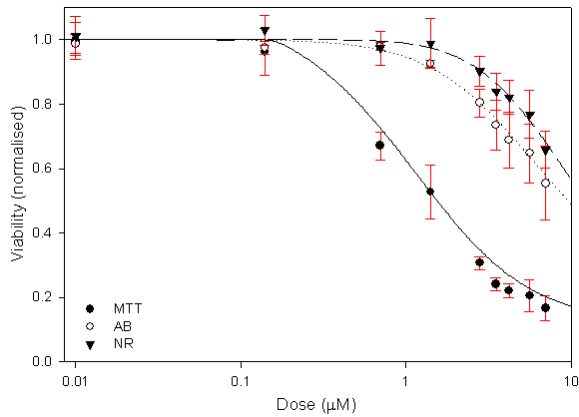
Figure 3.11-B: *m=2*
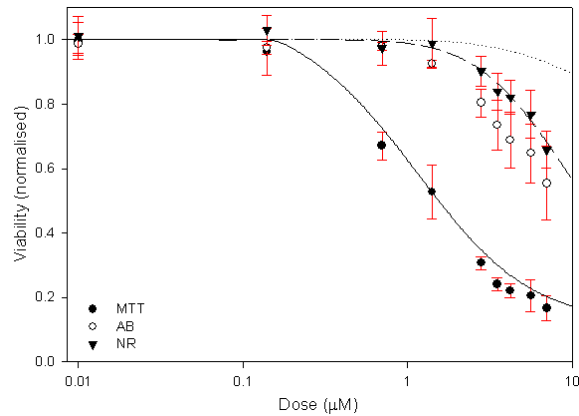
Figure 3.11-C: *m=3*
Figure S3.11(A-C): Effect of variation of the parameter *m (dotted line)* on simulated (lines)

viability compared to experimental data (symbols) for 3 different assay types . A: *m = 1*, B:

m = 2 and C: *m = 3.*

Figure S3.12 shows how the viability of the cells, as calculated using Equation 3.9 is affected by the exponent value "*p*" in Equation 3.14.
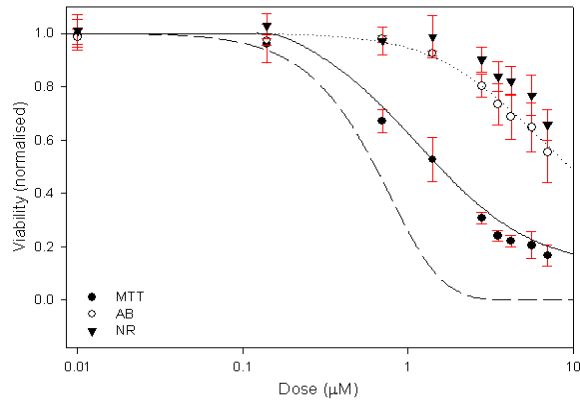
Figure 3.12-A: *p=2*
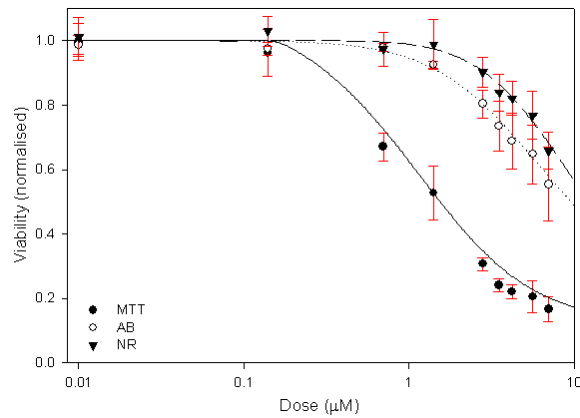
Figure 3.12-B: *p=3*
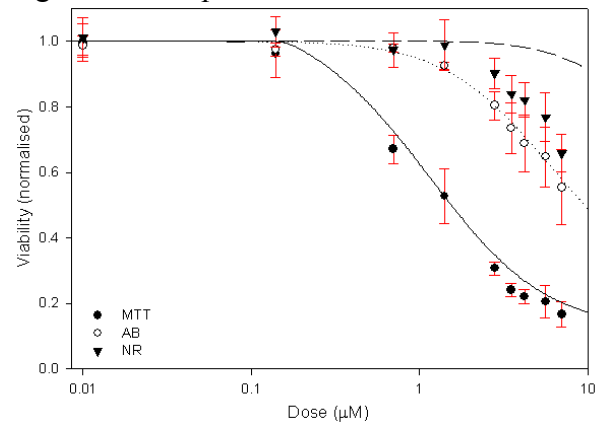
Figure 3.12-C: *p=4*
Figure S3.12(A-C): Effect of variation of the parameter *p (dashed line)* on simulated (lines) viability compared to experimental data (symbols) for 3 different assay types. A: *p=2*, B: *p=3* and C: *p=4*.

3.8.6 Supplementary information References for Chapter 3.

- Babior, B.M., Lambeth, J.D. and Nauseef, W. 2002. The neutrophil NADPH oxidase. *Arch. Biochem. Biophys.* **397**(2): 342–344.

- Bedard, K. and Krause, K.H. 2007. The NOX Family of ROS-Generating NADPH Oxidases: Physiology and Pathophysiology. *Physiol. Rev.,* **87**(1), 245–313.

- Chamulitrat, W., Stremmel, W., Kawahara, T., Rokutan, K., Fujii, H., Wingler, K., Schmidt, H.H. and Schmidt, R. 2004. A constitutive NADPH oxidase-like system containing gp91phox homologs in human keratinocytes. *J. Invest. Dermatol.,* **122**(4), 1000-1009.

- Dostert, C., Pétrilli, V., Van Bruggen, R., Steele, C., Mossman, B.T. and Tschopp, J. 2008. Innate Immune Activation Through Nalp3 Inflammasome Sensing of Asbestos and Silica. *Science,* **320**(5876), 674-677.

- Masuko, U.F. 2006. Localizing NADPH Oxidase–Derived ROS. *Science Signalling: The Signal Transduction Knowledge Environment,* **2006**(349), re8.

- Mukherjee, S.P. and Byrne H.J. 2013. Polyamidoamine dendrimer nanoparticle cytotoxicity oxidative stress, caspase activation and inflammatory response:

experimental observation and numerical simulation. *Nanomed: Nanotech. Bio. Med.,* **9**(2), 202-211.

- Mukherjee, S.P., Davoren, M. and Byrne H.J. 2010-A. *In vitro* mammalian cytotoxicological study of PAMAM dendrimers - towards quantitative structure activity relationships. *Toxicol. in Vitro,* **24**(1), 169-177.

- Mukherjee, S.P., Lyng, F.M., Garcia, A., Davoren, M. and Byrne H.J. 2010-B. Mechanistic studies of *in vitro* cytotoxicity of poly(amidoamine) dendrimers in mammalian cells. *Toxicol. Appl. Pharm.,* **248**(3), 259–268.

- Nabeshi, H., Yoshikawa, T., Matsuyama, K., Nakazato, Y., Tochigi, S., Kondoh, S., Hirai, T., Akase, T., Nagano, K., Abe, Y., Yoshioka, Y., Kamada, H., Itoh, N., Tsunoda, S. and Tsutsumi, Y. 2008. Amorphous nanosilica induce endocytosis-dependent ROS generation and DNA damage in human keratinocytes. *Part. Fibre Toxicol.,* 8(1), 10 pages

- Nel, A.E., Mädler, L., Velegol, D., Xia, T., Hoek, E.M.V., Somasundaran, P., Klaessig, F., Castranova, V. and Thompson, M. 2009. Understanding biophysicochemical interactions at the nano–bio interface. *Nature Materials*. **8**(7): 543 – 557.

- Salvati, A., Aberg, C., dos Santos, T., Varela, J., Pinto, P., Lynch, I. and Dawson K.A. 2011. Experimental and theoretical comparison of intracellular import of polymeric nanoparticles and small molecules: toward models of uptake kinetics. *Nanomed: Nanotech. Bio. Med.,* **7**(6), 818-826.

- Shuvaev, V.V., Han, J., Yu, K.J., Huang, S., Hawkins, B.J., Madesh, M., Nakada, M. and Muzykantov, V.R. 2011. PECAM-targeted delivery of SOD inhibits endothelial inflammatory response. *FASEB,* **25**(1), 348-357.

- Xia, T., Kovochich, M., Brant, J., Hotze, M., Sempf, J., Oberley, T., Sioutas, C., Yeh, J.I., Wiesner, M.R. and Nel, A.E. 2006. Comparison of the Abilities of Ambient and Manufactured Nanoparticles to Induce Cellular Toxicity According to an Oxidative Stress Paradigm. *Nano Lett.,* **6**(8), 1794-1807.

Chapter 4:

Numerical simulations of in vitro nanoparticle toxicity – the case of aminated polystyrene.

The work presented in this chapter is adapted from a manuscript currently under review in Toxicology *In Vitro*: Maher, M.A. and Byrne, H.J. 2016 – A. Numerical simulations of *in vitro* nanoparticle toxicity – the case of aminated Polystyrene. Submit to: *Toxicol. In Vitro*, January 2016.

4.1 Abstract

The *in vitro* cytotoxicity of 50nm and 100nm aminated polystyrene nanoparticles (PSNP-NH_2) is measured and modelled according to a phenomenological rate equation approach. Nanoparticle size was confirmed using Scanning Electron Microscopy and surface functionalisation measured using Nuclear Magnetic Resonance spectroscopy. The dose dependent cytotoxic response was measured using both the Alamar Blue (AB) and 3-(4,5-dimethylthiazol-2-yl)-2,5-diphenyltetrazolium bromide (MTT) assays, at time points of 6, 12, 24, 48 and 72hr. The systematic progression of the toxic response was modelled using a rate equation model previously developed for aminated dendritic polymeric nanoparticles, and it is shown that the experimental responses can be faithfully reproduced with identical model parameters, with the exception of the nanoparticle size dependent endocytotic rate and surface functionalisation dependent rate of generation of reactive oxygen species. The consistency of the model over the range of different points adds to the validity of such a numerical simulation approach to support toxicity screening strategies, including quantitative structure activity relationships and adverse outcome pathways.

4.2 Introduction

Nanoparticles are an emerging technology with many potential applications in a diverse number of fields, such as: medicine, electronics, engineering, cosmetics, food, textiles, packaging and many more (*PEN, 2015*). However, the potential applications in the biomedical sciences are of particular importance, whereby targeted drug delivery or more efficient gene delivery could be aided by advances in nanoscience (*Eichman et al., 2000*, *Duncan and Izzo, 2005*, *des Rieux et al., 2006* and *De Jong and Borm, 2008*). While the use of nanomaterials in the biomedical sciences holds many potential advantages, toxicity associated with these emerging materials has elicited the creation of the field of nanotoxicology (*Donaldson et al., 2004*). To fully unlock the potential of nanoparticles, it will be essential to understand the mechanisms and cellular events which give rise to these toxic responses.

In the domain of medical applications, there is a near limitless amount of different types of nanoparticles with potential uses, and, when combined with variations in parameters such as; size, shape and surface modification, it is clear that even within one type of nanoparticle, several variants can be created, each of which may have a different set of biological effects. Initial testing strategies focused on a case by case approach, whereby every nanoparticle was individually tested, however, such a strategy would make it impossible to keep up with the diverse amount of different nanoparticles being produced (*Clark et al., 2011*). The need for a more efficient and informed screening and testing solution for nanomaterials has been proposed by the EU Nano Safety Cluster (Working Group 10), based on a three tier system, whereby tier one identifies nanomaterials of interest and relevant exposure routes, tier two involves the use of standard and modified

testing methods which, critically, allows for the grouping of nanomaterials based on levels of risk, such that, in tier 3, higher risk materials are subject to more specialised tests and the evaluation of nanoparticle toxicity on full system models (for example: barrier models for nanomaterials which may cross cellular barriers such as upper respirator tract versus alveolar space) (*Oomen et al., 2014*). This type of testing can be use in conjunction with other advances in high content analysis approaches, which rapidly screen several different cell types for responses to nanoparticle toxicity (*Anguissola et al., 2014*).

Such grouping of responses is aided by studies of nanoparticles for which the physico-chemical properties are systematically variable and information on the toxic progression of the particles is known. In this context, dendritic polymeric nanoparticles are potentially important, as the particle size and surface chemistry are well defined, whereby surface groups can be modified to be cationic (via NH_2 addition), anionic (via COOH addition, for so called "half-generation" dendrimers) or neutral, and successive generations double the amount of such surface functional groups. Poly (amido amine) (PAMAM) dendrimers have been extensively studied and the cellular responses to exposure have been well characterised and seen to be well behaved as a function of the systematic variation of physico-chemical properties (*Naha et al., 2009 and 2010, Mukherjee et al., 2010-A and B* and *Mukherjee and Byrne, 2013*), potentially providing the basis for quantitative structure activity relationships (QSARS) and more specifically quantitative nanostructure activity relationships (QNARS) (*Clark et al., 2011*). PAMAM dendrimers are taken into the cell via endocytosis (*Mukherjee et al., 2010-B, Kitchens et al., 2007* and *Hong et al., 2004*) and, when internalised, an initial increase in oxidative stress via the production of reactive oxygen species (ROS) in and around the endosome is observed (*Mukherjee et al., 2010-A*

and B, *Naha et al., 2010* and *Khalid et al., 2015*). This initial ROS increase is countered by the cellular anti-oxidants (for example: Glutathione). However, if the anti-oxidant defence is insufficient, oxidative stress may occur (*Mukherjee and Byrne, 2013*). The dendrimer has also been shown to breach the endosome, in a process called endosomolysis and subsequently localise in the mitochondria (*Watson et al., 2005*), whereby a second phase increase in ROS is seen, coupled with loss of mitochondrial membrane potential and the induction of several pro-apoptotic factors, leading to cell death (via apoptosis) (*Naha et al., 2009 and 2010, Mukherjee et al., 2010-A and B, Mukherjee and Byrne, 2013* and *Khalid et al., 2015*). It was also found that, by systemically varying the generation of the nanoparticle, the toxicity also exhibited a systematic variance, whereby the higher generation dendrimers were more toxic than the preceding ones (G6>G5>G4) (*Naha et al., 2009 and 2010, Mukherjee et al., 2010-A and B,* and *Mukherjee and Byrne, 2013*). The systematic sequence of events involved in their toxicity can be interpreted as an adverse outcome pathway (AOP) (*Maher et al., 2014*), an approach which has been recently endorsed by the OECD as a way to categorise nanoparticle toxicity (*OECD, ENV/JM/MONO (2013)6*). The production of ROS is the identifiable Molecular Initiating Event (MIE), giving rise to the cascade of events, leading to the adverse outcome of apoptosis.

An adjunct strategy is the use of predictive models which can simulate nanoparticle toxicity and group responses according to common physico-chemical properties (*Clark et al., 2011*). Such an approach has been explored by *Mukherjee and Byrne* (*2012*) and *Maher et al.* (*2014*), utilising PAMAM dendrimers as model system, *in vitro*. These models use a set of Ordinary Differential Equations (ODEs), each of which describes a step in the

systematic sequence of events, ultimately leading to cell death via apoptosis. The successive steps of endocytosis, ROS generation, inflammatory response and apoptosis can be represented by independent rate constants, separating out the nanoparticle dependent MIE, and the subsequent cellular AOP. For the case of the PAMAM dendrimer time, dose, and generation dependent toxic response, the approach was shown to faithfully reproduce the experimentally observable responses, varying only the generation dependent nanoparticle properties, keeping all others constant. The key nanoparticle/generation dependent parameters identified were the endocytosis rate and the rate of production of ROS (*Maher et al., 2014*).

Several cationic terminal nanoparticles have been shown to follow such a paradigm of toxic response; for example, poly (propylene imine) (PPI) dendrimers (*Khalid et al., 2015*) and aminated polystyrene nanoparticles (PSNP-NH$_2$) (*Xia et al., 2008*, *Bexiga et al., 2011*, *Ruenraroengsak et al., 2012* and *Wang et al., 2013*). Notably, if the numerical simulation appropriately identifies and differentiates the MIE and the subsequent AOP, the PAMAM model should be readily adaptable to describe the toxic responses to such nanoparticles in the same *in vitro* exposure conditions, with minimum adjustment of the AOP rate constant parameters.

To further demonstrate the validity of such a rate equation based modelling approach, polystyrene nanoparticles, with amine modified surface groups (PSNP-NH$_2$), were studied. PSNP are of interest to biomedical science for several reasons, of particular note being their potential in drug delivery, in which potential advantages of these nanoparticles include: easy cellular uptake (*Lunov et al., 2011* and *Anguissola et al., 2014*), translocation between cells (*Kloet et al., 2011*) and crossing of biological barriers (such as the alveolar

epithelium) and subsequent entry into the blood system and transportation to more distal organs (*Yacobi et al., 2008*). Furthermore, PSNP have been identified as a potential standard for probing nanoparticle-cell interactions and for cellular nanoparticle tracking using methods such as Confocal Laser Scanning Microscopy (CLSM) and Raman Spectroscopy (*Dorney et al., 2012* and *Efeoglu et al., 2015*). Therefore, being able to predict their toxicity could be of great benefit in reducing the timescale of initial testing strategies. However, PSNP have a greater variability in their physico-chemical properties than other particles such as PAMAM and PPI, for which particle size and number of surface groups are chemically defined parameters. For PSNP, the mean size is usually reported with some associated variance and parameters such as number of surface groups is dependant on the synthetic method used. In this study PSNP-NH$_2$ with nominal diameters of 50nm and 100nm were used. These nanoparticles have been shown to be toxic to mammalian cells and adhere to a similar paradigm of toxicity as the PAMAM dendrimers (*Xia et al., 2006 and 2008* and *Anguissola et al., 2014*), which will aid modelling efforts based on the systematic sequence of events (*Maher et al., 2014*). To predicatively simulate toxicity for such nanoparticles, whose parameters include some variance, is imperative if the model is to be considered usable for a more diverse set of emerging nanomaterials.

4.3 Materials and Methods

4.3.1 Materials

Fluorescently labelled 50nm and 100nm amine surface modified polystyrene nanoparticles (PSNP-NH$_2$) and 100nm diameter polystyrene nanoparticles with no surface modifications (PSNP-neu) were purchased from Sigma-Aldrich, Ireland.

Both PSNP-NH$_2$ nanoparticles were supplied in 1mL suspension, 2.5% w/v solution (50nm stock = 2.07mM, 3.66 x 10^{14} particles/mL and 100nm stock = 2.05mM, 4.57 x 10^{13} particles/mL). PSNP-neu nanoparticles were supplied in 2mL suspension, 10% w/v solution, 8.69mM, 1.84 x 10^{14} particles/mL. Particle number calculation was performed in accordance with the manufacturer's guidelines and using their recommended equation: Section 4.9: Supplementary Information, Equation S4.1, (*Sigma-Aldrich, 2015*).

DMEM F12 HAM growth medium, Penicillin, Streptomycin, and 3-(4,5-dimethylthiazol-2-yl)-2,5-diphenyltetrazolium bromide (MTT) dye were also purchased from Sigma-Aldrich, Ireland. Fetal Bovine Serum (FBS), L-Glutamine, Alamar Blue (AB) and 5-(and-6)-carboxy-2',7'-dichlorodihydrofluorescein diacetate (carboxy-H$_2$DCFDA) dye were purchased from Life Technologies™, Bio-Sciences, Ireland. TrueLine 96-well cell culture plates were used for all cellular studies.

All fluorescence and absorbance readings were taken on a Molecular Devices SpectraMax M3 Spectrometer and EC$_{50}$ data analysis was performed using a four parameter fit on SigmaPlot v10.0 software.

4.3.2 Methods

4.3.2.1 Scanning Electron Microscopy (SEM)

50nm and 100nm PSNP-NH$_2$ were diluted from stock to a concentration of 10μM and prepared for SEM by spin coating. Samples were scanned using a Hitachi SU 6600 FESEM, a variable pressure FESEM with a Schottky field emission electron gun enabling in excess of 200nA probe current..

Both samples were imaged under low voltage (0.8 – 2.5 keV), to minimise charging due to the non-conductive nature of the sample. It should be noted that considerable drift was encountered, leading to some blurring at the edges of the images (Figure 4.1 and Supplementary Figure S4.1).

4.3.2.2 Nuclear Magnetic Resonance (NMR)

Unmodified 100nm PSNP-neu and amine surface modified 50nm and 100nm PSNP-NH$_2$ samples were dried in an oven at 40˚C over night and then placed in a desiccator for three days to ensure the complete removal of water. Samples were then made up at a concentration of 0.5mg/mL (41μM) in deuterium oxide (D$_2$O) and proton NMR (^{1}H NMR at 400 MHz) was performed using a Bruker Advance II 400 MHz instrument. Initially, a 16 scan cycle was performed, but due to a high degree of noise (most likely due to low sample concentration and poor solubility in D$_2$O) the samples were re-run using a 128 scan cycle, significantly reducing noise. The PSNP-NH$_2$ had identical Molar concentrations, although the particle number was different for 50nm and 100nm. PSNP-NH$_2$ 50nm = 7.31×10^{12} particles/mL, PSNP-NH$_2$ and PSNP-neu = 9.14×10^{11} particles/mL (*Sigma-Aldrich, 2015*).

4.3.2.3 Cell culture

HaCaT cells are an immortalised, non cancerous human keratinocyte cell line and were used for these experiments. The cells were cultured in Dulbecco's modified eagle medium (DMEM) F12 HAM supplemented with 10% FBS, 45 IU/mL penicillin, 45 IU/mL streptomycin, 2mM L-glutamine and 1μg/mL hydro-cortisone at 37˚C in 5% CO$_2$.

All assays carried out were performed in 96 well plates, which were plated at a concentration of 1×10^4 cells per well, in 100μL of DMEM F12 HAM. Cells were allowed 24hrs to attach and were then treated with 50nm or 100nm PSNP-NH$_2$ at various concentrations for the desired time points. Six replicates of each concentration were performed per plate and each plate was repeated in triplicate.

4.3.2.4 Viability assays

50nm and 100nm PSNP-NH$_2$ was used for each experiment and the Alamar Blue and MTT assays were used to determine cellular viability. For consistency with previous experimental studies and numerical models of dendrimer toxicity (*Naha et al., 2009 and 2010, Mukherjee et al., 2010-A and B, Mukherjee and Byrne, 2013* and *Maher et al., 2014*), PSNP-NH$_2$ doses are expressed as Molar concentrations and the gradient used was: 10, 5, 3.75, 2.5, 1.25, 0.625, 0.313 and 0.157μM and EC$_{50}$ values were calculated at time points: 6, 12, 24, 48 and 72 hours.

4.3.2.5 Alamar Blue

The Alamar Blue assay was made up by adding 500μL stock for every 10mL of medium (DMEM F12 HAM, was used for this, with no additional supplements). At the specified time point, the plates were removed from the incubator and the medium containing PSNP-NH$_2$ was removed, the cells were washed with 100μL PBS and then 100μL of DMEM (unsupplemented) containing Alamar Blue were added to each well. The plates were incubated for 3 hours at 37°C in 5% CO$_2$ to allow for conversion of the dye. The

fluorescence of each well was then read using the SpectraMax M3 spectrometer with $\lambda_{ex}=$ 555nm and $\lambda_{em}=$ 585nm.

4.3.2.6 MTT (3-(4,5-dimethylthiazol-2-yl)-2,5-diphenyltetrazolium bromide)

A stock solution of MTT was made at a concentration of 0.5mg/mL and 500μL of this stock were added for every 10mL of medium (DMEM F12 HAM, was used, with no additional supplements). At the specified time point, the plates were removed from the incubator and the medium containing PSNP-NH$_2$ was removed, the cells were washed with 100μL PBS and then 100μL of DMEM (unsupplemented) containing MTT were added to each well. The plates were incubated for 3 hours at 37°C in 5% CO_2 to allow for conversion of the dye. After 3 hours, any remaining dye was removed and each well was again washed with 100μL PBS, then 100μL DMSO was added and the plates were placed on a shaker for 10 minutes to allow for the dye to solubilise. The absorbance of each well was then read using the SpectraMax M3 spectrometer with $\lambda_{ABS}=$595nm.

4.3.2.7 Analysis and Modelling

Data analysis was performed using SigmaPlot™ (v10.0) and fluorescence was calculated based on the values of unexposed controls. Data is shown with error bars indicating ± the standard deviation. SigmaPlot™ (v10.0) was also used for calculating the EC$_{50}$ values, using a four parameter sigmoidal fit, which are shown ± standard error, as well as the p-value for each EC$_{50}$, and the R^2 values (shown in Section 4.9: Supplementary Information: Table S4.1 and S4.2). Simulation and modelling was also performed using SigmaPlot v10.0 and the system of equations based on those described by *Maher et al.* (*2014*).

4.4 Results

4.4.1 Particle Characterisation

a)   b)
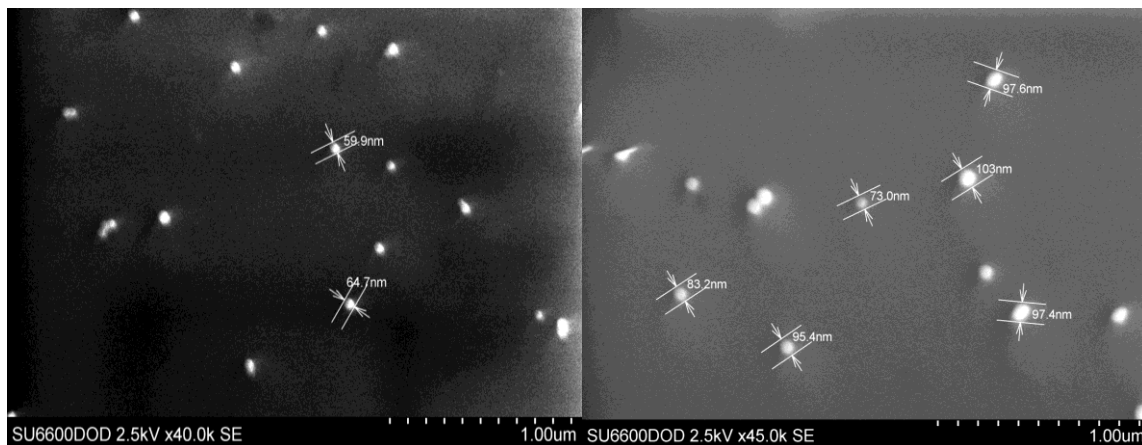
Figure 4.1 (a-b): SEM images of spin coated 50nm(a) and 100nm(b) polystyrene nanoparticles PSNP-NH$_2$. Images were taken on a Hitachi SU 6600 FESEM and low eV (0.8 – 2.5) was used due to the non-conductive nature of the sample.

SEM images were taken to characterise the samples in terms of particle size. In Figure 4.1, little to no aggregation was observed and it can be seen that the particles conform to the size specified by the supplier, with some associated variance. The 50nm sample appeared to show sizes which range from: 45-60nm, while for the nominally 100nm particles, the sizes were seen to vary between: 80-105nm. It should be noted that drift was encountered during the SEM analysis causing blurring of the edges of the sample images, which may affect the accuracy of the size of the particles. However, even with the variance, the clear difference in sizes between the two samples is observable (additional images available: Supplementary Figure: S4.1).

4.4.2 Viability Studies

4.4.2.1 50nm PSNP-NH₂ toxicity:

a)   b)
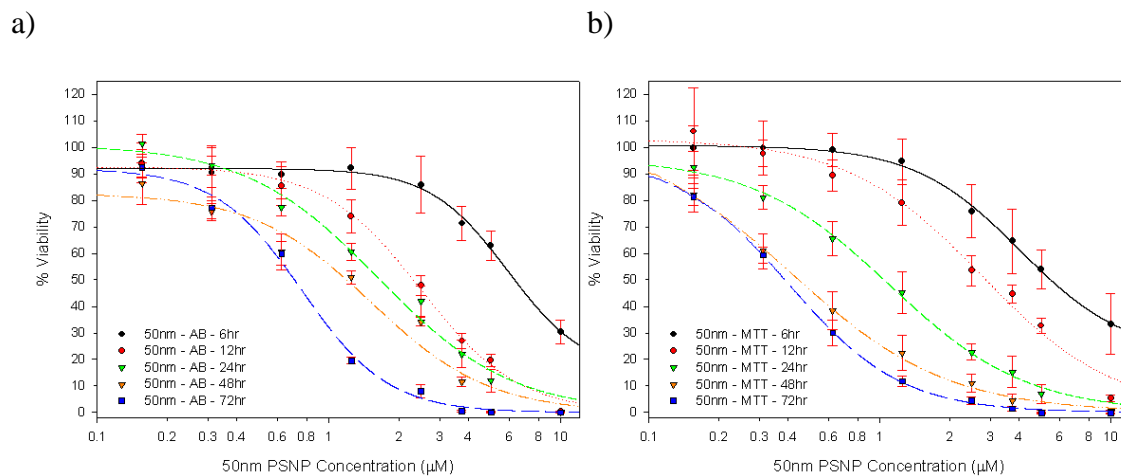
Figure 4.2: Toxicity of the 50nm PSNP-NH$_2$ according to the Alamar Blue (a) and MTT (b) assays. Data points are shown as the mean ± standard deviation. The lines shown are fits generated by SigmaPlot v10.0 for calculation of the EC$_{50}$ values.

As can be seen in Figure 4.2, the 50nm PSNP-NH$_2$ elicit a standard time and dose dependant toxicity, for both the AB (a) and MTT (b) assays. From these results, EC$_{50}$ values were calculated, and are listed in Table 4.1.

Table 4.1: EC$_{50}$ data for 50nm PSNP-NH$_2$ at each time point in HaCaT cells, according to the AB and MTT assay (expressed as µM ± standard error as calculated by SigmaPlot v10.0).

Time point (hours)	50nm PSNP-NH$_2$ AB EC$_{50}$ (µM)	50nm PSNP-NH$_2$ MTT EC$_{50}$ (µM)
6	5.9 ± 1.1	4.0 ± 0.3
12	2.5 ± 0.2	2.8 ± 0.7
24	1.6 ± 0.3	1.1 ± 0.1
48	1.5 ± 0.4	0.42 ± 0.10
72	0.77 ± 0.06	0.41 ± 0.02

Table 4.1 shows that the EC$_{50}$ value for MTT is consistently lower than that for AB, although at 12 hours, the AB shows a slightly lower value than that of the MTT. However, both sets of values are similar and the slight differences noted can be explained due to the different sensitivities associated with each assay to cellular events (*Maher et al., 2014*).

Figure 4.3 shows the fits to the data for each time point 6-72 hours for AB and MTT. This comparison shows that, at the two earliest time points of 6 and 12 hours, the AB and MTT give similar results. No clear difference is seen until 24 hours, at which time MTT shows a higher level of toxicity, which is maintained through the 48 and 72 hour graphs. Again, it can be seen that AB at 12 hours is more sensitive that the MTT, contrary to all other time points, although the difference is small.

Figure 4.3(a-e): AB and MTT dose dependant toxicity results for 50nm PSNP-NH$_2$ in HaCaT cells after 6, 12, 24, 48 and 72hrs. Viability is calculated as the percentage of living cells as compared to an unexposed control. Results are shown as mean ± standard deviation. The solid line represents the EC$_{50}$ curve fit to the AB data and the dotted line represents the EC$_{50}$ curve fit to the MTT data.

a)   b)

Figure 4.4: Toxicity of the 100nm PSNP-NH$_2$ according to the Alamar Blue (a) and MTT (b) assays. The lines shown were generated by SigmaPlot v10.0 for calculation of the EC$_{50}$ values. Data points are shown as the mean ± standard deviation.

The toxicity results for the 100nm PSNP-NH$_2$ show a similar trend to those for the 50nm, increasing toxicity with increasing time and dose. As can be seen from Table 4.2, a similar trend in EC$_{50}$ values to that of 50nm PSNP-NH$_2$ is observed. At 6 hours, both assays generate similar results, and again, as in the case of the 50nm PSNP-NH$_2$, the 12 hour AB response seems to be more sensitive than the MTT. This trend may in fact hold some information on the trafficking/localisation of the nanoparticle within the cell. From 24 to 72 hours, the Alamar Blue shows little change in the reported EC$_{50}$ value, as can be observed in figure 4.4(a). In the case of the MTT assay, the EC$_{50}$ decreases as time and dose increases.

Table 4.2: EC_{50} data for 100nm $PSNP-NH_2$ at each time point in HaCaT cells, according to the AB and MTT assay (expressed as μM ± standard error as calculated by SigmaPlot v10.0).

Time point (hours)	100nm $PSNP-NH_2$ AB EC_{50} (μM)	100nm $PSNP-NH_2$ MTT EC_{50} (μM)
6	7.0 ± 0.3	7.2 ± 2.0
12	3.0 ± 0.6	3.4 ± 0.3
24	1.5 ± 0.3	1.7 ± 0.1
48	1.5 ± 0.2	0.69 ± 0.06
72	1.5 ± 0.2	0.54 ± 0.04

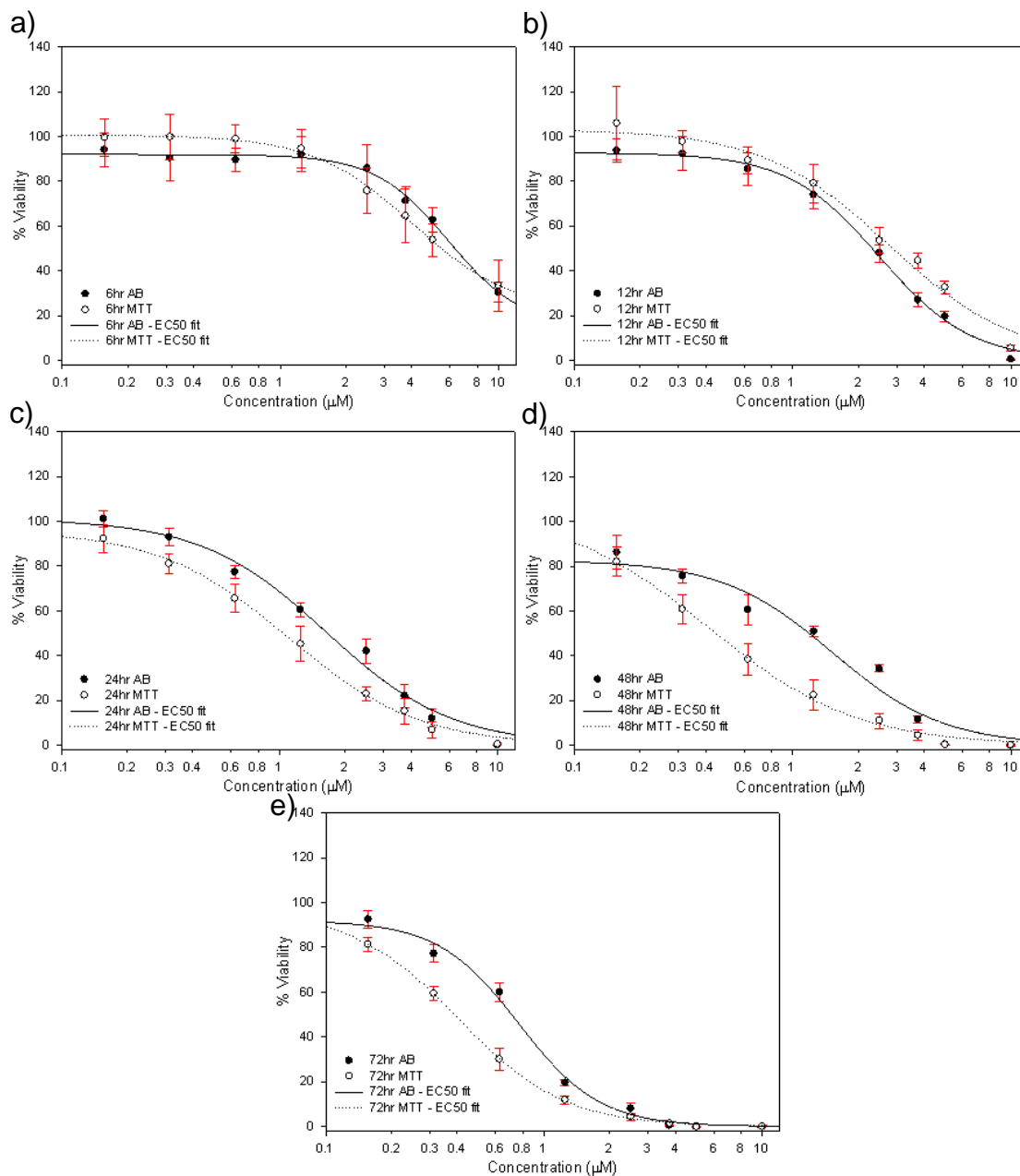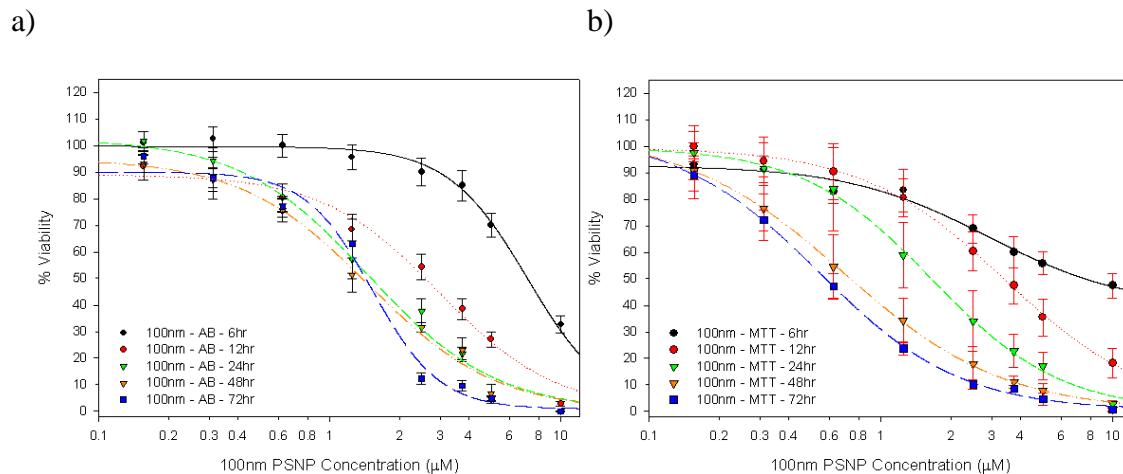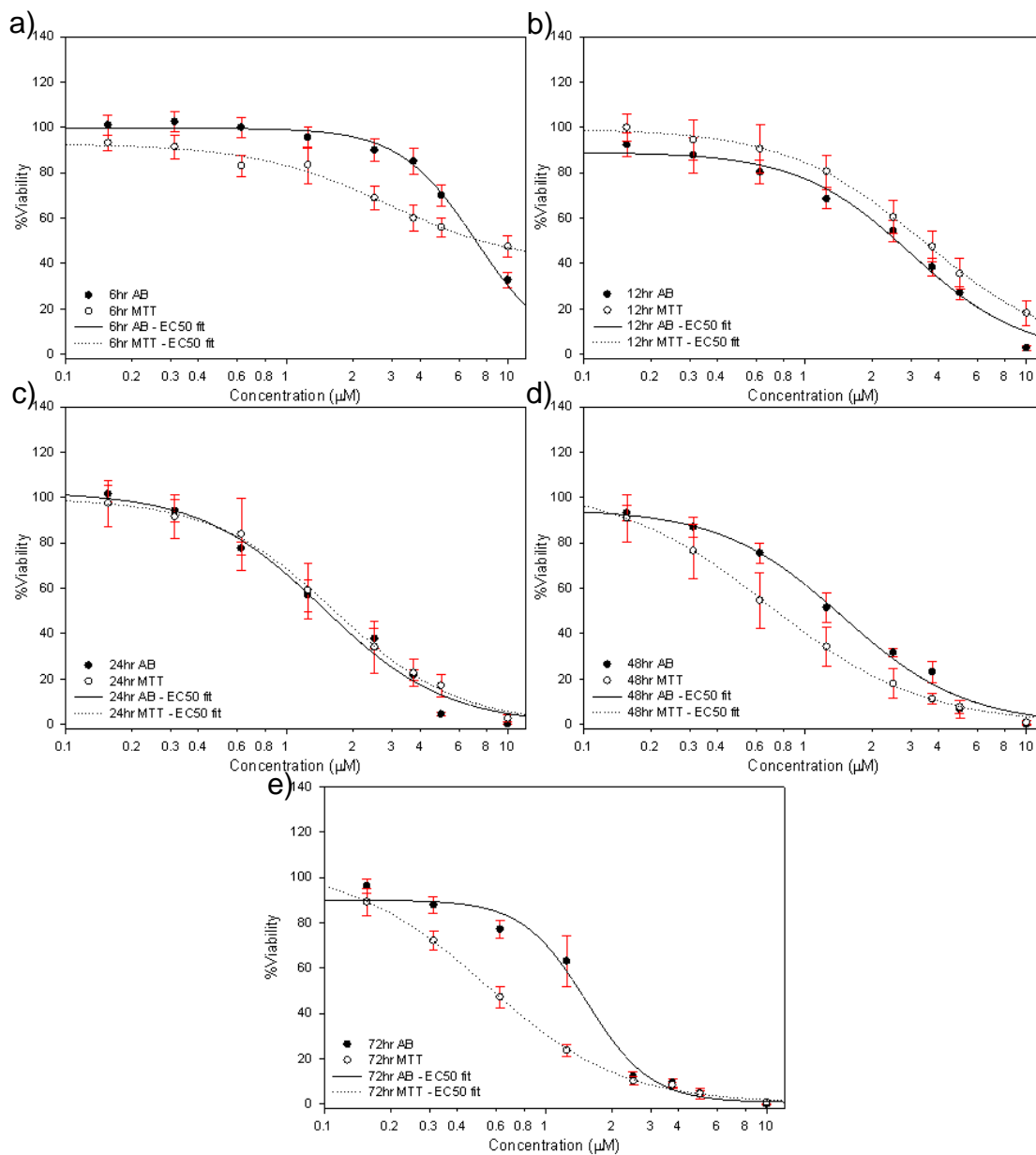Figure 4.5(a-e): AB and MTT dose dependant toxicity results for 100nm PSNP-NH$_2$ in HaCaT cells after 6, 12, 24, 48 and 72hrs. Viability is calculated as the percentage of living cells as compared to an unexposed control. Results are shown as mean ± standard deviation. The solid line represents the EC$_{50}$ curve fit to the AB data and the dotted line represents the EC$_{50}$ curve fit to the MTT data.

Figure 4.5 shows the fits to the 100nm toxicity data for each time point 6-72 hours for AB and MTT. Similar to the case for the 50nm PSNP-NH$_2$, the response to 100nm PSNP-NH$_2$ exposure shows MTT to be more sensitive at all time points except 12 hours, whereby AB presents a lower EC$_{50}$. While the AB response remains unchanged after 24 hours, the MTT continues to decrease.

4.4.2.3 50nm and 100nm Comparison
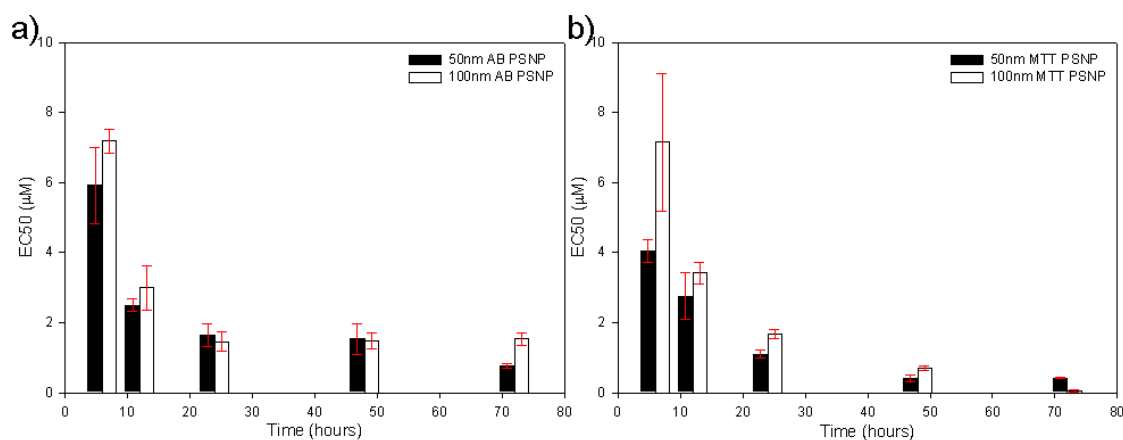
Figure 4.6: Comparison of 50nm and 100nm (a) Alamar Blue (AB) and (b) MTT EC$_{50}$ values as calculated by SigmaPlot V10.0; error bars show ± standard error on the EC$_{50}$ value.

Figure 4.6 shows a comparison of the EC$_{50}$ for 50nm and 100nm PSNP-NH$_2$ for both assays AB and MTT. The AB response shows that, at the earlier time points (6 and 12 hours), 50nm PSNP-NH$_2$ are more toxic than the 100nm, whereafter the toxicity appears to be equivalent from 24 and 48 hours. However, due to the error (standard deviation, as indicated by red bars), it is hard to determine if this increased toxicity is highly significant. At 72 hours it is clear that the 50nm elicit a more toxic response.

The MTT assay shows a more significant difference in the levels of toxicity between the 50nm and 100nm PSNP-NH$_2$. Higher toxicity is observed for 50nm PSNP-NH$_2$ at 6, 12, 24 and 48 hours, at 72 hours there is a slightly increased toxicity of the 100nm PSNP-NH$_2$. However, the EC$_{50}$ at this point for both series is quite low, below 1μM.

4.5 Discussion

The toxicity of aminated polystyrene nanoparticles follows a standard dose-response relationship, whereby increased dose and time results in increased toxicity. For each size (50nm and 100nm), the toxicity data shows that the MTT is a slightly more sensitive assay, yielding lower EC$_{50}$ values at each time point, except for 12 hours, at which time the AB shows an increased sensitivity (Tables: 4.1 and 4.2, Figures: 4.3 and 4.5). While the difference is slight for both assays, it may still be significant in terms of nanoparticle trafficking and localisation. PSNP-NH$_2$ have been previously studied in various cell lines and *Anguissola et al.* (*2014*) have reported 50nm PSNP-NH$_2$ have 24 hour EC$_{50}$ values of approximately 9μg/mL and 42μg/mL in RAW264.7 (mouse macrophage) cells and HEK293 (human kidney) cells, respectively. These EC$_{50}$ values were obtained using the MTS assay which has similar function to the MTT assay, in that both measure cellular mitochondrial activity (*Anguissola et al., 2014*). The EC$_{50}$ obtained from the 24 hour MTT assay in this study was 13.34μg/mL (via conversion of 1.1μM to μg/mL). In another study by *Bannunah et al.* (*2014*) Caco-2 (human intestine) cells showed 50nm and 100nm PSNP-NH$_2$ 4 hour MTS EC$_{50}$ values of 160-175μg/mL, which comes close to the upper range of the 100nm EC$_{50}$ reported here (112μg/mL via conversion from 9.2μM to μg/mL). However, this value was for 6 hours exposure and so it would be expected to be slightly lower

(*Bannunah et al.*, *2014*). Studies by *Dorney* (*2013*) showed that 60nm PSNP-NH$_2$ registered toxicity according to the AB and MTT assays for particle numbers between: 2.5×10^{11} and 5×10^{11} particles/mL for 24, 48 and 72 hours, which agrees with the toxicity based on particle number (see Table 4.3, Discussion section) (*Dorney, 2013*). Although differences between EC$_{50}$ values would be expected and may be due to factors such as different time points and different cell lines, it can be seen that the values obtained in this study are consistent with those reported in other studies. In other aminated nanoparticle studies, specifically with PAMAM dendrimers, the MTT has been seen to be a more sensitive assay (*Mukherjee et al., 2010-A and B*). This is due to the known routes of interaction of PAMAM dendrimers within the cell. After endocytosis of the PAMAM dendrimers, endosomolysis can occur, releasing the nanoparticles into the cytosol, from whence translocation to the mitochondria is observed (*Watson et al., 2005*). MTT is an assay based on mitochondrial activity (*Mosmann, 1983, Denizot and Lang, 1986* and *Hansen et al., 1989*) and the higher sensitivity of the MTT assay compared to AB reflects this systematic sequence of events (*Maher et al., 2014*). However, in the case of PSNP-NH$_2$, the method of action and cellular localisation are slightly different. Aminated polystyrene nanoparticles are also taken up by the endocytotic mechanism, but, endosomolysis has not been observed to occur at this early stage. The endosome transfers to a lysosome and subsequently, due to a combination of the proton sponge effect and the build up and retention of neutral and phospholipids in the lysosome, damage occurs, leading to lysosomolysis, the breaching of the lysosome and release of the PSNP-NH$_2$ (*Wang et al., 2013*).

The trafficking and progression of the nanoparticle in the endosomes has been studied by Efeoglu *et al.* (*2015*) for 40nm carboxy-PSNP (PSNP-COOH). PSNP-COOH are not as toxic as the aminated counterparts and are therefore better candidates for localisation and trafficking studies. Initially, endocytosis occurs, bringing the particles into the early endosomes, observed at 4 hours. These progress to late endosomes and then onto lysosomes at 12 hours, and are finally localised in the endoplasmic reticulum at 24 hours (*Efeoglu et al., 2015*). It has also been observed that the carboxylated polystyrene nanoparticles are transported more slowly that the neutral polystyrene nanoparticles of equivalent sizes (*Dorney, 2013*) due to their effective surface charge. It is also known that aminated nanoparticles, in general, are endocytosed rapidly, due to their effective positive surface charge (*Fröhlich, 2012*). However, it may be the case that, at the 12 hour time point, lysosomolysis occurs, releasing the $PSNP-NH_2$ and several other cytotoxic components of the lysosome into the cytosol. AB is a much less specific assay (compared to MTT) and measures cellular viability based on the overall activity of the cytosolic environment (*O' Brien et al., 2000*) and the breaching and release of the lysosomal content would initially affect the cytosol rather than any specific organelle, and so, more prominent changes would be noted for AB response.

In comparing the toxic response of the two $PSNP-NH_2$ nanoparticle sizes, it is important to note that although the EC_{50} value in Molar doses are similar, they are very different when expressed as particle number. When expressed in this form, per particle, the 100nm are considerably more toxic as can be seen in Table 4.3 and Figure 4.7 (a and b).

Table 4.3: EC_{50} data for 50nm and 100nm PSNP-NH_2 at each time point in HaCaT cells, according to the AB and MTT assay (expressed as particle number (± standard error), based on the EC_{50} data obtained by SigmaPlot v10.0^{TM} and calculated in accordance with manufacturers guidelines).

	50nm PSNP-NH_2 EC_{50} (Particle number x10^{11})		100nm PSNP-NH_2 EC_{50} (Particle number x10^{11})	
Time Point (hrs)	Alamar Blue	MTT	Alamar Blue	MTT
06	10.44 ± 1.95	7.08 ± 0.53	1.56 ± 0.07	1.61 ± 0.45
12	4.42 ± 0.35	4.96 ± 1.24	0.67 ± 0.13	0.76 ± 0.07
24	2.83 ± 0.53	1.95 ± 0.18	0.34 ± 0.07	0.38 ± 0.02
48	2.65 ± 0.71	0.74 ± 0.18	0.34 ± 0.04	0.15 ± 0.01
72	1.36 ± 0.11	0.73 ± 0.04	0.34 ± 0.04	0.12 ± 0.01
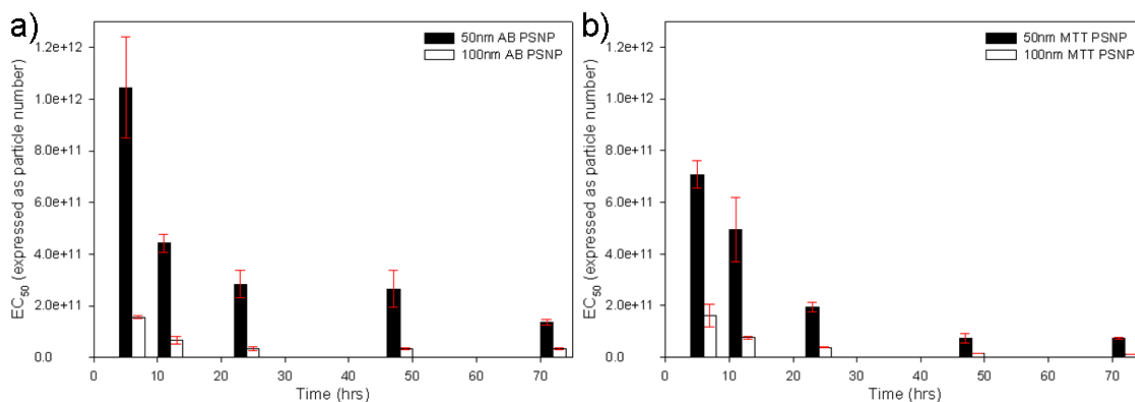
Figure 4.7: Comparison of 50nm and 100nm (a) Alamar Blue (AB) and (b) MTT EC_{50} values expressed as particle number; error bars were calculated based on the standard error of the EC_{50} value.

Other studies have also reported similar findings. *Bannunah et al.* (*2014*) found that 50nm and 100nm PSNP-NH$_2$ (4 hour MTS assay) gave similar EC$_{50}$ values in μg/mL. However, when this was converted to particle number (particles/mL), the 100nm particles were much more toxic (*Bannunah et al.*, *2014*). This highlights the need for awareness when choosing a dose metric and how the values obtained should be analysed.

The extensive studies of PAMAM toxicity demonstrated that the number of surface amine groups is a key parameter in the determination of nanoparticle toxicity (*Naha et al., 2009 and 2010, Mukherjee et al., 2010-A and B,* and *Mukherjee and Byrne, 2013*). It would therefore be expected that the 100nm aminated PSNP-NH$_2$ would be more toxic, due to the four times larger surface area, compared to the 50nm. No information regarding the degree of surface functionalisation was available from the manufacturers (*Sigma Aldrich, personal communication, 21st April 2015*). Therefore, ^{1}H NMR was carried out on the 50nm and 100nm PSNP-NH$_2$ and also on 100nm PSNP-neu (as a control) and the results are shown in Section 4.9: Supplementary Information (Supplementary Figure: S4.2). For 50nm and 100nm aminated nanoparticles, a clear peak is present at 2.939 ppm, this peak is absent in the 100nm unmodified sample and thus it was taken to be the chemical shift generated by the surface amines. Critically, when measured under identical Molar concentrations, the peak intensities for both 50nm and 100nm PSNP- NH$_2$ matched in chemical shift and intensity, indicating that both nanoparticles have a similar number of amino groups on the surface per Molar concentration. However, when this Molar quantity is converted to particle number, there is a larger difference. 100nm PSNP-NH$_2$ has a surface area four times larger than that of 50nm PSNP-NH$_2$. Therefore, it would be expected that, having the same number of amino groups per unit surface area, the overall amount present on the

100nm particle would be four times larger than on the 50nm. However, based on the particle number calculations (*Sigma-Aldrich, 2015*), it would appear that, at equivalent particle concentration, the 100nm has about 8 times the effective surface charge compared to 50nm, consistent with the significantly higher toxic response when expressed per particle (Table 4.3 and Figure 4.7).

The toxic responses to PSNP-NH$_2$ can be further elucidated using a numerical simulation approach. Previously, the *in vitro* toxicity of cationic PAMAM dendrimers (generations 4-6) were modelled using a set of ordinary differential equations applied to the systematic sequence of events leading to toxicity (*Maher et al., 2014*). The model identified two key nanoparticle dependent parameters which mediate the toxic response: the rate constant of endocytosis (k_{endo}) and the rate constant of generation of ROS.

Equation 4.1 describes the dose (D) dependant uptake of nanoparticles at a rate constant, k_{endo}, and the subsequent changes of that population based on the rate constant of cellular replication (k_λ) (*Salvati et al., 2011*). As the dose (D) is expressed as the Molar dose, for ease of comparison with the experimental data, N_{endo} is an expression of the Molar quantity (number per unit volume) of endocytosed dendrimer nanoparticles. In subsequent equations, the term "N" is used to denote the equivalent quantity denoted by the subscript text that follows.

$$\frac{dN_{endo}}{dt} = k_{endo} \cdot D - k_\lambda \cdot N_{endo}(t)$$

Equation 4.1

For a cell duplication time of 24hrs, k_λ will be $0.69/24\text{hr}^{-1}$.

The subsequent increase in levels of ROS, N_{ROS} can be simulated according to Equation 4.2:

$$\frac{dN_{ROS}}{dt} = k_A \cdot G^* \cdot (N_{endo}(t)^A) \cdot (N_{Source}(t)^B) - k_q \cdot N_{ROS}(t) \cdot N_{GSH}(t)$$

Equation 4.2

N_{GSH} is the amount of the intracellular antioxidant, GSH, and k_q is the rate constant at which the GSH is able to quench the ROS produced. The rate constant k_A describes the interaction of the nanoparticles and the source of ROS, and the values for A and B are empirical constants, whereby the dependence on the number of surface amino groups, N_{amg}, is contained within A and a value of $B=3$ was determined to produce the most faithful reproduction of the experimental responses (*Maher et al., 2014*):

$$A = \left(\frac{N_{amg}}{64} \right)^{0.75}$$

Several studies of PAMAM dendrimer toxicity have demonstrated a systematic correlation of the oxidative stress and increase in ROS levels with dendrimer generation and therefore N_{amg} (*Naha et al., 2009 and 2010, Mukherjee et al., 2010-A and B,* and *Mukherjee and Byrne, 2013*). In the simulation of this toxic response, this was accounted for by the generation dependent term $k_A \cdot G^*$:

$$G^* = \left(\frac{1}{N_{amg}^{0.25}} \right)$$

Which is used again for the simulation of response to PSNP-NH$_2$.

The viability for the MTT assay is simulated based on the loss of mitochondrial membrane potential (expressed in the model as k_{MMP}) and is calculated via the equation:

$$\frac{dN_{MMP}}{dt} = k_{MMP} \cdot N_{ROS}(t) - k_{TNF} \cdot N_{MMP}(t)$$

Equation 4.3

In Equation 4.3: N_{MMP} represents the population of cell where mitochondrial membrane potential is in decay, k_{MMP} is the rate constant at which this decay is occurring, the term: $k_{TNF}.N_{MMP}(t)$ accounts for the amount of cells progressing to the next step in the toxic cascade.

This is then converted to a % Viability via the equation:

$$\frac{dN_V}{dt} = k_{Rec}.N_{MMP}(t)^b.N_V(t) - k_V.N_{MMP}(t).N_V(t)$$

Equation 4.4

In Equation 4.4: N_V denotes the population of viable cells, k_V denotes the rate constant at which apoptosis occurs and k_{rec} is a recovery rate constant for cells, b is a power law dependence and all other parameters are the same as previously defined (*Maher et al., 2014*).

Figure 4.8 shows the dose dependant cytotoxicity of the 50nm (black symbols and solid line) and 100nm (white symbols and dotted line) PSNP-NH$_2$ as recorded by the MTT assay at 24 hrs. The lines shown are the simulated data from the model and, as can been seen, the predicted data matches well the experimental points for both sizes. A full list of parameters and values used for these simulations is listed in Section 4.9: Supplementary Information of this article (Supplementary information: Table: S4.3).
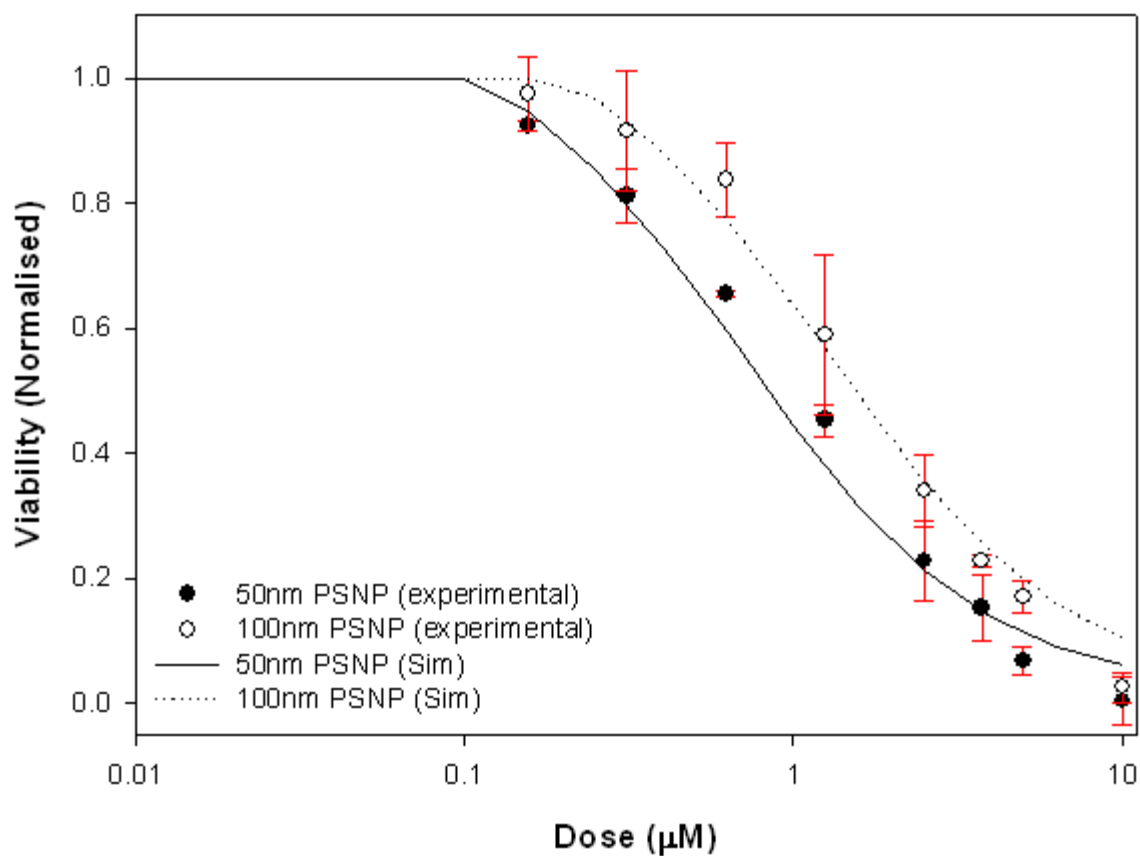
Figure 4.8: Experimental (symbols) and simulated (lines) dose dependent HaCaT cell

viability at 24 hrs, for 50nm (●) and 100nm (○) PSNP-NH$_2$ as measured using the MTT

assay. Error bars are the standard deviation of the experimental data.
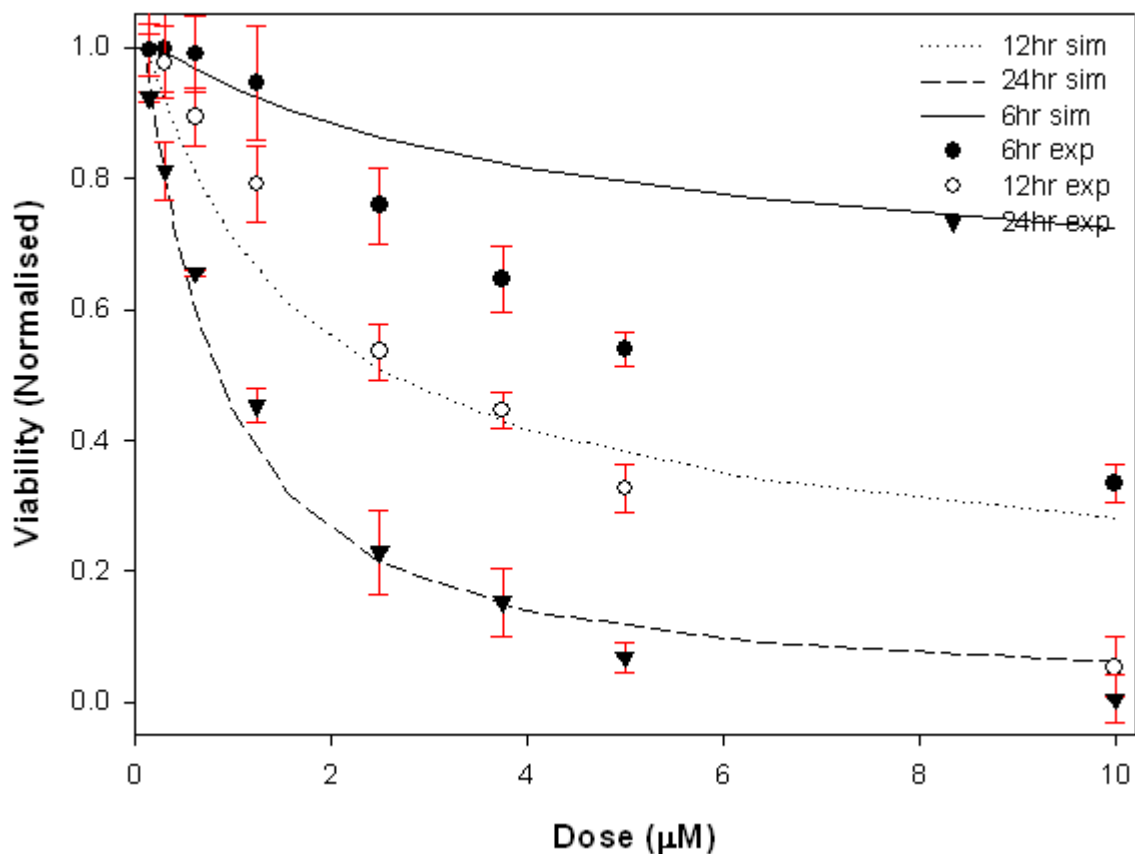
Figure 4.9: Experimental (symbols) and simulated (lines) dose dependent HaCaT cell viability at 6 ($\bullet$), 12($\circ$) and 24($\blacktriangledown$) hours, for 50nm PSNP-NH$_2$ as measured using the MTT assay. Error bars are the standard deviation of the experimental data.

In Figure 4.9, the dose dependant cytotoxicity of the HaCaT cells exposed to 50nm PSNP-NH$_2$ is shown for the exposure times: 6, 12 and 24 hours. The simulation of 12 hours (dotted black line) and 24 hours (dashed black line) faithfully reproduce the dose dependant experimental data quite well. However, for the 6 hour simulation (solid black line), only the initial doses match the model. Although several factors may affect this, it is most likely due to the fact that this model was initially designed to predict PAMAM dendrimer toxicity and while polystyrene is also toxic, the progression of the toxic cascade may be different for

each particle type (for example: between 0 – 6 hours the PAMAM dendrimers are seen to undergo endosomolysis, this does not occur for polystyrene until a later time point, possibly 12 hours, as indicated by the change in sensitivity of the AB assay results) (*Mukherjee et al., 2010-A and B*, *Wang et al., 2013* and *Efeoglu et al., 2015*). Therefore, differences in the earlier time points are not completely unexpected.

Most notably, however, with the exception of the expression of k_{endo} in Equation 4.1, all parameters used in the simulations of Figure 4.8 and 4.9 are identical to those used in the model for PAMAM generation dependent toxic responses (*Maher et al., 2014*).

For the case of PAMAM dendrimers, k_{endo}, took the form, $k_{endo}.(N_{amg})^c$, where c=0.25. N_{amg} systematically increases with dendrimer generation and is intimately linked with the surface reactivity, but also the particle size (*Maher et al., 2015*). Over the range of dendrimers examined, (G4-G6) the diameter increases only slightly, and a power law dependence of the N_{amg} versus diameter of form $D \propto N_{amg}^{0.25}$ can be seen. This term is therefore interpreted as a size dependence of the endocytosis rate. Therefore, the different toxicity profiles of each PSNP-NH$_2$ size particle were simulated according to different rates of endocytosis, being $3.795hr^{-1}$ for 50nm PSNP-NH$_2$ and $2.400hr^{-1}$ for 100nm PSNP-NH$_2$.

In the study of PAMAM dendrimers, the dependence of the toxic response on the surface chemistry parameter has been explored, as, for each generation of dendrimer, the number of amino groups doubled and so N_{amg} increased in a systematic way (*Naha et al., 2009 and 2010, Mukherjee et al., 2010-A and B,* and *Mukherjee and Byrne, 2013*). In comparison to dendrimers, the number of surface amino groups is not a well-defined parameter in PSNP-NH$_2$. However, NMR indicated that it was approximately the same, per Molar

concentration, for both sets of particles. A value of N_{amg} = 58 amino groups/μM for both sizes of particle provided a faithful simulation of the data.

The higher rate of endocytosis of the 50nm particles is consistent with studies by Chithrani *et al.* (*2006*) which have shown that optimal uptake by endocytosis for gold nanoparticles occurs at 50nm (*Chithrani et al., 2006*). It is generally accepted that, as nanoparticle size increases, endocytosis becomes less efficient as an uptake mechanism (*Chithrani et al., 2006* and *Lunov et al., 2011*). Since the process of endocytosis is equivalent for many cell types, it could be assumed that, for the case of 50nm PSNP-NH$_2$, this size dependence on uptake may also be observed.

It is also interesting to note that other studies have previously observed links between nanoparticle size and changes in uptake mechanisms. A study by Khalid *et al.* (*2015*), demonstrated changes in the size dependant uptake of nanoparticles at the lower end of the size scale, whereby using low generation Poly (propylene imine) (PPI) dendrimers, at approximately PPI G3, the uptake beings to shift from the active endocytosis to a more passive diffusive mechanism, dramatically reducing the toxicity, as the particles being to exhibit behaviour more associated with molecules as opposed to nanopolymers (*Khalid et al., 2015*).

Notably, although the endocytosis rate is higher for the smaller 50nm particle, the toxic response per nanoparticle is substantially higher for the larger, 100nm particle. This is consistent with the significantly higher surface functionalization of the larger, 100nm particles and the identification of the ROS generation as the key MIE in the toxic response.

Critically, in the case of endocytosed aminated nanoparticles, an identical numerical model can be employed to simulate the toxic response. For the same cell line, the extension of the model, including the MIE and AOP, to a new set of nanoparticles requires only information on the nanoparticle size and number of surface groups. It has also been demonstrated that the model can be extended to other cell lines by adjusting the cell specific rates, such those associated with the intracellular antioxidant levels (*Maher et al., 2014*).

4.6 Conclusions

The study demonstrates that the numerical simulation approach previously demonstrated for PAMAM dendrimers is readily extendable to describe the cytotoxic responses of different sizes of aminated polystyrene nanoparticles. Only the nanoparticle endocytosis rate is seen to vary, consistent with other reports of size dependent nanoparticle uptake. However, both types of cationic nanoparticle elicit a toxic response according to the same paradigm of oxidative stress, identified as the Molecular Initiating Event, potentially describable by quantitative structure property relationships. Notably, the subsequent cascade of cellular events are confirmed to be independent of nanoparticle type or size, supporting approaches to toxicology modelling according to strategies such as that of Adverse Outcome Pathways, and broadening the model in a systems biology approach could be of significant benefit to design strategies in nanomedicine.

4.7 Acknowledgements

4.8 References

- Anguissola, S., Garry, D., Salvati, A., O'Brien, P.J. and Dawson, K.A. 2014. High content analysis provides mechanistic insights on the pathways of toxicity induced by amine-modified polystyrene nanoparticles. *PLoS One.* **9**(9), e108025 (doi: 10.1371/journal.pone.0108025).

- Bannunah, A.M., Vllasaliu, D., Lord, J. and Stolnik, S. 2014. Mechanisms of nanoparticle internalization and transport across an intestinal epithelial cell model: effect of size and surface charge. *Mol. Pharm.* **11**(12): 4363-4373.

- Bexiga, M.G., Varela, J.A., Wang, F., Fenaroli, F., Salvati, A., Lynch, I., Simpson, J.C. and Dawson, K.A. (2011). Cationic nanoparticles induce caspase 3-, 7- and 9-mediated cytotoxicity in a human astrocytoma cell line. *NanoToxicology,* **5**(4): 557–567.

- Chithrani, B.D., Ghazani, A.A. and Chan, W.C. 2006. Determining the size and shape dependence of gold nanoparticle uptake into mammalian cells. *Nano Lett.* **6**(4): 662-668.

- Clark, K.A., White, R.H. and Silbergeld, E. K. 2011. Predictive models for nanotoxicology: Current challenges and future opportunities. *Regul. Toxicol. Pharm.* **59**(3): 361-512.

- De Jong, W. H. and Borm, P.J.A. 2008. Drug delivery and nanoparticles: Applications and hazards. *Int. J. Nanomedicine.* **3**(2): 133–149.

- Denizot, F. and Lang, R. 1986. Rapid colorimetric assay for cell growth and survival: Modifications to the tetrazolium dye procedure giving improved sensitivity and reliability. *J. Immunol. Methods.* **89**(2): 271-277.

- des Rieux, A., Fievez, V., Garinot, M., Schneider, Y.J. and Préat, V. 2006. Nanoparticles as potential oral delivery systems of proteins and vaccines: a mechanistic approach. *J. Control. Release,* **116**(1): 1-27.

- Donaldson, K., Stone, V., Tran, C.L., Kreyling, W. and Borm, P.J.A. 2004. Nanotoxicology. *Occup. Environ. Med.* **61**(9): 727-728.

- Dorney, J. (2013) Polystyrene: A Potential Standard for Developing *In Vitro* Cellular Tracking Methods for Nanotoxicology. *Thesis (PhD)*, Dublin Institute of Technology: 2012. Dublin: DIT.

- Dorney, J., Bonnier, F., Garcia, A., Casey, A., Chambers, G. and Byrne, H.J. 2012. Identifying and Localizing Intracellular Nanoparticles Using Raman Spectroscopy. Analyst, 137(5): 1111-1119.

- Duncan, R. and Izzo, L. 2005. Dendrimer biocompatibility and toxicity. *Adv. Drug. Deliv. Rev.* **57**(15): 2215– 2237.

- Efeoglu, E., Keating, M., McIntyre, J., Casey, A. and Byrne, H.J. 2015. Determination of nanoparticle localisation within subcellular organelles *in vitro* using Raman spectroscopy. Anal. Methods, 7(23): 1759-9660.

- Eichman, J.D., Bielinska, A.U., Kukowska-Latallo, J.F. and Baker, J.R.Jr. 2000. The use of PAMAM dendrimers in the efficient transfer of genetic material into cells. *J. Pharm. Sci. Technol*. **3**(7): 233-245.

- Fröhlich, E. 2012. The role of surface charge in cellular uptake and cytotoxicity of medical nanoparticles. *Int. J. Nanomed.* **7**(2012): 5577–5591.

- Hansen, M.B., Nielsen, S.E. and Berg, K. 1989. Re-examination and further development of a precise and rapid dye method for measuring cell growth/cell kill. *J. Immunol. Methods.* **119**(2): 203-210.

- Hong, S., Bielinska, A.U., Mecke, A., Keszler, B., Beals, J.L., Shi, X., Balogh, L., Orr, B.G., Baker, J.R.Jr and Banaszak Holl, M.M. 2004. Interaction of poly(amidoamine) dendrimers with supported lipid bilayers and cells: hole formation and the relation to transport. *Bioconjugate Chem.* **15**(4): 774–782.

- Khalid, H., Mukherjee, S.P., O'Neill, L. and Byrne, H.J. 2016. Structural dependence of the *In vitro* cytotoxicity, oxidative stress and uptake mechanisms of Poly (propylene imine) dendritic nanoparticles. *J. Appl. Toxicol.*, **36**(3), 464–473.

- Kitchens, K.M., Foraker, A.B., Kolhatkar, R.B., Swaan, P.W., Ghandehari, H. 2007. Endocytosis and interaction of poly (Amidoamine) dendrimers with Caco-2 cells. *Pharmaceut. Res.* **24**(11): 2138–2145.

- Kloet, S.K., Walczak, A.P., Louisse, J., van den Berg, H.H., Bouwmeester, H., Tromp, P., Fokkink, R.G., Rietjens, I.M. 2015. Translocation of positively and negatively charged polystyrene nanoparticles in an *in vitro* placental model. *Toxicol. In Vitro.* **29**(7): 1701-1710.

- Lunov, O., Syrovets, T., Loos, C., Beil, J., Delacher, M., Tron, K., Nienhaus, G.U., Musyanovych, A., Mailänder, V., Landfester, K. and Simmet, T. 2011. Differential uptake of functionalized polystyrene nanoparticles by human macrophages and a monocytic cell line. *ACS Nano,* **5**(3): 1657-1669.

- Maher, M.A., Khalid, H. and Byrne, H.J. 2016. Acellular reactivity of polymeric dendrimer nanoparticles as an indicator of oxidative stress *in vitro*. *Anal. Bioanal. Chem.* **408**(3): 695-703.

- Maher, M.A., Naha, P.C., Mukerjee, S.P. and Byrne, H.J. 2014. Numerical simulations of *in vitro* nanoparticle toxicity – the case of Poly(amido amine) dendrimers. *Toxicol. In Vitro.* **28**(8): 1449-1460.

- Mosmann, T. 1983. Rapid colorimetric assay for cellular growth and survival: Application to proliferation and cytotoxicity assays. *J. Immunol. Methods.* **65**(1): 55-63.

- Mukherjee S.P. and Byrne, H.J. 2013. Polyamidoamine Dendrimer Nanoparticle Cytotoxicity, Oxidative Stress, Caspase Activation and Infammatory Response: Experimental Observation and Numerical Simulation. *Nanomed. Nanotech. Biol. Med.* **9**(2): 202-211.

- Mukherjee, S.P., Davoren, M. and Byrne, H.J. 2010-A. *In vitro* mammalian cytotoxicological study of PAMAM dendrimers - towards quantitative structure activity relationships. *Toxicol. in Vitro,* **24**(1): 169-177.

- Mukherjee, S.P., Lyng, F.M., Garcia, A., Davoren, M. and Byrne H.J. 2010-B. Mechanistic studies of *in vitro* cytotoxicity of Poly(amidoamine) dendrimers in mammalian cells. *Toxicol. Appl. Pharmacol.* **248**(3): 259–268.

- Naha, P.C., Davoren, M., Casey, A. and Byrne H.J. 2009. An Ecotoxicological Study of Poly (amido amine) Dendrimers - Toward Quantitative Structure Activity Relationships. *Env. Sci. Technol.* **43**(17): 6864–6869.

- Naha, P.C., Davoren, M., Lyng, F.M. and Byrne, H.J. 2010. Reactive Oxygen Species (ROS) induced cytokine production and cytotoxicity of PAMAM dendrimers in J774A.1 cells. *Toxicol. Appl. Pharmacol.* **246**(1-2): 91-99.

- O'Brien, J., Wilson, I., Orton, T. and Pognan, F. 2000. Investigation of the Alamar Blue (resazurin) fluorescent dye for the assessment of mammalian cell cytotoxicity. *Eur. J. Biochem.* **267**(17): 5421-5426.

- Oomen, A.G., Bos, P.M.J., Fernandes, T.F., Hund-Rinke, K., Boraschi, D., Byrne, H.J., Aschberger, K., Gottardo, S., von der Kammer, F., Kühnel, D., Hristozov, D., Marcomini, A. and Migliore, L. 2014. Concern-driven integrated toxicity testing

strategies for nanomaterials - Report of the NanoSafety Cluster Working Group 10. *NanoToxicology,* **8**(3), 334-348.

- Organisation for Economic Co-Operation and Development (OECD): Guidance Document On Developing and Assessing Adverse Outcome Pathways, *OECD, ENV/JM/MONO(2013)6*, 2013.

- Project on Emerging Nanotechnologies (PEN), 2015. Accessed on 15-10-2015 – Available at: http://www.nanotechproject.org/

- Ruenraroengsak, P., Novak, P., Berhanu, D., Thorley, A.J., Valsami-Jones, E., Gorelik, J., Korchev, Y.E. and Tetley, T.D. (2012). Respiratory epithelial cytotoxicity and membrane damage (holes) caused by amine-modified nanoparticles. *NanoToxicology,* **6**(1): 94–108.

- Salvati, A., Aberg, C., dos Santos, T., Varela, J., Pinto, P., Lynch, I. and Dawson, K.A. 2011. Experimental and theoretical comparison of intracellular import of polymeric nanoparticles and small molecules: toward models of uptake kinetics. *Nanomed. Nanotechnol. Biol. Med.* **7**(6): 818–826.

- Sigma-Aldrich, 2015. Product Information Guide for Polystyrene Latex Beads. Available at: *http://www.sigmaaldrich.com/content/dam/sigma-*

aldrich/docs/Sigma/Product_Information_Sheet/2/lb1pis.pdf, Last Accessed: December 2015.

- Wang, F., Bexiga, M.G., Anguissola, S., Boya, P., Simpson, J.C., Salvati, A. and Dawson K.A. 2013. Time resolved study of cell death mechanisms induced by amine-modified polystyrene nanoparticles. *Nanoscale,* **5**(22):10868-10876.

- Wang, F., Yu, L., Salvati, A. and Dawson, K.A. (2013). The biomolecular corona is retained during nanoparticle uptake and protects the cells from the damage induced by cationic nanoparticles until degraded in the lysosomes. *Nanomedicine,* **9**(8): 1159–1168.

- Watson, P., Jones, A.T. and Stephens, D.J. 2005. Intracellular trafficking pathways and drug delivery: fluorescence imaging of living and fixed cells. *Adv. Drug Deliver. Rev.* **57**(1): 43-61.

- Xia, T., Kovochich, M., Brant, J., Hotze, M., Sempf, J., Oberley, T., Sioutas, C., Yeh J.I., Wiesner, M.R. and Nel, A.E. 2006. Comparison of the abilities of ambient and manufactured nanoparticles to induce cellular toxicity according to an oxidative stress paradigm. *Nano Lett.* **6**(8): 1794-1807.

- Xia, T., Kovochich, M., Liong, M., Zink, J.I. and Nel, A.E. (2008). Cationic polystyrene nanosphere toxicity depends on cell-specific endocytic and mitochondrial injury pathways. *ACS Nano,* **2**(1): 85–96.

- Yacobi, N.R., Demaio, L., Xie, J., Hamm-Alvarez, S.F., Borok, Z., Kim, K.J. and Crandall, E.D. 2008. Polystyrene nanoparticle trafficking across alveolar epithelium. *Nanomedicine,* **4**(2): 139-145.

4.9 Supplementary Information for Chapter 4:

4.9.1 Equation used for calculation of particle numbers

$$\text{Particles/mL} = \frac{(6 \times 10^{10})(\rho_{latex})(\%\text{Solids})}{(\pi)(\rho_{BP})(d^3)}$$

Equation S4.1

Where ρ_{latex} is the density of latex (1.005g/mL), ρ_{BP} is the density of bulk polymer (polystyrene; 1.05g/mL), % solids is the percentage solids in the suspension and d is the diameter of the polystyrene in μm (0.05μm for 50nm PSNP-NH$_2$, 0.1μM for 100nm PSNP-NH$_2$ and PSNP-neu) (*Sigma-Aldrich, 2015*).

4.9.2 EC$_{50}$ and R^2 data for 50nm and 100nm PSNP-NH$_2$ AB and MTT Assays.

Table S4.1: P-values calculated from the fitting of EC$_{50}$ data for 50nm and 100nm PSNP-NH$_2$ at each time point in HaCaT cells, according to the AB and MTT assay as calculated by SigmaPlot v10.0.

	Alamar Blue Assay		MTT Assay	
Time (Hrs)	50nm PSNP	100nm PSNP	50nm PSNP	100nm PSNP
6	0.0054	<0.0001	0.0002	0.0206
12	0.0002	0.0089	0.0139	0.0004
24	0.0065	0.0071	0.0005	0.0002
48	0.0250	0.0031	0.0145	0.0003
72	0.0003	0.0008	<0.0001	<0.0001

Table S4.2: R^2 values calculated from the fitting of EC_{50} data for 50nm and 100nm PSNP-NH$_2$ at each time point in HaCaT cells, according to the AB and MTT assay as calculated by SigmaPlot v10.0.

	Alamar Blue Assay		MTT Assay	
Time (Hrs)	50nm PSNP	100nm PSNP	50nm PSNP	100nm PSNP
6	0.998	0.975	0.996	0.967
12	0.993	0.972	0.975	0.998
24	0.977	0.973	0.994	0.996
48	0.937	0.982	0.993	0.998
72	0.990	0.977	0.999	0.998

4.9.3 SEM images for 50nm and 100nm PSNP-NH$_2$
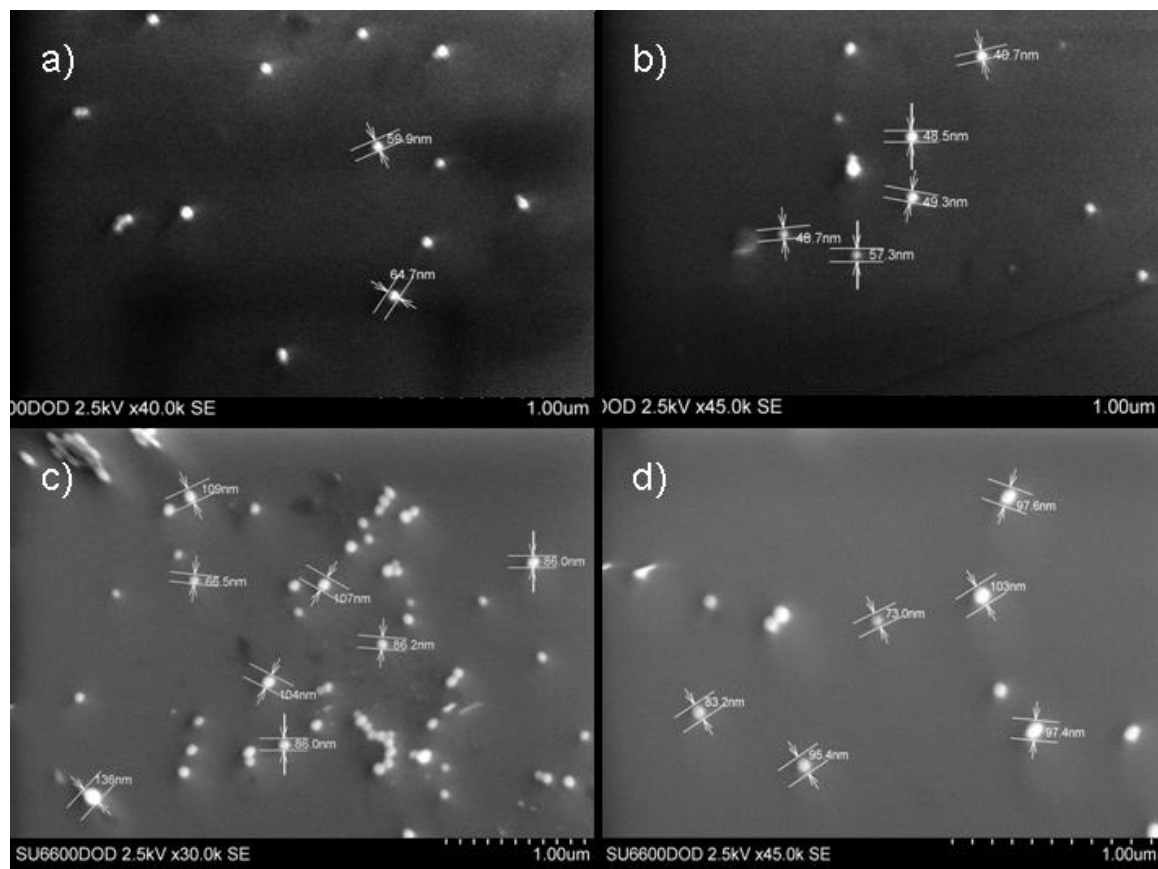
Figure S4.1: Additional SEM images of spin coated 50nm(a and b) and 100nm(c and d) polystyrene nanoparticles PSNP-NH$_2$. Images were taken on a Hitachi SU 6600 FESEM and low eV (0.8 – 2.5) was used due to the non-conductive nature of the sample.
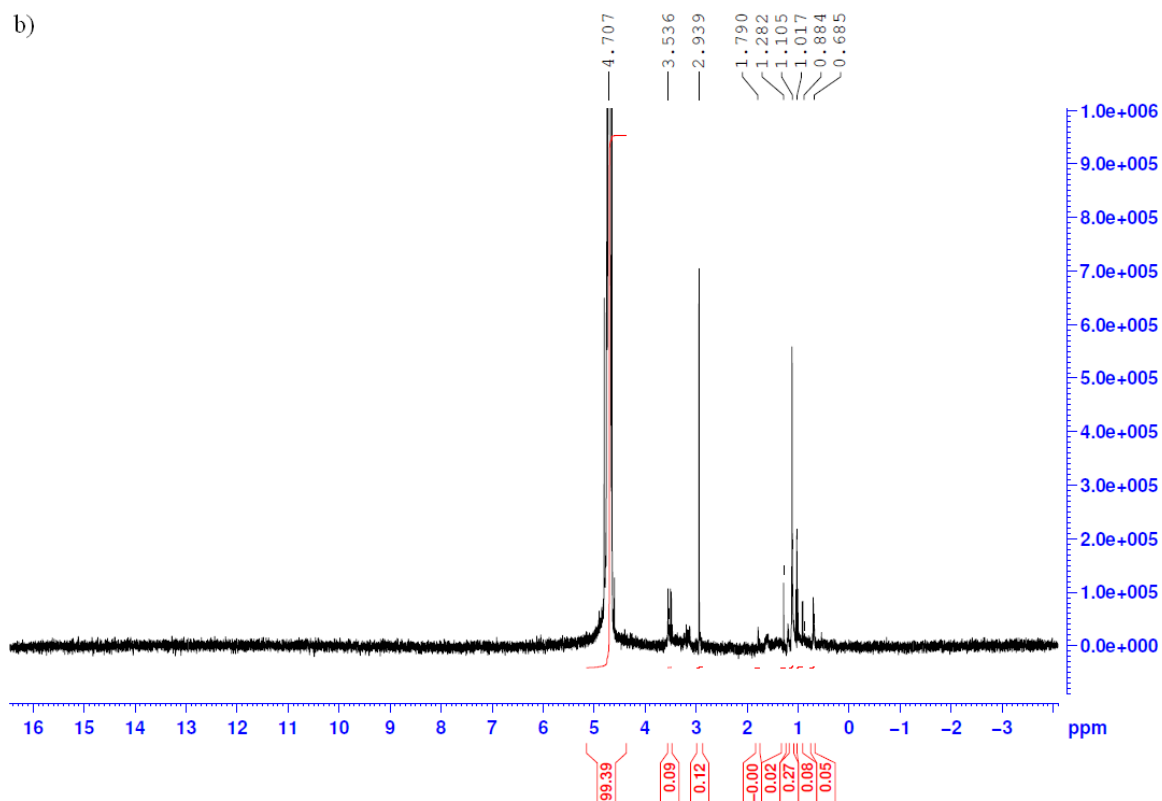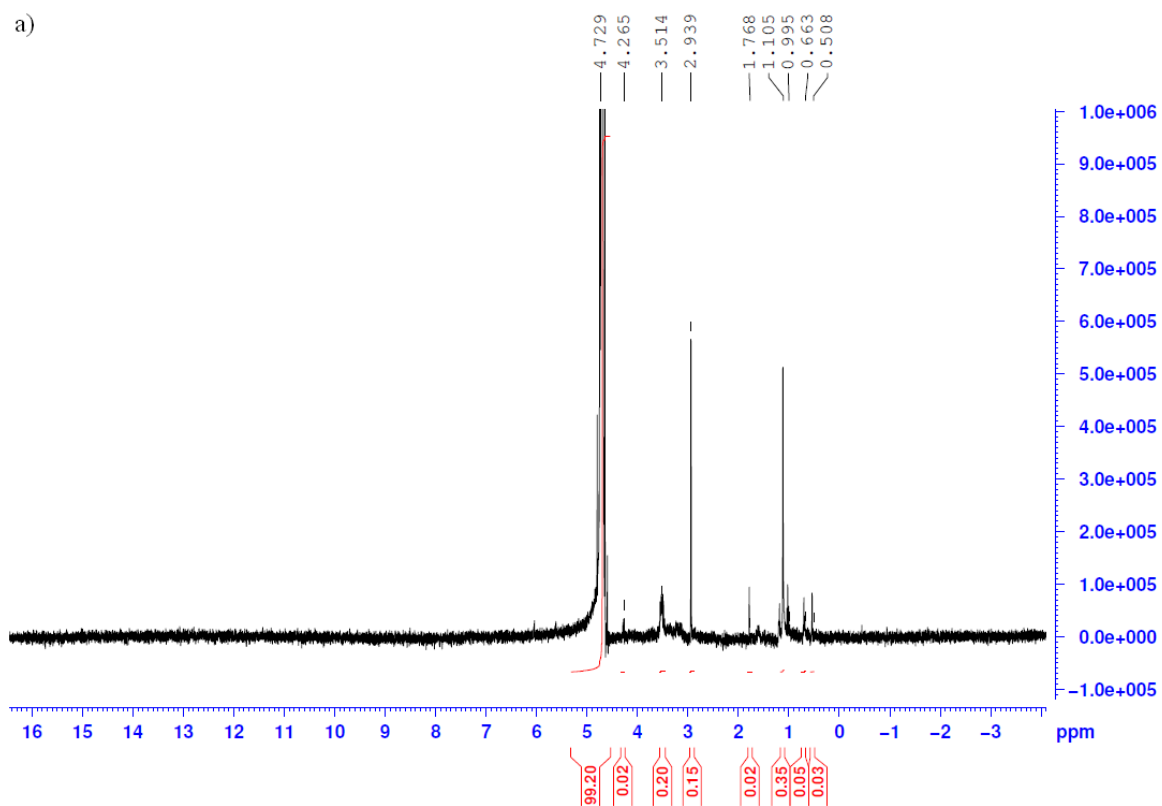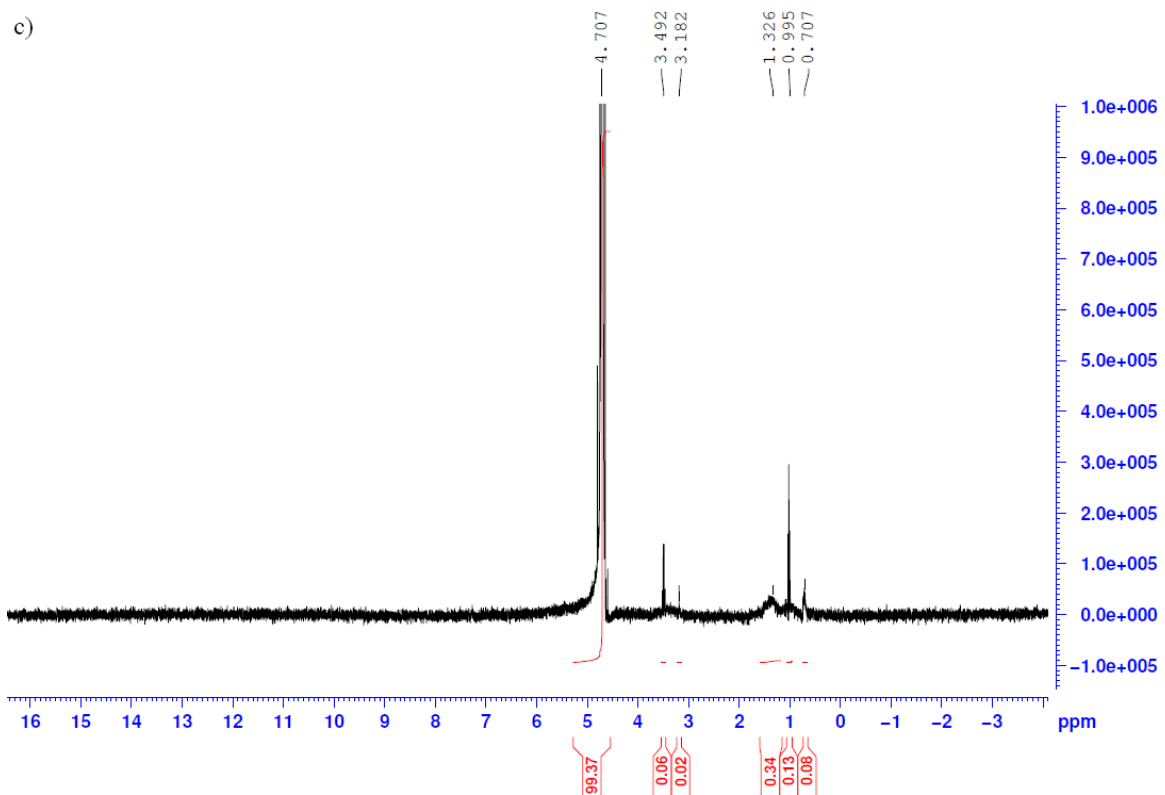
Figure S4.2: 1H-NMR spectra of 50nm PSNP-NH$_2$(a), 100nm PSNP-NH$_2$(b) and 100nm PSNP-neu(c) taken on a Bruker Advance II 400 MHz instrument, with D$_2$O used as the solvent for a 128 scan cycle.

4.9.5 Parameters used for data simulation.

Table S4.3: Parameters employed for the final simulated datasets for both the PSNP-NH$_2$ and PAMAM dendrimer.

Parameter	PSNP Model Value	PAMAM Model Value
dt	0.1hr	0.1hr
k_A	0.0011 hr^{-1}	0.0011 hr^{-1}
RT_0	10µM	10µM
k_{endo}	50nm: 3.795 hr^{-1} 100nm: 2.400 hr^{-1}	0.75 hr^{-1}
k_{GSH}	1.00 hr^{-1}	1.00 hr^{-1}
k_q	0.40 hr^{-1}	0.40 hr^{-1}
k_λ	(ln2/24) hr^{-1}	(ln2/24) hr^{-1}
B	3	3
$N_{Source(t=0)}$	10µM	10µM
k_{casp}	0.02 hr^{-1}	0.02 hr^{-1}
k_{casp2}	0.30 hr^{-1}	0.30 hr^{-1}
k_{mmp}	0.001 hr^{-1}	0.001 hr^{-1}
k_{tnf}	0.035 hr^{-1}	0.035 hr^{-1}
k_{IL-8}	0.10 hr^{-1}	0.10 hr^{-1}
k_V	8.00 hr^{-1}	8.00 hr^{-1}
k_{rec}	0.065 hr^{-1}	0.065 hr^{-1}

Chapter 5:

Modification of the in vitro uptake mechanism and antioxidant levels in HaCaT cells and resultant changes to toxicity and oxidative stress of G4 and G6 Poly (amido amine) dendrimer nanoparticles.

5.1 Abstract

The mechanism of cellular uptake by endocytosis and subsequent oxidative stress has been identified as the paradigm for the toxic response of cationically surface charged nanoparticles. In an attempt to circumvent the process, the effect of increased cellular membrane permeability on the uptake mechanisms of poly (amidoamine) dendrimers generation 4 (G4) and 6 (G6) *in vitro* was investigated. Immortalised, non-cancerous human keratinocyte (HaCaT) cells were treated with DL-Buthionine-(S,R)-sulfoximine (BSO). Active uptake of the particles was monitored using fluorescence microscopy to identify and quantify endosomal activity and resultant oxidative stress, manifest as increased levels of reactive oxygen species, monitored using the carboxy-H_2DCFDA dye. Dose dependent cytotoxicity for G4 and G6 exposure was registered using the cytotoxicity assays Alamar Blue and MTT, from 6 to 72 hours.

Reduced uptake by endocytosis is observed for both dendrimer species. A dramatic change, compared to untreated cells, is observed in the cytotoxic and oxidative stress response of the BSO treated cells. The significantly increased mitochondrial activity, dose dependent anti-oxidant behaviour and reduced degree of endocytosis for both dendrimer generations, in BSO treated cells, indicates enhanced permeability of the cell membrane, resulting in the passive, diffusive uptake of dendrimers, replacing endocytosis as the primary uptake mechanism. The complex MTT response reflects the importance of glutathione in maintaining redox balance within the mitochondria. The study highlights the importance of regulation of this redox balance for cell metabolism, but also points to the potential of controlling the nanoparticle uptake mechanisms, and resultant cytotoxicity, with implications for nanomedicine.

5.2 Introduction

Nanoparticle science is a rapidly advancing field which holds much promise in areas such as targeted drug and gene delivery (*Eichman et al., 2000*, *Duncan and Iszo, 2005* and *De Jong and Borm, 2008*). However, nanoparticle uptake into a cell has been demonstrated, particularly for nanoparticles with an effective cationic surface charge, to give rise to cytotoxic responses, raising concerns about the potential health and environmental impact of the proliferation of nanomaterials in consumer products (*Nel et al., 2006*). A systematic understanding of the mechanisms of toxicity and their dependence on nanoparticle physico-chemical properties on a cellular level is therefore required (*Jain et al., 2010*). In the context of nanomedical applications, understanding and controlling the uptake process and subcellular trafficking of the delivery vehicle and the bioavailability of the cargo are critically important.

Cellular uptake of nanoparticles principally occurs via endocytosis, whereby the nanoparticle is invaginated by the cellular membrane and is transported into the cell (*Xia et al., 2006*). As the low pH environment of the endosome attempts to digest the nanoparticle, the redox balance of the cell is disrupted, and, in the case of nanoparticles with an effective cationic surface charge, the process gives rise to an increase in the production of Reactive Oxygen Species (ROS), localised mainly around the endosome (or later lysosome) (*Xia et al., 2006*, *Mukherjee et al., 2010 – A* and *B*, *Naha et al., 2010*). Although intra cellular anti-oxidants attempt to neutralise the imbalance, ROS production can be sufficient to lead to oxidative stress (*Mukherjee and Byrne, 2013*). Subsequently, a cascade of events and the release of several characteristic cytokines and chemokines occurs, ultimately leading to cell death, a process which is the accepted paradigm of nanotoxicity of many nanoparticles *in*

vitro (*Xia et al., 2006*). The process has been well demonstrated for model nanoparticle systems such as amine functionalised polystyrene (*Anguissola et al., 2014*, *Paget et al., 2015* and *Lunov et al., 2011*), amorphous nanosilica (*Nabeshi et al., 2011*) and nanomeric polymeric dendrimers (*Mukherjee and Byrne, 2013*).

Aminated molecules are intrinsic antioxidants, however, and generally regarded as ROS scavengers. As examples, spermine and spermidine have both been shown to reduce Fe^{3+} to Fe^{2+} (*Mozdzan et al., 2006*) and the ferric reducing activity of these molecules has been identified as a measure of anti-oxidant potential (*Lotito and Frei, 2004*). Carnosine, an endogenous dipeptide, has been shown to scavenge both reactive oxygen and nitrogen species (*Hipkiss, 2009*). Notably, in a study by Khalid *et al.* (*2015*), while the larger, higher generations of the aminated nanoscale dendrimers Poly (propylene imine) (PPI) were demonstrated to elicit oxidative stress and significant toxicity, the smaller, lower generations exhibited intracellular antioxidant behaviour and low toxicity (*Khalid et al., 2015*). Examination of the uptake mechanisms indicated a transition from cellular uptake by passive diffusion at low generations to active endocytosis for higher generations. The study suggests that, in the case of catatonic nanoparticles, the endocytotic uptake and trafficking process is, in itself, a source of cellular toxicity. In the context of drug delivery, invagination of the delivery vehicle and cargo in this harsh environment may also be undesirable, and although escape by endosomolysis is a potential strategy (*Watson et al., 2005*), this too can be a harsh process, causing significant damage to the cell (*Mukherjee, 2012* and *Xia et al., 2008*). For these reasons, circumventing endocytosis appears to be a valid strategy for the reduction of toxicity associated with aminated nanoparticles, which would aid nanoparticle drug or gene delivery.

Guarnieri *et al.* (*2015*), demonstrated that functionalization of aminated polystyrene nanoparticles with the viral peptide gH625 (derived from *Herpes simplex virus – 1*), which has a membrane perturbing domain, enables translocation of particles to the cytoplasm, avoiding endocytosis and thus, dramatically reducing the cytotoxicity (*Guarnieri et al., 2014*). An alternative strategy to increase the permeability of the cellular membrane, *in vitro*, is through the application of DL-Buthionine-(*S,R*)-sulfoximine (BSO). BSO has previously been employed to study the effects of the reduction of levels of the intracellular antioxidant glutathione (GSH); and therefore oxidative stress (*Girard et al., 2013*, *He et al., 2003*, *Madesh et al., 1998* and *Tobi et al., 2000*) and has been shown to cause membrane permeabilisation (*Li et al., 1994* and *Zamam et al., 1995*). BSO works as an inhibitor of the enzyme Glutamate Cysteine Ligase (EC 6.3.2.2) (historically known as gamma-glutamylcysteine synthetase) which is the first step in the production of GSH in the cell (*Griffith, 1982*). This reduction in GSH causes several different effects, one being the induction of the membrane permeability transition in the mitochondria (*Armstrong and Jones, 2002*, *Chernyak and Bernardi, 1996* and *Reed and Savage, 1995*). The opening of this pore and the depletion of GSH allows ROS to diffuse from the mitochondria to the cell and via lipid peroxidation, cause damage to the cell membrane (*Zamam et al., 1995*), leading to increased permeability.

The reduction of GSH in the cell can have other adverse effects, however, mainly due to the fact that GSH is one of the main antioxidants involved in maintaining the redox balance of the mitochondria (*Circu and Aw, 2008*). In the mitochondria, endogenous ROS is produced as a by-product of normal metabolism and therefore completely eliminating GSH can leave the cell susceptible to damage from this ROS (*Lash, 2006*). Furthermore,

reductions in cellular GSH can also lead to changes in the regulation of Ca^{2+} distribution (*Beatrice et al., 1984*, *Lotscher et al., 1979* and *Olafsdottir et al., 1988*) and the activation/deactivation of signalling pathways involved with growth, differentiation and apoptosis (*Circu and Aw, 2008*, *Davis et al., 2001*, *Petit et al., 1996* and *Skulachev, 1996*). The loss of GSH and subsequent changes in the cell have been implicated in several disease states which is reviewed elsewhere (*Lash, 2006*).

This study explores the impact, for HaCaT cells, of BSO treatment on the cellular uptake of, and subsequent oxidative stress and toxic response to, Poly (amido amine) (PAMAM) dendrimers. These nanoscale aminated dendrimers have a systematically variable molecular structure, and the homologous series of increasing generation, and concomitant size and number of surface amino groups, has been demonstrated to be ideal to study the dependence of nanoparticle cellular interactions on the physico-chemical properties of the particles. Previous studies have examined the structurally dependent toxicity, and underlying mechanisms of endocytosis, oxidative stress, immune responses and consequent toxicity (*Mukherjee et al., 2010 – A* and *B*, *Naha et al., 2010* and *Mukherjee and Byrne, 2013*) and the responses have been numerically modelled, as a guide towards a predictive toxicology approach (*Mukherjee and Byrne, 2013* and *Maher et al., 2014*). For consistency and to allow comparisons with the previous work, the *in vitro* studies reported here were also carried out using the immortalised human keratinocyte cell line, HaCaT, and identical oxidative stress and cytotoxic assays. Furthermore, PAMAM dendrimers of Generation 4 and 6 were chosen as the extremes of the previously reported cytotoxicological response (*Mukherjee et al., 2010 – A* and *B*, *Naha et al., 2010* and *Mukherjee and Byrne, 2013*). In

comparison, it is demonstrated that treatment with BSO results in a significant change in the nanoparticle uptake mechanisms and cytotoxicity.

5.3 Materials and Methods

5.3.1 Materials

DMEM F12 HAM growth medium, Penicillin, Streptomycin, fluorescently labelled, Polystyrene nanoparticles, with amine surface modification (PSNP-NH$_2$) 100nm, DL-Buthionine-(*S,R*)-sulfoximine(BSO) and 3-(4,5-dimethylthiazol-2-yl)-2,5-diphenyltetrazolium bromide (MTT) dye were purchased from Sigma-Aldrich, Ireland. The PAMAM dendrimer nanoparticles, generations 4 (molecular weight: 14,214 g/mol) and 6 (molecular weight: 58,046 g/mol), were purchased from Sigma-Aldrich and manufactured by Dendritech Inc. ThiolTracker™ Violet (TTV), CellLight® Early Endosomes-RFP, BacMam 2.0, Fetal Bovine Serum (FBS), L-Glutamine, Alamar Blue (AB) and 5-(and-6)-carboxy-2',7'-dichlorodihydrofluorescein diacetate (carboxy-H$_2$DCFDA) dye were purchased from Life Technologies™, Bio-Sciences, Ireland. HaCaT cells were purchased from Cell Line Services (CLS), Eppelheim, Germany. TrueLine 96-well cell culture plates were used for all viability and ROS studies.

All fluorescence and absorbance readings were taken on a Molecular Devices SpectraMax M3 Spectrometer. Confocal Laser Scanning Fluorescence Microscopy (CLSM) images were taken on a Zeiss LSM 510 Confocal Laser Scanning Microscope and processed using ImageJ software (with co-localisation analysis performed with the JACoP plugin for ImageJ). All viability, ROS and GSH data analysis was performed using SigmaPlot v10.0 software.

5.3.2 Methods

5.3.2.1 Cell culture

HaCaT cells are an immortalised, non cancerous human keratinocyte cell line and were used for these experiments. The cells were cultured in DMEM F12 HAM supplemented with 10% FBS, 45 IU/mL penicillin, 45 IU/mL streptomycin and 2mM L-glutamine at 37˚C in 5% CO_2.

All assays carried out in this set of experiments were performed in 96 well plates, with cells plated at a concentration of $1x10^4$ cells/well in 100μL of DMEM medium. Cells were allowed 24 hours to attach and were then treated with BSO for an additional 18 hours (at a concentration of 200μM), after which cells were exposed to PAMAM G4 or G6 dendrimers (in DMEM F12 HAM, with 5% FBS, 45 IU/mL penicillin, 45 IU/mL streptomycin, 2mM L-glutamine and 200μM BSO) at various concentrations for the specified time points. Six replicates of each concentration were performed per plate and each plate was repeated in triplicate.

5.3.2.2 ThiolTracker™ Violet (TTV)

ThiolTracker™ Violet (TTV) is a GSH detection agent. Cells were plated as described above and a concentration gradient of BSO was applied. Cells were left for 18 hours at 37˚C in 5% CO_2 to allow for reduction of the amount of intracellular GSH. Cells were then washed twice with PBS, 100μL of TTV dye (at a final concentration of 20μM) were added to each well and the plates were allowed to incubate at 37˚C in 5% CO_2 for 30 minutes, after which the TTV solution was removed and replaced with PBS. The fluorescence of

each well was then read using the SpectraMax M3 spectrometer with λ_{ex}= 404nm and λ_{em}= 526nm. GSH values were calculated as compared to the unexposed control.

5.3.2.3 Viability assays

Alamar Blue and MTT assays were used to determine the changes in cell viability, after treatment with BSO as described above, as a result of exposure to both PAMAM G4 and G6 dendrimers. Both Alamar Blue and MTT were performed on the same plate. The PAMAM G4 concentrations used were: 0.16, 0.32, 0.65, 1.3, 2.6, 5.2, 7.8 and 10.4μM, while the PAMAM G6 concentrations were: 0.08, 0.16, 0.32, 0.65, 1.3, 2.6, 3.9 and 5.2μM. The lower initial value of the PAMAM G6 dendrimers was used due to their reported EC_{50} value being much lower than their G4 counterparts (*Mukherjee et al., 2010 – A* and *B*, *Naha et al., 2010*). Dose dependent viability percentages were calculated at time points: 6, 12, 24, 48 and 72 hours. Percentage viability was calculated as compared to a control which had been exposed to 200μM BSO, but had no nanoparticle treatment; this was to ensure any changes were caused by the nanoparticle and were not the result of BSO treatment. A separate control where no BSO was present was also performed and showed there was little difference between cells with no BSO exposure and cells which were exposed to BSO (Supplementary Information, Figure: S5.1).

5.3.2.4 Alamar Blue (AB)

The Alamar Blue assay was made up from 10X stock solution in medium (DMEM F12 HAM, with no additional supplements). At the specified time point, the plates were removed from the incubator and the medium containing PAMAM dendrimer was removed,

the cells were washed with 100μL PBS and then 100μL of DMEM F12 HAM(unsupplemented) containing Alamar Blue were added to each well. The plates were incubated for 3 hours at 37˚C in 5% CO_2 to allow for conversion of the dye. The fluorescence of each well was then read using the SpectraMax M3 spectrometer with $\lambda_{ex}=$ 555nm and $\lambda_{em}=$ 585nm.

5.3.2.5 MTT (3-(4,5-dimethylthiazol-2-yl)-2,5-diphenyltetrazolium bromide)

A stock solution of MTT was made at a concentration of 0.5mg/mL. 500μL of this stock were added for every 10mL of medium (DMEM F12 HAM, with no additional supplements). At the specified time point, the plates were removed from the incubator and the medium containing PAMAM dendrimer was discarded, the cells were washed with 100μL PBS and then 100μL of DMEM (unsupplemented) containing MTT was added to each well. The plates were incubated for 3 hours at 37˚C in 5% CO_2 to allow for conversion of the dye. After 3 hours, any remaining dye was removed and each well was again washed with 100μL PBS, after which 100μL of DMSO was added and the plates were placed on a shaker for 10 minutes to allow for the dye to solubilise. The absorbance of each well was then read using the SpectraMax M3 spectrometer with $\lambda_{abs}=$595nm.

5.3.2.6 Reactive Oxygen Species (ROS)

5-(and-6)-carboxy-2',7'-dichlorodihydrofluorescein diacetate (carboxy-H_2DCFDA) dye was used for the detection of ROS. The dye was made up to a final concentration of 10μM in sterile PBS. Before addition of PAMAM dendrimer, this dye was added to the cells and allowed to incubate for 1 hour, after which, the dye was removed, the cells were washed

thrice with PBS and the medium containing PAMAM dendrimer was added. At the specified time points the fluorescence was read by the SpectraMax M3 spectrometer with λ_{ex}= 488nm and λ_{em}= 535nm.

5.3.2.7 Confocal Laser Scanning Microscopy (CLSM)

Cells were plated onto MatTek 35mm glass bottom dishes at a concentration of 20,000 cells/dish in DMEM F12 HAM (supplemented with 10% FBS, 45 IU/mL penicillin, 45 IU/mL streptomycin and 2mM L-glutamine) and allowed to attach for 4 hours, at which point the medium was removed and replaced with medium containing Celllight® Early Endosomes-RFP, BacMam 2.0 at a concentration of 20 particles per cell. Early endosome formation was tracked with the Celllight® Early Endosome – RFP kit, which transfects, into the cell, a version of Rab5a with a bound Red Fluorescent Protein. The cells were allowed to incubate (37°C, 5% CO_2) for 16 hours to ensure transfection with the early endosome reagent. After this, the medium was removed and cells were washed twice with PBS. For cells being tested without BSO, medium was added for 18 hours (these samples are referred to as untreated cells/untreated controls in the text), while for cells being tested with BSO, medium containing 200µM BSO was added for 18 hours. Cells were again washed with PBS and carboxy-H_2DCFDA was added for 1 hour (10µM in 2mL PBS), after which cells were again washed twice with PBS. PAMAM dendrimers were added at a concentration of 3.21µM (G4) and 1µM (G6) and cells were allowed to incubate for 3 hours (G4) or 1 hour (G6) and were then washed twice with PBS and imaged with the Zeiss LSM 510 Confocal Laser Scanning Microscope. 100nm PSNP-NH_2 with attached Green Florescent Protein was used as a positive control to ensure the Celllight® Early Endosomes-RFP was

functioning as expected; the results of this test are available in the supplementary information section, Figure S5.2. Negative controls were also performed with cells which were not exposed to any nanoparticles, and little to no fluorescence was noted (data not shown). For ROS monitoring, doses and time points noted above were chosen based on the maximum responses previously reported in literature (*Mukherjee et al., 2010 - B*). All confocal images were analysed using ImageJ and co-localisation studies were performed using Manders split coefficients calculated with the JACoP plugin for ImageJ (*Zinchuk and Zinchuk, 2008*).

5.3.2.8 Data Analysis and Statistics

Data analysis was performed using SigmaPlot™ v10.0 and fluorescence was calculated based on the values of BSO controls (which were unexposed to nanoparticles, but had been treated with 200μM BSO for 18 hours). The cytotoxicity, GSH and ROS experiments were performed in 96-well microplates with six replicates per plate and each plate repeated three times. Therefore, data points shown represent the mean of 18 points, with error bars representing ± the standard deviation (as calculated by SigmaPlot™ v10.0). Confocal Images were taken on a Zeiss LSM 510 and processed using ImageJ software. Images were taken of eight cells/groups of cells and the images presented in the manuscript are representative of the sampled cell population.

5.4 Results

5.4.1 BSO treatment

While maximising the desired effect of the BSO on the cells, it is important that the viability of the cells is not affected. TTV showed a 40% reduction in intracellular levels of GSH for the HaCaT cells upon 200μM BSO exposure for 18 hours (adapted from the methods of: He *et al.* (*2003*)). This dose and time point were found to have a minimal impact on cellular viability as measured by the AB and MTT assays (data available in Supplementary Material, Figure: S5.3). Higher concentrations were found to have an effect on cellular viability, although a more pronounced effect was observed by CLSM, where signs of cellular stress were noted (data not shown). Therefore 200μM BSO exposure was chosen as optimal.

5.4.2 PAMAM G4 dendrimers

CLSM was employed as a way to examine the effect of BSO treatment on the cellular uptake mechanisms and subsequent oxidative stress. Early endosome formation was tracked with the Celllight$^{®}$ Early Endosome – RFP kit and the formation of ROS was also tracked using the carboxy-H_2DCFDA dye. Fluorescently labelled PSNP-NH_2 of 100nm diameter were employed as positive controls, and the results for those are shown in Supplementary Figure S5.2.
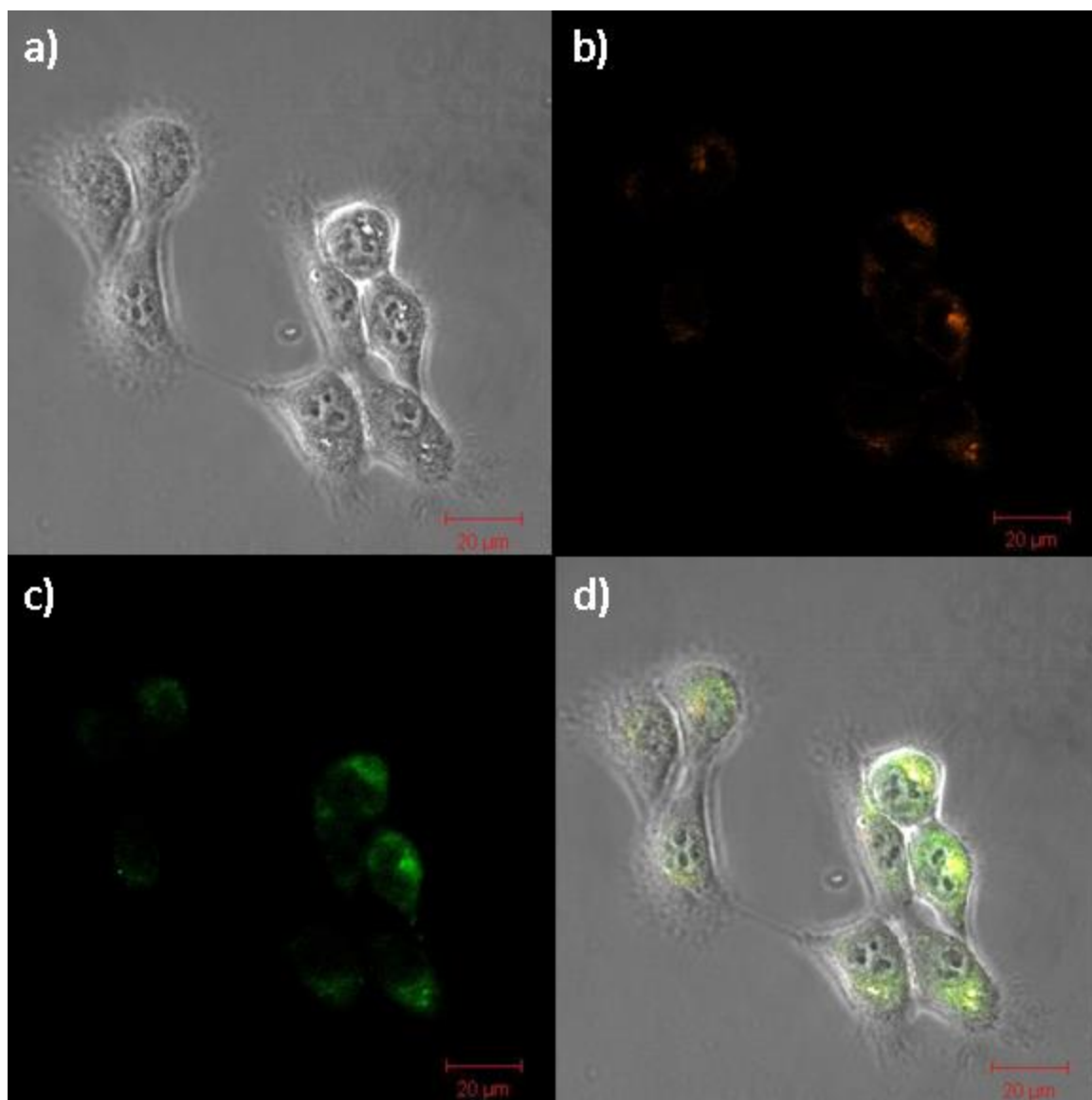
Figure 5.1: CLSM images of HaCaT (live) cells, upon exposure to 3.21μM PAMAM G4 dendrimer at 3 hours (no BSO is present in this sample). Image a) shows the bright field image of the cells, Image b) shows the fluorescence generated by the early endosomal red fluorescent protein, Image c) shows the fluorescence generated by the ROS (interacting with the carboxy-H_2DCFDA dye) and Image d) shows the overlay of images a-c, where yellow coloured areas indicate simultaneous endosomal and ROS activity.

Figure 5.1 shows the HaCaT cells following the reported paradigm of PAMAM G4 endocytosis and subsequent ROS generation at the endosomal sites (*Xia et al., 2006*, *Mukherjee et al., 2010 – A* and *B*, *Naha et al., 2010*). Co-localisation (performed on the images in Figure 5.1) shows that 91(±3)% of the generated ROS occurs in the neighbourhood of endosomes, and that 71(±4)% of endosomal formation resulted in increases in ROS production (the other 30% of endosomal activity is most likely due to endocytosis which would be routinely done by the cell and would not involve the dendrimers and therefore not produce ROS).
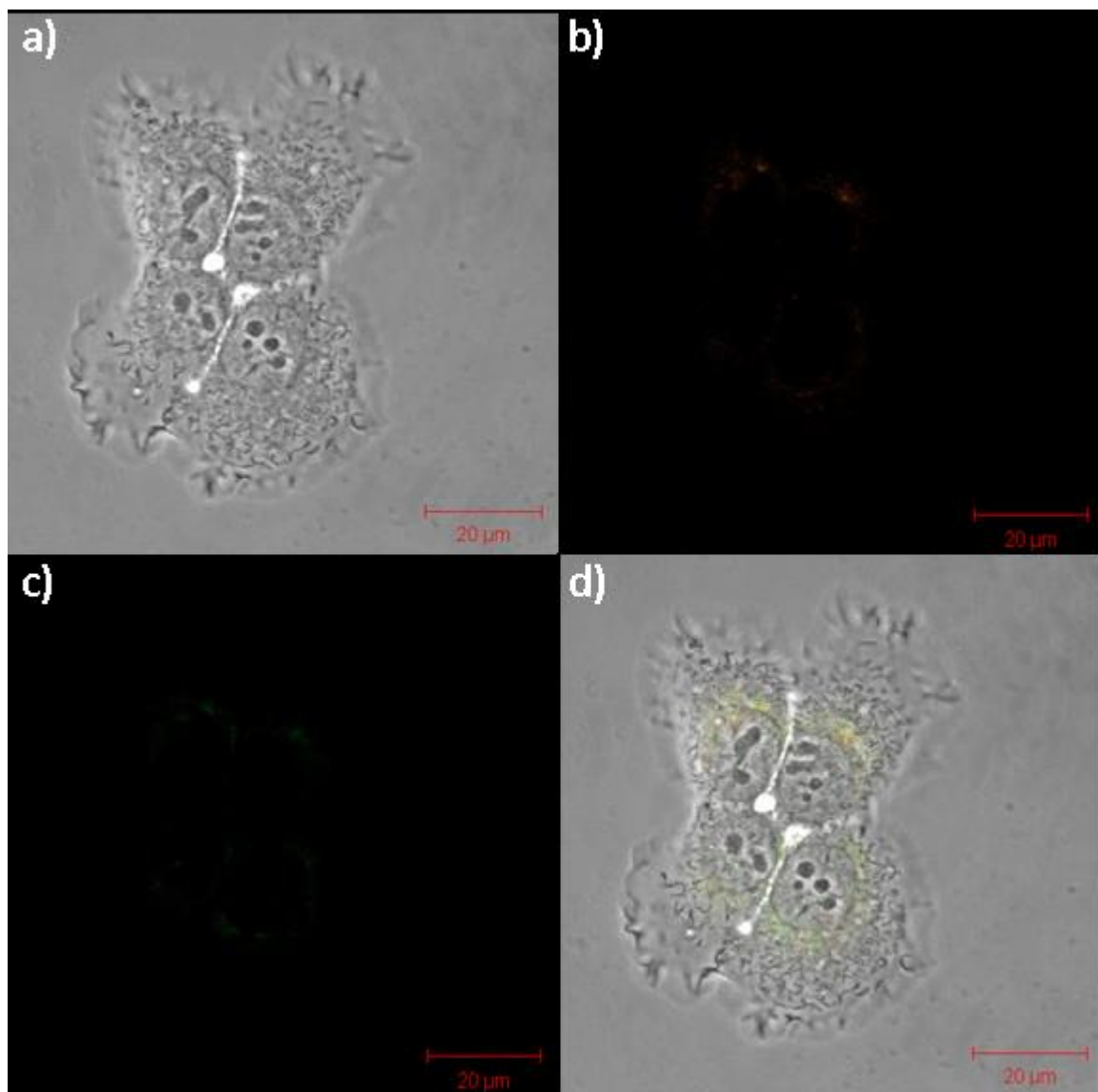
Figure 5.2: Confocal images of HaCaT (live) cells, upon exposure to 3.21μM PAMAM G4 dendrimer at 3 hours, with pre-treatment of BSO: 200μM for 18 hours. Image a) shows the bright field image of the cells, Image b) shows the fluorescence generated by the early endosomal red fluorescent protein, Image c) shows the fluorescence generated by the ROS (interacting with the carboxy-H_2DCFDA dye) and Image d) shows the overlay of images a-c, where yellow coloured areas indicate simultaneous endosomal and ROS activity.

In contrast, Figure 5.2 shows HaCaT cells which have been treated with BSO for 18 hours prior to PAMAM G4 exposure (BSO was still present in the media upon exposure, to ensure conditions were consistent). In images (b) and (c), the intensity of the endosomal RFP and ROS dye have been significantly reduced. Again co-localisation analysis was performed (on images in Figure 5.2) and showed that $30(\pm6)\%$ of the generated ROS was happening around the endosomes, and that $46(\pm14)\%$ of endosomal formation resulted in increases in ROS production. Intensity analysis of the red fluorescent protein produced by endocytosis, on average, showed a reduction in intensity of $70(\pm3)\%$ for cells treated with BSO.

Endosomal uptake was clearly reduced, although a decrease in the intensity of response of the ROS detection dye, carboxy-H_2DCFDA, was also noted, prompting a quantitative analysis of the ROS contents of the HaCaT cells: Figure 5.3.
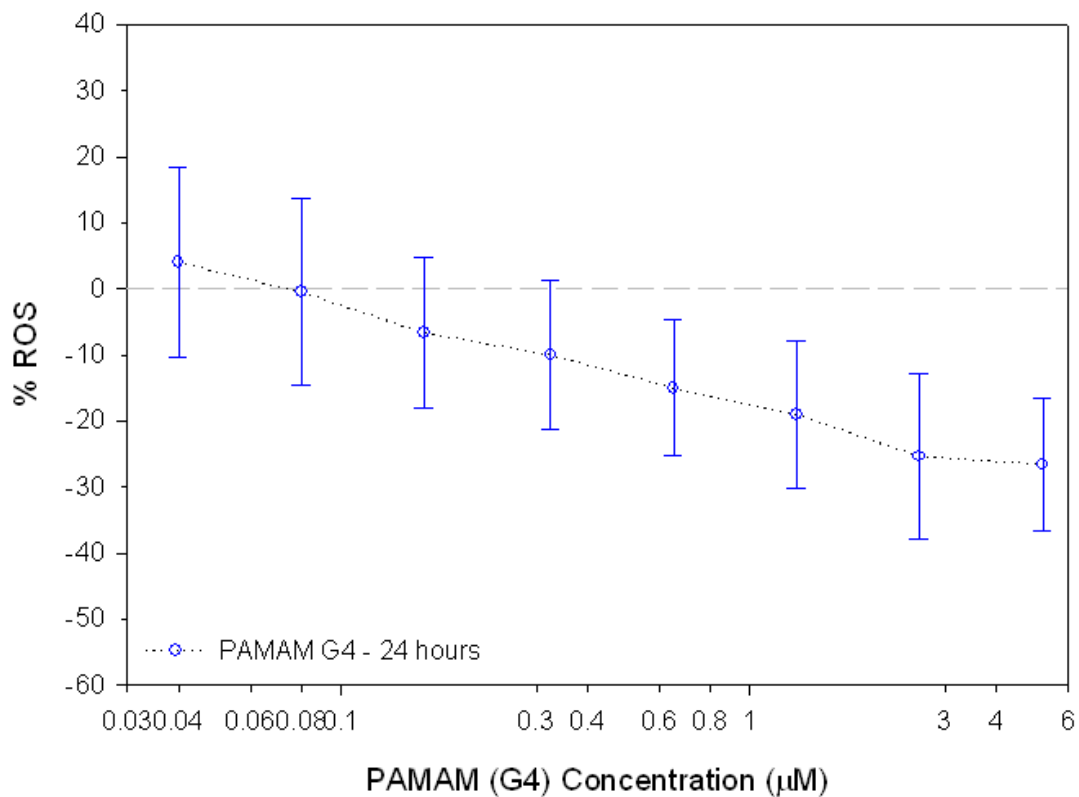
Figure 5.3: Dose dependant generation of ROS in HaCaT cells (shown for 24 hours for the PAMAM G4). ROS is compared to BSO control which was set to equal 0%. The X-axis is plotted logarithmically to allow for better visualisation of lower concentrations. Data points are the mean of 18 samples, with error bars showing (±) the standard deviation.

The analysis of ROS showed a net decrease at all doses tested; for clarity, only the dose dependence of the 24 hour test has been shown, the full data-set is available in Supplementary Figure S5.4. Over the dose range tested, the ROS response followed a monotonically decreasing trend. This result is again in contrast with previous observations, in which ROS levels were seen to increase above control levels in a dose dependant fashion, upon G4 dendrimer exposure (*Mukherjee et al., 2010 - B*).

To examine how these changes in both endocytosis and ROS production affected the viability of the cell AB and MTT assays were performed. HaCaT cells were exposed to 200μM BSO for 18 hours and subsequently exposed to varying concentrations of PAMAM G4 nanoparticles. Viability was measured at 6, 12, 24, 48 and 72 hours (Figure 5.4 (a) and (b)).
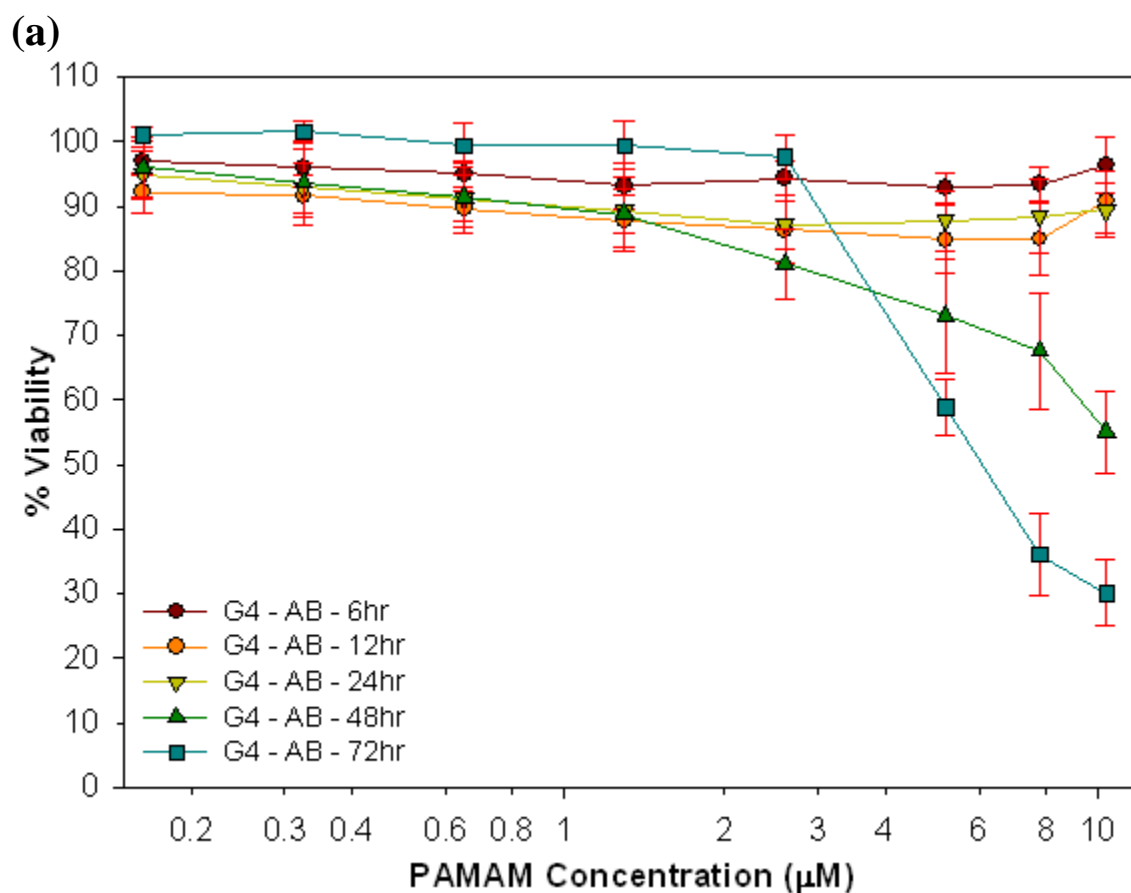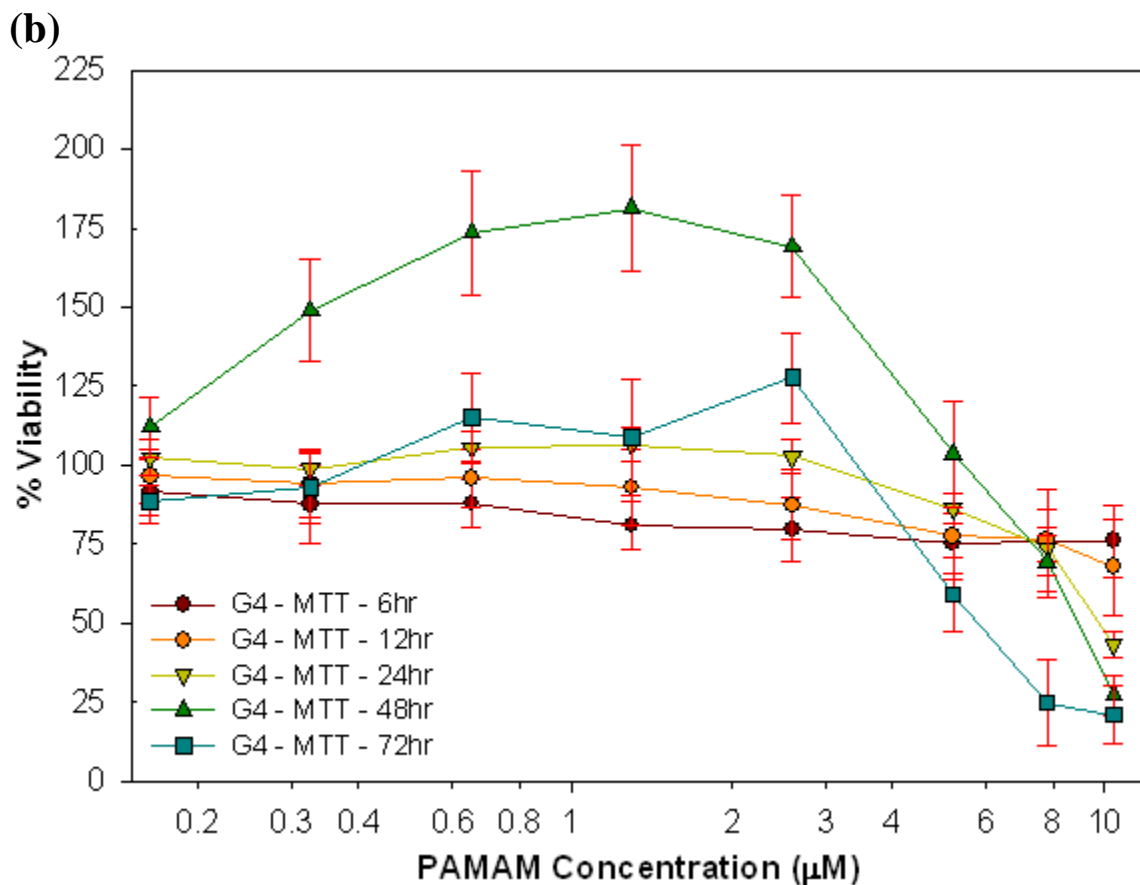
(a)

(b)

Figure 5.4: Alamar Blue (a) and MTT (b) dose dependant viability results for PAMAM G4 dendrimers in HaCaT cells after 6, 12, 24, 48 and 72 hours. Viability is calculated as the percentage of living cells as compared to BSO control. Data points are the mean of 18 samples, with error bars showing (±) the standard deviation.

The AB assay shows little or no toxicity of PAMAM G4 at time points 6, 12, and 24 hours, whereas the viability is reduced to 50% at 48 hours and 30% at 72 hours, for the higher dose exposures. In HaCaT cells which have not been treated with BSO, the EC_{50} obtained from AB is around 10μM at 24 hours (*Mukherjee et al., 2010 - A*), whereas, in Figure 5.4, at the same time point, it is clear that there is no significant toxicity. The MTT results show a dramatically different dose dependent cytotoxicity profile for the BSO dosed cells

compared to un-dosed (*Mukherjee et al., 2010 - A*). At 6 hours PAMAM exposure (Figure 5.4b), the viability is seen to be reduced to around 80% over the entire dose range. However, at exposure times of 12, 24, 48 and 72 hours, increases in viability are seen for the low-medium dose range. The effect is particularly pronounced at the 48 hour time point, at which the recorded MTT response is ~175% of control, for an exposure dose of ~1μM. For doses of ~2.6μM and higher, the MTT assay response registers a decrease in viability, which is more pronounced in the longer time point exposures.

5.4.3 PAMAM G6 dendrimers

Analysis of uptake and ROS production was again carried out using CLSM (with the same method as the PAMAM G4) incorporating the carboxy-H_2DCFDA dye and Celllight[®] Early Endosome – RFP kit (Figure 5.5 and 5.6).
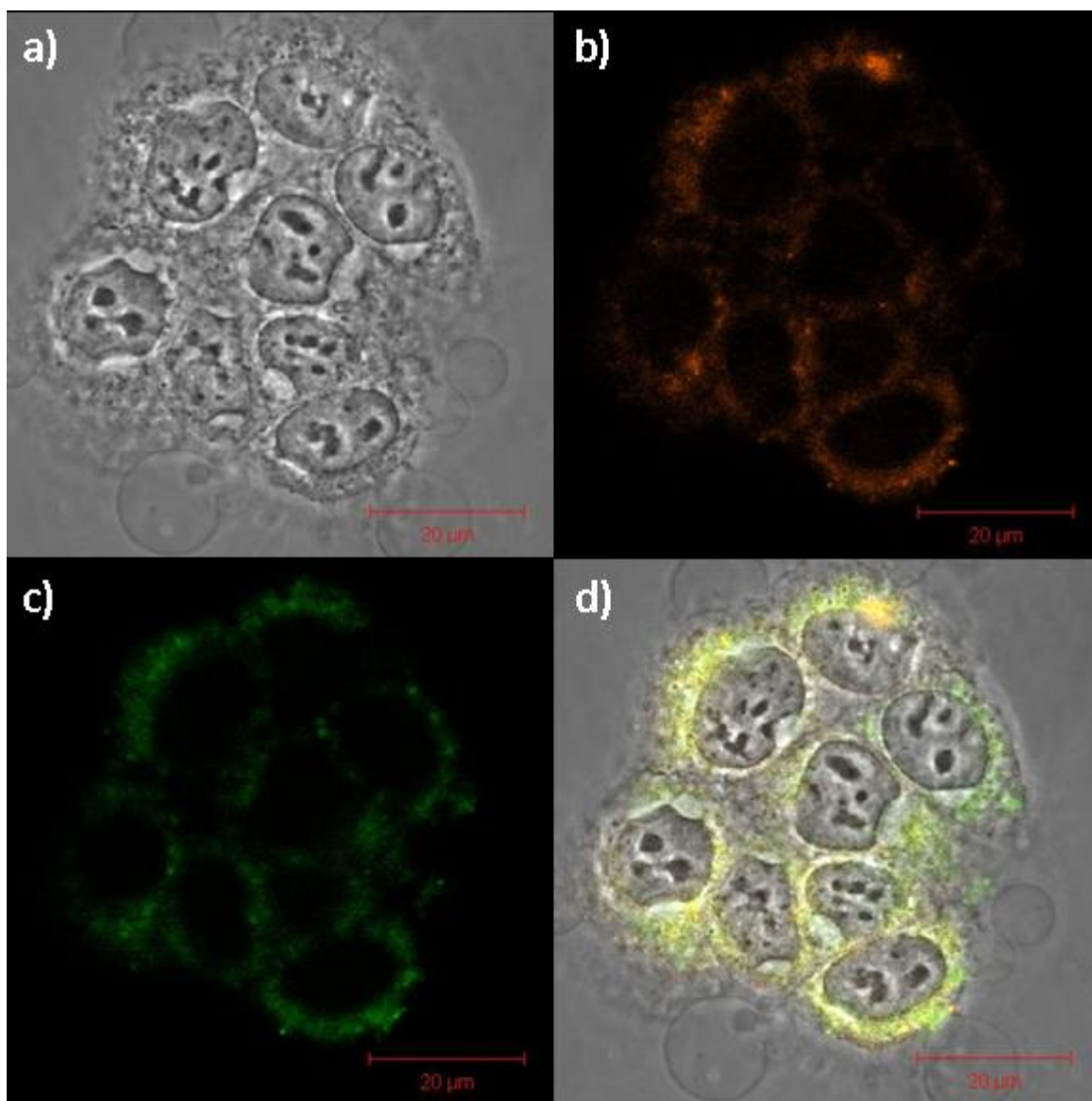
Figure 5.5: Confocal images of HaCaT (live) cells, upon exposure to 1µM PAMAM G6 dendrimer at 1 hour (no BSO is present in this sample). Image a) shows the bright field image of the cells, Image b) shows the fluorescence generated by the early endosomal red fluorescent protein, Image c) shows the fluorescence generated by the ROS (interacting with the carboxy-H_2DCFDA dye) and Image d) shows the overlay of images a-c, where yellow coloured areas indicate simultaneous endosomal and ROS activity.

In the absence of BSO, PAMAM G6 exposure, resulted in strong red fluorescence indicating a high level of endocytosis, complemented by strong green fluorescence indicating increased ROS production. Co-localisation analysis (of images in Figure 5.5) found that $75(\pm2)\%$ of the generated ROS occurred in the region of the endosomes, and that $92(\pm1)\%$ of endocytosis resulted in increases in ROS production. This strong level of co-localisation is indicative of the accepted paradigm of nanoparticle uptake by endocytosis, and ROS production at the site of endosomes.
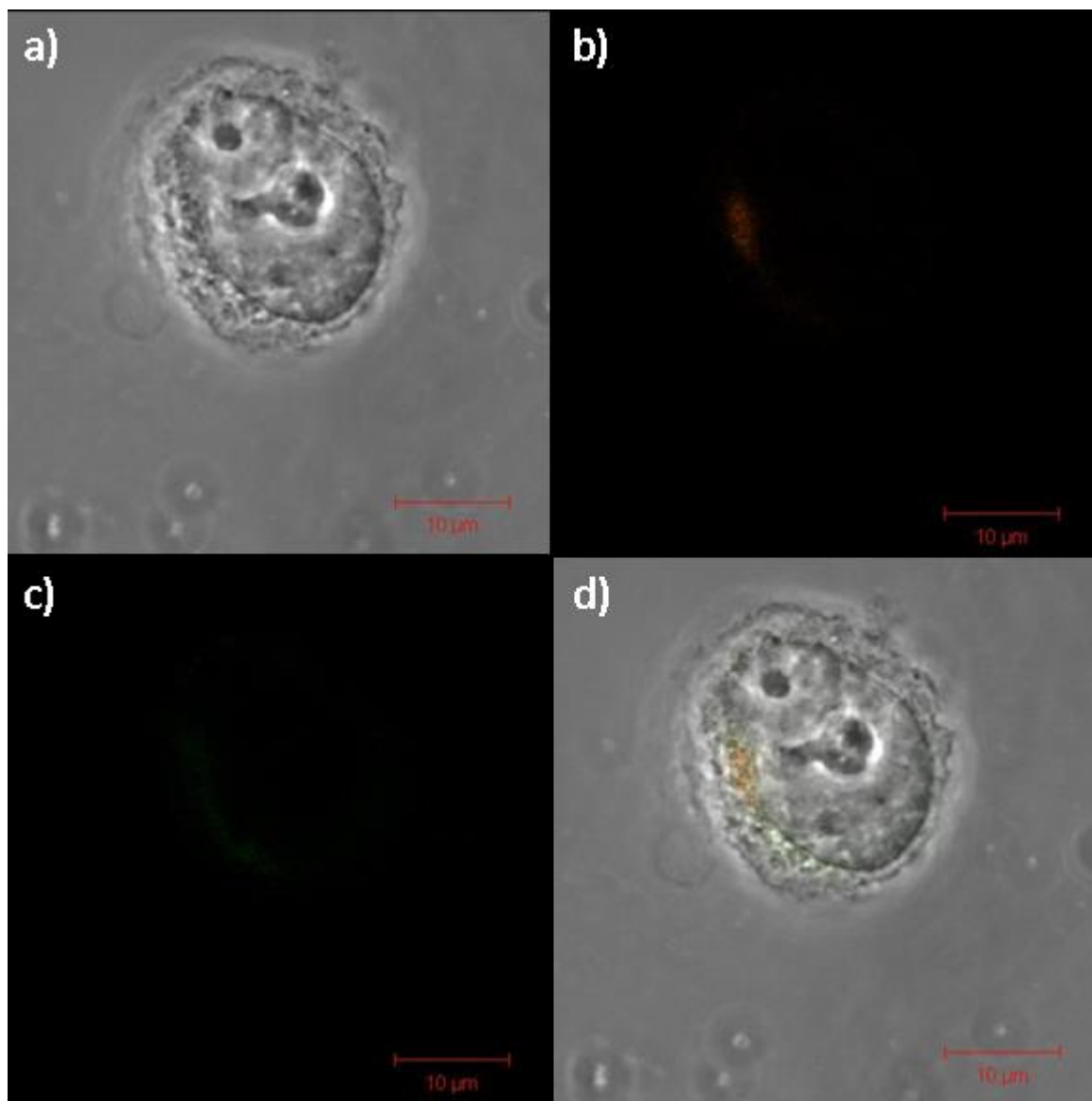
Figure 5.6: Confocal images of HaCaT (live) cells, upon exposure to 1μM PAMAM G6 dendrimer at 1 hour, with pre-treatment of BSO: 200μM. Image a) shows the bright field image of the cells, Image b) shows the fluorescence generated by the early endosomal red fluorescent protein, Image c) shows the fluorescence generated by the ROS (interacting with the carboxy-H_2DCFDA dye) and Image d) shows the overlay of images a-c, where yellow coloured areas indicate simultaneous endosomal and ROS activity.

In comparison to exposure of PAMAM G6 in cells without BSO treatment (un-dosed cells), there is a sparsity of endosomal activity and oxidative stress response in cells which had been pre-treated with BSO for 18 hours. Analysis (of the images in Figure 5.6) showed decreased levels of co-localisation between the ROS and endosomal formation: only 41($\pm$18)% of ROS production was recorded in areas where endosomes had formed and 55($\pm$10)% of endocytosis resulted in increases in ROS production. Intensity analysis of the red fluorescent protein produced by endocytosis, on average, showed a reduction in intensity of 61($\pm$1)% for cells treated with BSO when compared to the untreated cells. Again, in light of the reduced ROS response, quantitative analysis, using carboxy-H_2DCFDA was performed: Figure 5.7.
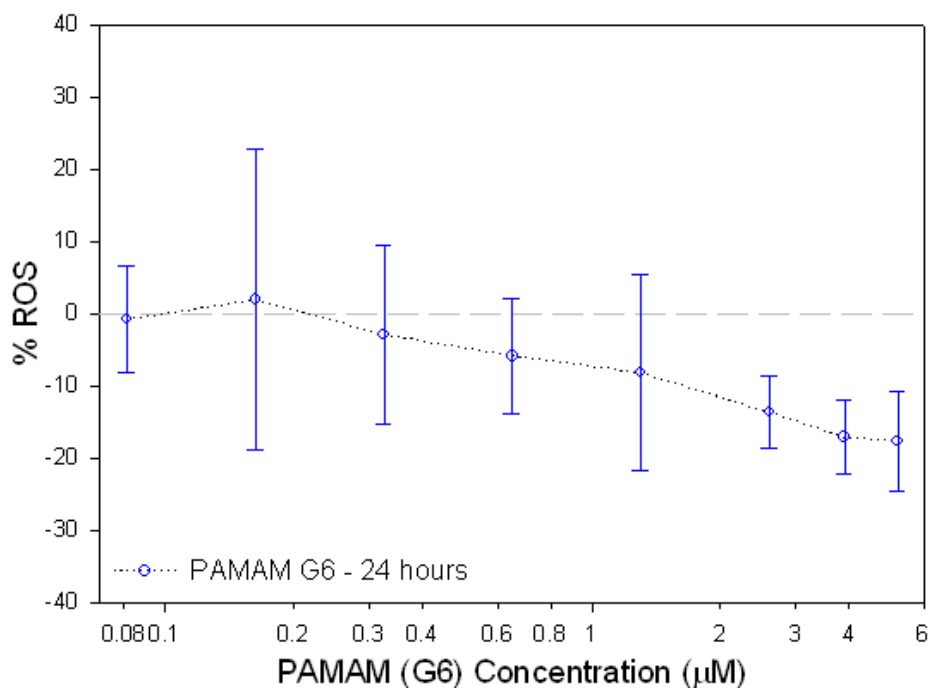
Figure 5.7: Dose dependant generation of ROS in HaCaT cells (shown at 24 hours for the PAMAM G6). ROS is compared to BSO control which was set to equal 0%. The X-axis is plotted logarithmically to allow for better visualisation of lower concentrations. Data points are the mean of 18 samples, with error bars showing ($\pm$) the standard deviation.

The dose response of the ROS generation shows similarities with the G4 in the overall progression of the response, pointing to a trend where increasing concentration leads to decreasing amounts of ROS, contrary to what has been observed in previous studies without BSO exposure (*Mukherjee et al., 2010 - B*). As with the G4 analysis, for clarity, only one of the eight concentrations tested have been shown, the full data-set is available in the Supplementary Figure S5.5. At all doses tested, the ROS response followed the same trend as shown in Figure 5.7.

To analyse the effect this had on viability, AB and MTT assays were performed: Figure 5.8.
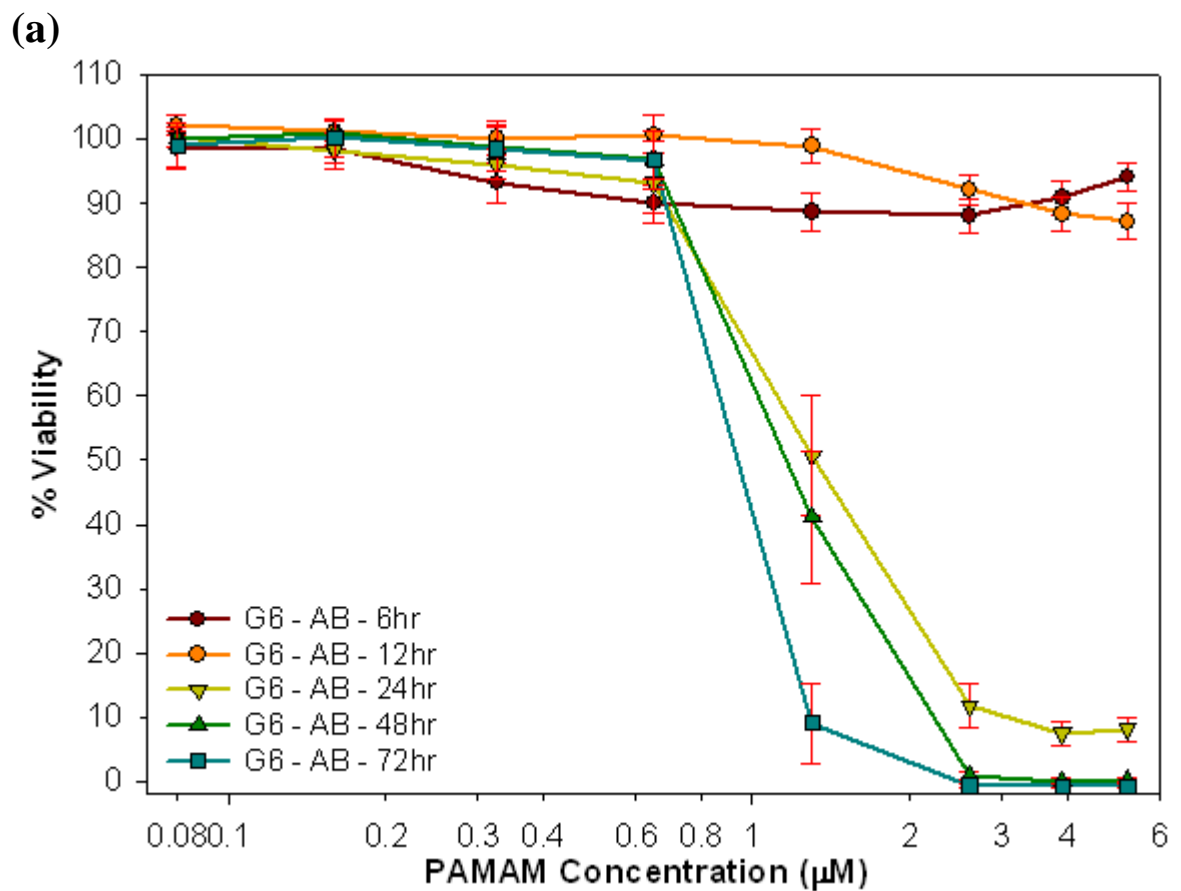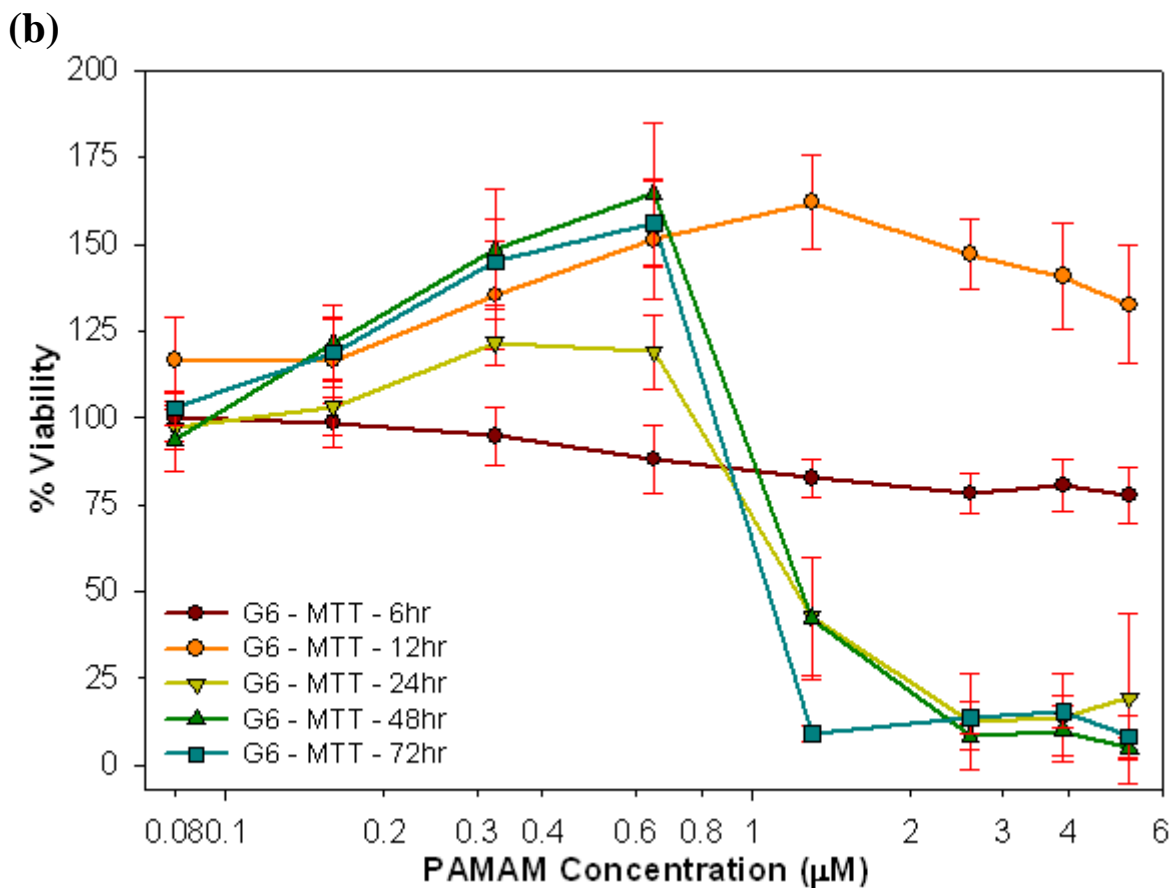
(a)

(b)

Figure 5.8: Alamar Blue (a) and MTT (b) dose dependant toxicity results for PAMAM G6 dendrimers in HaCaT cells after 6, 12, 24, 48 and 72 hours. Viability is calculated as the percentage of living cells as compared to a BSO control. The X-axis is plotted logarithmically to allow for better visualisation of lower doses. Data points are the mean of 18 samples, with error bars showing (±) the standard deviation.

The viability results of the PAMAM G6 dendrimers are similar to those observed in the G4 analysis. In Figure 5.8, for 6 and 12 hour exposure, little toxicity is recorded by AB, although the response is significantly stronger at the later time points. The previously reported EC_{50} obtained form the AB assay for PAMAM G6 dendrimers is in the range of 1μM-1.6μM at 24 hours (*Mukherjee et al., 2010 - B*), which would appear to agree with the

values obtained in this study. However, as was the case for PAMAM G4 exposure, the MTT assay registers increased percentage viability, compared to BSO control, for the intermediate doses, for all but the 6 hour exposure time point. A cytotoxic response is elicited for doses greater than 1μM, for the 24, 48 and 72 hour time points and the response is consistent with the previously reported EC_{50} values of 0.92μM-1.13μM (*Mukherjee et al., 2010 - A*).

5.4.4 PAMAM G4-G6 Comparative Analysis

PAMAM nanoparticle toxicity is a generation dependant process (*Mukherjee et al., 2010 – A* and *B*, *Naha et al., 2010*) therefore, a comparison of the response of BSO treated cells to G4 and G6 dendrimer exposure was performed, to establish whether a similar generation dependence of the cellular responses is still evident.

The AB and MTT assays were compared for PAMAM G4 and G6 dendrimers, and the results are shown in Figures 5.9 (AB) and 5.10 (MTT). For both dendrimers, approximately equivalent concentration ranges were used, although, for the PAMAM G6 dendrimers, a slightly lower initial concentration was used due to the higher associated toxicity (*Mukherjee et al., 2010 – A* and *B*, *Naha et al., 2010* and *Mukherjee and Byrne, 2013*).

(a)
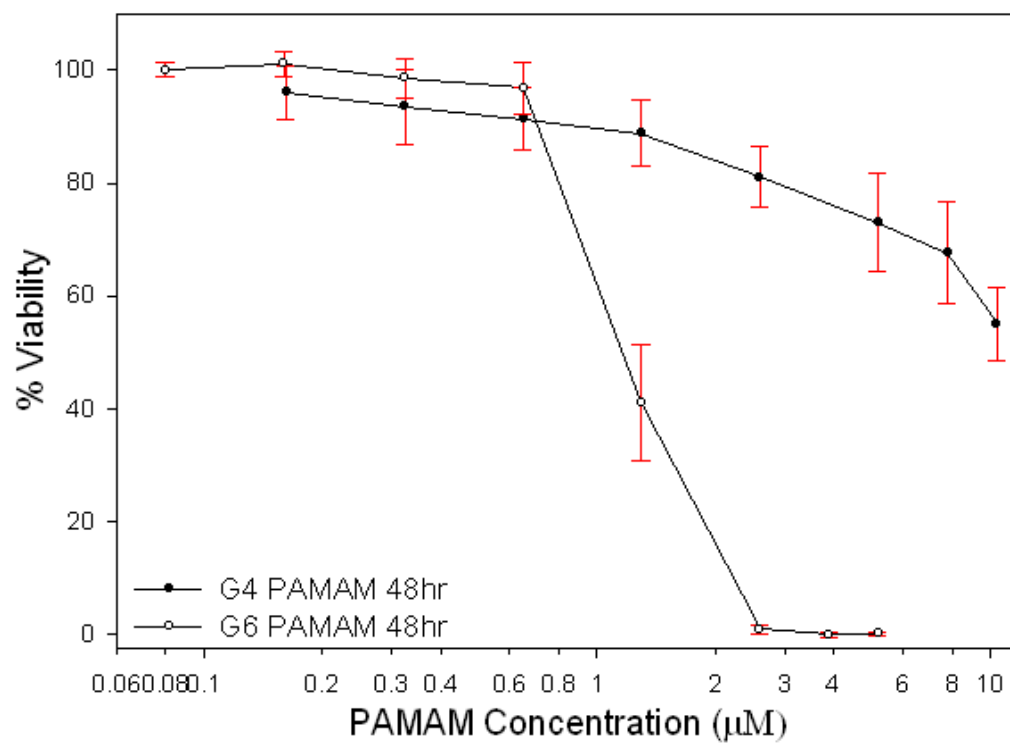
(b)
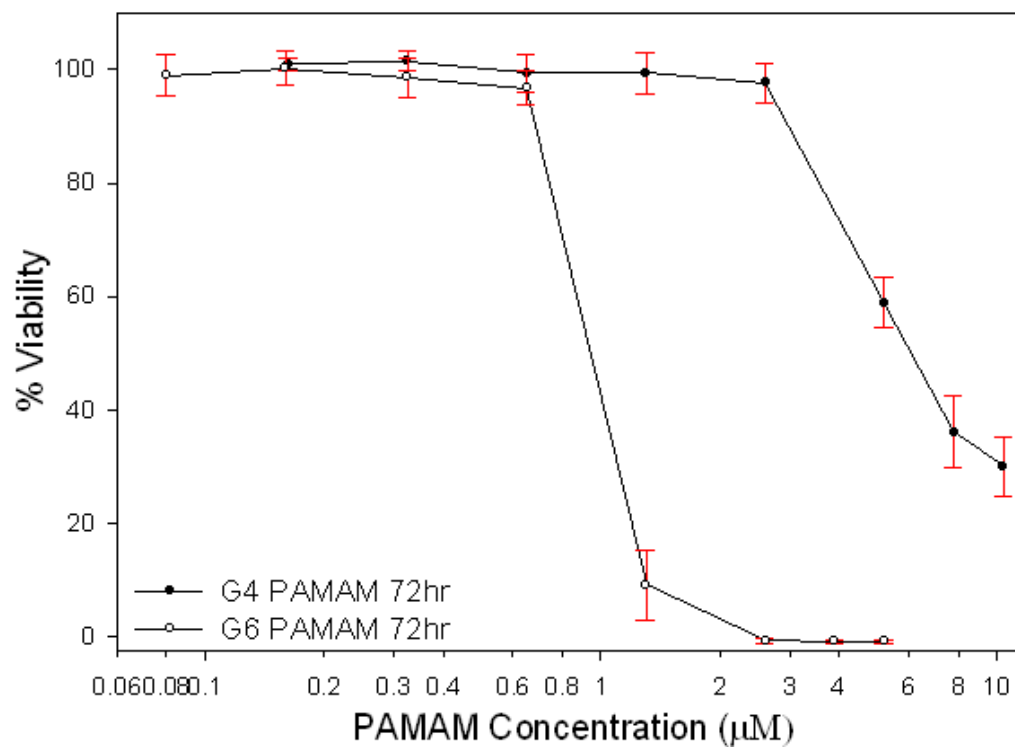
Figure 5.9: Alamar Blue (AB) dose dependant toxicity results comparing the PAMAM G4 and G6 dendrimers in HaCaT cells after 48 hours (a) and 72 hours (b). Viability is calculated as the percentage of living cells as compared to BSO control. Data points are the mean of 18 samples, with error bars showing (±) the standard deviation. The x-axis is plotted logarithmically to allow for better visualisation of lower doses. 6, 12 and 24 hour graphs can be seen in the supplementary information section (Figure S5.6).

Little or no significant cytotoxicity was registered by the AB assay for either dendrimer at the 6 and 12 hour time points. At 24 hours, the higher toxicity associated with the G6 dendrimers becomes apparent, while the G4 still shows no significant change (Supplementary Figure S5.6, c). At 48 hours (Figure 5.9(a)) the G4 dendrimers begin to elicit a significant toxic response and finally, at 72 hours (Figure 5.9(b)), the G4 toxic profile is beginning to match that of G6, although the reduction of viability is much higher for G6.

(a)
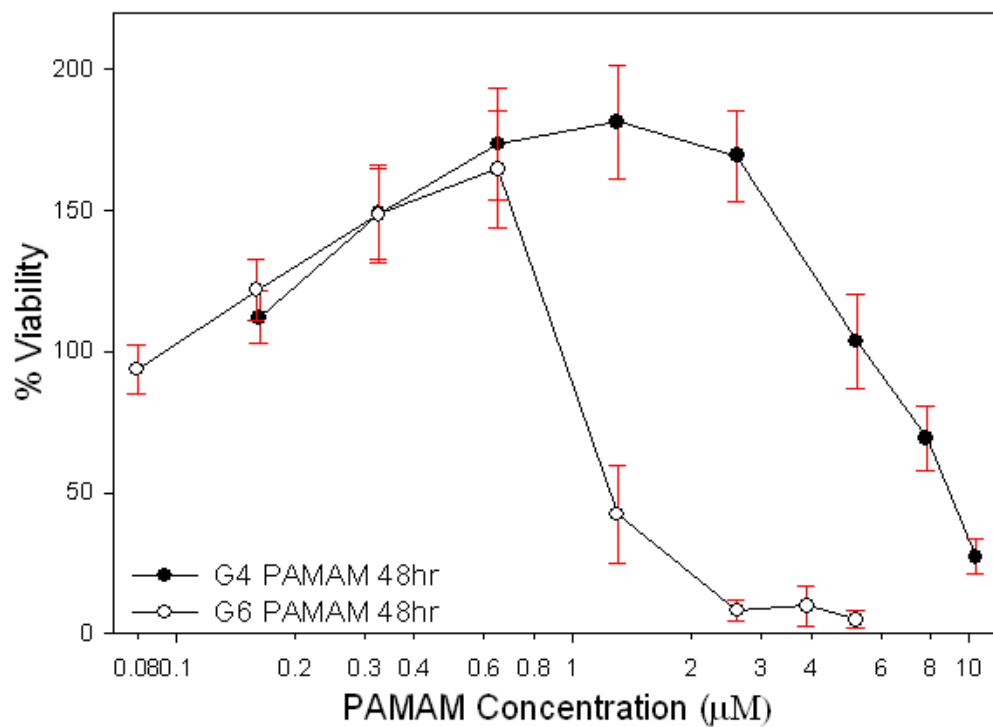
(b)
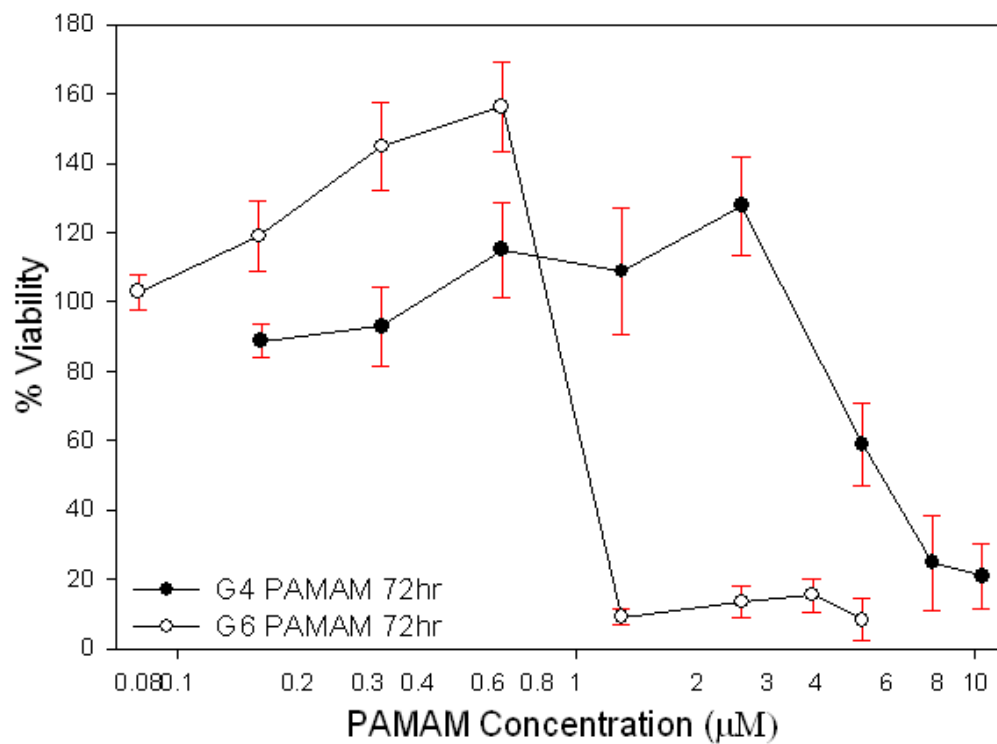
Figure 5.10: MTT dose dependant toxicity results comparing the PAMAM G4 and G6 dendrimers in HaCaT cells after 48 hours (a) and 72 hours (b). Viability is calculated as the percentage of living cells as compared to BSO control. Data points are the mean of 18 samples, with error bars showing (±) the standard deviation. The X-axis is plotted logarithmically to allow for better visualisation of lower doses. 6, 12 and 24 hour graphs can be seen in the supplementary information section (Figure S5.7).

In the MTT, similar to AB response, no significant difference was seen in the 6 hour analysis for the two dendrimers, although differences become apparent at 12 hours (Supplementary Figure S5.7, b), at which point the MTT response increases above that of controls for the G6 dendrimer. This increase in MTT response also occurs for the G4 dendrimers, although, it is not manifest until the later time point of 48 hours (Figure 5.10(a)). Similar to the AB response, cytotoxicity is registered by the MTT assay for both dendrimers beginning at 24 hours; however, the AB only reaches about 50% viability. At 48 and 72 hours a more complete toxic profile for both assays is seen and distinct generation dependence is observable, more consistent with that observed for untreated cells (*Mukherjee et al., 2010 - A*).
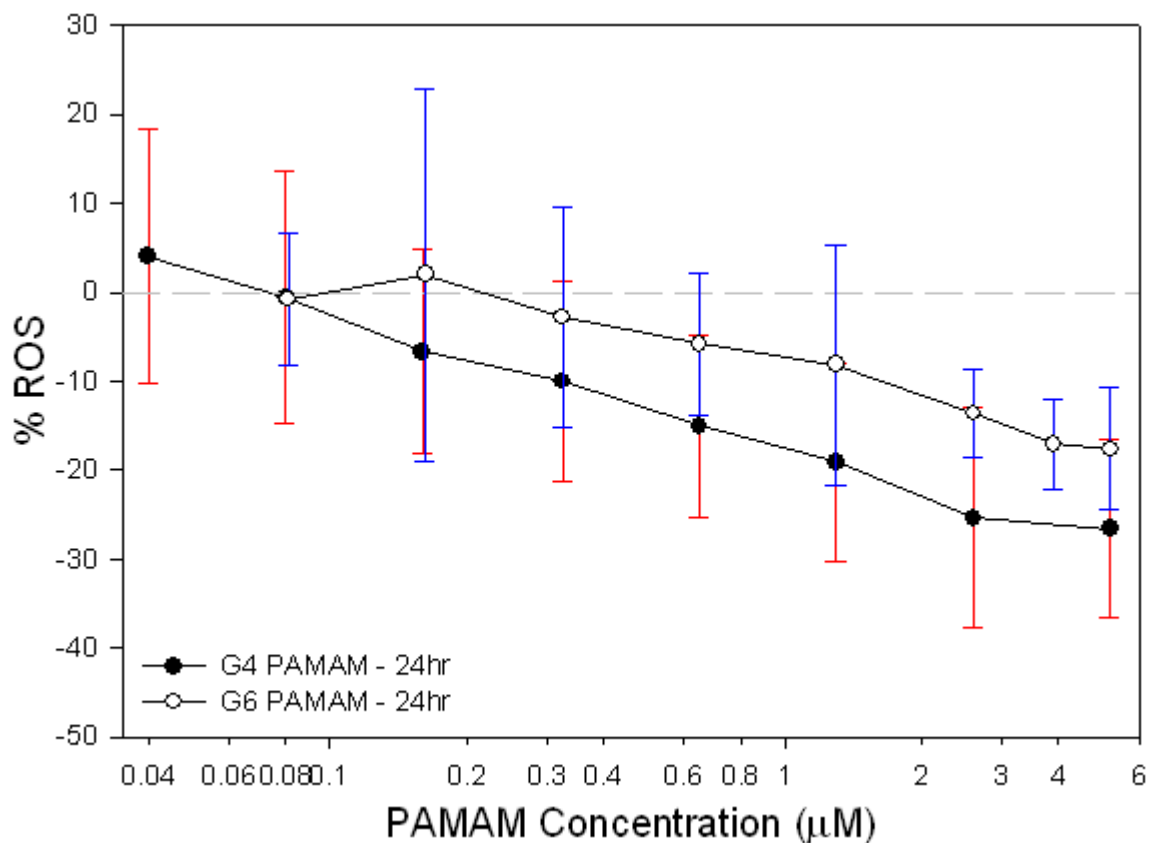
Figure 5.11: Dose dependant generation of ROS in HaCaT cells (shown at 24 hours for PAMAM G4 and G6). Data is compared to BSO control which was set to equal 0%. The X-axis is plotted logarithmically to allow for better visualisation of lower concentrations. Data points are the mean of 18 samples, with error bars showing (±) the standard deviation.

To further investigate any generation dependence, the dose response of the ROS was compared for the G4 and the G6 (Figure 5.11). It is notable that the generation dependence of the trends is reversed in Figure 5.11, where G4 elicits a more pronounced reduction in ROS levels than G6.

5.5 Discussion

The confocal images of Figures: 5.1 and 5.2 (PAMAM G4) and Figures: 5.5 and 5.6 (PAMAM G6) show that, for cells treated with 200μM BSO for 18 hours prior to PAMAM exposure, the rate of endocytosis has been markedly reduced. This reduction in endocytosis is accompanied by a similar reduction in intracellular ROS and a dramatic change in the responses of the cytotoxic assays. Nevertheless, the observed reduction of intracellular ROS and cytotoxic responses are systematically dependent on dendrimer exposure time, dose and generation, consistent with the intracellular action of the dendritic nanoparticles.

The demonstrated mechanism of PAMAM dendrimer toxicity is one of endocytosis (*Mukherjee et al., 2010 – B*, *Kitchens et al., 2007* and *Hong et al., 2004*), ROS production (*Mukherjee et al., 2010 – A* and *B*, *Naha et al., 2010* and *Khalid et al., 2015*), subsequent endosomolysis, whereby the nanoparticle bursts out of the endosome/lysosome into the cytosol (*Watson et al., 2005*), and localisation in the mitochondria (*Lee et al., 2009*). Mukherjee and Byrne (*2013*) identified two apoptotic pathways, the death-receptor pathway (extrinsic, Fas mediated FADD pathway (*Wajant, 2002*)) and the mitochondrial pathway (intrinsic, TNF-α mediated FADD (*Desagher and Martinou, 2000*)) (*Mukherjee and Byrne, 2013*). The former is initiated by the earlier stage ROS generation in the region of the endosomes, while the latter is initiated by the localisation of the dendrimers in the mitochondria. It has been proposed that the early stage ROS production is due to the action of NADPH oxidase (*Xia et al., 2006*) (producing superoxide anions (O_2^-) (*Shuvaev et al., 2011*)) and the v-ATPase proton pump (providing protons (*Nel et al., 2009*), ultimately leading to production of H_2O_2 (*Babior et al., 2002*) in and around the endosome. In cells treated with BSO, however, PAMAM dendrimers elicit a dramatically different

cytotoxicity profile, as registered by the AB and MTT assays, compared to that of untreated cells (*Mukherjee et al., 2010 – A* and *B*).

Studies by Khalid *et al.* (*2015*) of cellular uptake of PPI dendrimers have demonstrated that, although the larger generation PPI dendrimers are endocytosed and elicit similar responses to PAMAM equivalents in HaCaT cells, for smaller generation PPI dendrimers, uptake by passive diffusion occurs and, when the dendrimers enter the cell in this way, they were observed to act as antioxidants and elicit a significantly reduced cytotoxic effect (*Khalid et al., 2015*). BSO exposure has been shown to permeabilise the cell membrane (*Zamam et al., 1995*), and as a result, it is proposed that the PAMAM G4 and G6 dendrimers are able to circumvent the endocytotic process, are uptaken by passive diffusion, and, as PAMAM dendrimers are similar in structure to PPI dendrimers and have comparable surface chemistry, similarly behave as antioxidants in the cytosol, eliciting substantially reduced cytotoxic responses.

Alamar Blue is a non-specific assay and measures cellular viability based on the overall activity of the cytosolic environment (*O'Brien et al., 2000*). The significant reduction, rather than expected increase, of toxicity as registered by this assay reflects the reduction in the endocytosis process (which initiates the Fas mediated FADD (death-receptor) apoptotic pathway), in favour of the passive diffusion of nanoparticles across the membrane, and consequent reduction in ROS generation in the region of endosomes. However, endocytosis is not fully eliminated for either generation, and therefore, the activation of the Fas mediated pathway, on a much reduced scale, would in part explain why the generation dependent response is still observed for the PAMAMs.

The MTT assay measures mitochondrial activity as an indicator of cellular viability (*Mosmann, 1983*, *Denizot and Lang, 1986* and *Hansen et al., 1989*) and, in the case of the studies described here, the mitochondria are implicated in at least two different processes and changes in MTT responses reflect the dose and generation dependence of these processes at several time points. The first process is the loss of GSH from the cell, which has been shown to cause activation of mitochondrial signalling pathways and expression of genes associated with apoptosis, growth and differentiation (*Circu and Aw, 2008*, *Davis et al., 2001*, *Petit et al., 1996* and *Skulachev, 1996*). This overall increase in mitochondrial activity (observed in the low dose regime), is seen as the initial increase in MTT values above controls, associated with dose and generation dependent decrease in ROS below controls, due to the antioxidant effect of the passively uptaken dendrimer nanoparticles.

The second effect gives rise to a sharp decrease in mitochondrial activity (observed in the higher dose regime); consistent with PAMAM dendrimer localisation and disruption of the mitochondria (*Mukherjee et al., 2010 – A* and *B*) initiating the mitochondrial apoptotic pathway, leading to cell death in a dose dependant fashion, as observed for untreated cells (*Mukherjee et al., 2010 – A* and *B*). This process may be accelerated via the opening of the mitochondrial membrane permeability transition pore (*Armstrong and Jones, 2002*, *Chernyak and Bernardi, 1996* and *Reed and Savage, 1995*). Whether passively diffused into the cell, or released into the cytosol by endosomolysis after endocytosis, the result of free PAMAM dendrimers in the cytosol and subsequent localisation to the mitochondria should be equivalent, both resulting in disruption of the mitochondria, a second phase increase in ROS within the cell, subsequent decay in the mitochondrial membrane potential and finally the initiation of a cascade leading to apoptosis (*Mukherjee et al., 2010 – A* and

B, *Naha et al., 2010* and *Mukherjee and Byrne, 2013*). It should also be noted that in both cases the opening of the mitochondrial membrane transition pore occurs, either by the action of BSO (*Armstrong and Jones, 2002*, *Chernyak and Bernardi, 1996* and *Reed and Savage, 1995*) or due to the release of the endosomal/lysosomal contents causing intracellular release of Ca^{2+}, leading to calcium dependant opening of the pore (*Xia et al., 2008*). This would, in both cases, facilitate the entry of the dendrimer to the mitochondria. As a result, in the high dose regime, the observed toxic response of the BSO treated cells, as registered by the MTT assay, is not very different to that observed for untreated cells.

The passive diffusion of dendrimers across the cell membrane is a size dependant process (*Khalid et al., 2015*) and, the generation dependence of the cellular responses to the two PAMAM dendrimer generations, G4 and G6, (Figures: 5.1, 5.2, 5.5 and 5.6), is consistent with a higher uptake rate for the G4 dendrimer than the G6. The greater reduction of intensity of Rab-5a-RFP compared to controls (with no BSO treatment), G4 dendrimers (70%) compared to G6 (60%), indicates a higher diffusion rate for G4 dendrimers, leaving fewer available for endocytosis. This further explains the higher rate of anti-oxidative activity exhibited by the G4 dendrimers when compared to G6 (Figure 5.11). Overall, it would appear that the membrane has become more permeable to an extent that favours passive uptake, although not completely eliminating active endocytosis.

Within the framework of Adverse Outcome Pathways (AOPs), recently endorsed by the OECD (*OECD, 2007* and *OECD, 2013*) as a method to simplify the representation of the mode of action of a toxicant or agonist, the generation of ROS can be considered the key Molecular Initiating Event (MIE) of the AOP, which ultimately leads to the AO of loss of cell viability. The treatment with BSO causes a depletion of GSH, which would lead to the

expectation of much increased ROS levels after endocytosis. However, that was not observed and the result of the reduction of intrinsic GSH levels by BSO treatment was predominantly the increased permeability of the cell membrane, resulting in an increased rate of uptake of the PAMAM dendrimers by passive diffusion, making it a favoured uptake mechanism, more so for the smaller G4 dendrimer than the larger G6. The co-existence of the parallel uptake mechanisms increases the complexity of any model to describe the *in vitro* system, although it could prove a useful model to develop networks of AOPs, initiated by different MIEs. However, to fully examine the effect of reduction of GSH in terms of decreased anti-oxidant activity alone, an assay which did not cause decrease of the permeabilisation of the cell membrane would be necessary.

Considering the potential for PAMAM dendrimers in nanomedical applications, it is important to note that, when diffused into the cell, the aminated surface chemistry of the dendrimers lend them antioxidant activity, similar to small molecular anti-oxidants, such as N-acetylcysteine (NAC) and NAC amide (NACA - a more bio-available version of NAC). NACA has been extensively studied as an antioxidant in the cell, due to its ability to diffuse across the membrane and the presence of a terminal proton donor group (*Price et al., 2006* and *Grinberg et al., 2005*). Interestingly, it has also been shown to completely reverse the damage caused to the cell by depletion of GSH (*Carey et al., 2011*, *Penugonda et al., 2005* and *Sunitha et al., 2013*). NACA, due to this strong anti-oxidant ability, has been proposed in the treatment of several disorders and diseases, such as: HIV (*Banerjee et al., 2010*), Alzheimer's and Parkinson's disease (*Penugonda et al., 2005* and *Lee et al., 2007*), cataract formation (*Carey et al., 2011*), retinal degeneration (*Schimel et al., 2011*) and essentially any disease where ROS is identified as the potential MIE (*Sunitha et al., 2013*, and

references therein). If PAMAM dendrimers are seen to act in a similar way, it may potentially allow for their use in a plethora of different nano-medical applications. As a strategy for drug release, endosomolysis can be extremely disruptive to the cell (*Mukherjee, 2012*) and therefore, in the case of cationic nanoparticles for intracellular nanomedical applications, avoiding the process of endocytosis may be a valid strategy to pursue (*Guarnieri et al., 2014*). In terms of therapeutic applications, direct entry into the cytosol may be a more convenient route for drug or gene delivery.

5.6 Conclusions

Although PAMAM dendritic nanoparticles are known to elicit significant cytotoxic responses *in vitro*, the cellular response mechanisms can be notably altered by treatment of the cells with BSO. The treatment increases the cell membrane permeability, enabling uptake of the particles by passive diffusion, where after, they act as antioxidants in the cytosol, rather than producing oxidative stress in the region of endosomes. The ability to tune the cellular uptake mechanism allows direct entry into the cytosol and may have important implications for nanotoxicity as well as drug and gene delivery using nanovehicles.

5.7 Acknowledgements

5.8 References

- Anguissola, S., Garry, D., Salvati, A., O'Brien, P.J. and Dawson, K.A. 2014. High Content Analysis Provides Mechanistic Insights on the Pathways of Toxicity Induced by Amine-Modified Polystyrene Nanoparticles. *PLoS ONE*, **9**(9), e108025. doi:10.1371/journal.pone.0108025

- Armstrong, J.S. and Jones, D.P. 2002. Glutathione depletion enforces the mitochondrial permeability transition and causes cell death in Bcl-2 overexpressing HL60 cells. *FASEB J.,* **16**(10), 1263-1265.

- Babior, B.M., Lambeth, J.D. and Nauseef, W. 2002. The neutrophil NADPH oxidase. *Arch. Biochem. Biophys.,* **397**(2), 342–344.

- Banerjee, A., Zhang, X., Manda, K.R., Banks, W.A. and Ercal, N. 2010. HIV proteins (gp120 and Tat) and methamphetamine in oxidative stress-induced damage in the brain: potential role of the thiol antioxidant N-acetylcysteine amide. *Free Radic. Biol. Med*., **48**(10), 1388-1398.

- Beatrice, M.C., Stiers, D.L. and Pfeiffer, D.R. 1984. The role of glutathione in the retention of Ca^{2+} by liver mitochondria. *J. Biol. Chem.,* **259**(2), 1279–1287.

- Carey, J.W., Pinarci, E.Y., Penugonda, S., Karacal, H. and Ercal, N. 2011. *In vivo* inhibition of l-buthionine-(S,R)-sulfoximine-induced cataracts by a novel antioxidant, N-acetylcysteine amide. *Free Radic. Biol. Med*., **50**(6), 722–729.

- Chernyak, B.V. and Bernardi, P. 1996. The mitochondrial permeability transition pore is modulated by oxidative agents through both pyridine nucleotides and glutathione at two separate sites. *Eur. J. Biochem.,* **238**(3), 623–630.

- Circu, M.L. and Aw, T.Y. 2008. Glutathione and apoptosis. *Free Radic. Res.,* **42**(8), 689–706.

- Davis, W.Jr., Ronai, Z. and Tew, K.D. 2001. Cellular thiols and reactive oxygen species in drug-induced apoptosis. *J. Pharmacol. Exp. Ther.,* **296**(1), 1–6.

- De Jong, W. H. and Borm, P.J.A. 2008. Drug delivery and nanoparticles: Applications and hazards. *Int. J. Nanomedicine.,* **3**(2), 133–149.

- Denizot, F. and Lang, R. 1986. Rapid colorimetric assay for cell growth and survival: Modifications to the tetrazolium dye procedure giving improved sensitivity and reliability. *J. Immunol. Methods.,* **89**(2), 271-277.

- Desagher, S. and Martinou, J.C. 2000. Mitochondria as the central control point of apoptosis. *Trends Cell Biol.,* **10**(9), 369-377.

- Duncan, R. and Izzo, L. 2005. Dendrimer biocompatibility and toxicity. *Adv. Drug. Deliv. Rev.,* **57**(15), 2215– 2237.

- Eichman, J.D., Bielinska, A.U., Kukowska-Latallo, J.F. and Baker, J.R.Jr. 2000. The use of PAMAM dendrimers in the efficient transfer of genetic material into cells. *J. Pharm. Sci. Technol.,* **3**(7), 233-245.

- Girard, P-M., Graindorge, D., Smirnova, V., Rigolet, P., Francesconi, S., Scanlon, S. and Sage, E. 2013. Oxidative Stress in Mammalian Cells Impinges on the Cysteines Redox State of Human XRCC3 Protein and on Its Cellular Localization. *PLoS ONE.,* DOI: 10.1371/journal.pone.0075751

- Griffith, O.W. 1982. Mechanism of Action, Metabolism, and Toxicity of Buthionine Sulfoximine and Its Higher Homologs, Potent Inhibitors of Glutathione Synthesis. *J. Biol. Chem.,* **257**(22), 13704-13712.

- Grinberg, L., Fibach, E., Amer, J. and Atlas, D. 2005. N-acetylcysteine amide, a novel cell permeating thiol, restores cellular glutathione and protects human red blood cells from oxidative stress. *Free Radic. Biol. Med.,* **38**(1), 136–145.

- Guarnieri, D., Sabella, S., Muscetti, O., Belli, V., Malvindi, M.A., Fusco, S., De Luca, E., Pompa, P.P. and Netti, P.A. 2014. Transport across the cell-membrane

dictates nanoparticle fate and toxicity: a new paradigm in nanotoxicology. *Nanoscale,* 6(17), 10264-10273.

- Hansen, M.B., Nielsen, S.E. and Berg, K. 1989. Re-examination and further development of a precise and rapid dye method for measuring cell growth/cell kill. *J. Immunol. Methods,* **119**(2), 203-210.

- He, Y-Y., Huang, J-L., Ramirez, D.C. and Chignell, C.F. 2003. Role of Reduced Glutathione Efflux in Apoptosis of Immortalized Human Keratinocytes Induced by UVA. *J. Biol. Chem.,* **278**(10), 8058–8064.

- Hipkiss A.R. 2009. Carnosine and its possible roles in nutrition and health. *Adv. Food Nutr. Res.,* **57**(2009), 87-154.

- Hong, S., Bielinska, A.U., Mecke, A., Keszler, B., Beals, J.L., Shi, X., Balogh, L., Orr, B.G., Baker, J.R.Jr and Banaszak Holl, M.M. 2004. Interaction of poly(amidoamine) dendrimers with supported lipid bilayers and cells: hole formation and the relation to transport. *Bioconjugate Chem.,* **15**(4), 774–782.

- Jain, K.K., Kesharwani, P., Gupta, U. and Jain, N.K. 2010. Dendrimer toxicity: Let's meet the challenge. *Int. J. Pharm.,* **394**(1-2), 122–142.

- Khalid, H., Mukherjee, S.P., O'Neill, L. and Byrne, H.J. 2016. Structural dependence of the *In vitro* cytotoxicity, oxidative stress and uptake mechanisms of Poly (propylene imine) dendritic nanoparticles. *J. Appl. Toxicol.*, **36**(3), 464–473.

- Kitchens, K.M., Foraker, A.B., Kolhatkar, R.B., Swaan, P.W., Ghandehari, H. 2007. Endocytosis and interaction of poly (Amidoamine) dendrimers with Caco-2 cells. *Pharmaceut. Res.,* **24**(11), 2138–2145.

- Lash, L.H. 2006. Mitochondrial Glutathione Transport: Physiological, Pathological and Toxicological Implications. *Chem. Biol. Interact.,* **163**(1-2), 54–67.

- Lee, J.H., Cha, K.E., Kim, M.S., Hong, H.W., Chung, D.J., Ryu, G. and Myung, H. 2009. Nanosized polyamidoamine (PAMAM) dendrimer-induced apoptosis mediated by mitochondrial dysfunction. *Toxicol. Lett.,* **190**(2), 202–207.

- Lee, K.S., Kim, S.R., Park, H.S., Park, S.J., Min, K.H., Lee, K.Y., Choe, Y.H., Hong, S.H., Han, H.J., Lee, Y.R., Kim, J.S., Atlas, D. and Lee, Y.C. 2007. A novel thiol compound, N-acetylcysteine amide, attenuates allergic airway disease by regulating activation of NF-kappaB and hypoxia-inducible factor-1alpha. *Exp. Mol. Med.,* **39**(6), 756-768.

- Li, X.Y., Donaldson, K., Rahman, I. and Mac Nee, W. 1994. An investigation of the role of glutathione in increased epithelial permeability induced by cigarette smoke *in vivo* and *in vitro*. *Am. J. Respir. Crit. Care Med.,* **149**(6), 1518-1525.

- Lotito, S.B. and Frei, B. 2004. Relevance of apple polyphenols as antioxidants in human plasma: contrasting *in vitro* and *in vivo* effects. *Free Radic. Biol. Med.,* **36**(2), 201-211.

- Lotscher, H.R., Winterhalter, K.H., Carafoli, E. and Richter, C. 1979. Hydroperoxides can modulate the redox state of pyridine nucleotides and the calcium balance in rat liver mitochondria. *Proc. Natl. Acad. Sci. USA,* **76**(9), 4340–4344.

- Lunov, O., Syrovets, T., Loos, C., Beil, J., Delacher, M., Tron, K., Nienhaus, G.U., Musyanovych, A., Mailänder, V., Landfester, K. and Simmet, T. 2011. Differential Uptake of Functionalized Polystyrene Nanoparticles by Human Macrophages and a Monocytic Cell Line. *ACS Nano.,* **5**(3), 1657-1669.

- Madesh, M., Benard, O. and Balasubramanian, K.A. 1998. Glutathione modulates lipid composition of human colon derived HT-29 cells. *Int. J. Biochem. Cell Biol.,* **30**(12), 1345-1352.

- Maher, M.A., Naha, P.C., Mukerjee, S.P. and Byrne, H.J. 2014. Numerical simulations of *in vitro* nanoparticle toxicity – the case of Poly(amido amine) dendrimers. *Toxicol. In Vitro,* **28**(8), 1449-1460.

- Mosmann, T. 1983. Rapid colorimetric assay for cellular growth and survival: Application to proliferation and cytotoxicity assays. *J. Immunol. Methods,* **65**(1), 55-63.

- Mozdzan, M., Szemraj, J., Rysz, J., Stolarek, R.A. and Nowak, D. 2006. Anti-oxidant activity of spermine and spermidine re-evaluated with oxidising system involving iron and copper ions. *Int. J. Biochem. Cell Biol.,* **38**(1), 69-81.

- Mukherjee S.P. and Byrne, H.J. 2013. Polyamidoamine Dendrimer Nanoparticle Cytotoxicity, Oxidative Stress, Caspase Activation and Infammatory Response: Experimental Observation and Numerical Simulation. *Nanomed. Nanotech. Biol. Med.,* **9**(2), 202-211.

- Mukherjee, S.P. 2012. Towards Structure Activity Relationships for *in vitro* Toxicity of Polyamidoamine Dendritic Nanoparticles. *Thesis (PhD)*, Dublin Institute of Technology: 2012. Dublin: DIT.

- Mukherjee, S.P., Davoren, M. and Byrne, H.J. 2010. *In vitro* mammalian cytotoxicological study of PAMAM dendrimers - towards quantitative structure activity relationships. *Toxicol. in Vitro,* **24**(1), 169-177.

- Mukherjee, S.P., Lyng, F.M., Garcia, A., Davoren, M. and Byrne H.J. 2010. Mechanistic studies of *in vitro* cytotoxicity of Poly(amidoamine) dendrimers in mammalian cells. *Toxicol. Appl. Pharmacol.,* **248**(3), 259–268.

- Nabeshi, H., Yoshikawa, T., Matsuyama, K., Nakazato, Y., Tochigi, S., Kondoh, S., Hirai, T., Akase, T.,Nagano, K., Abe, Y., Yoshioka, Y., Kamada, H., Itoh, N., Tsunoda, S. and Tsutsumi, Y. 2011. Amorphous nanosilica induce endocytosis dependent ROS generation and DNA damage in human keratinocytes. *Part. Fibre Toxicol.,* **8**(1), 10 pages.

- Naha, P.C., Davoren, M., Lyng, F.M. and Byrne, H.J. 2010. Reactive Oxygen Species (ROS) induced cytokine production and cytotoxicity of PAMAM dendrimers in J774A.1 cells. *Toxicol. Appl. Pharmacol.,* **246**(1-2), 91-99.

- Nel, A., Xia, T., Mädler, L. and Li, N. 2006. Toxic potential of materials at the nanolevel. *Science,* **311**(5761), 622-627.

- Nel, A.E., Mädler, L., Velegol, D., Xia, T., Hoek, E.M.V., Somasundaran, P., Klaessig, F., Castranova, V. and Thompson, M. 2009. Understanding

biophysicochemical interactions at the nano–bio interface. *Nature Materials*, **8**(7), 543 – 557.

- O'Brien, J., Wilson, I., Orton, T. and Pognan, F. 2000. Investigation of the Alamar Blue (resazurin) fluorescent dye for the assessment of mammalian cell cytotoxicity. *Eur. J. Biochem.,* **267**(17), 5421-5426.

- Olafsdottir, K., Pascoe, G.A. and Reed, D.J. 1988. Mitochondrial glutathione status during Ca2+ ionophore-induced injury to isolated hepatocytes. *Arch. Biochem. Biophys.,* **263**(1), 226–235.

- Organisation for Economic Co-Operation and Development (OECD). 2007. Guidance Document on the Validation of (Quantative) Structure Activity Relationships [(Q)SAR] Models, *OECD, ENV/JM/MONO(2007)2*.

- Organisation for Economic Co-Operation and Development (OECD). 2013. Guidance Document On Developing and Assessing Adverse Outcome Pathways, *OECD, ENV/JM/MONO(2013)6*.

- Paget, V., Dekali, S., Kortulewski, T., Grall, R., Gamez, C., Blazy, K., Aguerre-Chariol, O., Chevillard, S., Braun, A., Rat, P and Lacroix, G. 2015. Specific Uptake and Genotoxicity Induced by Polystyrene Nanobeads with Distinct Surface

Chemistry on Human Lung Epithelial Cells and Macrophages. *PLoS ONE,* **10**(4), e0123297. doi:10.1371/journal.pone.0123297

- Penugonda, S., Mare, S., Goldstein, G., Banks, W.A. and Ercal, N. 2005. Effects of N-acetylcysteine amide (NACA), a novel thiol antioxidant against glutamate-induced cytotoxicity in neuronal cell line PC12. *Brain Research,* **1056**(2), 132–138.

- Petit, P.X., Susin, S.A., Zamzami, N., Mignotte, B. and Kroemer, G. 1996. Mitochondria and programmed cell death: Back to the future. *FEBS Lett.,* **396**(1), 7–13.

- Price, T.O., Uras, F., Banks, W.A. and Ercal, N. 2006. A novel antioxidant N-acetylcysteine amide prevents gp120- and Tat-induced oxidative stress in brain endothelial cells. *Exp. Neurol.,* **201**(1), 193–202.

- Reed, D.J. and Savage, M.K. 1995. Influence of metabolic inhibitors on mitochondrial permeability transition and glutathione status. *Biochim. Biophys. Acta.,* **1271**(1), 43–50.

- Schimel, A.M., Abraham, L., Cox, D., Sene, A., Kraus, C., Dace, D.S., Ercal, N. and Apte, R.S. 2011. N-acetylcysteine amide (NACA) prevents retinal degeneration by up-regulating reduced glutathione production and reversing lipid peroxidation. *Am. J. Pathol.,* **178**(5), 2032-2043.

- Shuvaev, V.V., Han, J., Yu, K.J., Huang, S., Hawkins, B.J., Madesh, M., Nakada, M. and Muzykantov, V.R. 2011. PECAM-targeted delivery of SOD inhibits endothelial inflammatory response. *FASEB J.,* **25**(1), 348-357.

- Skulachev, V.P. 1996. Why are mitochondria involved in apoptosis? Permeability transition pores and apoptosis as selective mechanisms to eliminate superoxide-producing mitochondria and cells. *FEBS Lett.,* **397**(1), 7–10.

- Sunitha, K., Hemshekhar, M., Thushara, R.M., Santhosh, M.S., Yariswamy, M., Kemparaju, K. and Girish, K.S. 2013. N-Acetylcysteine amide: a derivative to fulfill the promises of N-Acetylcysteine. *Free Radic. Res.,* **47**(5), 357-367.

- Tobi, S.E., Paul, N. and McMillan T.J. 2000. Glutathione modulates the level of free radicals produced in UVA-irradiated cells. *J. Photochem. Photobiol. B.,* **57**(2-3), 102–112.

- Wajant, H. 2002. The Fas signaling pathway: more than a paradigm. *Science,* **296**(5573), 1635-1636.

- Watson, P., Jones, A.T. and Stephens, D.J. 2005. Intracellular trafficking pathways and drug delivery: fluorescence imaging of living and fixed cells. *Adv. Drug Deliver. Rev.,* **57**(1), 43-61.

- Xia, T., Kovochich, M., Brant, J., Hotze, M., Sempf, J., Oberley, T., Sioutas, C., Yeh, J.I., Wiesner, M.R. and Nel, A.E. 2006. Comparison of the Abilities of Ambient and Manufactured Nanoparticles to Induce Cellular Toxicity According to an Oxidative Stress Paradigm. *Nano Lett.,* **6**(8), 1794-1807.

- Xia. T., Kovochich, M., Liong, M., Mädler, L., Gilbert, B., Shi, H., Yeh, J.I., Zink, J.I. and Nel, A.E. 2008. Comparison of the mechanism of toxicity of zinc oxide and cerium oxide nanoparticles based on dissolution and oxidative stress properties. *ACS Nano,* **2**(10), 2121-2134.

- Zaman, G.J., Lankelma, J., van Tellingen, O., Beijnen, J., Dekker, H., Paulusma, C., Oude Elferink, R.P., Baas, F. and Borst, P. 1995. Role of glutathione in the export of compounds from cells by the multidrug-resistance-associated protein. *Proc. Natl. Acad. Sci. USA,* **92**(17), 7690-7694.

- Zinchuk, V. and Zinchuk, O. 2008. Quantitative colocalization analysis of confocal fluorescence microscopy images. *Curr. Protoc. Cell Biol,* **Ch.4**(Unit 4.19), 1-16.

5.9 Supplementary Information for Chapter 5:

5.9.1 Effect of 200μM BSO on HaCaT Cell Viability
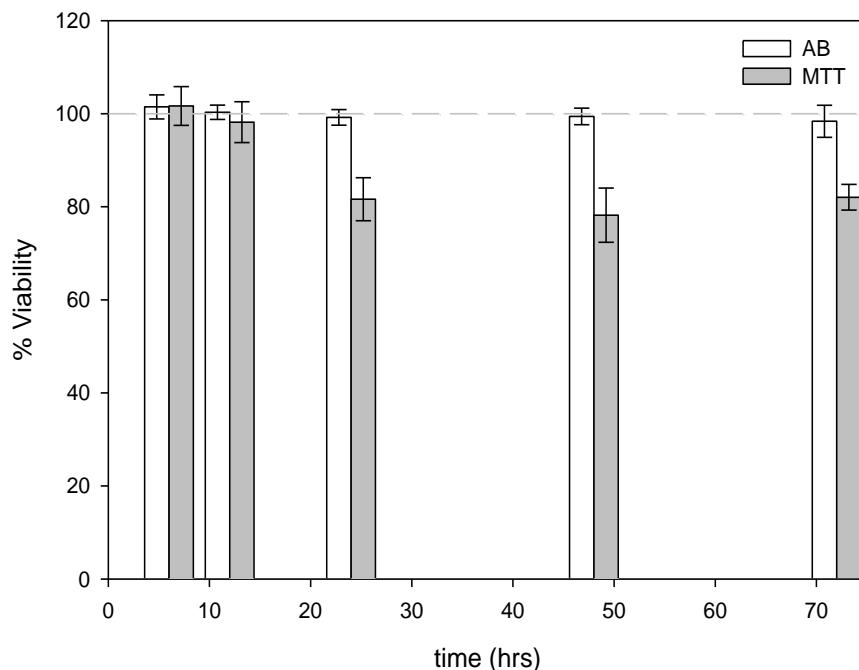
Figure S5.1: Graph comparing unexposed control cells (dashed line) to cells with 200μM BSO at 6, 12, 24, 48 and 72 hours as registered by the AB and MTT assays (white and grey bars, respectively). Data points are the mean of 18 samples, with error bars showing (±) the standard deviation.

Figure S5.1 shows the %Viability of cells with 200μM BSO compared to unexposed cells (set at 100% Viability). The results show no difference for AB at all time points and no difference for MTT at 6 and 12 hours. For 24, 48 and 72 hours, the MTT drops to around 80% Viability. To account for this, all values for PAMAM exposures were compared to the control with 200μM BSO to show changes cause by the dendrimer presence only.
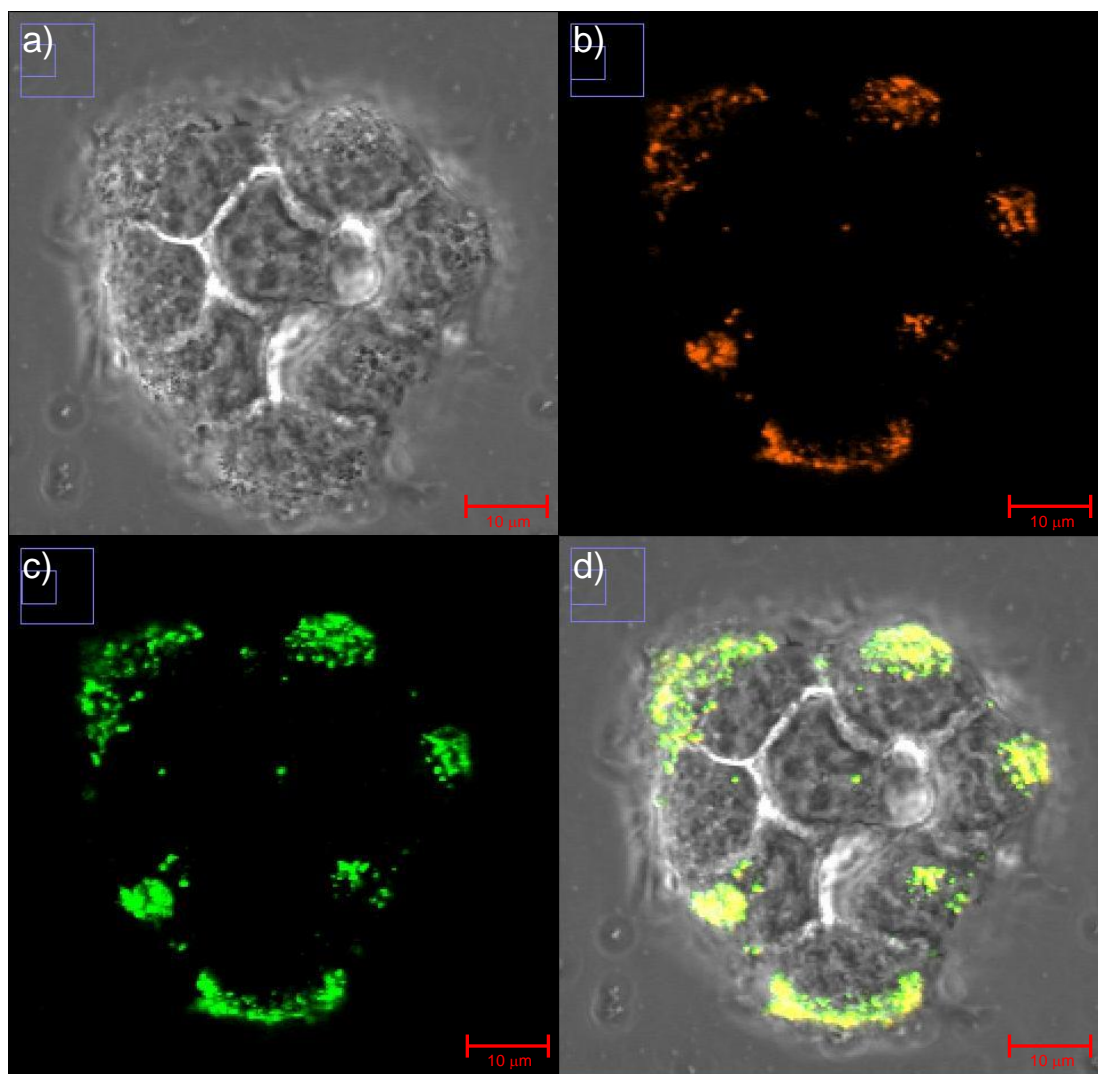
Figure S5.2: Confocal images of HaCaT (live) cells, upon exposure to 1μM PSNP 100nm with green fluorescent dye bound. Image a) shows the greyscale picture of the cells, Image b) shows the fluorescence generated by the early endosomal red fluorescent protein, Image c) shows the fluorescence generated by 100nm PSNP and Image d) shows the overlay of images a-c, where yellow coloured areas indicate the simultaneous presence of endosomes and PSNP (100nm).

100nm PSNP are known to be taken into the cell via endocytosis. Therefore, they were used as a positive control to conform that the early endosome red fluorescent protein was functioning as expected. 100nm PSNP had a green fluorescent dye bound to allow for their visualisation in the cell. It is important to note that, in this image, contrary to the images in the main text, green indicates the presence of 100nm PSNP and not ROS. The yellow colour seen in Figure S5.2d indicates that the PSNP and endosomes are located at the same area in the cell and therefore the red fluorescent protein is functioning as expected and the sites of endosomal activity can be visualised. This is supported by co-localisation analysis (using Manders split coefficients calculated with the JACoP plugin for ImageJ) that shows 90($\pm$2)% of the 100nm PSNP are located within endosomes and 98($\pm$1)% of endosomal formation correlates with the presence of 100nm PSNP.

5.9.3: Effect of BSO on HaCaT cells.
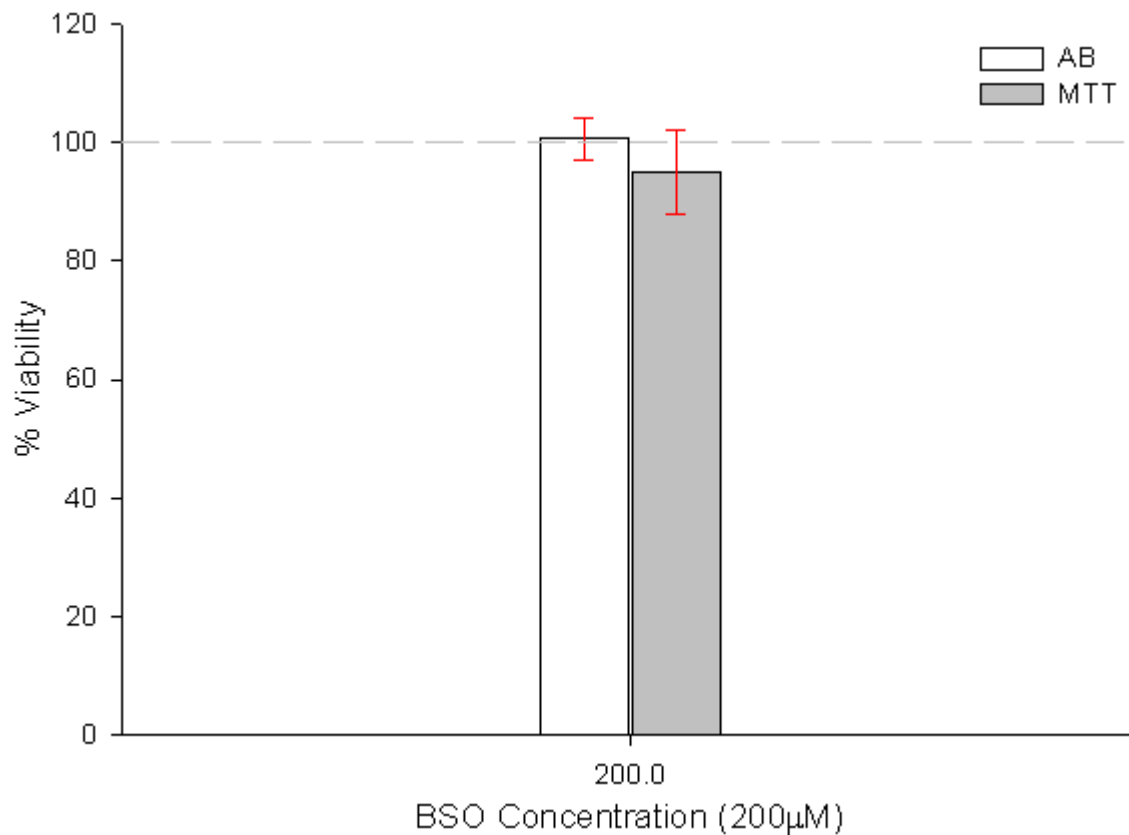
Figure S5.3: The % Cellular Viability (compared to unexposed control) according to the

AB and MTT assays, for 200μM BSO in the Human Keratinocyte (HaCaT) cell line.

Figure S5.3 shows the % Viability (registered by AB and MTT) for HaCaT cells when

exposed to 200μM BSO for 18 hours. The results show no adverse effect on cell viability.

5.9.4 Full Dose dependant ROS at all time points

Figure S5.4: The full dose dependant ROS production for PAMAM G4 for times: 0, 1, 2, 3, 4, 6, 12 and 24 hours. a) Shows the results with the associated error bars (± standard deviation) and b) Shows the data without the error bars, to allow for easier visualisation of the overall trend. As with graphs in the main text, the x-axis is plotted logarithmically to allow for better visualisation of lower doses. Data points are the mean of 18 samples, with error bars showing (±) the standard deviation.

Figure S5.5: The full dose dependant ROS production for PAMAM G6 for times: 0, 1, 2, 3, 4, 6, 12 and 24 hours. a) Shows the results with the associated error bars (± standard

Figures S5.4 and S5.5 show the dose dependant reduction in ROS for all time points tested: 0-24 hours, for PAMAM G4 (Figure S5.4) and PAMAM G6 (Figure S5.5). Each graph is shown with the associated error bars (a) and then again without the error bars (b) to allow for a clearer visual of the overall trend observed. The graphs appear to follow a time and dose dependant reduction in % ROS, with only a slight deviation for the 12 hour result for PAMAM G4.

5.9.5 6, 12 and 24 hour Cell Viability Results
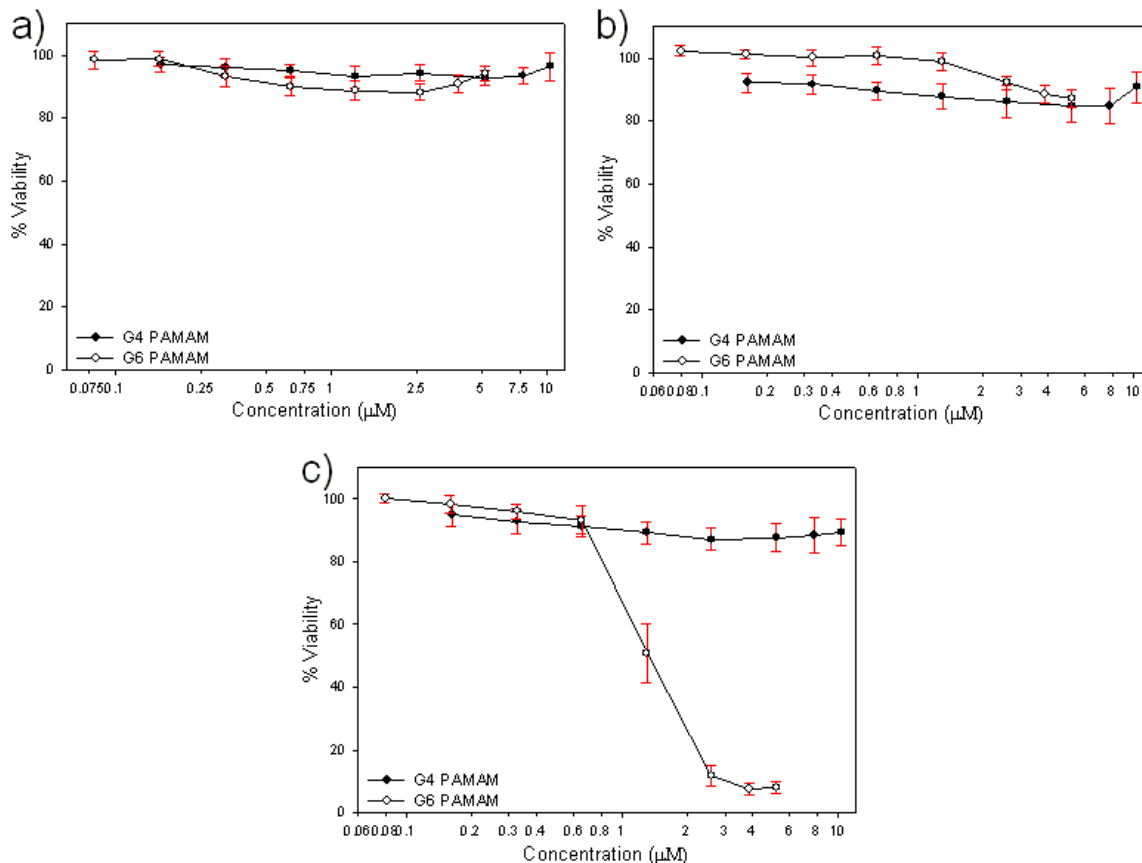
Figure S5.6: Alamar Blue (AB) dose dependant toxicity results comparing the PAMAM G4 and G6 dendrimers in HaCaT cells after 6(a), 12(b) and 24 hours(c). Viability is calculated as the percentage of living cells as compared to a 200µM BSO control. Results are shown as mean ± standard deviation. The X-axis is plotted logarithmically to allow for better visualisation of lower doses. Data points are the mean of 18 samples, with error bars showing (±) the standard deviation.

Figure S5.6 shows the 6, 12 and 24 hours percentage viability as registered by the AB assay for the PAMAM G4 and G6. The 6 and 12 hour show little change in viability for both generations of nanoparticle, only at 24 hours is a change noted for the G6 viability.

The G6 EC_{50} would appear to be in the range of 1μM-2μM, consistent with previous experiments performed without BSO treatment, from which an EC_{50} of 1μM-1.6μM was obtained (*Mukherjee et al., 2010-A*).
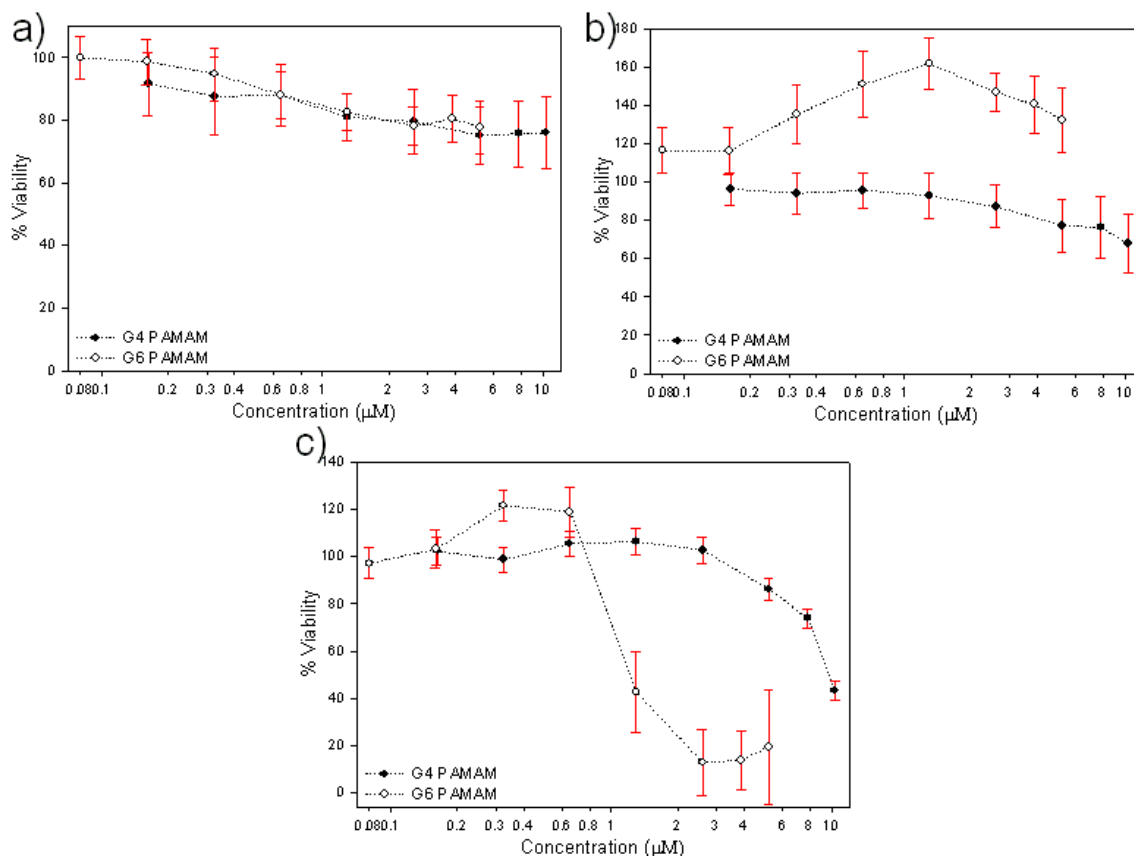
Figure S5.7: MTT dose dependant toxicity results comparing the PAMAM G4 and G6 dendrimers in HaCaT cells after 6(a), 12(b) and 24 hours(c). Viability is calculated as the percentage of living cells as compared to a 200μM BSO control. Results are shown as mean ± standard deviation. The X-axis is plotted logarithmically to allow for better visualisation of lower doses. Data points are the mean of 18 samples, with error bars showing (±) the standard deviation.

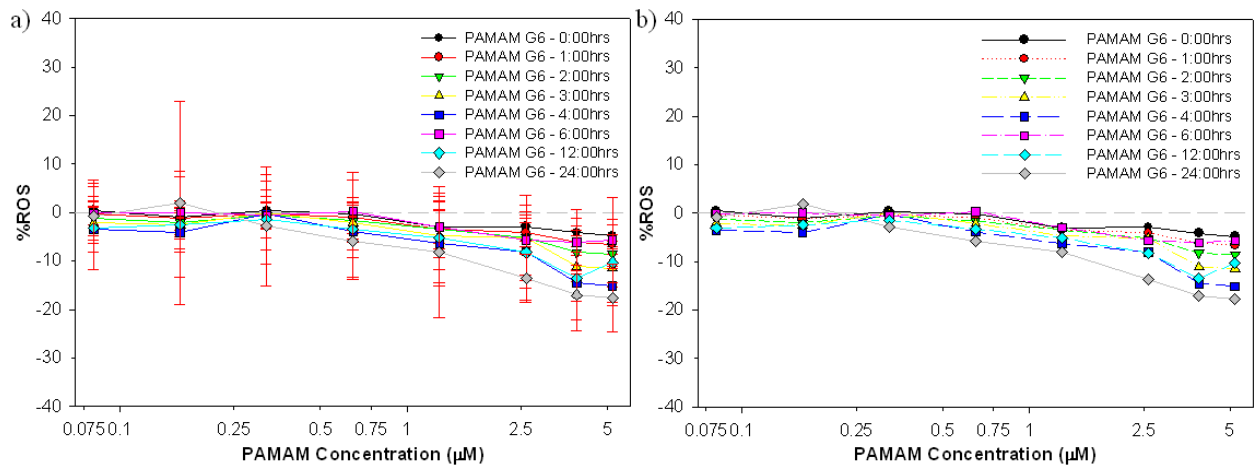Figure S5.7 shows the 6, 12 and 24 hours percentage viability, as registered by the MTT assay for the PAMAM G4 and G6. Little change is noted at the 6 hour time point. However, as the test progresses to 12 hours the G6 viability is seen to increase, while the G4 shows a slight decrease. At 24 hours, the increase seen in G6 begins to subside and some loss of viability is observed, while the G4 treatment shows a slight increase and subsequent loss of viability at the higher doses. The MTT data indicates an EC_{50} between 0.8μM-2μM, consistent with experimental results, performed without BSO treatment, from which an EC_{50} of 0.92μM-1.13μM was obtained (*Mukherjee et al., 2010-A*).

4.9.6 Supplementary Information References for Chapter 5.

- Mukherjee, S.P., Davoren, M. and Byrne, H.J. 2010-A. *In vitro* mammalian cytotoxicological study of PAMAM dendrimers - towards quantitative structure activity relationships. *Toxicol. in Vitro,* **24**(1): 169-177.

Chapter 6:

Acellular reactivity of polymeric dendrimer nanoparticles as an indicator of oxidative stress in vitro.

6.1 Abstract

The need for rapid and cost effective pre-screening protocols of the toxicological response of the vast array of emerging nanoparticle types is apparent and the emerging consensus on the paradigm of oxidative stress by generation of intracellular reactive oxygen species as a primary source of the toxic response suggests the development of acellular assays to screen for nanoparticle surface reactivity. This study explores the potential of the monoamine oxidase A (MAO-A) enzyme based assay with polymeric dendrimers as cofactors and serotonin as substrate, which generates H_2O_2, quantified by the conversion of the Carboxy-H_2DCFDA dye to its fluorescent form. A range of generations of both PAMAM (Poly (amido amine)) (G4-G7) and PPI (Poly (propylene imine)) (G0-G4) dendritic polymer nanoparticles are used as test particles to validate the quantitative nature of the assay response as a function of nanoparticle physico-chemical properties. The assay is well behaved as a function of dose, over low dose ranges and the acellular reaction rate (ARR) is well correlated with the number of surface amino groups for the combined dendrimer series. For each series, the ARR is also well correlated with the previously documented cytotoxicity, although the correlation is substantially different for each series of dendrimers, pointing to the additional importance of cellular uptake rates in the determination of toxicity.

6.2 Introduction

Nanoparticle science has seen a surge of interest in recent years which continues to increase. Already there are over 1600 listed products and technologies which in some way utilise nanoscience in the areas of: electronics, engineering, cosmetics, food, textiles, packaging and many more (*PEN, 2015*). However the use of nanoparticles in the fields of medicine and drug delivery continues to be of particular importance (*De Jong and Borm, 2008*). It is known that nanoparticles have the ability to enter into mammalian cells, and while this has many potential medical applications, it also initiates a toxic response which can lead to cell death (*Jain et al., 2010*). Therefore, it is important to evaluate the toxic potential of nanoparticles.

Currently, the first step in evaluating toxicity is the use of *in vitro* cytotoxicity assays such as: Alamar Blue (AB), Neutral Red (NR) and 3-(4,5-dimethylthiazol-2-yl)-2,5-diphenyltetrazolium bromide (MTT) (*Kroll et al., 2009*). These assays are both time consuming and relatively costly in terms of their application and optimisation. It is becoming apparent, that to keep up with the immense range of emerging nanoparticles, efforts must be made to both increase the efficiency of current methods and to develop alternative methods to rapidly screen nanoparticles for toxic potential (*Kroll et al., 2009*, *Oomen et al., 2014*, *Meng et al., 2009* and *Clark et al., 2011*).

One way to aid in this endeavour is the development of predictive models for toxicity. These models can be guided by, or identify, Adverse Outcome Pathways (AOPs), a systematic sequence of causally linked events which leads to an adverse health (or ecotoxicological) outcome (*OECD, 2013*). However, our current understanding of nanoparticle toxicity at the cellular level is lacking, therefore such models require an

extensive amount of screening and analysis of nanoparticle toxic responses and mechanisms, ultimately using *in vitro* and *in vivo* methods (*Maher et al., 2014* and *Mukherjee and Byrne, 2013*). Modelling efforts can also be aided by quantitative structure activity relationships (QSARs), which extend the use of the existing knowledge by correlating adverse outcomes with physico-chemical characteristics, which can ultimately guide synthetic strategies (*OECD, 2007*).

The report of the EU Nanosafety Cluster, Working Group 10 has advocated a hierarchical, concern driven approach to nanoparticle testing, in which tier 1 is based on physico-chemical properties and for example structure–activity relationships (*Oomen et al., 2014*). Oxidative stress has been identified as one of the initial adverse system responses giving rise to nanoparticle toxicity *in vitro* (*Xia et al., 2006*), and this is most prominent in nanoparticles with cationic effective surface charges, such as aminated nanoparticles (*Wolinsky and Grinstaff, 2008*). It can be argued, therefore, that to develop a protocol for determination of nanoparticle surface reactivity would be an invaluable first tier procedure in a hierarchical nanotoxicology screening strategy. Such a pre-screening approach could aid in the optimisation of current *in vitro* methods, thereby reducing the overall time needed for the initial screening process.

For the development and validation of such an assay, it is important to use a set of structurally well defined nanoparticles. In this study, PAMAM (Poly (amido amine)) and PPI (Poly (propylene imine)) dendritic polymer nanoparticles are used, as they have the required well defined structures and have been shown to produce systematically variable toxic responses in mammalian cells (*Mukherjee and Byrne, 2013*, *Mukherjee et al., 2010-A and B* and *Naha et al., 2010*) and in a battery of eco-toxicological assays (*Naha et al., 2009*

and *Naha and Byrne, 2013*). These particles are created via the addition of branches onto a core molecule, whereby the addition of each set of branches results in successive dendrimer generations. The added branches each have two terminal groups which can be used for the addition of further branches, so that the number of termini increases with increasing generation.(*Images available at: symo-chem.nl, 2015 & dendritech.com, 2015*). These termini can then be modified to be cationic, anionic or neutral. Studies show that cationic nanoparticles can enter into human cells and initiate a toxic response more readily than their anionic or neutral counterparts (*Ryman-Rasmussen et al., 2006*). Both PAMAM and PPI dendrimers have several potential applications, including: drug delivery agents (*Kesharwani et al., 2014 and Nanjwade et al., 2009*), gene delivery agents (*Eichman et al., 2000* and *Duncan and Izzo, 2005*), exploring and altering cellular signalling pathways (*Akhtar et al., 2015*) and to probe cellular uptake mechanisms (*Khalid et al., 2015*). PAMAM and PPI dendrimers are in the lower range of the definition of a nanoparticle (1nm – 100nm) (*EC: 2011/696/EU*). PAMAMs used in this study have sizes (as determined by AFM): 2.1-2.8nm (G4), 4.1-4.6nm (G5), 4.2 – 5.8nm (G6) (*Khalid et al., 2015*) and G7 ≈ 8.1nm (G7 theoretical diameter determined by: *Dendritech, 2015*)**.** PPI sizes (as determined by AFM) are: ≈1.23nm (G0), ≈1.8nm (G1), 1.7 – 1.9nm (G2), 1.8 – 2.6nm (G3) and 2.5 – 3.5nm (G4) (*Khalid et al., 2015*). The lower generation PPI are at the extreme of the nanoparticle definition and have been used to probe the interface where active cellular uptake gives way to passive diffusion (*Khalid et al., 2015*), and therefore a definition of "nano-scale macromolecules" may be more appropriate for these species. However, for the purpose of this study, they make excellent model particles due to the aforementioned systematically variable physico-chemical properties.

Reactive Oxygen Species (ROS) generation, upon dendrimer endocytosis, has been identified as the initial step in the toxic response (*Khalid et al., 2015*, *Mukherjee et al., 2010-B* and *Naha et al., 2010*) and, in the case of cationic nanoparticles in the acidifying environment of endosomes, it is reported that the unsaturated surface amino groups sequester protons that are supplied by the v-ATPase (proton pump) and may be mediated via NADPH oxidase activity (*Nel et al., 2009*). The generation of ROS is counteracted by the natural intracellular antioxidant processes, although the ROS generation can dominate, leading to oxidative stress and ultimately apoptosis via subsequent mitochondrial damage (*Mukherjee et al., 2010-B*). A number of studies have demonstrated that the response is systematically dependent on the number of surface amino groups (*Khalid et al., 2015*, *Mukherjee and Byrne, 2013*, *Mukherjee et al., 2010-A and B* and *Naha et al., 2010*) and *Maher et al. (2014)* have modelled the uptake and intracellular responses, leading to apoptosis, using a rate equation model. The rate of generation of ROS is dependent on the number of surface amino groups on the nanoparticle and this also governs the surface reactivity. Therefore, the *in vitro* toxicity is intrinsically linked with the surface reactivity of the nanoparticles, which, it is proposed, can be measured acellularly. Acellular based assay systems have previously been used to assess the surface reactivity of nanoparticles (*Shi et al., 2012*).

In this work, the Monoamine Oxidase A (MAO-A) enzyme is employed to probe the acellular production of ROS by homologous series of polymeric dendrimer nanoparticles. The use of the two related, homologous dendrimer series, PAMAM and PPI, enables an evaluation of the ability of the assay to not only register surface activity, but also to quantify the activity in relation to the systematically varied dendrimer structure. Attempts

can then be made to correlate the acellular reactivity with the cellular cytotoxicity as previously measured using established cytotoxicity assays. The study is a route towards establishing a time efficient alternative method for the analysis of nanoparticle toxicity and may also aid predictive modelling based on structure activity relationships.

6.3 Materials and Methods

6.3.1 Materials

Serotonin hydrochloride, Horseradish peroxidise (HRP), Monoamine Oxidase-A (MAO-A)FAD-bound (E.C:1.4.3.4) were purchased form Sigma-Aldrich. The Poly (amido amine) nanoparticles (PAMAM) generations 4-7, were purchased from Sigma-Aldrich and manufactured by Dendritech Inc. The Poly (propylene imine) (PPI) dendrimers generation 0-4, were purchased from SyMO-Chem. The Carboxy-H$_2$DCFDA was purchased from Invitrogen. The 96 well plates used were purchased from TrueLine and all plates were analysed in a Molecular Devices SpectraMax M3 spectrometer.

6.3.2 Methodology

6.3.2.1 Enzymatic reaction

An enzymatic approached was taken using Monoamine Oxidase-A (MAO-A), a flavin-containing amine oxidoreductase, which catalyses the oxidative deamination of its substrate, producing an aldehyde and an amine, as shown in Figure 6.1. Hydrogen peroxide (H$_2$O$_2$) is produced as a by-product. In this study, the substrate chosen was serotonin, which is converted to 5-hydroxyindole acetaldehyde with the release of ammonia (NH$_3$) and hydrogen peroxide (H$_2$O$_2$). The production of hydrogen peroxide can be easily detected

with the dye: 6-carboxy-2',7'-dichlorodihydrofluorescein diacetate (Carboxy-H_2DCFDA), a fluorescein derivative, which is converted to its fluorescent form via the cleavage of its acetate groups and oxidation by ROS.
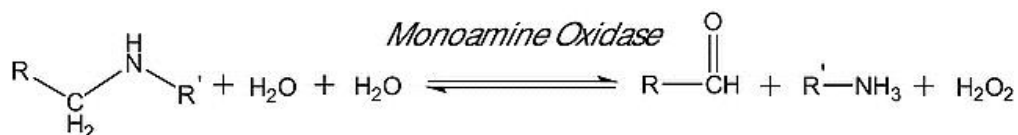
Figure 6.1: Generalised reaction mechanism of Monoamine Oxidase-A In the case of this study, serotonin was used as a substrate (therefore R' is H) and the products are 5-hydroxyindole acetaldehyde, hydrogen peroxide (H_2O_2) and ammonia (NH_3) (*Sigma-Aldrich, 2015*).

The reaction was carried out in PBS, which ensured that more than enough water was present to allow the amount of serotonin to be the limiting factor in the reaction. It is proposed that, in the presence of aminated nanoparticles, the production of H_2O_2 (via enzymatic action) is further promoted and thus can be used to measure the surface reactivity (*Fubini and Hubbard, 2003*, *Kim et al., 2004* and *Yeber et al., 2000*).

6.3.2.2 Surface Amine Calculation

For both dendrimer series, the number of surface amino groups can be calculated via the formula:

$$N_{amg} = N_{BP(G0)}.2^G \hspace{4cm} \text{Equation 6.1}$$

Where N_{amg} is the number of surface amino groups, $N_{BP(G0)}$ is the number of initial binding sites on the core of the particle (for PAMAM and PPI dendrimers: $N_{BP(G0)}$=4), and G is the generation of the nanoparticle (*Maher et al., 2014*).

6.3.2.3 Experimental Procedure

An 800μM solution of Serotonin was made up in Phosphate Buffer Solution (PBS). PAMAM or PPI nanoparticles were made up in this solution. The concentration range used for PAMAM was: 0.08-5.2μM for all generations (G4, G5, G6 and G7). The concentration ranges used for PPI were: G0: 25-3500μM, G1: 5-3000μM, G2: 5-35μM, G3: 0.325-3.5μM, and G4: 0.6-3.0μM. The concentration ranges were chosen to encompass and span the effective concentration for 50% loss of viability (EC_{50}) in the immortal keratinocyte (HaCaT) cell line for each particle, as determined by the 3-(4,5-dimethylthiazol-2-yl)-2,5-diphenyltetrazolium bromide (MTT) assay (*Khalid et al., 2015*, *Mukherjee and Byrne, 2013*, *Mukherjee et al., 2010-A and B* and *Naha et al., 2010*). 100μL of each concentration was added to the 96-well plate. Six replicates of each concentration were made on the plate and the enzyme MAO-A (concentration: 0.0075mg/mL) was added to the first 3 wells of each concentration (the second 3 wells contained no enzyme and were used as a control – see Section 6.8: Supplementary Information for a more detailed explanation of experimental setup). The plate was then left at 37˚C for 10 minutes to allow the MAO-A to act on the serotonin and produce ROS. After 10 minutes incubation, 100μL of the Carboxy-H_2DCFDA dye (containing 2.2U/mL HRP to enhance fluorescence) (*Venkatachari et al., 2015*) was added to the wells to a final concentration of 10μM and this was again left at

37˚C for 10 minutes to allow for colour development. The plates were then read using a Molecular Devices SpectraMax M3 spectrometer with: λ_{ex} = 488nm and λ_{em}= 535nm.

6.3.2.4 Data Analysis

SigmaPlot™ (v.10.0) was used for all data analysis and generation of graphs; error bars are ± standard deviation for Figure 6.2 and are ± standard error for Figures 6.3 and 6.4. Each plate contained three replicates of each concentration and each plate was repeated three times. Numerical simulations were performed by integration using the iterative Euler approach and again SigmaPlot™ (v.10.0) was used to generate the values and graphs.

6.4 Results

6.4.1: PAMAM and PPI ROS Generation and ARR Determination
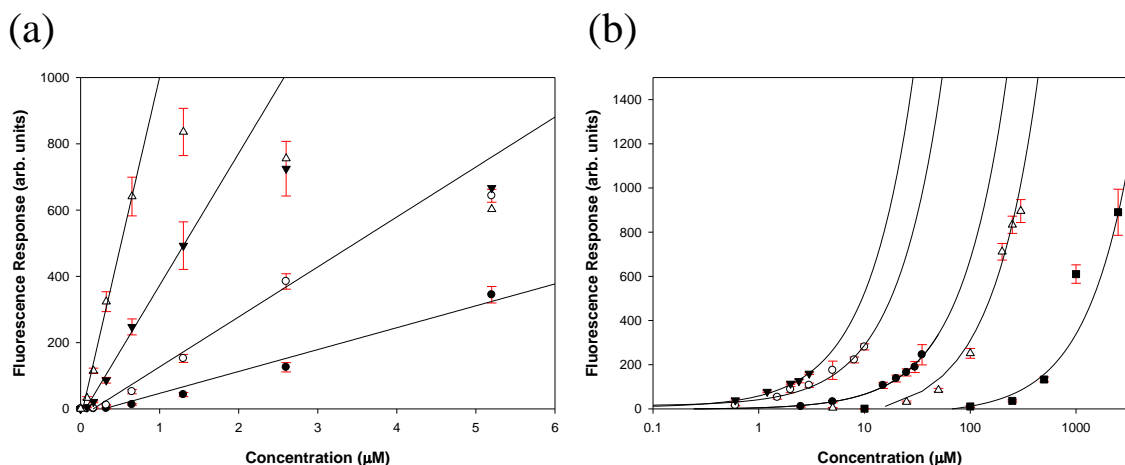
(a)   (b)

Figure 6.2 (a): Plot of the concentration dependent fluorescence intensity for PAMAM dendrimers G4(●), G5(○), G6(▼), G7(Δ) (b): Plot of the concentration dependent fluorescence intensity for PPI dendrimers G0(■), G1(Δ), G2(●), G3(○) , G4 (▼). The lines are a linear regression fit to the data.

263

Figure 6.2a shows the concentration dependence of the fluorescence generated by the PAMAM dendrimer nanoparticles over the concentration range 0.08 – 5.2μM for generations G4 - G7. In this experimental setup, the increasing fluorescence is a result of increasing dose and generation of ROS and their interaction with the dye (Carboxy-H_2DCFDA). Figure 6.2b shows the similar concentration dependence of the fluorescence generated by the PPI dendrimer nanoparticles over the concentration range 0-3500μM for generations G0 – G4. The extended range is necessary due to the reduced activity of the lower generation PPI dendrimers, and the data is shown in a semi-log plot for best visualisation of the full range of concentrations employed.

The fluorescence generation is dependent on the combined presence of the enzyme and the dendrimer (see Section 6.8: Supplementary Information), the latter in a dose dependent fashion. Therefore, it is proposed that the increased H_2O_2 generation is analogous to a measurement of nanoparticle reactivity. This reactivity increases linearly over the initial concentration range tested, although deviation at the higher concentrations for higher dendrimer generations is observed. Regression to the lower concentration range produces a linear fit, the slope of which is a measure of the Acellular Reaction Rate (ARR) of the nanoparticles (solid lines in Figure 6.2).

6.4.2 Comparison of ARR with Particle Physico-Chemical Properties
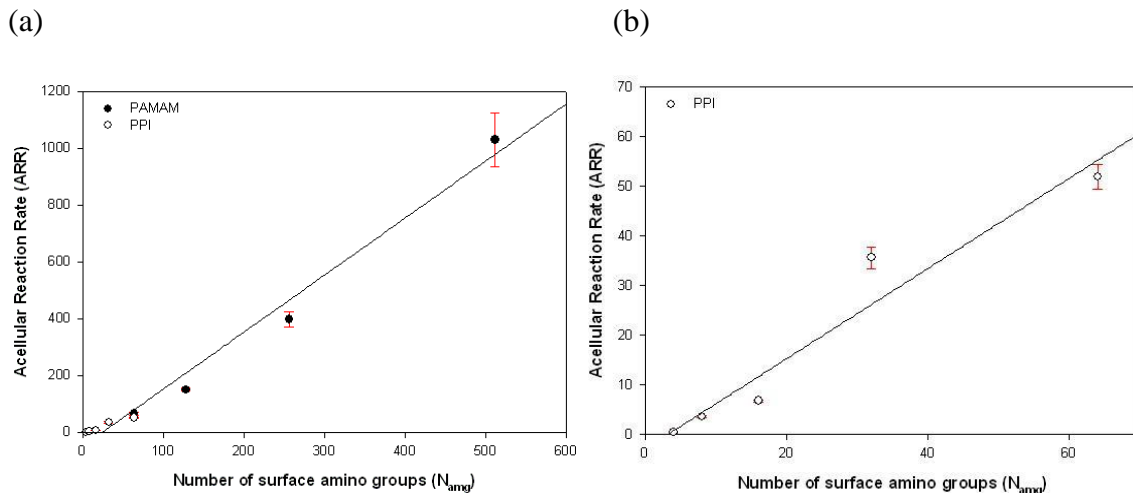
(a)   (b)

Figure 6.3: (a) Plot of the slope as a function of Number of Surface Amino Groups (N_{amg}) for all PAMAM and PPI dendrimers. The solid line shows a fit to a linear dependence for the combined dendrimer series. (b) Plot of the slope as a function of Number of Surface Amino Groups for PPI dendrimers. The solid line shows a fit to a linear dependence.

The concentration dependent fluorescence generation, indicative of the ROS response, elicited by PAMAM and PPI dendrimers, is not only concentration dependence but is clearly also generation dependent. For both homologous dendrimer series, increased generation and therefore number of surface amino groups (N_{amg}) produces an increase of the ARR. Figure 6.3(a) shows a combined plot of the ARR for both PAMAM and PPI dendrimer series, versus N_{amg} for progressive dendrimer generations, while Figure 6.3(b) focuses on the PPI response. The graph shows a clear correlation of ARR with N_{amg} for both series. The generation dependence of the conversion of the dye to its fluorescent form is therefore clearly dependent on the surface properties of the dendrimer. Notably, the approximately linear trend is similar for the two dendrimer series, indicating that the ARR

is determined by the surface amino groups, independent of the differences in core structure of the PAMAM and PPI dendrimers.

6.4.3 Comparison of ARR with Toxicity Data

Critically, the *in vitro* cytotoxicity of both PAMAM and PPI dendrimers shows a similar dose and generation dependence (*Khalid et al., 2015*, *Mukherjee and Byrne, 2013*, *Mukherjee et al., 2010-A and B* and *Naha et al., 2010*) and it has been demonstrated that the initial stages of the cellular response are associated with oxidative stress in endosomes, upon endocytosis (*Mukherjee et al., 2010-B*). *Maher et al. (2014)* have demonstrated that this *in vitro* oxidative stress can be modelled according a rate equation system, in which the rate of ROS production is dependent on generation and therefore N_{amg} (*Maher et al., 2014*), prompting a comparison of the ARR with the measured cytotoxicity of the nanoparticles. Figure 6.4a shows a plot of the acellular ROS activity against the cytotoxicity for both dendrimer series (Figure 6.4b for the PPI series alone), as previously determined in the HaCaT cell line using the MTT assay at 24hrs, represented by the inverse EC_{50} (*Mukherjee et al., 2010-A and B* and *Naha et al., 2010*). A good, approximately linear, correlation is observed between the two parameters, although the relationship is clearly different for each of the dendrimer series. The correlation within each individual series is a clear indication that the ARR is a measure of the intracellular ROS generation, *in vitro*, which in turn is predictive of the *in vitro* cytotoxic response.
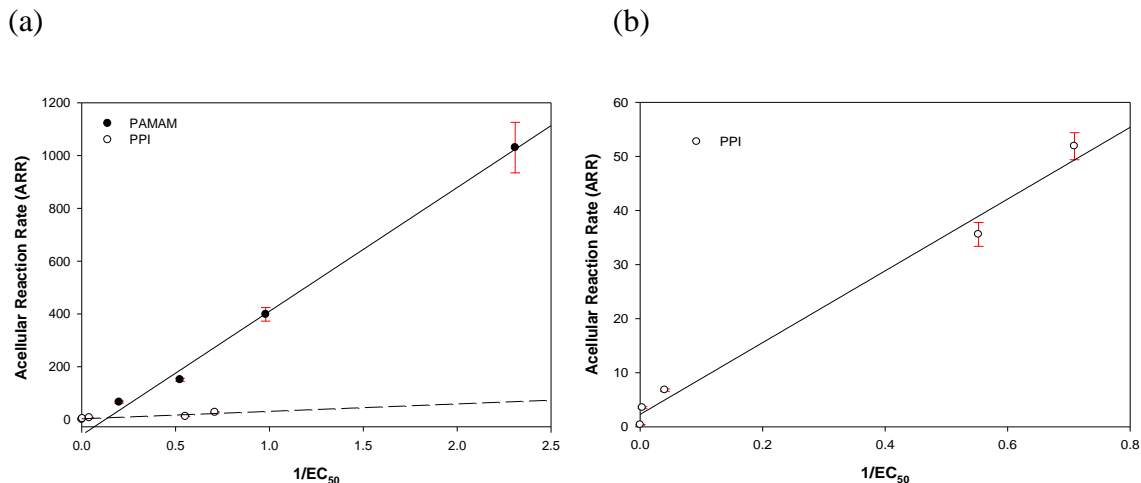
(a)

(b)

Figure 6.4 (a): Plot of the Acellular reaction rate (ARR) for all PAMAM and PPI dendrimers versus the inverse cytotoxicity as previously measured using the MTT assay (*Mukherjee et al., 2010-A and B* and *Naha et al., 2010*) (b): Plot of the Acellular reaction rate (ARR) for PPI dendrimers versus the inverse cytotoxicity as previously measured using the MTT assay. The lines show a fit of linear dependences.

Notably, however, the assay does not translate between the two related homologous series, indicating that it cannot be universally applied to all nanoparticles with apparently equivalent surface chemistry. The origin of the difference in the responses is explored further in the following section. The error bars shown for the ARR (Figures 6.3 and 6.4) are the standard error of the linear regression fit to the data of Figure 6.2, as generated by SigmaPlot™ (v.10.0).

6.5 Discussion

Polymeric dendrimers are homologous series of nano-meter scale molecules with systematically variable cytotoxic responses, which have been shown to correlate with the precisely variable surface structure, in the case of PAMAM and PPI, the number of surface amino groups. Upon endocytosis, the initial stage of the cellular response has been demonstrated to be oxidative stress, which has also been seen to correlate well with the dendrimer generation and therefore number of surface amino groups (*Khalid et al., 2015*, *Mukherjee and Byrne, 2013*, *Mukherjee et al., 2010-A and B* and *Naha et al., 2010*).

In a rate equation model of the cellular responses and cytotoxicity, the oxidative stress and subsequent inflammatory cascade and loss in viability, keeping all cellular parameters constants, it was demonstrated that variation of the single generation dependent parameter, representing surface reactivity, resulted in a faithful simulation of the range of responses for PAMAM G4-G6 (*Maher et al., 2014*). It can therefore be argued that measurement of this surface reactivity, acellularly, can serve as a predictor for the *in vitro* toxicity of the nanoparticles, with significant time, labour and cost savings.

Both homologous dendrimer series, PPI and PAMAM, showed a generation and concentration dependant conversion of serotonin and resultant generation of H_2O_2, as monitored by the fluorescent ROS assay, Carboxy-H_2DCFDA. The relationship between generated fluorescence and dendrimer dose was seen to be linear, at least over the lower dose range (Figures 6.2a and b) and the rate of increase as a function of dose can be considered representative of the rate of reactivity of the NPs in an acellular environment, or the Acellular Reaction Rate (ARR). In Figure 6.3, the ARR is seen to be approximately linearly dependant on the N_{amg} (and therefore dendrimer generation) for both series,

independent of the core structure. Crucially, a similar relationship (between N_{amg} and ROS) can be seen in various toxicological studies (*Khalid et al., 2015*, *Mukherjee and Byrne, 2013*, *Mukherjee et al., 2010-A and B* and *Naha et al., 2010*).

The acellular assay used in this work exploits the conversion of the dye Carboxy-H_2DCFDA to its fluorescent form by interaction with the generated H_2O_2. The control reactions detailed in Section 6.8: Supplementary Information confirm that the measured fluorescence generation is dependent on the simultaneous presence of the enzyme and dendrimer. To confirm the role which the dendrimer nanoparticles play in the reaction, the system can be modelled with a rate equation system:

$$\frac{dN_{H2O2}}{dt} = (k_{ROS}.N_{sero}(t).N_{H2O}(t)) - (k_{enz}.k_{21}.N_{ald}(t).N_{ami}(t).N_{H2O2}(t)) - (k_{31}.N_{DCF}(t).N_{H2O2}(t)^n) -$$

Equation 6.2

Where N_{H2O2} denotes the number of H_2O_2 species generated, at a rate constant k_{ROS}, depending on the number of serotonin, N_{sero}, and water, N_{H2O}, molecules present. The rate is reduced by the reverse reaction of the product species N_{ald} and N_{ami}, at a rate constant k_{21}, and by the interaction of the H_2O_2 species generated with the dye concentration, N_{DCF}, to produce the fluorescent form of the dye N_F at a rate constant k_{31}, according to the equation

$$\frac{dN_F}{dt} = (k_{31}.N_{DCF}(t).(N_{H2O2}(t)^n)) - (k_q.N_F(t).N_D(t)) \qquad \text{Equation 6.3}$$

The rate constant k_{ROS} is determined by the dendrimer dose, N_D, and generation (represented by number of surface amino groups, N_{amg}), as well as the enzyme concentration, which determines the enzymatic reaction rate constant (k_{ENZ}), according to the equation:

$$k_{ROS} = (k_{ENZ}).(N_D).(A).(k_{12}) \qquad \text{Equation 6.4}$$

-where k_{12} is a dose and generation independent rate constant, and

$A = N_{amg}(G+1)$

Figure 6.5 shows a simulation of the response for dendrimers of generation 3-7 (independent of dendrimer type). The parameter varied between the simulations for each dendrimer generation is N_{amg}. In the simulation, a value of the empirical factor $n=2$ for the interaction of the H_2O_2 with the Carboxy-H_2DCFDA dye is used, consistent with cleavage of two acetate groups by oxidation to produce the fluorescent form of the dye (*Setareh-biotech, 2015*). The simulated response faithfully reproduces the experimentally observed generation dependence across all generations. Notably, the reduction of fluorescence at higher doses for the higher order generations is best reproduced by a quenching of the fluorescence of the converted dye by interaction with the dendrimers, indicated by the second term of equation 6.3 at a rate constant k_q, rather than a fouling or consumption of the enzyme or dendrimers in the primary reaction of equation 6.2.
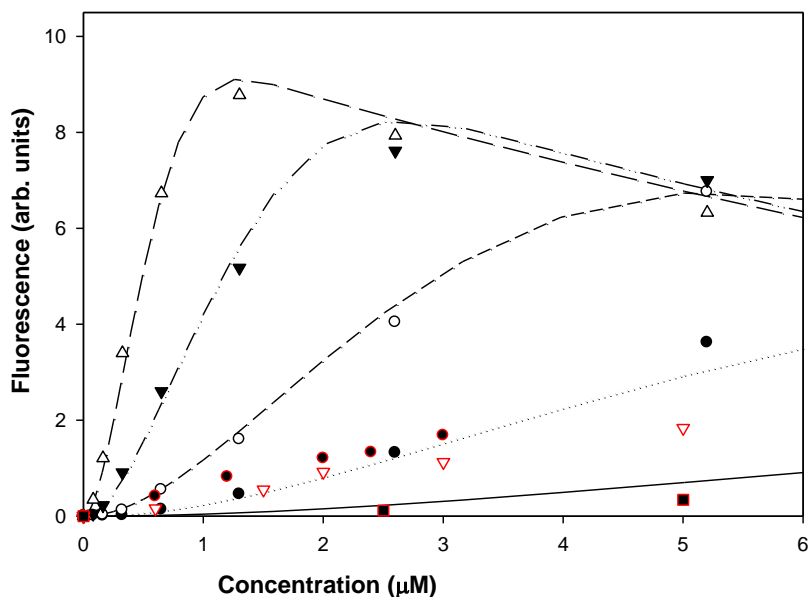
Figure 6.6: Simulated generation of fluorescence based on the rate equation model of
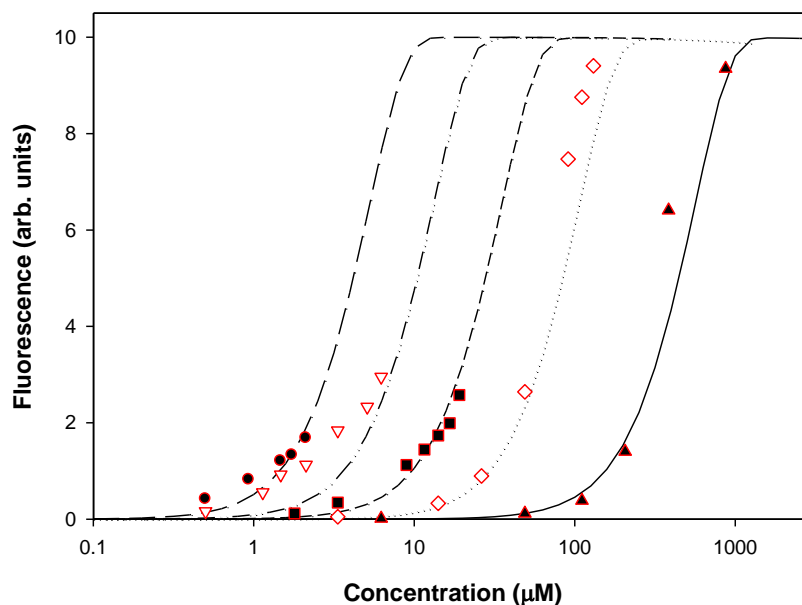
Equations 6.2-6.4, for PPI dendrimer generations 0-4 (lines). Also shown are the

experimental data for PPI dendrimers G4(●), G3(▽), G2(■), G1(◇), G0(▲).

Critically, the model confirms that the rate of increase of the dye fluorescence is explicitly

related to the number of surface amino groups of the dendrimer species. Notably, the same

equations and fit parameters for PAMAM give an acceptable simulation of the responses

for the higher order generations of PPI (G2-G4). However, the simulations deviate from the

observed experimental data substantially for lower PPI generations. A better reproduction

of the generation dependent behaviour of the PPI series is achievable by utilising the same Equations 6.2-6.4, with a slightly increased initial reaction rate and a substantial reduction of the rate of quenching of the fluorescence in the presence of the PPI dendrimers (see Section 6.8: Supplementary Information; Table S6.1).

The simulation of the reaction based on a rate equation model supports the assumption that the acellular reaction of Figure 6.1, catalysed by the MAO-A enzyme, is further promoted by the presence of the polymeric dendrimers, and that the generation of H_2O_2 and subsequently Carboxy-H_2DCFDA fluorescence is quantitatively related to the number of surface amino groups and therefore surface reactivity of the dendrimer nanoparticles. The saturation of the reaction at high concentrations is a result of quenching of the dye by the dendrimers, rather than a fouling of the catalytic action during the reaction process.

This observed relationship suggests that the assay may be used to link the acellular NP reactivity and the *in vitro* toxic response, and this is supported by the correlations observed between ARR and $1/EC_{50}$ for each series (figure 6.4). However, the observed correlations are different for each series. PAMAM and PPI are related polymeric dendrimer series whose branches terminate in primary amino groups. PAMAM dendrimers contain a two carbon ethylenediamine core, whereas PPI contains a four carbon diaminobutane core.(*Images available at: symo-chem.nl, 2015 & dendritech.com, 2015*). Although it may be assumed that their surface reactivity is determined by the number of surface amino groups and thus equivalent generations have similar reactivity, the PAMAM dendrimers are larger in diameter than the PPI series, even though PPI have a larger core (*Crooks et al., 2002*). In terms of the simulated responses, the experimental data can be well reproduced with almost identical reaction rates, indicating a similar reactivity of the dendrimers with

equivalent N_{amg}, although there is a slight difference in k_{12} for each dendrimer series and a substantial difference in quenching rate constant, k_q. The somewhat different reactivity of PPI and PAMAM dendrimers may be due to conformation change of PPI dendrimers causing the branches to fold-in, rendering the surface groups inactive (*He et al., 2002*).

Khalid et al. (2015) have demonstrated that for both PAMAM and PPI dendrimers, once internalised in the cells, the early stage ROS is the primary source of the cytotoxic response after 24hrs, and that for each dendrimer series, a similar degree of early stage oxidative stress results in a similar degree of cytotoxicity (*Khalid et al., 2015*). In the models of *Mukherjee and Byrne (2013)*, and *Maher et al. (2014)*, the simulated uptake of PAMAM dendrimers was seen to be generation (or size) dependent, and, translating the model to the PPI series, the observed higher levels of intracellular ROS generation and toxic response are consistent with a higher rate of internalisation of the PPI G3 and G4 dendrimers, which are, as already mentioned, substantially smaller in diameter than their PAMAM counterparts, according to literature values (*Crooks et al., 2002*). Therefore, although for both homologous dendrimer series, the ARR is well correlated with the previously determined generation dependent cytotoxicity, indicating its potential as a predictive screening tool for toxicity, it is clear that the structural dependence of the cytotoxic response is not only determined by the surface reactivity and that size dependent cellular uptake rates and mechanisms should also be considered. In this context, it is noteworthy that this assay was also used to evaluate the acellular reactivity of polystyrene nanoparticles (PSNP), with diameter of 50nm and amine modified surface coatings. While these particles do give EC_{50} values comparable to those of PAMAM and PPI dendrimers (in the HaCaT cell lines tested), the acellular data showed little to no reactivity, which may point to

different modes of cellular toxicity. However, data on the extent of surface functionalisation of the PSNP's was unavailable and so direct comparison of the number of surface amino groups was impossible.

Other enzymes such as NADPH Oxidase (which has been implicated in the build up of ROS upon nanoparticle uptake (*Dostert et al., 2008* and *Nabeshi et al., 2008*)) could have been used. In living cells, nanoparticles are taken up into endosomes via the process of endocytosis and shortly afterwards, an initial increase of ROS is observed. This initial ROS increase is thought to be caused by NADPH Oxidase; an enzyme which is present in nearly all cell types. It produces superoxide anions (O_2^-) via the transfer of an electron from NADPH, via FAD, to oxygen (O_2). The resulting (O_2^-) is then rapidly dismutated to hydrogen peroxide (H_2O_2). This process may be facilitated by the v-ATPase proton pump mechanism. It is reported that the unsaturated surface amino groups sequester protons that are supplied by the v-ATPase (proton pump) (*Nel et al., 2009*). This process keeps the pump functioning and leads to the retention of one Cl^- ion and one water molecule per proton.

However, MAO was used in this study as it has several advantages. The reaction is relatively simple and the FAD co-factor for the enzyme was already bound in the as-supplied product. Furthermore, NADPH oxidase produces super oxide (O_2^-) as an ROS, which would not be directly measurable via Carboxy-H_2DCFDA, and to use another dye would deviate from the intracellular data used for comparison.

In summary, while the assay shows potential for the development of experimental systems which can quantify NP reactivity and therefore toxicity acellularly, additional testing is required. The results from this assay, to date, have only been compared to the cytotoxicity

of single cell line (HaCaT) and a more comprehensive set of comparisons with toxicological data from various cell lines will be essential to validate the accuracy and applicability of the assay. The PAMAM and PPI dendrimers have a well defined structure and elicit well defined acellular responses. However, it would be necessary to test the assay system with a vast range of different classes of nanoparticles, notably to correlate the differing trends of correlation of ARR with toxicity for differing nanoparticle sizes and cellular uptake rates.

6.6 Conclusion

The need for rapid and cost effective pre-screening protocols of the toxicological response of the vast array of emerging nanoparticle types is apparent and the emerging consensus on the paradigm of oxidative stress by generation of intracellular reactive oxygen species as a primary source of the toxic response suggests the development of acellular assays to screen for nanoparticle surface reactivity. In the quantitative validation of such assays, the use of homologous series of polymeric dendrimer nanoparticles in which the physico-chemical properties are precisely and systematically variable is invaluable.

This study has explored the potential of a MAO-A enzyme based assay, which generates the ROS H_2O_2, quantified by the conversion of the Carboxy-H_2DCFDA dye to its fluorescent form. The assay response is well correlated with nanoparticle dose and reactivity over a range of doses, for two different dendrimer series, independent of structure. For each dendrimer series, the assay response correlates well with the experimentally observed physico-chemical dependences of the cytotoxicological response. However, it is observed that the acellular assay/cytotoxicity correlations for the different

dendrimer series are significantly different; indicating that the intermediate steps of cellular uptake rates must be considered in the development of a more universal acellular screening solution.

6.7 References

- Akhtar, S., Al-Zaid, B., El-Hashim, A.Z., Chandrasekhar, B., Attur, S., Yousif, M.H.M. and Benter, I.F. 2015. Cationic Polyamidoamine Dendrimers as Modulators of EGFR Signaling *In Vitro and In Vivo*. PLoS ONE, **10**(7), doi:10.1371/journal.pone.0132215

- Clark, K.A., White, R.H. and Silbergeld, E. K. 2011. Predictive models for nanotoxicology: Current challenges and future opportunities. *Regul. Toxicol. Pharm.,* **59**(3), 361-512.

- Crooks, R.M., Lemon III, B.I., Yeung, L.K. and Zhao, M. 2001. Dendrimers III: Design, Dimension, Function: Dendrimer-encapsulated Metals and Semiconductors: Synthesis, Characterisation and Applications. *Topics in Current Chemistry,* **212**, 81-135.

- De Jong, W. H. and Borm, P.J.A. 2008. Drug delivery and nanoparticles: Applications and hazards. *Int. J. Nanomed.,* **3**(2), 133–149.

- Dendritech. 2015. *Accessed on: 05-09-2015*, Available at: http://www.dendritech.com/pamam.html

- Dostert, C., Pétrilli, V., Van Bruggen, R., Steele, C., Mossman, B.T. and Tschopp, J. 2008. Innate Immune Activation Through Nalp3 Inflammasome Sensing of Asbestos and Silica. *Science,* **320**(5876), 674-677.

- Duncan, R. and Izzo, L. 2005. Dendrimer biocompatibility and toxicity. *Adv. Drug. Deliv. Rev.* **57**(15), 2215– 2237.

- Eichman, J.D., Bielinska, A.U., Kukowska-Latallo, J.F. and Baker, J.R.Jr. 2000. The use of PAMAM dendrimers in the efficient transfer of genetic material into cells. *J. Pharm. Sci. Technol.* **3**(7), 233-245.

- European Commission (EC) Recommendation of 18 October 2011 on the definition of nanomaterials. 2011. *Official Journal of the European Union*, **2011/696/EU**, L275/38 – L275/40.

- Fubini, B. and Hubbard, A. 2003. Reactive oxygen species (ROS) and reactive nitrogen species (RNS) generation by silica in inflammation and fibrosis. *Free Radic. Biol. Med.* **34**(12), 1507–1516.

- He, D. 2002. Studies of PPI Dendrimers – Structures, Properties and Potential Applications. *MSc, Marshall University,* Huntington, West Virginia**.**

- Jain, K., Kesharwani, P., Gupta, U. and Jain, N.K. 2010. Dendrimer toxicity: Let's meet the challenge. *Int. J. Pharm.,* **394**(1-2), 122–142.

- Kesharwani, P., Jain, K. and Jain, N.K. 2014. Dendrimer as nanocarrier for drug delivery. *Prog. Polym. Sci.* **39**(2), 268– 307.

- Khalid, H., Mukherjee, S.P., O'Neill, L. and Byrne, H.J. 2016. Structural dependence of the *In vitro* cytotoxicity, oxidative stress and uptake mechanisms of Poly (propylene imine) dendritic nanoparticles. *J. Appl. Toxicol*., **36**(3), 464–473.

- Kim, S.Y., Nishioka, M. & Taya, M. 2004. Promoted proliferation of an SOD-deficient mutant of Escherichia coli under oxidative stress induced by photoexcited TiO2. *FEMS Microbiol. Lett.*, **236**(1), 109–114.

- Kroll, A., Pillukat, M.H., Hahn, D. and Schnekenburger, J. 2009. Current *in vitro* methods in nanoparticle risk assessment: Limitations and challenges. *Int. J. Pharm. Biopharm.* **72**(2): 370-377.

- Maher, M.A., Naha, P.C., Mukerjee, S.P. and Byrne, H.J. 2014. Numerical simulations of *in vitro* nanoparticle toxicity – the case of Poly(amido amine) dendrimers. *Toxicol. In Vitro.* **28**(8): 1449-1460.

- Meng, T., Xia, T., George, S., and Nel, A.E. 2009. A Predictive Toxicological Paradigm for the Safety Assessment of Nanomaterials. *ACS Nano,* **3**(7), 1620 – 1627.

- Mukherjee, S.P. and Byrne H.J. 2013. Polyamidoamine dendrimer nanoparticle cytotoxicity oxidative stress, caspase activation and inflammatory response: experimental observation and numerical simulation. *Nanomed: Nanotech. Bio. Med.,* **9**(2), 202-211.

- Mukherjee, S.P., Davoren, M. and Byrne H.J. 2010-A. *In vitro* mammalian cytotoxicological study of PAMAM dendrimers - towards quantitative structure activity relationships. *Toxicol. in Vitro,* **24**(1), 169-177.

- Mukherjee, S.P., Lyng, F.M., Garcia, A., Davoren, M. and Byrne H.J. 2010-B. Mechanistic studies of *in vitro* cytotoxicity of poly(amidoamine) dendrimers in mammalian cells. *Toxicol. Appl. Pharm.,* **248**(3), 259–268.

- Nabeshi, H., Yoshikawa, T., Matsuyama, K., Nakazato, Y., Tochigi, S., Kondoh, S., Hirai, T., Akase, T., Nagano, K., Abe, Y., Yoshioka, Y., Kamada, H., Itoh, N.,

Tsunoda, S. and Tsutsumi, Y. 2008. Amorphous nanosilica induce endocytosis-dependent ROS generation and DNA damage in human keratinocytes. *Part. Fibre Toxicol.,* 8(1), 10 pages.

- Naha, P.C. and Byrne, H.J. 2013. Generation of Intracellular Reactive Oxygen Species and Genotoxicity effect to Exposure of Nanosized Polyamidoamine (PAMAM) dendrimers in PLHC-1 cells *in vitro*. *Aquatic Toxicology,* **132-133**, 61-72.

- Naha, P.C., Davoren, M., Casey, A. and Byrne, H.J. 2009. An Ecotoxicological Study of Poly(amidoamine) Dendrimers-Toward Quantitative Structure Activity Relationships. *Env. Sci. Technol.,* **43**(17), 6864–6869.

- Naha, P.C., Davoren, M., Lyng, F.M. and Byrne, H.J. 2010. Reactive oxygen species (ROS) induced cytokine production and cytotoxicity of PAMAM dendrimers in J774A.1 cells. *Toxicol. Appl. Pharm.,* **246**(1-2), 91–99.

- Nanjwade, B.K., Bechra, H.M., Derkar, G.K., Manvi, F.V. and Nanjwade, V.K. 2009. Dendrimers: Emerging polymers for drug-delivery systems. *Eur. J. Pharm. Sci.* **38**(3), 185-196.

- Nel, A.E., Mädler, L., Velegol, D., Xia, T., Hoek, E.M.V., Somasundaran, P., Klaessig, F., Castranova, V. and Thompson, M. 2009. Understanding

biophysicochemical interactions at the nano–bio interface. *Nature Materials*. **8**(7): 543 – 557.

- Oomen, A., Bos, P., Fernandes, T., Hund-Rinke, K., Boraschi, D., Byrne, H. J., Aschberger, K., Gottardo, S., von der Kammer, F., Kühnel, D., Hristozov, D., Marcomini, A ., Migliore, L., Scott-Fordsmand, J., Wick, P. and Landsiedel, R. 2014. Concern-driven integrated toxicity testing strategies for nanomaterials - Report of the NanoSafety Cluster Working Group 10. *Nanotox.,* **14**, 195-216.

- Organisation for Economic Co-Operation and Development (OECD): Guidance Document On Developing and Assessing Adverse Outcome Pathways, *OECD,* ENV/JM/MONO(2013)**6**. 2013.

- Organisation for Economic Co-Operation and Development (OECD): Guidance Document on the Validation of (Quantative) Structure Activity Relationships [(Q)SAR] Models, *OECD,* ENV/JM/MONO(2007)**2**. 2007.

- Project on Emerging Nanotechnologies (PEN), 2015. Accessed on 15-10-2015 – *Available at: http://www.nanotechproject.org/*

- Ryman-Rasmussen, J.P., Riviere, J.E. and Monteiro-Riviere, N.A. 2006. Penetration of Intact Skin by Quantum Dots with Diverse Physicochemical Properties. *Toxicol. Sci.,* **91**(1), 159-165.

- Setareh-biotech. 2015. *Accessed on:* *05-09-2015*, Available at:http://www.setarehbiotech.com/details.cfm?ProdID=158

- Shi, M., Kwon, H.S., Peng, Z., Elder, A. and Yang H. 2012. Effects of Surface Chemistry on the Generation of Reactive Oxygen Species by Copper Nanoparticles. *ACS Nano,* **6**(3), 2157–2164.

- Sigma-Aldrich. 2015. *Accessed on:* *05-09-2015*, Available at: http://www.sigmaaldrich.com/catalog/product/sigma/m7316

- SyMO-Chem. 2015. *Accessed on: 05-09-2015*, Available at: http://www.symo-chem.nl/

- Venkatachari, P., Hopke, P.K., Grover, B.D. and Eatough, D.J. 2005. Measurement of Particle-Bound Reactive Oxygen Species in Rubidoux Aerosols. *J. Atmos. Chem.* **50**, 49-58.

- Wolinsky, J.B. and Grinstaff, M.W. 2008. Therapeutic and diagnostic applications of dendrimers for cancer treatment. *Adv. Drug Delivery Rev.,* **60**(9), 1037–1055.

- Xia, T., Kovochich, M., Brant, J., Hotze, M., Sempf, J., Oberley, T., Sioutas, C., Yeh, J.I., Wiesner, M.R. and Nel, A.E. 2006. Comparison of the Abilities of

Ambient and Manufactured Nanoparticles to Induce Cellular Toxicity According to an Oxidative Stress Paradigm. *Nano Lett.,* **6**(8), 1794-1807.

- Yeber, M.C., Rodriguez, J., Freer, J., Duran, N. and Mansilla, H.D. 2000. Photocatalytic degradation of cellulose bleaching effluent by supported TiO2 and ZnO. *Chemosphere*, **41**(8), 1193–1197.

6.8 Supplementary Information for Chapter 6:

6.8.1 Rates and Initial Values for Numerical Simulation.

Table S6.1: Table showing all the factors and rates used for modelling the PAMAM and

PPI nanoparticles (**bold** used to highlight changes in rates between the two models).

Factor	Value(Units) - PAMAM	Value(Units) - PPI
N_{sero}	$800(\mu M)$	$800(\mu M)$
N_{H2O}	$10000(\mu M)$	$10000(\mu M)$
N_{dcf}	$10(\mu M)$	$10(\mu M)$
N_{ami}	$0(\mu M)$	$0(\mu M)$
N_{ald}	$0(\mu M)$	$0(\mu M)$
N_{H2O2}	$0(\mu M)$	$0(\mu M)$
N_F	$0(\mu M)$	$0(\mu M)$
$\mathbf{k_{12}}$	$\mathbf{1.1x10^{-6}\ (min^{-1})}$	$\mathbf{1.2x10^{-6}\ (min^{-1})}$
k_{21}	$1.0x10^{-5}\ (min^{-1})$	$1.0x10^{-5}\ (min^{-1})$
k_{31}	$5.0x10^{-4}\ (min^{-1})$	$5.0x10^{-4}\ (min^{-1})$
k_{enz}	$7.0x10^{-5}\ (min^{-1})$	$7.0x10^{-5}\ (min^{-1})$
$\mathbf{k_q}$	$\mathbf{1.5x10^{-2}\ (min^{-1})}$	$\mathbf{1x10^{-7}\ (min^{-1})}$

6.8.2 Method and Plate Set-Up.

Having several different components in the reaction meant it was essential to carry out suitable blanks and controls to make sure that the readings obtained were due to the nanoparticles interacting with the enzymatic activity. 96 well plates were used for all assays.

The plate was set up with 3 rows, which would have all components of the reaction present: Serotonin, enzyme (MAO) and nanoparticle (at various concentrations). The blank used for these contained serotonin and enzyme – which showed how much ROS was generated without the nanoparticle present. This result was set as 0 and samples containing nanoparticles concentrations were compared to it.

However, another source of background could be readings caused by the nanoparticles themselves. So another 3 rows were set up, containing: Serotonin and nanoparticle (at various concentrations – corresponding to the concentrations used in the first 3 rows). The blank used for these contained serotonin and was set as 0.

This meant that two sets of results were obtained, set 1: Values for ROS generated in the presence of Nanoparticles and set 2: Values for background reading from the nanoparticles. Readings from set 2 were subtracted from set 1, meaning that the values used should be only from nanoparticles interacting with the enzyme during the generation of ROS.
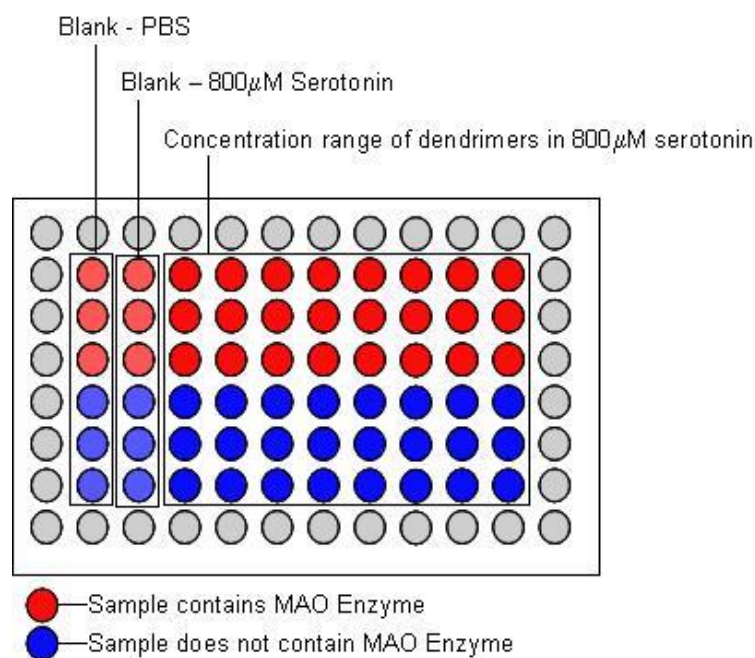
Figure S6.1: Schematic representation of the experimental set-up of the 96 well plates.

6.8.3 Blank Value Comparison.

Due to the different generations used in the study: PPI (G: 0-4) and PAMAM (G: 4-7), the only overlap in generation comes at G4. However, since the concentrations used were based on the EC_{50} values, different concentration ranges were used (PAMAM: 0.08, 0.16, 0.33, 0.65, 1.30, 2.60 and 5.20μM, PPI: 0.6, 1.5, 2.0, 3.0, 5.0, 8.0, 10.0μM). However, some overlap in these ranges makes a limited comparison available at concentrations: PAMAM 0.65μM vs. PPI 0.6μM, PAMAM 1.3μM vs. PPI 1.5μM and PAMAM 5.2μM vs. PPI 5.0μM, as can be seen in the table S6.2:

Table S6.2: Comparison of PAMAM and PPI dendrimer blank values at comparable concentrations.

	PAMAM	PPI
Concentration (μM)	0.65	0.60
Average (fluorescence)	**38.28 ± 0.96**	**21.19 ± 0.45**
Concentration (μM)	1.3	1.5
Average (fluorescence)	**69.88 ± 2.21**	**29.88 ± 0.95**
Concentration (μM)	5.2	5.0
Average (fluorescence)	**328.77 ± 11.40**	**55.34 ± 2.12**

Each individual series shows increasing blank values as concentration increases (this was the reason blanks were necessary; these values were then subtracted from the values with enzyme present). As can be seen from table S6.2, PAMAM dendrimers have a higher blank

value that PPI at almost equivalent concentrations. This is most likely due to the much larger size of the PAMAMs compared to the PPI dendrimers and then this size would become more apparent as more nanoparticles were present, hence increases with increasing concentration.

Chapter 7

Summary and Conclusions

7.1 Summary of Research

This project was aimed at the development of an alternative method for testing the toxicity of nanoparticles, using a numerical simulation approach, reducing the dependence on time and resource intensive *in vitro* studies. The model developed was capable of simulating the interaction of two types of nanoparticle with cells *in vitro*; firstly, PAMAM dendrimers and subsequently, PSNPs. For both series, particles with amine modified surface groups were used, as in previous studies these particles were shown to give well defined toxic responses in several cell lines, including HaCaT (*Mukherjee et al., 2010 – A and B, Naha et al., 2009, 2010 and 2013* and *Mukherjee and Byrne, 2013*).

PAMAM dendrimers of generations four, five and six, were initially modelled, as their well defined set of physico-chemical properties meant that non-systematic variability, in terms of the particles themselves, was minimised. This allowed the direct correlation of cytotoxic responses to nanoparticle properties with a level of confidence in the homogeneity of the particle structure, size and surface functionalisation, not always possible with other types of nanomaterial. Critically, the model identified that the rate of endocytosis and rate of ROS production (which was mainly dependant on N_{amg} and therefore surface chemistry) were two of the key parameters in determining the toxicity of the PAMAM dendrimers, and, throughout all simulations, the only parameter changed was *G*, which determined the number of surface amino groups (N_{amg}) (*Maher et al., 2014*).

However, a wider range of applicability was required to validate the model; therefore, simulation of the toxic response of HaCaTs to PSNP-NH$_2$ was performed. Polystyrene nanoparticles have already been used in some applications and still hold potential for future products and technologies (as discussed in Chapter 5: Modification of the *in vitro* uptake

mechanism and antioxidant levels in HaCaT cells and resultant changes to toxicity and oxidative stress of G4 and G6 Poly (amido amine) dendrimer nanoparticles (*Maher and Byrne, 2016 – B*). While PSNP are useful also as model particles, they are not as well defined as PAMAM dendrimers, for which the particle parameters of size and number of surface groups are both chemically defined. PSNP-NH$_2$ of nominal diameters 50nm and 100nm were employed. However, through SEM analysis some variance in the size was noted. Furthermore, the number of surface amino groups was unknown for each particle size. Even with the associated variance, simulation of the observed results was possible with identical cellular based rates as in the PAMAM simulation, the only two parameters requiring modification being: the number of surface amino groups (N$_{amg}$) and the rate of endocytosis, both of which had been identified by the first version of the model as key parameters governing toxicity. N$_{amg}$ was chemically defined for the PAMAM dendrimers, but had to be determined via NMR spectroscopy for the PSNP-NH$_2$. Endocytosis is a size dependant property and changes in this parameter reflect the huge disparity in sizes between the PAMAM and PSNP-NH$_2$.

The polystyrene nanoparticle toxicity modelling shed light on the importance of rate of endocytosis. However, another key parameter was the rate of generation of ROS. Therefore, to gain insight into this parameter, an experiment was planned to reduce the cellular antioxidant GSH (a key defence in the build up of ROS and initiation of oxidative stress), thereby leading to a proposed faster and more intense ROS production. However, due to an unforeseen set of cellular events, later attributed to the use of BSO, this experiment, in contrast, allowed for a direct observation of the effect of endocytosis and highlighted that the formation of an endosome had a critical role in increasing intracellular

ROS, and subsequently inducing toxicity. Permeabilisation of the cell membrane and passive diffusion of the nanoparticles into the cytosol was observed and when taken into the cell via passive diffusion the nanoparticles do not appear to initiate the ROS associated with the induction of toxicity seen in previous studies (*Mukherjee et al., 2010 – B* and *Naha et al., 2009* and *Naha and Byrne, 2013*), instead acting as anti-oxidants. These findings also strengthened the hypothesis that ROS was produced by NADPH Oxidase, a membrane bound enzyme which resides on the endosome when formed (*Chamulitrat et al., 2004*). While toxicity was still observed, it was associated with the PAMAM localisation and subsequent damage to the mitochondria, leading to apoptosis (*Lee et al., 2009, Mukherjee et al., 2010 – A and B*). However, mitochondrial localisation is not observed for all nanoparticles and therefore, the bypassing of endocytosis (and subsequent ROS production) may provide a strategy for overcoming toxicity.

In the final study of this thesis, an acellular assay was employed to study the reactivity of the nanoparticles based on their physico-chemical properties, mainly the N_{amg}, which was strongly linked to the uptake rate of particles and subsequent generation of ROS and, therefore, induction of toxicity. PAMAM and similarly structured PPI dendrimers were used and the systematic nature of the responses prompted the modelling of the system. A clear link was found between the Acellular Reaction Rate (ARR) and the number of amino groups (N_{amg}), and this relationship persisted when ARR was compared to EC_{50} data (*Mukherjee et al., 2010 – A and B, Naha et al., 2009 and 2010, Naha and Byrne, 2013, Mukherjee and Byrne, 2013* and *Khalid et al., 2016*). However, the relationship was different for each series of dendrimer, meaning that factors such as nanoparticle size of the overall orientation of the branch termini may also have an effect. The acellular assay is fast

and could easily be run on any series of nanoparticles to give an estimation of reactivity based on a variable physico-chemical property, which could be beneficial in the early stages of nanoparticle toxicity testing or could provide a preliminary way to group nanoparticles based on the ARR.

7.2 Modelling and current nanoparticle testing strategies

Nanoparticle science is rapidly advancing and to facilitate this growth, faster and more efficient methods for evaluating nanomaterial toxicity are required (*Clark et al., 2011*). The model presented here helps to meet this requirement; however, for the model and, in general, the field of nano-bioscience to achieve its full potential, a more integrated approach to nanotoxicity testing is required. The NanoSafety Cluster: Working Group 10 was set up by the European Commission to help establish a directed strategy for the evaluation of toxicity of nanomaterials, which they describe as: Integrated Approaches to Testing and Assessment (IATA) (*Oomen et al., 2014*). In their most recent report, they proposed a three tier approach to nanomaterial testing (*Oomen et al., 2014*), whereby tier one identifies nanomaterials which are know to elicit or may potentially elicit a toxic effect. In this tier the properties of nanomaterials, and the effect they may have, are also taken into consideration, these include:

Particle effects: These are effects caused by the primary particle, via properties such as charge due to modified surface groups.

Chemical Effects: This would relate to any material formed by the break down of the particle, such as the release of ions or secondary nanomaterials.

Catalytic Effects: The creation of molecules due to the catalytic effects from the interaction with the surface of the nanomaterial.

Tier one also takes into account a relevant exposure scenario; whether the particle will agglomerate/aggregate or be mono-disperse and whether the material has been observed to adsorb proteins to its surface, creating a protein corona. This tier is proposed as the first step in the grouping of nanomaterials, which is a key aim of this IATA (*Oomen et al., 2014*).

Tier two of this approach uses standard (and modified, if necessary for nanotoxicity) test methods to assess key areas associated with toxicity, at present four domains have been identified: biokinetics, genotoxicity, local point-of-contact effects and short term effects (including inflammation and cell death). The aim is to use a group of relevant tests in the most efficient way to still obtain a meaningful and informative set of results. Relevant exposure scenarios identified in tier one are used to inform this step, such as: exposure concentration, route and duration. From this data, decisions can be made as to whether to progress to tier three or stop research and development of a specific material (*Oomen et al., 2014*).

If the decision from tiers one and two is to progress, then in tier three a set of more specific tests will be performed and will address more relevant conditions. Proposals for the types of tests to be included in this tier are, for example: instead of using only primary lung cells to evaluate potential inhalation toxicity, a more relevant tissue like organisation of cells to mimic particle transportation and final destination would be employed. Similar tissue like structures could also be constructed for skin and gastro-intestinal tract studies (skin, gastro-

intestinal tract and lungs being three of the most likely initial exposure routes for nanomaterials)(*Oomen et al., 2014*).

The studies performed as part of this thesis are able to fit well with the objectives of this three tier system. The Acellular model described in Chapter 6: Acellular reactivity of polymeric dendrimer nanoparticles as an indicator of oxidative stress *in vitro* (*Maher et al., 2016*) would be helpful as part of tier one to identify nanomaterial properties. For instance, it was thought that the positive surface charge associated with amine modified dendrimers was the key defining parameter governing toxicity. However, when tested acellularly; increased production of ROS was noted. This showed that the nanoparticles also fall into the category of having a catalytic effect and overall, the nanomaterial effects are more likely due to a combination of both the particle effect of surface charge, coupled with the catalytic effect possessed by contact with the surface of the material. The importance of this distinction becomes more apparent when considering PSNP-NH$_2$. PSNP-NH$_2$ have been observed to follow a very similar paradigm of toxicity as the PAMAM dendrimers (*Mukherjee et al., 2010 – A and B, Naha et al., 2009 and 2010, Naha and Byrne, 2013* and *Mukherjee and Byrne, 2013*). However, preliminary data from the acellular assay showed little to no catalytic effect. While, initially, information such as this may seem contradictory, it should be helpful in figuring out the finer points on how physico-chemical properties interact with cellular bodies and affect the overall toxicity. Information form acellular studies could be used in conjunction with any toxicity data already known, to generate applicable dose ranges and time points for use in tier two.

In tier two, the model shown in chapters 3: Numerical simulations of *in vitro* nanoparticle toxicity – the case of Poly (amido amine) dendrimers (*Maher et al., 2014*) and Chapter 4:

Numerical simulations of *in vitro* nanoparticle toxicity – the case of aminated Polystyrene (*Maher and Byrne, 2016 – A*) would be useful. In combination with the acellular data from tier one, the model can be used to simulate how a potential dose range or time point may effect the cell population. In this way, the model alone would not be a fully conclusive result, but would rather be used initially to help decide how best to apply tests as part of tier two. The model would also be helpful in the grouping or classification of nanomaterials. Although at present only one potential Adverse Outcome Pathway (AOP) is described, as more data becomes available and more AOPs for nanomaterial toxicity are elucidated, it would be possible to: review toxicity data obtained in tier two, compare it to simulated toxicity form several different potential AOPs, and finally, see which one would be the most likely for that nanomaterial. This could then be verified using a set of tests which look for key markers in that pathway. To achieve this, much more research into the predictive modelling aspect of nanomaterial science would be needed and, in itself, this research would require a targeted, AOP based approach to model design. However, the modelling and acellular works described in this thesis are applicable to the current direction and strategies of the IATA approach to nanomaterial toxicity testing.

The use of AOPs also has potential in this new framework, as described in Chapter 3 Numerical simulations of *in vitro* nanoparticle toxicity – the case of Poly (amido amine) dendrimers (*Maher et al., 2014*), the modelling approach and Systematic Sequence of Events (SSoE) can be considered as part of an AOP (*OECD, 2013*). However, the way in which AOPs are constructed is adapting to also allow for a more integrated approach (*Oomen et al., 2014*). Classic AOP format would involve the entire step-by-step sequence of events, such as in figure: 7.1.
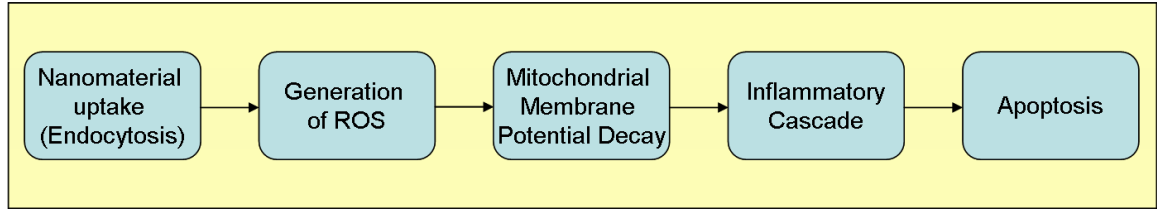
Figure 7.1: Classic AOP format, adapted from the Systematic sequence of events upon amine modified PAMAM exposure to HaCaT cells. This shows particle uptake by endocytosis, leading to increased ROS production, causing mitochondrial membrane potential decay (MMPD) and the subsequent induction of the inflammatory cascade and apoptosis. However, it should be noted that this is a simplified representation of an AOP.

This type of AOP is somewhat limited, however, and would be more associated with a case-by-case approach where each particle may end up having its own AOP, in conflict with the emerging IATA. A more flexible approach is currently under consideration, whereby the cellular events are decoupled from the initiating event. Therefore, the Molecular Initiating Event (MIE) would be well defined and particle dependant, but the resulting AOP would be "chemically agnostic" and applicable to several different MIEs and therefore, several different particles (*Oomen et al., 2014*). The AOP of Figure 7.1 would thus look more like that of Figure 7.2.
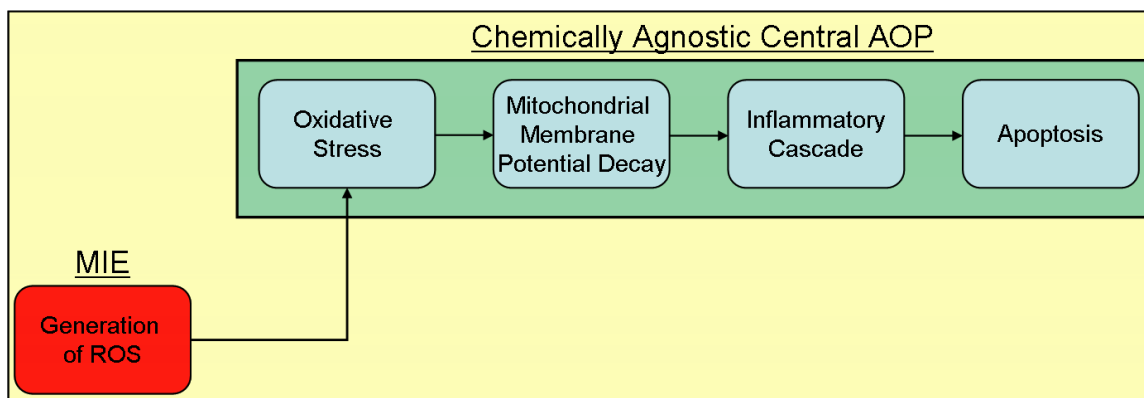
Figure 7.2: Chemically agnostic AOP design. Again a simplified representation of amine modified PAMAM toxicity is depicted here, based on the SSoE of Chapter 3: Numerical simulations of *in vitro* nanoparticle toxicity – the case of Poly (amido amine) dendrimers (*Maher et al., 2014*). Here the central AOP presented is chemically agnostic; meaning that all the steps occurring within it are based on cellular events, these events were initiated by a Molecular Initiating Event (MIE), which in this case is identified as increased ROS production. In this set up several different MIEs could be incorporated into the AOP at the appropriate step in the pathway.

In such an approach, the MIE also represents an interface between chemically agnostic AOPs and the chemically specific approach of QSARs. In the field of toxicology, QSARs operate under the basis that similar molecular structures initiate similar toxic responses. A crucial aspect to the development of a QSAR, especially in development of a QSAR model, is defining a molecular descriptor (*OECD, 2007*). The MIE approach to AOP formation relates the physico-chemical properties of a nanomaterial to a toxic initiation event, thereby aiding in the development of a molecular descriptor for toxicity. In this context, acellular assays such as that described in Chapter 6: Acellular reactivity of polymeric dendrimer

nanoparticles as an indicator of oxidative stress *in vitro* (*Maher et al., 2016*) may be a valuable initial screening strategy.

While the approach of Figure 7.2 is more useful and allows for a single AOP to have a much larger rage of applicability, it does not necessarily take the uptake pathway into account. Chapter 5: Modification of the *in vitro* uptake mechanism and antioxidant levels in HaCaT cells and resultant changes to toxicity and oxidative stress of G4 and G6 Poly (amido amine) dendrimer nanoparticles (*Maher et al., 2016-B*), highlighted the importance of the uptake method in the initiation of toxic effects and showed that if the endocytosis method is bypassed and the PAMAMs are diffused passively into the cell, the particles do not cause the first phase ROS usually associated with their uptake. The particles actually exhibit an anti-oxidant effect, associated with the amine surface groups. However, at higher concentrations of particle toxicity was seen to occur and, interestingly, the EC_{50} values obtained from the MTT and AB assays appeared to match well the EC_{50} values from previous work on toxicity where the normal endocytotic route was followed. This led to the realisation that, although the uptake method was different, the subsequent toxic pathway may have been the same. One explanation of this would be that passive diffusion through the cell membrane and the breaching of the endosome (endosomolysis) would be equivalent processes, both leading to free nanoparticle in the cytosol. The next step: localisation to the mitochondria would be the same. However, in the case of passive uptake this localisation would be the MIE, bypassing the oxidative stress and entering into the pathway at a later stage. Therefore, perhaps to have a more complete AOP, this uptake paradigm should also be taken into account, as illustrated in Figure 7.3.
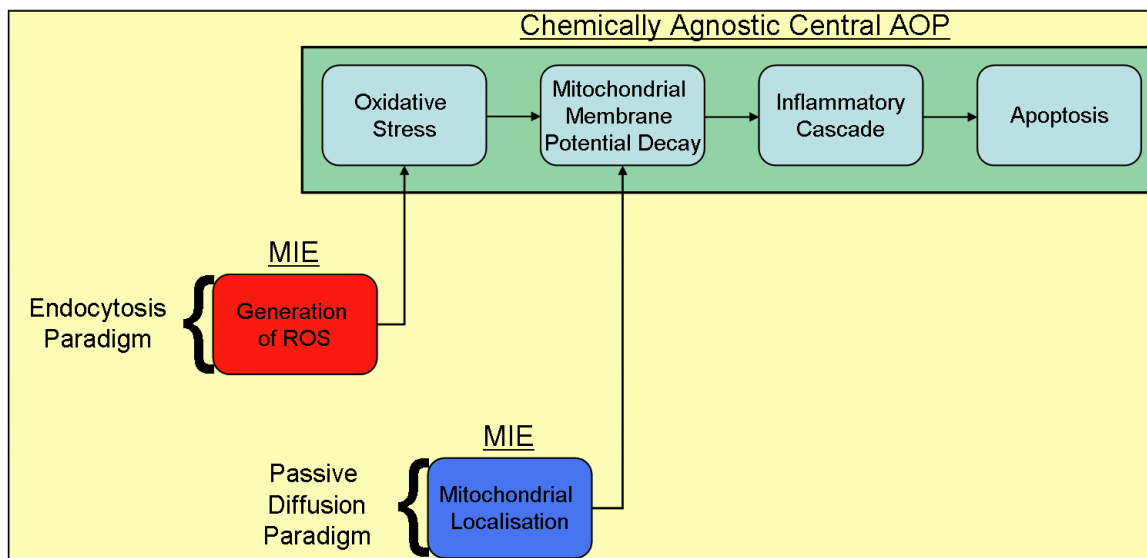
Figure 7.3: Here the proposed AOP of Figure 7.2, based on PAMAM exposure to HaCaT cells is expanded upon to take nanoparticle entry route into account. The MIE for passive diffusion is not fully defined, but is currently associated with localisation to and subsequent disruption of the mitochondria, such an AOP system can be updated when a molecular event is found and, critically, the central AOP is maintained in a chemically agnostic state. Again this representation is a simplified version of an AOP.

Using this AOP system would be beneficial as the central AOP is still based only on cellular events and therefore, is still "chemically agnostic", the uptake method is accounted for and its associated MIE is defined and the point at which this event enters the pathway is also shown. This AOP system maximises the information available and also retains the ability to be applicable to many different particles and MIEs.

This AOP system can also be applied to the development of a QSAR model for predictive toxicology and fits with the current OECD guidelines for QSAR development (*OECD, 2007*).

Currently a QSAR should be associated with the following attributes:

- A defined endpoint

- An unambiguous algorithm

- A defined domain of applicability

- Appropriate measures of goodness of fit, robustness and predictivity

- A mechanistic interpretation (where possible)

An AOP can be applied to the generation of an unambiguous algorithm, it is in itself a defined domain of applicability, the MIE gives it a mechanistic interpretation and there is a defined endpoint. Furthermore, if the AOP is correct then it will aid in the overall goodness of fit, robustness and predictivity of the QSAR (*OECD, 2007*).

7.3 Observations on nanotoxicity reporting

In Chapter 4: Numerical simulations of *in vitro* nanoparticle toxicity – the case of aminated Polystyrene (*Maher and Byrne, 2016 – A*), PSNP-NH$_2$ toxicity was evaluated and when processing that data, the EC$_{50}$ values were calculated and expressed as µM values, this was done as to allow direct comparisons to the data used in Chapter 3: Numerical simulations of *in vitro* nanoparticle toxicity – the case of Poly (amido amine) dendrimers (*Maher et al., 2014*), however, studies have been shown to report data using several different dose metrics (µM, µg/mL and particles/mL). To help further nanoparticle science, a central dose metric should be established, allowing the direct comparison of values as they become available. Furthermore, as discussed in Chapter 4: Numerical simulations of *in vitro* nanoparticle toxicity – the case of aminated Polystyrene (*Maher and Byrne, 2016 – A*), the use of µM showed similar EC$_{50}$ values for the two different sizes of PSNP-NH$_2$ under comparison.

However, when this was converted to particle/mL, stark differences were noted. Similar observations have been made by *Bannunah et al.* (*2014*) where their values in μg/mL were quite different when converted to particle number. If nanotoxicity data is only reported using μM or μg/mL values, important information on the particle number may be lost or overlooked. Therefore, in choosing a dose system to follow, perhaps particles/mL (also abbreviated as ppml) may provide the most logical choice when reporting data from studies involving nanoparticle suspensions.

7.4 Final Conclusions

The work presented in this thesis has allowed valuable insights into both the modelling and mechanisms of nanoparticle toxicity. It has shown that it is possible to simulate nanoparticle data and that a case-by-case approach for this toxic evaluation is not the only way to elucidate information (*Clark et al., 2011*). The future of this work may come by combination with high throughput analysis methods, such as those developed by *Anguissola et al.* (*2014*) to elucidate more steps in the AOP. Finally, the combination of preliminary data from the acellular model, coupled with the cellular predictive model and a full understanding of the MIE and entry points into the AOP will allow for a better simulation of nanoparticle toxicity, thereby allowing for faster and more efficient acquisition of data, and enabling nano-bioscience to keep pace with the speed at which new materials are being generated.

7.5 References

- Anguissola, S., Garry, D., Salvati, A., O'Brien, P.J. and Dawson, K.A. 2014. High content analysis provides mechanistic insights on the pathways of toxicity induced by amine-modified polystyrene nanoparticles. *PLoS One.* **9**(9), e108025 (doi: 10.1371/journal.pone.0108025).

- Bannunah, A.M., Vllasaliu, D., Lord, J. and Stolnik, S. 2014. Mechanisms of nanoparticle internalization and transport across an intestinal epithelial cell model: effect of size and surface charge. *Mol. Pharm.* **11**(12): 4363-4373.

- Chamulitrat, W., Stremmel, W., Kawahara, T., Rokutan, K., Fujii, H., Wingler, K., Schmidt, H.H. and Schmidt, R. 2004. A constitutive NADPH oxidase-like system containing gp91phox homologs in human keratinocytes. *J. Invest. Dermatol.,* **122**(4), 1000-1009.

- Clark, K.A., White, R.H. and Silbergeld, E. K. 2011. Predictive models for nanotoxicology: Current challenges and future opportunities. *Regul. Toxicol. Pharm.,* **59**(3), 361-512.

- Khalid, H., Mukherjee, S.P., O'Neill, L. and Byrne, H.J. 2016. Structural dependence of the *In vitro* cytotoxicity, oxidative stress and uptake mechanisms of Poly (propylene imine) dendritic nanoparticles. *J. Appl. Toxicol.,* **36**(3), 464–473.

- Lee, K.S., Kim, S.R., Park, H.S., Park, S.J., Min, K.H., Lee, K.Y., Choe, Y.H., Hong, S.H., Han, H.J., Lee, Y.R., Kim, J.S., Atlas, D. and Lee, Y.C. 2007. A novel thiol compound, N-acetylcysteine amide, attenuates allergic airway disease by regulating activation of NF-kappaB and hypoxia-inducible factor-1alpha. *Exp. Mol. Med.* **39**(6), 756-768.

- Maher, M.A. and Byrne, H.J. 2016 – A. Numerical simulations of *in vitro* nanoparticle toxicity – the case of aminated Polystyrene. Submit to: *Toxicol. In Vitro*, January 2016.

- Maher, M.A. and Byrne, H.J. 2016 – B. Modification of the *in vitro* uptake mechanism and antioxidant levels in HaCaT cells and resultant changes to toxicity and oxidative stress of G4 and G6 Poly (amido amine) dendrimer nanoparticles. *Anal. Bioanal. Chem.,* DOI: 10.1007/s00216-016-9623-8.

- Maher, M.A., Khalid, H. and Byrne, H.J. 2016. Acellular reactivity of polymeric dendrimer nanoparticles as an indicator of oxidative stress *in vitro*. *Anal. Bioanal. Chem.,* **408**(3), 695–703.

- Maher, M.A., Naha, P.C., Mukerjee, S.P. and Byrne, H.J. 2014. Numerical simulations of *in vitro* nanoparticle toxicity – the case of Poly (amido amine) dendrimers. *Toxicol. In Vitro*, **28**(8), 1449-1460.

- Mukherjee, S.P. and Byrne H.J. 2013. Poly amidoamine dendrimer nanoparticle cytotoxicity oxidative stress, caspase activation and inflammatory response: experimental observation and numerical simulation. *Nanomed: Nanotech. Bio. Med.,* **9**(2), 202-211.

- Mukherjee, S.P., Davoren, M. and Byrne H.J. 2010-A. *In vitro* mammalian cytotoxicological study of PAMAM dendrimers - towards quantitative structure activity relationships. *Toxicol. in Vitro,* **24**(1), 169-177.

- Mukherjee, S.P., Lyng, F.M., Garcia, A., Davoren, M. and Byrne H.J. 2010-B. Mechanistic studies of *in vitro* cytotoxicity of poly (amido amine) dendrimers in mammalian cells. *Toxicol. Appl. Pharm.,* **248**(3), 259–268.

- Naha, P.C. and Byrne, H.J. 2013. Generation of Intracellular Reactive Oxygen Species and Genotoxicity effect to Exposure of Nanosized Poly (amido amine) (PAMAM) dendrimers in PLHC-1 cells *in vitro*. *Aquatic Toxicology,* **132-133**(2103), 61-72.

- Naha, P.C., Davoren, M., Casey, A. and Byrne H.J. 2009. An Ecotoxicological Study of Poly (amido amine) Dendrimers-Toward Quantitative Structure Activity Relationships. *Env. Sci. Technol.,* **43**(17), 6864–6869.

- Naha, P.C., Davoren, M., Lyng, F.M. and Byrne, H.J. 2010. Reactive oxygen species (ROS) induced cytokine production and cytotoxicity of PAMAM dendrimers in J774A.1 cells. *Toxicol. Appl. Pharm.,* **246**(1-2), 91–99.

- Oomen, A.G., Bos, P.M.J., Fernandes, T.F., Hund-Rinke, K., Boraschi, D., Byrne, H.J., Aschberger, K., Gottardo, S., von der Kammer, F., Kühnel, D., Hristozov, D., Marcomini, A. and Migliore, L. 2014. Concern-driven integrated toxicity testing strategies for nanomaterials - Report of the NanoSafety Cluster Working Group 10. *NanoToxicology,* **8**(3), 334-348.

- Organisation for Economic Co-Operation and Development (OECD), 2007. Guidance Document on the Validation of (Quantative) Structure Activity Relationships [(Q)SAR] Models, *OECD*, **ENV/JM/MONO(2007)2**, 2007.

- Organisation for Economic Co-Operation and Development (OECD), 2013. Guidance Document On Developing and Assessing Adverse Outcome Pathways, *OECD,* **ENV/JM/MONO(2013)6**. 2013.

Appendix

Publications

<u>First author Publications</u>

Maher, M.A., Khalid, H. and Byrne, H.J. 2016. Acellular reactivity of polymeric dendrimer nanoparticles as an indicator of oxidative stress *in vitro*. *Anal. Bioanal. Chem.,* **408**(3), 695–703.

Maher, M.A., Naha, P.C., Mukerjee, S.P. and Byrne, H.J. 2014. Numerical simulations of *in vitro* nanoparticle toxicity – the case of Poly (amido amine) dendrimers. *Toxicol. In Vitro*, **28**(8), 1449-1460.

Maher, M.A. and Byrne, H.J. 2016 – B. Modification of the *in vitro* uptake mechanism and antioxidant levels in HaCaT cells and resultant changes to toxicity and oxidative stress of G4 and G6 Poly (amido amine) dendrimer nanoparticles. *Anal. Bioanal. Chem.,* DOI: 10.1007/s00216-016-9623-8.

<u>Currently Under Review</u>

Maher, M.A. and Byrne, H.J. 2016 – A. Numerical simulations of *in vitro* nanoparticle toxicity – the case of aminated Polystyrene. Submit to: *Toxicol. In Vitro*, January 2016.

<u>Other Publications</u>

Sharkey, M.A., Maher, M.A., Guyonvarch, A. and Engel, P.C. 2011. Kinetic characterisation of recombinant *Corynebacterium glutamicum* NAD^+-dependent LDH over-expressed in *E. coli* and its rescue of an $lldD^-$ phenotype in *C. glutamicum*: the issue of reversibility re-examined. *Archives of Microbiology,* **193**(10), 731-740.

Farhane, Z., Bonnier, F., Maher, M.A., Bryant, J., Casey, A. and Byrne, H.J. 2016. Differentiating responses of lung cancer cell lines to Doxorubicin exposure: *in vitro* Raman micro spectroscopy, oxidative stress and bcl-2 protein expression. *J. Biophotonics,* **in press** (DOI: jbio.201600019R1).

Conferences Attended

Q-nano / NanoImpactNet Conference, University College Dublin, Dublin 2012.

European Society of Toxicology *in Vitro*, 17th International Congress, Escola Superior de Tecnologia da Saúde de Lisboa, Lisbon 2012.

Euro Nano Forum, Dublin Convention Centre, Dublin 2013.

Quantitative Biology and Bioinformatics in Modern Medicine, Queens University Belfast, Belfast 2013.

Modules Completed

Introduction to NanoScience, University of Limerick, 2011.

Introduction to Animal Cell Culture: Theory and Techniques, Dublin City University, 2011.

Biomedical Materials, Athlone Institute of Technology, 2012 [online]

Advanced Data Processing Using Microsoft Excel, Dublin City University, 2013.

Modelling Workshops at European Society of Toxicology *in Vitro*, Q-nano and Quantitative Biology and Bioinformatics in Modern Medicine Conferences.

<u>Career Development</u>

2012 – 2015: Demonstrator at School of Food Science and Environmental Health, College of Sciences and Health, Dublin Institute of Technology.

Demonstration for Modules: Biochemistry, Biology, Foundation Chemistry, Medicinal Chemistry and Organic Chemistry.

2016 – Present: Assistant Lecturer at School of Food Science and Environmental Health, College of Sciences and Health, Dublin Institute of Technology.

Modules Include: Foundation Organic Chemistry and Foundation General Chemistry.